SENSORY AND AUTONOMIC INNERVATION OF THE SKIN OF THE RAT LOWER LIP

by

Isabella Ruocco

A thesis submitted to the Faculty of Graduate Studies and Research
of McGill University in partial fulfillment of the requirements
for the Degree of Doctor of Philosophy

September, 2001

Department of Pharmacology and Therapeutics
McGill University
Montreal, Quebec

This thesis is dedicated to my father.
The sacrifices you have made have allowed me to reach my goals and, for that, I shall be eternally grateful.

I owe part of this thesis to my mother, for her constant support and encouragement throughout the years.

Carrissimi genitori vi ringrazio per la vostra pazienza, il vostro affetto, e il vostro amore.

I also owe part of this thesis to my husband for always putting a smile on my face, even in times of despair. Freddy, I thank you for your love, encouragement and understanding.

Bahebak keteer ya habeeby.

ABSTRACT

In this thesis, the innervation patterns by substance P- (SP), dopamine-β-hydroxylase- (DβH) and the vesicular acetylcholine transporter- (VAChT) immunoreactive (IR) fibres were investigated in the skin of the rat lower lip, in order to provide a morphological basis for the possible interactions between sensory and autonomic fibres in the periphery. Our immunocytochemical approach revealed that SP-IR sensory fibres were widely distributed throughout the epidermis and dermis. In the dermis, they were associated with blood vessels, hair follicles, sebaceous glands and mast cells. Electron microscopical quantification revealed that SP-IR fibres equally innervated arterioles, capillaries and venules, all of which were shown to possess SP receptor (NK-1r) immunoreactivity within their walls. DβH- and VAChT-IR fibres were present around blood vessels in the lower dermis, but not in the upper dermis, indicating that these fibres are not as widely distributed as the SP-IR fibres. SP-DβH, SP-VAChT and DβH-VAChT fibre combinations were observed around lower dermal blood vessels. The absence of single labeled blood vessels suggested that blood vessels in the lower dermis are innervated by all three fibre-types. Quantification at the ultrastructural level revealed that DβH- and VAChT-IR terminals lie closer to their targets than SP-IR terminals. Bilateral lesions of the mental nerve, a purely sensory nerve, led to the total loss of SP-IR fibres from the lower lip skin, and to the migration of DβH-IR fibres into the upper dermis, a territory from which they are normally absent. These sprouted fibres remained in their new territory despite the reinnervation of the lower lip by SP-IR fibres. The bilateral removal of the superior cervical ganglia (SCG) caused the complete degeneration of DβH-IR fibres and a transient SP-IR fibre sprouting and NK-1r up-regulation. The

number of SP-IR fibres and the content of SP within these fibres was increased both in the upper and lower dermis following SCG removal. In the lower dermis however, the effect was greater than in the upper dermis.

Therefore we can conclude that SP-, DβH- and VAChT-IR fibres all innervate the same blood vessels in the lower dermis of the rat lower lip skin. Furthermore, the plastic changes observed in the association between SP- and DβH-IR fibres following trauma to peripheral nerve injuries, may lead to painful sensations and, possibly, abnormal blood flow in the affected region.

ABRÉGÉ

Dans cette thèse, les tracés d'innervation par les fibres immunoréactives à la substance P (SP), la dopamine-β-hydroxylase (DβH) et le transporteur vésiculaire de l'acétylcholine (VAChT) ont été étudiés, dans la peau de la lèvre inferieure du rat, afin de mieux comprendre les liens morphologiques qui existent entre les fibres sensorielles et autonomes dans la périphérie. Notre approche immunocytochimique révèle que les fibres sensorielles SPergiques sont largement distribuées à travers l'épiderme et le derme. Dans le derme, ces fibres sont associées avec des vaisseaux sanguins, des follicules pileux, des glandes sébacées et des mastocytes. La quantification en microscopie électronique révèle que les terminaisons SPergiques innervent tout autant les artérioles, les capillaires et les veinules. On a démontré la présence de récepteurs de la SP (NK-1r) sur la paroi de ces vaisseaux sanguins. Les fibres DβHergiques et VAChTergiques sont présentes autour des vaisseaux sanguins du derme inférieur, mais pas autour de ceux du derme supérieur. Cette observation indique que les fibres DβHergiques et VAChTergiques ne sont pas aussi largement distribuées que les fibres SPergiques. Les combinaisons de fibres SPergiques-DβHergiques, SPergiques-VAChTergiques et DβHergiques-VAChTergiques ont été observées autour des vaisseaux sanguins du derme inférieur. L'absence de marquage simple autour des vaisseaux du derme inférieur suggère que ces vaisseaux sont innervés par les trois types de fibres. L'analyse quantitative ultrastructurale révèle que les terminaisons DβHergiques et VAChTergiques se situent plus près de leur cible que les fibres SPergiques. Des lésions bilatérales du nerf mentonnier, un nerf purement sensoriel, produisent la perte totale des fibres SPergiques dans la peau de la lèvre inférieure ainsi que la migration des fibres DβHergiques vers le derme supérieur, un territoire dont elles

sont normalement absentes. Ces fibres DβHergiques persistent dans leur nouveau territoire malgré la réinnervation de la lèvre inférieure par les fibres SPergiques. L'ablation bilatérale du ganglion cervical supérieur (SCG) produit la dégénérescence complète des fibres DβHergiques, ainsi que des effets de courte durée dont, le bourgeonnement des fibres SPergiques et l'accroissement du nombre de récepteurs NK-1. Le nombre de fibres SPergiques ainsi que leur contenu en SP s'accroit dans le derme supérieur et inférieur à la suite de l'ablation du SCG ; toutefois ces effets sont plus marqués dans le derme inférieur.

Nous pouvons donc conclure que les fibres SPergiques, DβHergiques et VAChTergiques innervent les mêmes vaisseaux sanguins dans le derme inférieur de la peau de la lèvre inférieure du rat. De plus, la plasticité dont font preuve les fibres SPergiques et DβHergiques à la suite de lésions des nerfs périphériques peut causer des sensations douloureuses, et possiblement un afflux sanguin anormal dans la région affectée.

TABLE OF CONTENTS

LIST OF FIGURES

LIST OF TABLES

GLOSSARY

ABC	Avidin-biotin complex
ACh	Acetylcholine
AChE	Acetylcholinesterase
AMPA	α-amino-3-hydroxy-5-methyl-isoxazole
ANOVA	Analysis of variance
AVA	Arterivenous anastomoses
CCI	Chronic constriction injury
CRPS	Complex regional pain syndrome
CGRP	Calcitonin gene-related peptide
CP-96,344	(2R,3R)-cis-(diphenylmethyl)-N-[(2-methoxyphenyl)-methyl-1-azabicyclo-[2.2.2]-octan-3-amine]
CP-96,345	(2S,3S)-cis-(diphenylmethyl)-N-[(2-methoxyphenyl)-methyl-1-azabicyclo-[2.2.2]-octan-3-amine]
CNS	Central nervous system
DAB	3,3'-Diaminobenzidine tetrahydrochloride
DβH	Dopamine-beta-hydroxylase
DRG	Dorsal root ganglion
FRAP	Fluoride-resistant acid phosphatase
GAM	Goat anti-mouse immunoglobulin G
GAP 43	Growth-associated protein 43
GDNF	Glial cell line-derived neurotrophic factor
GSA-IB4	Griffonia simplicifolia A-isolectin B4
HRP	Horseradish peroxidase
ICC	Immunocytochemistry
IgG	Immunoglobulin
i.p.	Intraperitoneal
IR	Immunoreactive
L-NAME	N^G-nitro-L-arginine methyl ester
NGF	Nerve growth factor
NGS	Normal goat serum
NK-1r	Neurokinin-1 receptor
NK-2r	Neurokinin-2 receptor
NK-3r	Neurokinin-3 receptor
NKA	Neurokinin A
NKB	Neurokinin B
NMDA	N-methyl-D-aspartate
NSAIDs	Non-steroidal anti-inflammatory drugs
MN	Mental nerve
NPY	Neuropeptide Y

OCT	Optimal cutting temperature medium
PB	Phosphate buffer
PBS	Phosphate buffered saline
PBS+T	Phosphate buffered saline containing 0.2% Triton X-100
PGP 9.5	Protein gene product 9.5
PGSN	Postganglionic sympathetic neuron
PKC	Protein kinase C
PNS	Peripheral nervous system
PPT	Preprotachykinin
PSL	Partial sciatic nerve ligation
P2X	Purinergic receptor subtype 2X
ROD	Relative optical density
RSD	Reflex sympathetic dystrophy
s.c.	Subcutaneous
SCG	Superior cervical ganglion
SIP	Sympathetically independent pain
SMP	Sympathetically maintained pain
SNL	Spinal nerve ligation
SP	Substance P
TrkA	Tyrosine receptor kinase A
TTX_R	Tetrodotoxin-resistant
TTX_S	Tetrodotoxin-sensitive
VAChT	Vesicular acetylcholine transporter
VIP	Vasoactive intestinal polypeptide
v/v	Volume/volume
VR1	Vanilloid receptor 1

ACKNOWLEDGMENTS

First, and foremost, I thank my supervisor **Dr. Alfredo Ribeiro-da-Silva** for believing in me. You never ceased to encourage and support me. You have taught me to always push further and that good is just not good enough. Your pursuit of excellence has taught me how to be critical of my work and to always expect more of myself. You have made me discover things I never thought I was capable of.

I am grateful to **Dr. A. Claudio Cuello** for his constructive criticism in the preparation of the manuscripts and for teaching me how to perform mental nerve lesions and superior cervical ganglia extractions.

To the office staff who was always there throughout the years and made sure that things ran as smoothly as possible: **Mona Azar, Hélène Duplessis, Jennifer Marleau and Pam Moore.**

To **Sid Parkinson,** for his editorial assistance and his help in the submission of the manuscripts. Your help has contributed to improving my writing skills.

To the wonderful ladies with whom I have shared my lunches over the years, for your friendship and support (sorry about all the wedding talk). **Annie Constantin, Adriana Ducatenzeiler, Anna McNicoll, Johanne Ouellette, Manon St-Louis and Johanne Théberge**, you always brought joy to my day.

To **Mary Balak**, thanks to your expertise in electron microscopy I was able to process difficult material and obtain remarkable tissue preservation.

To **Alan Forster**, for developing all those pictures. It was a lot of work and I know that I was pretty demanding at times.

To **Sylvain "mon oncle" Côté** I shall always be indebted. Your critical mind and perfectionism have allowed me to achieve remarkable working standards. I shall miss all our conversations (work-related and not so work-related). Your friendship through the years has helped me through the good and bad times. Thank you for always being there to listen to me even when poor Francine was waiting for you. Your patience and consideration of others are qualities that make you a remarkable person.

To **Manon St-Louis,** for your friendship, support and encouragement. I am grateful for all your help with the photocopies and the preparation of the thesis.

To **Eilis Dowd, Michele Ramien, Mirna Sirinyan** for their friendship and help in revising my thesis.

To **Emmanuelle Roux** for revising my French abstract.

To **Amber McLeod,** for her friendship, support and encouragement.

I wish to thank the **Department of Pharmacology and Therapeutics** for granting me the F.C. MacIntosh prize in Pharmacology (2000).

GUIDELINES FOR THESIS PREPARATION

The " Guidelines for Thesis Preparation", which have been reproduced hereunder, state that:

> Candidates have the option of including, as part of the thesis, the text of one or more papers submitted, or to be submitted for publication, or the clearly-duplicated text of one or more published papers. These texts must conform to the "Guidelines for Thesis Preparation" with respect to font size, line spacing and margin sizes and must be bound together as an integral part of the thesis.
>
> The thesis must be more than a collection of manuscripts. All components must be integrated into a cohesive unit with a logical progression from one chapter to the next. In order to ensure that the thesis has continuity, connecting texts that provide logical bridges between the different papers are mandatory.
>
> The thesis must include a table of contents, an abstract in English and French, an introduction which clearly states the rational and objectives of the research, a comprehensive review of the literature and a final conclusion and summary.
>
> As manuscripts for publication are often very concise documents, where appropriate, additional material must be provided (e.g. appendices) in sufficient detail to allow a clear and precise judgement to be made of the importance and originality of the research reported in the thesis.
>
> In general, when co-authored papers are included in a thesis, the candidate must have made a substantial contribution to all papers included in the thesis. In addition, the candidate is required to make an explicit statement in the thesis as to who contributed to such work and to what extent. This statement should appear in a single section entitled "Contributions of Authors" as a preface to the thesis. The supervisor must attest to the accuracy of this statement at the doctoral oral defense. Since the task of the examiners is made more difficult in these cases, it is in the candidate's interest to clearly specify the responsabilities of all the authors of the co-authored papers.
>
> When previously published copyright material is presented in a thesis, the candidate must obtain, if necessary, signed waivers from the co-authors and publishers and submit these to the Thesis Office with the final deposition.

Irrespective of the internal and external examiners reports, if the oral defense committee feels that the thesis has major omissions with regard to the above guidelines, the candidate may be required to resubmit an amended version of the thesis.

In no case can a co-author of any component of a thesis serve as an external examiner for that thesis.

CONTRIBUTIONS OF AUTHORS

This thesis is based on data obtained for the generation of the following four manuscripts, which are found in chapters two to five:

CHAPTER 2: Light and Electron Microscopic Study of the Distribution of Substance P- Immunoreactive Fibres and Neurokinin-1 Receptors in the Skin of the Rat Lower Lip.
I. Ruocco, A.C. Cuello, R. Shigemoto, A. Ribeiro-da-Silva
Journal of Comparative Neurology 432:466-480 (2001)

CHAPTER 3: Skin Blood Vessels are Simultaneously Innervated by Sensory, Sympathetic and Parasympathetic Fibres.
I. Ruocco, A.C. Cuello, A. Parent, A. Ribeiro-da-Silva
To be submitted: Journal of Comparative Neurology (2001)

CHAPTER 4: Peripheral Nerve Injury Leads to the Establishment of a Novel Pattern of Sympathetic Fibre Innervation in the Rat Skin.
I. Ruocco, A.C. Cuello, A. Ribeiro-da-Silva
Journal of Comparative Neurology 422:287-296 (2000)

CHAPTER 5: Sympathectomies Lead to Transient Sensory Fibre Plasticity in the Rat Skin.
I. Ruocco, A.C. Cuello, R. Shigemoto, A. Ribeiro-da-Silva
In press: Neuroscience (2001)

Responsabilities of authors and co-authors:

Dr. A. Ribeiro-da-Silva: Principal investigator of all projects. Provided the main intellectual influence in all manuscripts. Performed the immunocytochemistry and took the picture for figures 2.8 and 6.2. Edited all manuscripts.

Dr. A.C. Cuello: Investigator of all projects. Intellectual contribution in all manuscripts. Showed I. Ruocco how to perform both mental nerve lesions and sympathectomies. Edited all manuscripts.

Dr. R. Shigemoto: Provided the antibody against the NK-1r.

Dr. A. Parent: Provided the monkey tissue.

I. Ruocco: Investigator for all projects. Planned all experiments, performed all surgeries and immunocytochemical stainings, analysed and quantified all the data, and obtained all light and electron micrographs (except figures 2.8 and 6.2) included in the thesis. Wrote the initial version of all manuscripts presented herein.

CHAPTER 1

GENERAL INTRODUCTION

1.1 Statement of the problem and purpose of the investigation

Neuropathic pain has been defined as "pain resulting from noninflammatory dysfunction of the peripheral or central nervous system without peripheral nociceptor stimulation or trauma" (MacFarlane B.V. et al., 1997). Under normal circumstances, pain sensations serve a protective role and allow for proper tissue repair to occur. However, neuropathic pain is "abnormal" in that the pain persists following tissue repair and the amplitude of the pain responses is grossly exaggerated. Furthermore, this condition is extremely difficult to treat as the pain is unresponsive to non-steroidal anti-inflammatory drugs and is usually insensitive to opioids (Woolf C.J. and Mannion R.J., 1999).

In the United States, 1.5% of the population is said to suffer from neuropathic pain which manifests itself as lower back pain, diabetic neuropathy, post-herpetic neuralgia, cancer-related pain, causalgia or reflex sympathetic dystrophy (Bennett G.J., 1998). In the United Kingdom, 1% of the population is said to suffer from neuropathic pain, 50% of which is over 65 years of age (Bowsher D., 1991). Thus, as the average life expectancy is constantly increasing, neuropathic pain sufferers will account for a considerably larger proportion of the population over time. The economical impact of neuropathic pain *per se* is not known. Regarding diabetes, the second greatest contributor to neuropathic pain, in 1986 the United States estimated that they were spending 240 million dollars for the care of these diabetic neuropathic pain sufferers. In 1994, 110 million people worldwide had diabetes and it is estimated that this number will escalate to 220 million by the year 2010, of which an estimated 50% with a 25-year history will develop diabetic neuropathies [for review see (Thomas P.K., 1999)].

Despite the extensive literature concerning neuropathic pain, we still appear to be far from an effective treatment. In fact, although peripheral neuropathies often occur following peripheral nerve damage, the aetiology of the underlying insult may vary considerably. For instance, compression, hereditary, ischaemic, metabolic, traumatic, toxic, infectious, or immune-mediated injuries may all lead to neuropathic pain. Multiple symptoms may result from a single mechanism, different mechanisms may cause the same symptoms and, more importantly, mechanisms may change over time [for review see (Woolf C.J. and Mannion R.J., 1999)]. Therefore, it becomes obvious that attempting to find a single effective treatment for such a complex syndrome is quite tedious, and is further complicated by the fact that important aspects of the normal arrangement of the central and peripheral nervous systems still remain unknown or misunderstood. Furthermore, little attention has been given to the terminal arborizations of peripheral fibres and most studies have based their findings on results obtained in dorsal root ganglia (DRG). This is somewhat surprising since changes in innervation patterns and nerve function in the periphery might be of great significance as fibres that convey pain-related information are ultimately activated peripherally, i.e. at the pain receptor (nociceptor) level.

Consequently, the object of this thesis is to investigate the innervation patterns of the skin by sensory and autonomic systems under normal and abnormal conditions, in an attempt to unravel the mechanisms underlying peripheral neuropathies. Peripheral neuropathies have been characterized by a variety of central nervous system (CNS) and DRG plastic changes. However, no attempt has been made to characterize the changes occurring more peripherally. The ultimate aim of this thesis is to characterize the sensory

and sympathetic terminal field changes that occur following peripheral nerve lesions, and their possible contribution in the establishment of neuropathic pain.

1.2 Basic anatomical and functional description of the skin

The skin is the largest and heaviest organ of the human body. It accounts for 16% of total body weight and in adults its surface ranges from 1.2 - 2.3 m^2 (Montagna W.W. and Parakkal P.F., 1974). The major function of the skin is one of protection from the external environment (Montagna W.W. and Parakkal P.F., 1974). For instance, the skin protects us from impact and friction injuries, from bacterial invasion, from excessive water loss and from the sun's ultraviolet radiation. The glands, blood vessels and adipose tissue play a role in thermoregulation, body metabolism and excretion (e.g. sweat glands). The skin is also important for the continuous reception of sensory stimuli such as touch, temperature and pain from the environment. The elastic property of the skin allows us to adapt to situations such as oedema and pregnancy (Junqueira L.C. et al., 1998). In certain areas of the body, human skin possesses very unique patterns of ridges and grooves. These dermatoglyphs, better known as fingerprints, confer individuality, as no two people possess the same set of fingerprints.

The skin is comprised of two major layers: the epidermis and the dermis. Each layer has its own functions. Furthermore, the skin can be divided into two main types: 1) glabrous and thick skin (0.4 – 0.6 mm), 2) non-glabrous (hairy) and thin skin (0.075 – 0.15 nm) (Gartner L.P. and Hiatt J.L., 1997). The former occurs on the skin of palms and soles, whereas the latter occurs on the rest of the body. In the above description, skin thickness is based on the thickness of the epidermis alone. A summary description of the

skin layers and appendages follows. However for a more complete review, the reader is referred to the following textbooks, as the information above and hereafter was obtained from these sources: 1) Bloom and Fawcett, a Textbook of Histology (Fawcett D.W., 1986), 2) Cell and Tissue Biology (Anonymous, 1988), 3) Pharmacology of the Skin (Anonymous, 1992), 4) di Fiore's Atlas of Histology with Functional Correlations (Eroschenko V.P., 1993), 5) Color Textbook of Histology (Gartner L.P. and Hiatt J.L., 1997), 6) Basic Histology (Junqueira L.C. et al., 1998), 7) Color Atlas of Histology (Gartner L.P. and Hiatt J.L., 2000).

1.2.1 **Epidermis**

The epidermis is a highly proliferative avascular tissue (Montagna W. and Lobitz W.C.Jr., 1964). It is divided into 5 layers: basal, spinous, granular, transition zone and corneal, which are also respectively referred to as stratum germinativum, stratum spinosum, stratum granulosum, stratum lucidum and stratum corneum (MacKenzie I.L., 1972). These layers are considerably thicker in glabrous skin than in hairy skin. Keratinocytes are the major epidermal cell type and are involved in the production of keratin. Of these cells, those in the proliferative state are located in the lower layers (basal and spinous) of the epidermis. The cells gradually migrate towards the outer layer (corneal) of the skin and along the way they mature into highly differentiated non-dividing cells. These differentiated cells are eventually shed in a process of desquamation (Williams M., 1984). Thus, the human epidermis is renewed every 15 – 30 days depending on age and body region.

1.2.1.1 *Basal layer*

The cells of the basal layer constitute the major epidermal cell type, accounting for over 90% of epidermal cells. These keratinocytes are the most undifferentiated and constitute stem cells (Lavker R.M. and Sun T.-T., 1982). They lie at the dermal-epidermal junction over the basal lamina that physically separates the epidermis from the dermis. Being immature cells, they do not possess biological markers, as these are present in more differentiated cells only. These cells also show intense mitotic activity, especially at night. Numerous desmosomes bind the cells on their lateral and upper surfaces (Allen T.D. and Potten C.S., 1975), allowing the basal cell layer to serve as a protective sheath against pathogen invasion and fluid loss.

The basal cell layer also houses the pigment cells better known as melanocytes (Billingham R.E. and Silvers W.K., 1960). It should be noted, however, that these cells also occur in the superficial dermis. Melanin granules are produced in melanocyte organelles known as melanosomes. Upon release, these granules accumulate in the apical region of basal and spinous cells, thus protecting the cell nuclei from the damaging effects of sunrays. Racial variations in skin colour are the result of melanosome number and size and melanin location within the cell, as the number of melanocytes in the skin is constant across races (800-2300 / mm^2) (Fitzpatrick T.B. et al., 1979). Melanin is not the only factor responsible for skin colour. Other factors such as skin carotene content, the number of blood vessels in the skin, and the colour of the blood flowing through these blood vessels are also involved in determining skin colour (Junqueira L.C. et al., 1998).

Another cell type, which occurs in the basal layer of the epidermis, is the Merkel cell. These cells are more abundant in thick skin, particularly in the fingertips. A disk-

shaped free nerve ending is present at the base of these cells forming Merkel cell-neurite complexes (Mihara M. et al., 1979).

1.2.1.2 *Spinous layer*

The spinous layer lies just above the basal layer and constitutes the thickest layer of the epidermis. The keratinocytes in this layer are firmly held together by cytoplasmic spines and desmosomes, which give the cell surface a studded appearance, hence its name (Holbrook K.A. and Wolff K., 1987). The cytoplasmic spines are filled with tonofibrils that are involved in maintaining cohesion amongst cells and in resisting abrasion. The spinous layer is thickest in areas undergoing constant friction and pressure such as the soles of feet.

The spinous layer may play an important role in initiating immunological reactions due to the presence of Langerhan's cells (Edelson R.L. and Fink J.M., 1985). These cells are present throughout the epidermis, accounting for 2-3% of epidermal cells, but are mostly concentrated in the spinous layer. Langerhan's cells possess numerous long processes and thus are sometimes referred to as dendritic cells (Wolff K. and Stingl G., 1983). These macrophage derivatives, by binding antigen (Ia, Fc and C3 receptors are present on the cell surface) and presenting it to T lymphocytes, are capable of directly stimulating T lymphocytes (Rowden G., 1977).

1.2.1.3 *Granular layer*

The granular layer is not very prominent in thin skin in which it is often represented only by isolated cells (Anonymous, 1992; Eroschenko V.P., 1993; Gartner

L.P. and Hiatt J.L., 2000). It gets its name from the presence of non-membrane coated keratohyalin granules in the keratinocytes (Junqueira L.C. et al., 1998). These keratinocytes also possess membrane-coated lamellar granules (Junqueira L.C. et al., 1998). Upon fusing with the cell plasma membranes, these granules release their contents in the form of lipid-containing sheaths into the intracellular space. The lipid sheath provides a protective barrier against the invasion of foreign material and, most importantly, a sealing effect upon the skin. It is this sealing of the skin, among other things, during evolution that allowed for the development of terrestrial life. The cells above the granular layer are deprived of nutrients and thus die rapidly.

1.2.1.4 *Transition zone*

This region is the transition between the viable layers (basal, spinous and granular) and the non-viable layer (corneal) of the epidermis. It is a thin translucent layer that is present only in thick skin (palms of hands and soles of feet). Extensive cellular remodelling occurs in this portion of the epidermis (Elias P.M., 1983). The organelles, DNA and RNA within the cells, are destroyed by active proteases and nucleases, while the entire cellular lipid content is extruded into the extracellular matrix. The keratin filaments are restructured into a more stable form and the cornified envelope is formed.

1.2.1.5 *Corneal layer*

It is in this layer that keratinocytes undergo their final differentiation into corneocytes (Anonymous, 1992). The corneocytes are dead keratinocytes with keratin-filled cytoplasm. Modified desmosomes and interdigitations of grooves and ridges help

maintain the cells together (Fawcett D.W., 1986; Anonymous, 1992). Cells near the surface of the skin are without desmosomes. These horny cells or squames are ready to be sloughed or desquamated (Williams M., 1984). This highly organized array of interlocking keratinocytes constitutes the most important permeability barrier for the skin.

1.2.2 **Dermis**

The dermis lies just beneath the epidermis and is the thickest layer of the skin (Montagna W. et al., 1970). It comprises 90% of the skin and its thickness varies according to body region, ranging from 0.6-3.0 mm. A basal lamina separates the basal layer of the epidermis from the dermis. This area of junction between dermis and epidermis is referred to as the dermal-epidermal junction (Briggaman R.A. and Wheeler C.E.Jr., 1975). This region is characterized by highly irregular upward projections of dermis (also known as dermal papillae) that interdigitate with downward epidermal projections (also called rete ridges). These interdigitations serve to reinforce the dermal-epidermal junction and are more frequently encountered in skin areas that are under considerable pressure such as the foot soles. They are also responsible for the formation of the dermatoglyphs.

The major cell types encountered in the dermis are fibroblasts, macrophages and mast cells (Anonymous, 1992). Fibroblasts are responsible for synthesizing and remodelling connective tissue proteins. Connective tissue is the major constituent of the dermis and it provides skin with its strength. The macrophages present antigens to immunocompetent cells and, in doing so, are involved in preventing or controlling

infection. Mast cells are mostly concentrated around blood vessels. These cells are capable of responding to various stimuli such as light, cold, vibration, pressure, chemical, immunological, as well as to acute trauma.

The dermal layer has a rich network of blood and lymphatic vessels. The main blood vessels encountered are arterioles, capillaries and venules (Winkelmann R.K. et al., 1961). The blood vessels of the dermis are crucial for skin homeostasis, as they are the only source of nourishment to the avascular epidermis. Furthermore, the dermis also houses nerves and various skin appendages. Skin appendages and glands are epidermal derivatives that invaginate into the dermis. Such structures include hairs, nails, sebaceous glands, eccrine and apocrine sweat glands.

The dermis is composed of two layers: the papillary layer also known as the superficial or upper dermis, and the reticular layer commonly referred to as the deeper or lower dermis. No clear boundary separates these layers.

1.2.2.1 *Papillary layer (upper dermis)*

The papillary layer lies directly below the epidermis (Montagna W. et al., 1970). It is a thin layer of loose connective tissue. This layer derives its name from the fact that it is the major constituent of the dermal papillae. Fibroblasts are the most prominent cell type of this layer. They are involved in synthesizing collagen fibres, which in this region are quite small.

An encapsulated receptor is a connective tissue capsule that is invested by the end portion of a terminal axon. In the papillary layer, such receptors include Meissner

corpuscles and Krause end bulbs, which function as mechanoreceptors (Halata Z., 1975; Gartner L.P. and Hiatt J.L., 1997).

1.2.2.2 *Reticular layer (lower dermis)*

The reticular layer is the thickest layer of the skin and lies just above the hypodermis (Montagna W. et al., 1970). It is composed of irregular connective tissue. This layer contains more collagen fibres, larger fibre bundles and fewer cells than the papillary layer. Although elastic fibres are found throughout the dermis, thick elastic fibres are a characteristic of the reticular layer.

Pacinian corpuscles and Ruffini endings are the specialized encapsulated receptors found in the reticular layer (Cauna N. and Mannan G., 1958; Gartner L.P. and Hiatt J.L., 1997). These structures are responsible for conveying information about pressure or vibration and tensional forces, respectively.

1.2.3 **Hypodermis**

The hypodermis lies directly below the dermal reticular layer and is composed mainly of adipocytes – fat-producing cells (Fawcett D.W., 1986). The hypodermis is not part of the skin, but rather forms the underlying fascia or subcutaneous tissue. Its main function is to provide a cushion separating the skin from bone and muscle. It also provides an energy reserve, allows for skin mobility, moulds body contours and insulates the body. The elastic and collagen fibres of the hypodermis are continuous with those of the dermis.

1.3 Skin microcirculation

1.3.1 Blood vessel distribution in the skin

The dermis is highly vascularized by the arterial system and its vascularization exceeds the metabolic demands of the skin. The vasculature of the skin is referred to as skin microcirculation and its most prominent role is that of thermoregulation (Braverman I.M. and Yen A., 1977). Blood vessels in the skin are arranged into two networks or plexuses (Winkelmann R.K. et al., 1961). The deepest plexus is found between the dermal reticular layer and the hypodermis. Branches from the latter supply hair follicles, sebaceous glands and sweat glands. The more superficial plexus is located between the papillary and reticular dermal layers. Branches from this plexus vascularize the dermal papillae (Braverman I.M. and Yen A., 1977). Each dermal papilla receives a single capillary loop that is composed of an ascending arteriole, a capillary portion and a descending venular portion. This arrangement allows for nourishment of the avascular epidermis.

Human skin vasculature is characterized by the presence of numerous arteriovenous anastomoses (AVA). These shunts are generally found throughout the body, but they are most prominent in the upper reticular layer of fingertips, toes, nail beds, nose and lips. AVA occur in the deep and superficial dermis and are important for thermoregulation (Hales J.R. et al., 1978). Blood from the arteriolar system is shunted rapidly into the venous system without going through capillaries. This allows for heat conservation in extremely cold conditions, as heat loss through the skin surface is avoided. The AVA occur in small vessels and are under adrenergic and cholinergic control (Cauna N., 1970).

1.3.2 **Anatomical description of skin blood vessels**

Normally blood flows through skin blood vessels in the following sequence: from arterioles to metarterioles to capillaries to post-capillary venules and finally into venules. Each blood vessel type possesses its own characteristic features.

Arterioles: Arterioles are small arteries involved in pressure regulation with lumen diameters of less than 0.5 mm in humans (Rhodin J.A., 1967). They are referred to as efferent vessels and their function is to carry nutrient- and oxygen-filled blood to the tissue.

Metarterioles: Metarterioles, also referred to as terminal arterioles, branch to be continued capillary networks with a large surface area. Constriction of the metarterioles regulates blood flow but does not completely prevent flow into capillaries. Pre-capillary sphincters composed of a single discontinuous layer of smooth muscle cells are a characteristic feature of metarterioles (Rhodin J.A., 1967). Constriction of the sphincters completely blocks blood flow into capillaries and thus shunts blood into the AVA. The sphincters respond to changes in the immediate environment.

Capillaries: Capillaries are arranged in a network with a great surface area and a diameter of 8-10 μm in humans (Palade G., 1953). It is at the level of these vessels that interchanges between blood and tissue occur (Florey H., 1961). Circulation through capillaries is controlled by neural and hormonal mechanisms. Capillaries function as a selective permeability membrane. They are also involved in synthetic and metabolic activities, as well as preventing platelet aggregation (antithrombogenic) to the connective tissue in the blood vessel wall following vessel damage. The vessels are characterized by

surrounding pericytes, which are modified smooth muscle cells (Bennett H.S. et al., 1959).

Post-capillary venules: Post-capillary venules are the transition vessels between capillaries and venules. These vessels operate more like venules than capillaries, and have a 15-20 μm diameter in humans (Rhodin J.A., 1968). Metarterioles and post-capillary venules are commonly called transition vessels.

Venules: Venules are small veins that transport products of metabolism towards the heart. These are afferent vessels with a diameter of 0.2-1 mm in humans (Movat H.Z. and Pernando N.V.P., 1964; Rhodin J.A., 1968). The capillary networks all converge into venules.

All the information presented above refers to the arrangement of human blood vessels. In rodents, the blood vessel anatomy is much simpler, the transition between blood vessel types is less obvious, and fewer smooth muscle cells are present in the blood vessel walls (Rhodin J.A.G., 1974). For instance, rodent arterioles will have one or two complete layers of smooth muscle cells compared with one to five in humans. Rodent venules will have one incomplete smooth muscle layer in their blood vessel wall, instead of one to two complete layers in humans.

1.4 Skin innervation

The skin is the largest sense organ of the body and thus is highly innervated. The skin is equipped to perceive sensory modalities such as touch, heat, cold and pain and these sensations serve to protect and guide us in our environment.

1.4.1 **Sensory nervous system**

The skin is innervated by the peripheral processes of primary sensory neurons and by autonomic fibres. Although the sensory innervation of the skin is described in textbooks and taught to medical students, the emphasis is on Merkel disks and encapsulated receptors that are associated with thick myelinated afferents. For a comprehensive review of such receptors, related to sensory modalities other than nociception, the reader is referred to Iggo and Andres (Iggo A. and Andres K.H., 1982) or Jones (Jones E.G., 1988).

The small diameter sensory fibres correspond to C (unmyelinated) and Aδ (thinly myelinated) fibres. Most of these small diameter fibres convey pain-related information and, therefore, are often named nociceptors. However, the term "nociceptor" should be restricted to the fibre terminals. These small diameter fibres represent the peripheral processes of pseudo-unipolar neurons of small or medium size located in the dorsal root ganglia and trigeminal ganglion. The central processes of these neurons terminate in the superficial laminae of the dorsal horn of the spinal cord and trigeminal subnucleus caudalis [for reviews see (Ribeiro-da-Silva A., 1995; Grant G., 1995)]. The first unequivocally identified subset of sensory fibres with a likely nociceptive function was the substance P (SP)-immunoreactive (IR) population (Hökfelt T. et al., 1975; Hökfelt T. et al., 1977). The primary sensory origin of these fibres was experimentally demonstrated by Cuello et al. (Cuello A.C. et al., 1978). Immunoreactivity for other neuropeptides, such as neurokinin A (Hua X.-Y. et al., 1985), somatostatin (Hökfelt T. et al., 1976), calcitonin gene-related peptide (Wiesenfeld-Hallin Z. et al., 1984), galanin (Ju G. et al., 1987) and endomorphine-2 (Martin-Schild S. et al., 1998), was also demonstrated in

primary sensory fibres.

1.4.1.1 Tachykinins

SP is a member of the mammalian tachykinin family, which is also comprised of neurokinin A (NKA) and neurokinin B (NKB). The tachykinins are encoded by the preprotachykinin (PPT) I (or PPT A) and PPT II (or PPT B) genes, two distinct, but related, genes. Following elaborate posttranscriptional and posttranslational processing SP and NKA are generated from the PPT I gene, while NKB is generated from the PPT II gene [for reviews see (Nakanishi S., 1987; Fong T.M., 1996)]. Alternative splicing of the PPT A gene generates three mRNA species, α-PPT A, β-PPT A and γ-PPT A. α-PPT A mRNA encodes only for SP, while β- and γ-PPT A mRNAs encode for both SP and NKA (Nawa H. et al., 1984; Krause J.E. et al., 1987). Interestingly, in the rat CNS and peripheral tissues, α-PPT A mRNA represents less than 1% of the PPT A gene splice product, whereas β- and γ-PPT A mRNAs represent 80 and 20% respectively (Krause J.E. et al., 1987; Carter M.S. and Krause J.E., 1990). The tachykinins are found both centrally and peripherally, where they exert a variety of biological functions [for review see (Otsuka M. and Yoshioka K., 1993)]. In the periphery, SP and NKA are the most abundant, while NKB remains virtually at undetectable levels. SP, NKA and NKB respectively bind to the mammalian neurokinin-1 (NK-1), NK-2 and NK-3 G-protein coupled receptors (Iversen L.L. et al., 1987). The tachykinins are capable of binding to all three neurokinin receptors, although with varying degrees of affinities (Fong T.M., 1996).

1.4.1.2 Calcitonin gene-related peptide

In the early 1980's, a new 37-amino acid sensory neuropeptide was identified: calcitonin gene-related peptide (CGRP) (Amara S.G. et al., 1982). There are two isoforms of CGRP, α-CGRP and β-CGRP, and they differ by a single amino acid [for reviews see (Emeson R.B., 1996; Hall J.M. and Brain S.D., 1996)]. Studies in the rat have shown that α- and β-CGRP are preferentially expressed in sensory neurons and enteric neurons, respectively (Mulderry P.K. et al., 1988).

CGRP immunoreactivity has been shown to occur in almost all neuropeptide-containing sensory neurons. Numerous immunocytochemical studies have shown CGRP to be co-localized with SP in primary sensory neurons, while some neurons contained CGRP only (Lee Y. et al., 1985; Skofitsch G. and Jacobowtiz D.M., 1985; Gibbins I.L. et al., 1985; Lee Y. et al., 1985). It was later found that virtually, if not all, SP-IR sensory neurons co-localize CGRP immunoreactivity (Wiesenfeld-Hallin Z. et al., 1984; Ju G. et al., 1987), although only a proportion of CGRP-IR neurons co-localized SP immunoreactivity. The issue of the proportion of CGRP-IR neurons co-localizing SP immunoreactivity is not clearly established in the literature. For instance, Gibbins et al. (1987) showed that 25% of CGRP-IR neurons in human skin also contained SP immunoreactivity, while the remaining 75% contained somatostatin immunoreactivity. However, Dalsgaard et al. (1989) reported that, in human skin, the majority of CGRP-IR fibres contained SP immunoreactivity, while only a minority of CGRP-IR fibres were also immunoreactive for somatostatin. These discrepancies can probably be explained more by differences in the antibodies and/or protocols used, rather than by inter-species differences. Furthermore, the values obtained by Dalsgaard et al. are in agreement with

data obtained at the DRG level by other investigators. Nonetheless, CGRP has been shown to be amongst the most abundant neuropeptides in human skin (Gibbins I.L. et al., 1987).

CGRP(8-37), the C-terminal fragment of human α-CGRP has been shown to be a competitive antagonist of CGRP receptors (Chiba T. et al., 1989; Dennis T. et al., 1990). Using this antagonist, the existence of two CGRP receptor subtypes has been proposed (Dennis T. et al., 1990). These consist of $CGRP_1$ and $CGRP_2$ receptors. The former are blocked by CGRP(8-37), while the latter are insensitive to the antagonist.

1.4.1.3 Non-peptidergic sensory fibres

Since a seminal article by Hunt and Rossi in 1985 (Hunt S.P. and Rossi J., 1985), the concept of the occurrence of two populations of sensory fibres conveying nociceptive information, the peptidergic and non-peptidergic, has emerged. The first would express sensory neuropeptides, in particular SP, and the second would display fluoride-resistant acid phosphatase (FRAP) activity. This concept was largely neglected for a decade while investigators focused mostly on the terminations of fibres expressing sensory neuropeptides, in particular SP, but interest in it has been revived in recent years (see discussion). It was clarified that the population that expressed FRAP activity, originally described a few years earlier by two groups independently (Coimbra A. et al., 1970; Knyihár E., 1971; Knyihár E. and Gerebtzoff M.A., 1973; Coimbra A. et al., 1974), could specifically bind the isolectin GSA-IB4 and be recognized by the monoclonal antibody LA4 (Dodd J. and Jessell T.M., 1985; Jessell T.M. and Dodd J., 1985; Jessell T.M. and Dodd J., 1989; Alvarez F.J. et al., 1989a; Alvarez F.J. et al., 1989b). However, the real

interest in the non-peptidergic population arose following the dramatic discovery that the two populations differed in neurotrophic support in the adult rat. In fact, during development, both populations require nerve growth factor (NGF) for survival, but shortly after birth only the peptidergic continues to respond to NGF, whereas the non-peptidergic population starts to respond to glial cell line-derived neurotrophic factor (GDNF) instead (Bennett D.L.H. et al., 1998). Accordingly, the peptidergic population expresses the NGF high affinity receptor, trkA, whereas the non-peptidergic expresses GDNF receptors. It was also shown that the latter population also expresses the purinergic receptor $P2X_3$ (Snider W.D. and McMahon S.B., 1998; Bradbury E.J. et al., 1998). Although the distinction between two populations of primary sensory fibres, peptidergic and non-peptidergic, seems attractive, it is not fully accurate as a small proportion of sensory fibres that co-localize CGRP and somatostatin do not respond to NGF in the adult and bind the lectin GSA-IB4 (Alvarez F.J. and Fyffe R.E.W., 2000). CGRP and FRAP are co-localized in the dorsal horn of the rat spinal cord and are of primary sensory origin as demonstrated by their depletion by neonatal capsaicin (Carr P.A. et al., 1990).

1.4.1.4 Receptors on sensory fibres

Besides the signal transducers mentioned above, nociceptive sensory fibre terminals in the periphery have been shown to express several receptors for neurotransmitters/neuromodulators that likely change the excitability of these afferents (Coggeshall R.E. and Carlton S.M., 1997). Although the occurrence of SP receptors (NK-1r) in peptidergic sensory fibres has been questioned, *in situ* hybridization and

immunocytochemical studies have confirmed their occurrence (Li H.-S. and Zhao Z.-Q., 1998; Von Banchet G.S. and Schaible H.G., 1999). These receptors likely represent auto-receptors and are probably important in the control of SP release at the level of the nociceptors. The presence of glutamate receptors in the periphery is well established and both NMDA and non-NMDA receptors have been located on unmyelinated sensory fibres of the skin by immunocytochemistry (Carlton S.M. et al., 1995; Carlton S.M. and Coggeshall R.E., 1999; Du J. et al., 2001) and, importantly, contribute to the sensitization of the nociceptors to noxious stimuli. Opioid receptors also occur in nociceptors and are thought to be responsible for the peripheral effects of opioid analgesics (Minami M. et al., 1995; Zhou L. et al., 1998). Cholinergic receptors, both nicotinic and muscarinic, occur on sensory fibres as well (Flores C.M. et al., 1996; Haberberger R. et al., 1999). Alpha$_2$-adrenergic receptors have been localized on sensory fibres and are thought to contribute to the sensitization of the terminals to noxious stimuli (Kinnman E. et al., 1997; Perl E.R., 1999). However, the evidence for the identification of α_2-adrenergic receptors on sensory fibres is not convincing. The vanilloid receptor (VR1), is a heat-activated ion channel that has also been demonstrated on primary sensory fibres (Caterina M.J. et al., 1997; Tominaga M. et al., 1998). This receptor is better known as the capsaicin receptor. Although other cation channels have been described recently and may also play a role in signal transduction in nociception [for review see (Alvarez F.J. and Fyffe R.E.W., 2000)], the other transducer that deserves analysis here is the purinergic receptor $P2X_3$, which occurs in the non-peptidergic population of nociceptive sensory fibres (Bradbury E.J. et al., 1998; Guo A. et al., 1999). $P2X_3$ receptors are important, since sympathetic fibres, tumour cells and cells damaged following mechanical injury are

all capable of releasing ATP (Burnstock G., 2000). Although most sensory ganglia neurons express purinergic receptors, the specific localization of the $P2X_3$ receptor on the non-peptidergic population of nociceptive afferents suggest an important role for ATP in the activation of these nociceptors [for review see (Ding Y. et al., 2000)]. Other receptors such as bradykinin, prostaglandin, serotonin and adenosine receptors, to name just a few, have been indentified on nociceptive sensory fibres, but will not be discussed herein [for review see (Cesare P. and McNaughton P., 1997; Levine J.D. and Reichling D.B., 1999; Bevan S., 1999)].

1.4.1.5 Sensory fibres and neurogenic inflammation

Neurogenic inflammation is a well documented peripheral phenomenon (Levine J.D. et al., 1985; Chahl L.A., 1988; Maggi C.A. and Meli A., 1988; Barnes P.J. et al., 1991; Lundberg J.M., 1996). It is characterized by: 1) reddening of the skin due to local small vessel dilatation, 2) a flare reaction as a result of the spreading of the dilatation by an axon reflex, 3) a wheal reaction due to increased permeability of local vessels (Lewis T., 1927). It is an inflammatory process in which the sensory nervous system plays a crucial role, hence the term *neurogenic*. Following sensory fibre stimulation (activation) by a tissue-damaging, high-intensity initiating stimulus, neuropeptides (e.g. SP, CGRP and NKA) are released, which in turn cause plasma extravasation and vasodilatation following the direct effect of these transmitters on receptors on the blood vessel wall, or an indirect effect via the activation of mast cells or leukocytes (Holzer P., 1998). Mast cells and leukocytes then release inflammatory mediators, leading to the sensitization of the afferent nerve endings and the establishment of a positive feedback loop (Baluk P.,

1997; Holzer P., 1998).

The sensory fibres responsible for mediating antidromic vasodilatation and plasma extravasation are small diameter, capsaicin-sensitive, polymodal nociceptive C and Aδ primary sensory afferents (Hinsey J.C. and Gasser H.S., 1930; Celander O. and Folkow B., 1953; Kenins P., 1981; Kenins P., 1982; Szolcsányi J., 1988). Stimulation of capsaicin-insensitive afferents or of sympathetic efferents does not produce a neurogenic inflammatory response (Szolcsányi J. et al., 1992).

1.4.2 **Autonomic nervous system**

1.4.2.1 Sympathetic nervous system

Sympathetic fibres that innervate the skin, exit the spinal cord via thoracic and lumbar spinal nerves (T1-L2-3). Their pre-ganglionic fibres are short and their post-ganglionic fibres very long, since the ganglia are located in the paravertebral sympathetic chain, which lies close to the spinal cord. Sympathetic fibres innervate the smooth muscle of the *arrector pili* and blood vessels with noradrenergic fibres, and the sweat glands with cholinergic fibres (Rang H.P. and Dale M.M., 1991). This system is involved in non-shivering thermogenesis, cutaneous vasoactivity, sweating and piloerection (Hemingway A. and Price W.M., 1968). Upon stimulation, the sympathetic system releases less noradrenaline in skin than in muscle, but the vasoconstrictor effect is the same on both tissues (Zimmerman B.G. and Whitmore L, 1967). The sympathetic system is also capable of vasodilatation in the skin (Rolewicz T.F. and Zimmerman B.G., 1972). This effect appears to be the result of post-stimulatory sympathetic activity (Abboud F.M. and Weinberg S.M., 1965; Pollard A.A. and Beck L., 1971). The reflex control of the

cutaneous vasculature by sympathetic fibres has been reviewed extensively (Rowell L.B., 1977). Under normal conditions, the skin microcirculation is under tight sympathetic control (Hassan A.A.K. et al., 1986).

1.4.2.2 Parasympathetic nervous system

Parasympathetic fibres exit the central nervous system via cranial nerves III, VII, IX and X and spinal nerves S2-S4. These fibres possess very long pre-ganglionic fibres, which synapse onto relatively short post-ganglionic neurons and, in the enteric nervous system, the parasympathetic ganglia are often located within the walls of the target organs (Rang H.P. and Dale M.M., 1991). The parasympathetic fibre innervation of the skin is still not fully established, although there is sufficient evidence from the literature to state that it occurs, at least in certain territories. In the skin, cholinergic fibres definitely occur in areas where sweat glands are found, but these are sympathetic in origin (Katzung B.G., 2001). Some reports using indirect markers for parasympathetic fibres, such as vasoactive intestinal polypeptide (VIP) or cholinesterase activity have suggested that some vascular beds may receive cholinergic parasympathetic fibres (Kaji A. et al., 1988). The problem with these studies (Kaji A. et al., 1988; Fundin B.T. et al., 1997) is that VIP immunoreactivity and cholinesterase activity or immunoreactivity are not restricted to the cholinergic system, and thus cannot be used as reliable markers on their own. However, the experimental studies by Kaji and collaborators are quite interesting as they use VIP immunoreactivity and/or cholinesterase detection combined with tracing methods to provide evidence that suggests the occurrence of a *bona fide* parasympathetic innervation of the skin of the rat lower lip (Kaji A. et al., 1988; Kaji A.

et al., 1991). Furthermore, there is physiological evidence in the cat for parasympathetic vasodilatation in the lip skin (Izumi H. and Karita K., 1993).

1.5 Peripheral neuropathies

1.5.1 General description of the problem

Peripheral neuropathies are a complex group of syndromes that by definition arise from disturbances in structure and/or function of the peripheral nervous system. These syndromes manifest different symptoms depending on whether there is a sensory, motor and/or sympathetic component involved (Riaz S.S. and Tomlinson D.R., 1996). Peripheral neuropathies are commonly encountered in the clinic, however, to this day, successful treatments are unavailable. The pain experienced by patients is referred to as neuropathic pain since the underlying cause is essentially a disturbance of neuronal function. Damage to peripheral nerves may result from trauma (compression or entrapment of nerves following a fall or surgery), from diseases like diabetes or herpes zoster, from cancer (due to nerve compression by increasing tumour mass over time) or following chemical nerve injury, as occurs during the treatment of AIDS. The most prevalent, according to estimates in the U.S. population, are diabetic neuropathies, postherpetic neuralgia and cancer-related pain (Bennett G.J., 1998).

The challenge for the clinicians is the reduced effectiveness of the available therapies for neuropathic pain. Standard drugs such as NSAIDs and morphine are good at targeting normal pain, leaving neuropathic pain mostly unrelieved (Dellemijn P., 1999). To date, a variety of drugs, acting on central or peripheral mechanisms, are currently used or being developed for the treatment of neuropathic pain [for reviews see (MacFarlane

B.V. et al., 1997; Woolf C.J. and Mannion R.J., 1999)]. These include sodium channel blockers, sympathetic blockers, NMDA and NK-1 receptor antagonists, antidepressants, anticonvulsants, capsaicin and growth factors, just to name a few.

Neuropathic pain has been referred to as 'abnormal pain' and, unlike normal pain, has no protective role for the organism. Normal pain is induced by a noxious (pain-producing) stimulus. Neuropathic pain is characterized by allodynia and hyperalgesia. The former is the sensation of pain from a non-noxious stimulus, whereas the latter is an exaggerated painful response to a noxious (pain-producing) stimulus. In the past ten years much effort has been put into developing appropriate animal models that could help to unravel the mechanism(s) underlying peripheral neuropathic pain.

1.5.2 **Complex regional pain syndromes**

In 1864, Mitchell first described causalgia as the burning pain experienced by soldiers following peripheral nerve injuries due to gunshots (Mitchell S.W. et al., 1864). Later, Evans introduced the term *reflex sympathetic dystrophy* (RSD) to account for the sympathetic involvement in the abnormal peripheral activity (Evans J.A., 1946). Over the years, the involvement of the sympathetic system in the pathogenesis of RSD and causalgia was not clear, and a recent revision of the taxonomy led to the introduction of the terms complex regional pain syndrome (CRPS) I and CRPS II (Stanton-Hicks M. et al., 1995). As a result, RSD became CRPS I, and causalgia became CRPS II. For a CRPS diagnosis to be emitted, the patient must present the following symptoms: 1- spontaneous burning pain, allodynia or hyperalgesia which is disproportionate to the injury, 2- oedema and abnormalities in skin blood flow and sudomotor activity in the region of pain, 3- no

other underlying cause that could account for these symptoms (Stanton-Hicks M. et al., 1995). Trophic changes of the skin and appendages and motor dysfunction may also be present (Wong G.Y. and Wilson P., 1997). The only differentiating factor between CRPS I and CRPS II is the absence or presence, respectively, of a known nerve injury. As CRPS II is characterized by an identifiable nerve injury, much attention has been focused on unravelling the cascade of events leading to abnormal pain sensations (neuropathic pain), following nerve injury.

There exist two divisions of neuropathic pain: sympathetically maintained pain (SMP) and sympathetically independent pain (SIP) (Roberts W.J., 1986). To complicate matters further, some SMP sufferers are only partially and temporarily relieved by sympathectomies, suggesting that a SIP component be involved. Also, at later stages of the disorder, the pain is refractory to sympathectomies (Gracely R.H. et al., 1992).

1.5.3 **Animal models of neuropathic pain**

The development of rat animal models of neuropathic pain has helped further our understanding of the peripheral and central mechanisms involved in the genesis of pain following peripheral nerve injuries. The first model was developed by Bennett and Xie, and is known as the Bennett or chronic constrictive injury (CCI) model (Bennett G.J. and Xie Y.-K., 1988). It consists of four loose ligatures placed around the sciatic nerve. These animals display hyperalgesia to mustard oil and noxious thermal and mechanical stimuli, as well as mechanical and cold allodynia, as of the second day post operative, and these behaviours are still present after two months. The second model to be developed was the Seltzer or partial sciatic nerve ligation (PSL) model (Seltzer Z. et al., 1990). Following

the placement of a tight ligature around the dorsal third to the dorsal half of the sciatic nerve, symptoms start to appear as early as one hour post-surgery and are still present seven months later. The symptoms range from heat and mechanical hyperalgesia to heat and touch allodynia. Two years later, another model was introduced, the Chung or spinal nerve ligation (SNL) model, which consists of a complete ligation of L_5 or L_5 and L_6 spinal nerves (Kim S.H. and Chung J.M., 1992). The SNL model is characterized by heat and mechanical hyperalgesia and mechanical allodynia, which last for five and ten weeks respectively. In all three models described above, the animals develop spontaneous pain. However, autotomy is only observed in the CCI model. Furthermore, and most interesting for this thesis, sympathectomies alleviate the symptoms in all three models (Attal N. et al., 1990; Kim S.H. and Chung J.M., 1991; Shir Y. and Seltzer Z., 1991). More recently a fourth model was developed, the Kruger model (Mosconi T. and Kruger L., 1996). This is a variant of the CCI model in which four fixed-diameter polyethylene cuffs are placed along the sciatic nerve. In this model, mechanical and cold hyperalgesia become apparent during the second week post-surgery and recovery is observed by the fourth week post-surgery. More recently, using an adaptation of the Kruger model, which consists of placing only one polyethylene cuff on the sciatic nerve, it was reported that rats displayed signs of mechanical hyperalgesia and allodynia as early as day 1 post-surgery and these persisted up until day 145, the last time point studied (Pitcher G.M. et al., 1999).

1.5.4 **Peripheral mechanisms**

1.5.4.1 Dorsal root ganglia

1.5.4.1.1 Sympathetic fibre contribution

It has long been known that, following peripheral nerve injury, blocking sympathetic activity through nerve blocks or sympathectomies alleviates the pain in some patients. Sato and Perl (1991) showed that, following lesions to the great auricular nerve, sympathetic stimulation or noradrenaline administration caused the excitation of 40% of C-fibre polymodal nociceptors. These researchers also showed that the adrenergic receptor antagonists, yohimbine and rauwolscine were more effective than prazosin in inhibiting the C-fibre excitation, thus suggesting that this effect was mediated by α_2- and not α_1-adrenergic receptors. Interestingly, α_2-receptors are upregulated in neuromas (see below) and DRG as suggested by radioautography showing increased clonidine binding at these sites (McMahon S.B., 1991; Nishiyama K. et al., 1993). It would later be shown that following a SNL, the mRNA levels for the α_{2A}- and α_{2C}-adrenergic receptors are increased and decreased respectively (Cho H.-J. et al., 1997). Using immunocytochemistry and a variant of the PSL model, an increase in α_{2A}-adrenergic receptor immunoreactivity was detected on DRG neurons, although no changes in α_{2C}-adrenergic receptors were observed (Birder L.A. and Perl E.R., 1999). More recently, using *in situ* hybridization, researchers have reported increases in α_{2A}-adrenergic receptor mRNA levels in the DRG following sciatic nerve transections (Shi T.-J.S. et al., 2000). The involvement of adrenergic receptors in neuropathic pain is reviewed in a recent article (Perl E.R., 1999).

In 1993, a landmark article by McLachlan et al. reported than noradrenergic

(sympathetic) fibres form basket-like structures around large-diameter DRG cells following ligation and transection of sciatic nerves (McLachlan E.M. et al., 1993), which suggested that the sympathetic fibre sprouting was the anatomical basis for SMP. These observations were reproduced by another group (Chung K. et al., 1993). McLachlan showed that the sprouted fibres originated from sympathetic perivascular plexuses. Sensory fibre excitation was blocked by the non-selective α-receptor antagonist phentolamine, thus making it impossible to determine the adrenergic receptor subtype involved. Studies using cultures of L4 and L5 DRG cells 11-25 days post-sciatic nerve ligation, have shown that the spontaneous firing and responsiveness of the cells to noradrenaline is due to changes in the membrane properties of the nerve cell bodies (Petersen M. et al., 1996). A few years later, more complete behavioural, quantitative and morphological analyses of the sympathetic fibre sprouting onto DRG neurons were conducted using the SNL model (Chung K. et al., 1996). Pain behaviours were well established by the third day post-surgery and were still above pre-surgery values at twenty weeks. Sympathetic fibre sprouting occurred as early as two days post-surgery. Removal of the sympathetic ganglia from L_2 to S_1 resulted in an almost complete ablation of sprouted sympathetic fibres. As for pain behaviours, the sympathectomies were especially effective at suppressing mechanical allodynia and spontaneous pain. The sprouted sympathetic fibres were in close proximity and occasionally apposed to the somata of DRG neurons (Chung K. et al., 1997).

When comparing the effects of a complete versus a partial sciatic nerve lesion, it was found that the sprouting induced by a CCI model occurs more rapidly than following a complete sciatic nerve transection (Ramer M.S. and Bisby M.A., 1997). This suggests

that, following CCI, the degenerating nerve most likely releases a variety of products, such as NGF, which are available to the degenerating and regenerating axons (see introduction of chapter 4 for further information). This notion has been further investigated by the use of degeneration-deficient mice, in which sympathetic fibre sprouting was absent following CCI or SNL (Ramer M.S. et al., 1997; Ramer M.S. and Bisby M.A., 1998). Based on these results, a mechanism for sympathetic sprouting onto DRG neurons was proposed [for review see (Ramer M.S. and Bisby M.A., 1998)]. Briefly, nerve crushing following CCI induces the sprouting of perivascular sympathetic fibres. The actual severing of fibres, as in the SNL model, causes the formation of a neuroma, which blocks regenerating sympathetic fibres from accessing the periphery. Therefore, these fibres are directed towards the DRG cells and sprouting is said to occur via the misdirected growth of regenerating sympathetic fibres. Therefore, some of the differences encountered in these animal models might be a reflection of the proximity of the lesion to the DRG. In accordance with this, Kim et al. have shown that the extent of sympathetic fibre sprouting onto DRG neurons is inversely related to the distance between the injury site and the DRG (Kim H.J. et al., 1996). Damage to peripheral nerves can impair their production or transport of neurotrophic factors, as well as the machinery involved in signal transduction. Efforts have been invested towards restoring neurotrophic factor levels in the injured system (Riaz S.S. and Tomlinson D.R., 1996).

In recent years, a comparative study of three animal models of neuropathic pain, CCI, PSL and SNL, reported that baskets of sympathetic fibres form *de novo* around neurons in dorsal root ganglia (Lee B.H. et al., 1998). However the sprouting is most significant in the SNL model and only occurs at later time points following CCI and PSL

peripheral nerve injuries. Transgenic animals that over-express NGF in glial cells show more sympathetic sprouting in the DRG following CCI of the sciatic nerve than non-transgenic animals; these transgenic animals also display increased neuropathic pain behaviours (Ramer M.S. et al., 1998). However, it should be noted that NGF itself contributes to these behaviours, as it decreases pain thresholds (Lewin G.R. and Mendell L.M., 1993). A recent review suggests that other factors such as leukemia inhibitory factor and interleukin-6, produced in the periphery following nerve degeneration, may also play a role in sympathetic sprouting (Ramer M.S. et al., 1999).

More recently, a functional coupling has been suggested within the DRG, as opposed to a strictly anatomical sympathetic-sensory fibre coupling (Häbler H.-J. et al., 2000). These researchers show that increasing vascular resistance, by vasoconstrictor agents such as N^G-nitro-L-arginine methyl ester (L-NAME), causes an increased responsiveness of lesioned afferents in the DRG to lumbar sympathetic stimulation or to other constrictor agents such as VIP or noradrenaline. This suggests that sensory-sympathetic coupling in the DRG is unmasked only in the presence of impaired blood supply to the DRG.

1.5.4.1.2 Sodium channel contribution

Dynamic changes in the expression of sodium channels have been reported following peripheral nerve injuries. Two types of sodium channels have been identified: tetrodotoxin-sensitive (TTX_S) and TTX-resistant (TTX_R). TTX_S channels include PN1/hNE, α-I, Na6, NaG, while the TTX_R channels include PN3/SNS and NaN/SNS2. The restricted distribution of the TTX_R channels on capsaicin-sensitive small diameter

DRG neurons (Caffrey J.M. et al., 1992; Elliott A.A. and Elliott J.R., 1993; Arbuckle J.B. and Docherty R.J., 1995; Gold M.S. et al., 1996) has made them interesting candidates for the aberrant firing of DRG neurons in neuropathic pain conditions. Of the two TTX_R channels, PN3/SNS appears to be the only one involved in repetitive firing following peripheral nerve injuries. Also, PN3/SNS channels appear to be involved only in aberrant pain, since channel knock-down, using antisense oligonucleotides, does not seem to affect normal pain sensation. Therefore, these channels could become potential therapeutic targets in the treatment of neuropathic pain due to their selective presence on sensory primary afferent fibres [for reviews see (Porreca F. et al., 1999; Waxman S.G. et al., 1999)].

1.5.4.2 Peripheral nerve fibre terminal fields

1.5.4.2.1 Sensory-sympathetic coupling in the peripheral terminals

For neuropathic pain to arise there must be an underlying peripheral nerve injury. Indeed peripheral inputs are necessary, at least for the initiation of a neuropathic condition. Local anaesthetic blocks, performed by subcutaneous injection of lidocaine, have been shown to suppress mechanical and cold allodynia, as well as spontaneous pain, in human patients with RSD (Gracely R.H. et al., 1992). Furthermore, studies whereby the ventral and/or dorsal roots were sectioned, produced no signs of neuropathic pain and indicated that the injury must be distal to the DRG (Sheen K. and Chung J.M., 1993).

Denervation causes catecholamine supersensitivity in skin microvessels and nociceptive sensory fibres, indicating that sensory fibres may have become responsive to catecholamines as a consequence of nerve injury (Perl E.R., 1993). In RSD, these types

of terminal region sensory abnormalities may underlie the pain, a notion supported by the knowledge that sympathectomies alone induce painful sensations in the sympathectomized region (Litwin M.S., 1962). An increase in sympathetic impulses at the site of injury has been suggested (Kurvers H.A.J.M. et al., 1996). Subsequently, locally released noradrenaline would be capable of activating sensory fibres at the injury site (Schwartzman R.J. and McLellan T.L., 1987; Schwartzman R.J., 1993). Following ligation of the rabbit great auricular nerve, the upregulation of α_2-adrenergic receptors in the receptive terminal region of cutaneous C-fibre nociceptors causes sympathetic stimulation- and noradrenaline administration-induced excitation of these fibres (Sato J. and Perl E.R., 1991). This provides further evidence that changes in the cutaneous terminal region of sensory fibres may have a role to play in neuropathic pain.

1.5.4.2.2 Peripheral terminal expression of sodium currents and channels

Although the majority of the available data on sodium channels was obtained in the DRG, there is evidence suggesting the existence of TTX_R sodium currents in peripheral terminals. In corneal peripheral afferents, these channels play a role in the generation of action potentials (Brock J.A. et al., 1998). Following CCI, or a complete transection of the sciatic nerve, PN3/SNS protein is translocated from the cell bodies to the axons at the site of injury, as evidenced by a decreased intensity of immunolabelling in the DRG, with a concomitant increase in immunolabelling at the site of injury (Novakovic S.D. et al., 1998).

1.5.5 **Spinal cord mechanisms**

Although beyond the scope of this thesis, the recent advances in spinal cord changes occurring following peripheral nerve injuries deserve to be mentioned [for reviews see (Woolf C.J. and Mannion R.J., 1999; Mayer D.J. et al., 1999; Yaksh T.L. et al., 1999)]. Sustained intense peripheral nerve input to the spinal cord causes central sensitization, which leads to allodynia, hyperalgesia and spontaneous pain sensations (Basbaum A.I. and Woolf C.J., 1998). The reorganization of the spinal dorsal horn is at the heart of the mechanisms underlying these pain states, and includes the upregulation of transmitters, their receptors and/or second messengers, the sprouting of primary afferent fibres and/or the induction of genes. Neurotransmitters such as glutamate, SP and CGRP, influence the second order neurons in the superficial layers of the dorsal horn by activating AMPA/NMDA, NK-1 and CGRP receptors, respectively.

Scientists have looked at the spinal mechanisms responsible for abnormal pain sensations. Two important studies have shown that, in fact, specific pathways can be manipulated, leaving the normal perception of pain unaffected. In the first study, Mantyh and colleagues showed that administering a SP-saporin conjugate to rats leads to the ablation of lamina I dorsal horn neurons, following the internalization of this complex (Mantyh P.W. et al., 1997). The ablation left the responses of these animals to mild noxious stimuli unchanged, but abolished their responses to noxious stimuli producing mechanical and thermal hyperalgesia. The second study showed that PKC_{γ}-deficient mice respond normally to acute painful stimuli, but do not develop the neuropathic pain syndrome following PSL (Malmberg A.B. et al., 1997; Basbaum A.I., 1999). Fibre sprouting in the spinal cord may also be responsible, in part, for the abnormal pain

sensations that accompany neuropathic pain. Aβ fibres normally respond to non-noxious stimuli and are absent from lamina II of the spinal cord, which receives information about noxious stimuli. However, peripheral nerve injury triggers the sprouting of these Aβ fibres into lamina II, most likely as a result of C-fibre damage (Woolf C.J. et al., 1992; Mannion R.J. et al., 1996). Consequently, non-noxious information may be conveyed to lamina II neurons that normally receive noxious information, making it possible for the nervous system to misinterpret the non-noxious stimulus for a noxious one (Woolf C.J. and Doubell T.P., 1994). This could be the basis for allodynia. Furthermore, the sprouted Aβ fibres begin to express neuropeptides such as CGRP (Miki K. et al., 1998). Furthermore, it is suggested that this phenotypic switch occurs simultaneously with the down-regulation of neurotransmitters from Aδ and C fibres (Woolf C.J. and Mannion R.J., 1999).

1.6 Animal model: the rat lower lip

In this thesis, the skin of the rat lower lip was used as an experimental model. In contrast to some very specialized models, such as the mystacial pad (Fundin B.T. et al., 1997) -- which is essentially a specialized sensory organ -- the skin of the rat lower lip represents regular hairy skin that has been used for studies of neurogenic inflammation (Couture R. and Cuello A.C., 1984; Couture R. et al., 1985; Couture R. et al., 1985). Various independent groups have also studied the innervation of various structures in this tissue, thus lending more credibility to the use of this skin model (Hökfelt T. et al., 1977; Kaji A. et al., 1988; Ribeiro-da-Silva A. et al., 1991; Verzé L. et al., 1999). As sensory innervation to the rat lower lip skin originates from the mental nerve – a branch of the

trigeminal nerve – and the sympathetic innervation originates from the superior cervical ganglion, we can thus independently lesion one system or the other and observe the changes that occur in the terminal fields.

1.7 Objectives and rationale

Skin is the largest organ of the body and, as such, it receives a myriad of stimuli from the external environment. Much of how this information is interpreted depends on the state of the peripheral nervous system. Unfortunately, it remains difficult for the clinician to target pain-related problems arising in the skin, as the organization of the peripheral nervous system under normal circumstances remains poorly characterized, and much less is known on the changes following peripheral nerve injury. Thus, I propose that continued improvements in the control of neurogenic inflammatory reactions and the treatment of neuropathic pain syndromes can only be achieved if the exact nature of the interactions between the various components of the peripheral nervous system (PNS) are understood.

In defining the aims of this thesis, we took into account: (1) that despite SP's involvement in mediating pain and neurogenic inflammation, its precise association with blood vessels had not been properly described; (2) the availability of an anti-NK-1r antibody that labels blood vessels in the skin; (3) that studies on sensory and autonomic innervation of the skin had not been simultaneously performed in the same animals and tissue and that no systematic quantification of these terminals with respect to their targets had been performed; (4) the lack of studies describing the terminal fields of sensory and sympathetic fibres following peripheral nerve lesions; (5) that the occurrence of

sympathetic sprouting distal to the DRG had never been investigated, despite the fact that, following nerve damage, sympathetic stimulation or noradrenaline administration leads to the activation of C-fibre nociceptors in their receptive terminal region. Based on the above we used light and electron microscopy to provide a complete anatomical and quantitative description of the innervation patterns in the rat lower lip skin. The following working hypotheses were formulated:

Hypothesis I: **Skin blood vessels are simultaneously innervated by sensory, sympathetic and parasympathetic fibres.**

Hypothesis II: **Sensory-sympathetic fibre associations/interactions occur in the skin terminal field region following peripheral nerve lesions.**

These hypotheses were tested by setting specific objectives, which were:

1) To study the exact innervation pattern of the rat lower lip skin by sensory fibres and compare it to that of autonomic fibres under normal conditions.
2) To determine the changes in the terminal fields of sensory and sympathetic fibres following sensory denervations.
3) To determine the changes in the terminal fields of sensory and sympathetic fibres following sympathectomies.

CHAPTER 2

Light and Electron Microscopic Study of the Distribution of Substance P-Immunoreactive Fibres and Neurokinin-1 Receptors in the Skin of the Rat Lower Lip

Isabelia Ruocco, A. Claudio Cuello, Ryuichi Shigemoto
and Alfredo Ribeiro-da-Silva

The Journal of Comparative Neurology
432:466-480 (2001)

ABSTRACT

Cutaneous antidromic vasodilatation and plasma extravasation, two phenomena that occur in neurogenic inflammation, are partially blocked by substance P (SP) receptor antagonists, and are known to be mediated in part by mast cell-released substances such as histamine, serotonin and nitric oxide. In an attempt to provide a morphological substrate for the above phenomena, we applied light and electron microscopic immunocytochemistry to investigate the pattern of SP innervation of blood vessels and its relationship to mast cells in the skin of the rat lower lip. Furthermore, we examined the distribution of SP (neurokinin-1) receptors and their relationship to SP-immunoreactive (IR) fibres. Our results confirmed that SP-IR fibres are found in cutaneous nerves and that terminal branches are observed around blood vessels and penetrating the epidermis. Substance P-IR fibres also innervated hair follicles and sebaceous glands. At the ultrastructural level, SP-IR varicosities were observed adjacent to arterioles, capillaries, venules and mast cells. The varicosities possessed both dense core and agranular synaptic vesicles. We quantified the distance between SP-IR varicosities and blood vessel endothelial cells. Substance P-IR terminals were located within 0.23 to 5.99 μm from the endothelial cell layer in 82.7% of arterioles, in 90.2% of capillaries and in 86.9% of venules. Although there was a trend for SP-IR fibres to be located closer to the endothelium of venules, this difference was not significant. Neurokinin-1 receptor (NK-1r) immunoreactivity was most abundant in the upper dermis and was associated with the wall of blood vessels. NK-1r were equally located on the wall of arterioles, capillaries and venules which were innervated by SP-IR fibres. The present results favour the concept of a participation of SP in cutaneous neurogenic vasodilatation and plasma

extravasation both by an action on blood vessels following binding to the NK-1r and by causing the release of substances from mast cells after diffusion through the connective tissue.

INTRODUCTION

Since its discovery in 1931 by von Euler and Gaddum (von Euler U.S. and Gaddum J.H., 1931), substance P (SP) has been extensively studied. It is well established that SP is found both in the peripheral and central nervous systems. Its peripheral actions have been mainly associated with neurogenic inflammation that is characterised by vasodilatation and plasma extravasation. Substance P's most prominent role is in plasma extravasation, which is blocked following the depletion of sensory nerve terminals by capsaicin (Jancsó N. et al., 1967; Lembeck F. and Holzer P., 1979; Saria A. et al., 1983; Saria A., 1984), or pre-treatments with SP receptor antagonists (Lembeck F. et al., 1982; Couture R. and Cuello A.C., 1984; Garret C. et al., 1991; Lei Y.-H. et al., 1992; Lembeck F. et al., 1992). The above observations suggest a specific role for SP in neurogenic inflammation, and more precisely in plasma extravasation, via the activation of SP (neurokinin-1) receptors. Substance P's C-terminal portion has also been suggested to interact with the endothelial cell NK-1 receptors (Devillier P. et al., 1986; Fuller R.W. et al., 1987).

Substance P-induced neurogenic inflammation is not due solely from its effects on NK-1r. In fact, SP is capable of stimulating mast cells to release histamine, nitric oxide, serotonin and prostaglandins (Holzer P., 1998). Substance P's actions on mast cells are probably non-NK-1 receptor-mediated, as SP appears to interact directly with the mast cell plasma membranes via its N-terminal basic residues, leading to G-protein activation (Fewtrell C.M. et al., 1982; Foreman J.C. et al., 1983; Lowman M.A. et al., 1988; Devillier P. et al., 1989; Mousli M. et al., 1990; Holzer P., 1992). Close proximities, suggesting contacts, between mast cells and primary afferent fibres in the

skin have been shown (Wiesner-Henzel L. et al., 1981; Newson B. et al., 1983); however these are probably infrequent as mast cells abound in the lower dermis whereas primary afferents are confined mostly to the upper dermis (Kowalski M.L. et al., 1990). Also permeable vessels occur in higher density in the upper 120 μm of the dermis (Baraniuk J.N. et al., 1990). In consequence, it has been suggested that mast cells intervene in later rather than in the initial stages of neurogenic inflammation (Kowalski M.L. and Kaliner M.A., 1988; Yano H. et al., 1989; Baraniuk J.N. et al., 1990), possibly because sufficient amounts of SP must diffuse to the lower dermis for mast cell activation to occur. Studies in humans and rats have suggested that mast cells may play a role in neurogenic inflammation as a result of their proximity to blood vessels and nerve fibres (Eady R.A. et al., 1979). Despite the available information, the precise relationship between sensory fibres and mast cells is not yet fully established.

Other neuropeptides of primary sensory origin are also capable of producing neurogenic-type phenomena. In fact, calcitonin gene-related peptide (CGRP) has been shown to produce vasodilatation in the skin. CGRP is, to date, the most potent dilator of cutaneous arterioles and this effect is blocked by $CGRP_1$ receptor antagonists (Brain S.D., 1996). Although CGRP does not seem to be directly involved in plasma extravasation, it indirectly influences extravasation as a result of its dilatory capabilities or, possibly, by inhibiting SP degradation (Holzer P., 1992; Brain S.D., 1996). Conversely, SP can influence the outcome of CGRP-induced vasodilatation (Brain S.D. and Williams T.J., 1988). In addition, neuropeptides such as neurotensin, vasoactive intestinal polypeptide and somatostatin may also be involved in neurogenic inflammation

(Chahl L.A., 1979; Fjellner B. and Hagermark O., 1981; Carraway R. et al., 1982; Scofitch G. et al., 1983).

One of the models used to study neurogenic inflammation is the trigeminal system. Electrical stimulation of the mental nerve – a sensory branch of the trigeminal nerve - causes vasodilatation and plasma protein extravasation in the rat lower lip probably due to the release of SP from primary afferents (Couture R. and Cuello A.C., 1984). Upon release, it has been suggested that SP diffuses through the connective tissue (Lembeck F., 1983; Szolcsányi J., 1991) to reach NK-1 receptors located on the blood vessel endothelium (Deguchi M. et al., 1989). Evidence from radioautography has identified NK-1 receptors on human capillaries and on rat arterioles and venules (Deguchi M. et al., 1989). Although many superficial studies have addressed SP innervation of the skin in general qualitative terms, the details of SP innervation of the skin have not yet been investigated. The available qualitative data has shown that SP-immunoreactive fibres associate with blood vessels (Hökfelt T. et al., 1975; Dalsgaard C.-J. et al., 1983), sweat glands (Hökfelt T. et al., 1975; Dalsgaard C.-J. et al., 1983; Tainio H. et al., 1987), hair follicles (Cuello A.C. et al., 1978) and Meissner corpuscles (Dalsgaard C.-J. et al., 1983; Bloom S.R. and Polak J.M., 1983). Also SP-immunoreactive fibres were shown to lie beneath the epithelium and occasionnally penetrate it as free nerve endings (Hökfelt T. et al., 1975; Hökfelt T. et al., 1977) (Wiesner-Henzel L. et al., 1981; Nawa H. et al., 1983; Skofitsch G. et al., 1985)

The purpose of this study was to perform a novel, in-depth investigation at the light and electron microscopic levels, of the distribution pattern of SP fibres in the rat lower lip, which is innervated by a purely sensory branch of the trigeminal nerve, the

mental nerve. The rat lower lip skin has been used in studies of antidromic vasodilatation and plasma extravasation (Couture R. and Cuello A.C., 1984; Couture R. et al., 1985) and has the advantage of allowing the separate manipulation of the sensory and sympathetic innervation (Ruocco I. et al., 2000). In this study we took advantage of the exceptional properties for both light and electron microscopy of a bispecific monoclonal antibody against SP and HRP (Suresh M.R. et al., 1986). If, as discussed above, the role of SP in neurogenic inflammation is mostly in the induction of plasma protein extravasation, it would be logical to suggest that it acts preferentially on venules rather than on arterioles or capillaries. To test this hypothesis, we quantified the relationship of SP to various blood vessel types and studied the blood vessel localization of NK-1 receptors. Finally, as the involvement of mast cells in neurogenic inflammation is still ambigous, we analyzed the relationship between mast cells, SP fibres and blood vessels.

MATERIALS AND METHODS

Male Wistar rats weighing 250-350 g (Charles River, Canada) were used. The animals were treated in accordance with the guidelines of the McGill University Animal Care Committee and the Canadian Council on Animal Care.

For these studies, the dermal layer of the rat lower lip skin was divided into upper and lower dermis. The upper dermis corresponds to the area above the opening of the sebaceous glands into the hair follicles, whereas the lower dermis corresponds to the area below the sebaceous gland openings. The sebaceous glands could easily be identified, due to their classical histological features and their association with hair follicles, by closing the diaphragm of the microscope or applying interference-contrast optics.

Substance P immunostaining for light microscopy. Animals were anesthetized with Equithesin (0.4ml/kg) and transcardially perfused with 4% paraformaldehyde, 15% picric acid (v/v) and 0.1% glutaraldehyde in 0.1M phosphate buffer (PB), pH 7.4, for 30 minutes and for a subsequent 30 minutes in 4% paraformaldehyde and 15% picric acid (v/v) in 0.1M PB. The rat lower lips were collected, post-fixed in the later fixative for one hour at 4^0C and then stored for a minimum of twelve hours in 30% sucrose at 4^0C. A portion of tissue was placed on tissue holders and embedded in Tissue-Tek (OCT). Fifty μm-thick sections were obtained at -20^0C on a Reichert-Jung 2800 Frigocut N cryostat. The sections were washed in phosphate-buffered saline (PBS) containing 0.2% Triton X-100 (T), incubated for 30 minutes in 50% ethanol (Llewellyn-Smith I.J. and Minson J.B., 1992), washed in PBS+T and finally treated with 1% sodium borohydride in PBS for 30 minutes. After extensive washing, the sections were incubated overnight at 4^0C in a rat bispecific antibody against SP and horseradish peroxidase (HRP) (Medicorp, Canada) (Suresh M.R. et al., 1986) diluted 1:10 in PBS+T. The sections were rinsed in PBS+T, prior to a one hour incubation in HRP (Sigma type VI, 5 μg/ml of PBS+T). The sections were then washed in PBS+T and the antigenic sites revealed by treating with diaminobenzidine (DAB) and H_2O_2. The sections were mounted onto gelatin-subbed slides, dehydrated in ascending alcohol concentrations, cleared through xylene and cover slipped with Entellan (BDH).

Some slides were counterstained with toluidine blue (Fisher) prior to the dehydration. This was performed by rehydrating the sections with distilled water for 30 seconds before adding 100-200 μl of a 1% toluidine blue solution per slide for 15

seconds. The sections were then rinsed with distilled water, dehydrated through ascending alcohols, cleared with xylene and cover slipped with Entellan.

Substance P immunostaining for electron microscopy. The rats were perfused as mentioned above. Prior to sectioning, a portion of the lower lip was snap frozen in liquid nitrogen, thawed in 0.1M PB and finally placed on a tissue holder and embedded in Tissue-Tek (OCT). From this point on the immunocytochemistry was performed as above with the exception that Triton X-100 was omitted from all solutions and that the sections were incubated for 3 days at 4^0C in the antibody. Furthermore, SP immunoreactivity was revealed using cobalt and nickel intensified DAB (Ribeiro-da-Silva A. et al., 1993). The sections were osmicated in 1% OsO_4 in PB for one hour and dehydrated in ascending alcohols and propylene oxide. The sections were then flat-embedded in Epon as described in detail elsewhere (Ribeiro-da-Silva A. et al., 1993). The 50 μm-thick sections selected for ultrastructural analyses were re-embedded into Epon blocks and serial 4 μm-thick sections were obtained and attached to glass slides as described in detail elsewhere (De Koninck Y. et al., 1993). The selected 4 μm-thick sections were re-embedded and ultrathin sections obtained with an ultramicrotome using a diamond knife, collected on single-slot, formvar-coated grids and counterstained using uranyl acetate and lead citrate. The material was observed using a Philips 410 LS electron microscope.

Quantification. Substance P-IR terminals from four rats were studied. Four Epon blocks per rat were used for semithin sectioning. Four non-consecutive semithin sections per Epon block were chosen for re-embedding and ultrathin sectioning. Only one ultrathin section per semithin block was observed under the electron microscope. The distance between SP-immunoreactive (SP-IR) terminals and blood vessel endothelial

cells was measured directly from electron micrographs using a ruler. The blood vessel type (arteriole, capillary or venule) was determined by direct visual observation at the time the pictures were taken, based on pre-established histological parameters. Once the quantification was completed, the farthest distance between a SP-IR terminal and a blood vessel endothelial cell was determined. This distance was divided into four equal distance intervals. Thus each SP-IR terminal was classified according to its distance to the blood vessel endothelial cell and the type of blood vessel it associated with. The total number of SP-IR terminals associated with each blood vessel type was considered as 100%. A total of 420 terminals were measured and counted.

Substance P and NK-1 receptor double labelling. The tissue sections were obtained as described above. Following the ethanol and sodium borohydride treatments, the sections were treated with 5% normal goat serum for 30 minutes. Subsequently, the sections were incubated in a mixture of primary antibodies containing rat bispecific anti-substance P anti-HRP (1:10) and a polyclonal rabbit serum generated against the NK-1 receptor (1:250) (Shigemoto R. et al., 1993; Nakaya Y. et al., 1994) in PBS+T for 2 days at 4^0C. The sections were washed, and the SP antigenic sites were revealed as described above. Following the DAB reaction, the sections were washed and incubated in biotinylated goat anti-rabbit IgG (1:800, Vector Labs) for one hour, washed again and finally incubated in an ABC complex (1:400, Vector Labs) for one hour. The sections were then washed and incubated in the SG chromogen (Vector Labs) to reveal the NK-1 receptor antigenic sites. Finally, sections were rinsed with distilled water, mounted on gelatin-subbed slides, dehydrated in ascending ethanol concentrations, cleared with xylene and cover slipped with Permount (Fisher).

Neurokinin-1 receptor immunostaining for electron microscopy. For this immunostaining, all washes and incubations were performed in PBS instead of PBS+T. The sections were obtained and treated with ethanol, sodium borohydride and normal goat serum as described above, prior to incubating in the NK-1 receptor serum for 3 days at 4^0C. Following washes, the sections were incubated in biotinylated goat anti-rabbit IgG (1:800) for one hour, washed and incubated in an ABC complex (1:400) for one hour. After further washes, NK-1 receptor immunoreactivity was revealed using a cobalt and nickel intensified DAB reaction. The sections were then osmicated for one hour, dehydrated in ascending alcohols and propylene oxide and embedded in Epon. Ultrathin sections were then obtained. For further details see the section on *SP immunostaining for electron microscopy* (above).

Controls. Controls were obtained by incubating the sections in the absence of primary antibody. In all cases this resulted in a complete loss of immunoreactivity.

RESULTS

Substance P innervation of the epidermis

Substance P-IR fibres were observed as bundles in small cutaneous nerves (Fig. 2.1 – big arrows) in the dermis and hypodermis. These SP-IR fibre bundles split into individual fibres as they approached the upper dermis (Fig. 2.1 – small arrows). At this level, SP-IR fibres were seen to give off branches which coursed towards the epidermis (Fig. 2.2). Often, these fibres penetrated the epidermis up to the corneal layer (Fig. 2.2A-B). Some SP-IR fibres branched upon entering the epidermis (Fig. 2.2A and 2.2C). This resulted in the enlargement of the terminal field area covered by a single original fibre.

The terminal branches of the SP-IR fibres displayed numerous varicosities, particularly in the upper dermis and epidermis. The non-varicose segments separating the varicosities were shorter in the epidermis than in the dermis (Fig. 2.2C).

Substance P innervation of mast cells, hair follicles and sebaceous glands

Mast cells were very abundant in the rat lower lip skin (Fig. 2.3) and were usually in the proximity of SP-IR fibres. Substance P-IR fibres came close to the mast cells but contacts between these fibres and mast cells were never observed. The lower dermis contained approximately four times more mast cells than the upper dermis (arrows in Fig. 2.3A-B). Triadic arrangements between SP-IR fibres, mast cells and blood vessels were frequently observed (Fig. 2.3C-D and Fig. 2.4). In fact, 30% of mast cells encountered were part of a triad. The minimal distance from the plasma membrane of the mast cell to the plasma membrane of the SP-IR varicosity was found to be from 0.4 μm to 2 μm. In some cases, several varicosities could be found close to the same mast cell (data not shown). Substance P-IR fibres also innervated hair follicles (Fig. 2.5). The fibres penetrated through the glassy membrane and entered the external root sheath and were seen to run along the internal root sheath. Substance P-IR fibres associated with hair follicles also possessed numerous varicosities. The lower portions of the follicles, the hair bulbs, were not innervated by SP-IR fibres. Substance P-IR fibres were also seen travelling along the outer border of sebacous glands (Fig. 2.6).

Substance P innervation of blood vessels

By light microscopy, SP-IR fibres were seen to run along the wall of blood vessels. Further investigation by electron microscopy revealed that the SP-IR terminals were observed close to the endothelial cell layer of blood vessels (Fig. 2.7). In some instances, SP-IR terminals were wrapped in Schwann cell processes (fig. 2.7A and 2.7C-E) while in others the terminals had completely lost their association with Schwann cells (Fig. 2.7B) indicating probable sites of release. Occasionally, two or more terminals were wrapped by the same Schwann cell (Fig. 2.7E). Substance P-IR varicosities were filled with agranular synaptic vesicles and a few dense core vesicles (Fig. 2.8). Most varicosities contained mitochondria as well (Fig. 2.8).

The distance between SP-IR terminals and the outer surface of the endothelial cells was measured and then divided into four equal segments for analytical purposes. Substance P-IR terminals were found within a distance of 0.23 μm to 5.99 μm from the endothelial cells in 82.7% of arterioles, 90.2% of capillaries and in 86.9% of venules (Table 2.1). The remaining SP-IR terminals (between 6.00μm to 11.99 μm) were located at a greater distance from the endothelial cell layer. There was a trend towards the preferential innervation of venules, although in the 3.00 μm to 5.99 μm range SP-IR fibres associated mostly with capillaries. In fact, in the upper dermis, the majority of blood vessels were classified as being capillaries and thus, SP-IR fibres were encountered most frequently close to capillaries, less frequently close to venules and least frequently close to arterioles (Fig. 2.9 and Table 2.1). However, none of these differences are statistically significant. Substance P-IR terminals never made contact with endothelial cells, smooth muscle cells or pericytes.

Relationship between SP-IR fibres and NK-1 receptors

In the upper dermis, the walls of all blood vessels were immunoreactive for the NK-1r. Substance P-IR fibres could be seen to run along the wall of the NK-1r-IR blood vessels (Fig. 2.10). In some instances, the SP-IR fibres wrapped around the blood vessels. In the lower dermis, the labelling of NK-1r-IR blood vessels was less intense and fewer SP-IR fibres innervated these vessels. By electron microscopy we determined that NK-1r were present on the walls of arterioles, capillaries and venules (Fig. 2.11). Neurokinin-1r labelling was associated with endothelial cells, smooth muscle cells and pericytes. Immunoreactivity for NK-1r was never found on mast cells.

DISCUSSION

In this study we describe, for the first time, that SP-IR terminals are equally associated with arterioles, capillaries and venules. These SP-IR terminals are located within the same distance ranges to all three blood vessel types indicating, contrary to common knowledge, that SP-IR terminals in the skin do not preferentially innervate venules. Furthermore NK-1r are associated with the endothelial cell layer of all three blood vessel types described in this study. This suggests that NK-1r are located in the proximity of the site of release of their putative ligand, SP. Thus the above findings, combined with our data showing the proximity of SP-IR terminals to mast cells, provide morphological evidence substantiating SP's role in neurogenic phenomena.

Substance P-IR fibre distribution

Substance P-IR fibres, which are a subset of primary sensory fibres thought to be involved in nociception and neurogenic inflammation, were found throughout the rat lower lip skin. Their overall distribution indicated that SP-IR fibre bundles in cutaneous nerves coursed from the deeper layers of the skin towards the most superficial layer of the epidermis - the corneal layer. As a result of nerve branching, SP-IR fibres would innervate structures such as hair follicles, sebaceous glands, mast cells and bloods vessels along the way. Upon reaching the dermal-epidermal junction, individual SP-IR fibres ran parallel to the epidermis before penetrating it and branching. The distribution of SP-IR fibres described in this study is similar to that already described in human digital skin (Dalsgaard C.-J. et al., 1983; Dalsgaard C.-J. et al., 1989) with a few differences. For instance, we did not see SP-IR fibres innervating sweat glands, as they are absent from the rat lower lip skin, neither did we detect SP-IR fibres innervating Meissner corpuscles. Although SP-IR terminals associated with blood vessels and mast cells appear to be important in neurogenic inflammation, the precise significance of SP-IR terminal innervation of other skin structures still remains ambiguous or unknown.

The presence of agranular vesicles in SP-IR terminals suggests that these terminals may also contain glutamate. In fact, Battaglia and Rustiono showed that glutamate and SP co-exist in dorsal root ganglion (DRG) neurons of rat and monkey (Battaglia G. and Rustioni A., 1988). Furthermore, glutamate immunoreactivity appears to be found in terminals containing round vesicles, like the agranular vesicles described in this paper (Helfert R.H. et al., 1992). The round vesicle-containing terminals are known as R terminals and have been described in cats, rats, guinea pigs and macaques

(Somogyi P. et al., 1986; Beitz A.J., 1990; Clements J.R. et al., 1990; De Biasi S. and Rustioni A., 1990). The co-localization of SP and glutamate within peripheral terminals suggests that they might both have a role to play in neurogenic inflammation.

Substance P-IR fibres: proximity to blood vessels and mast cells

Because of the localization of SP-IR fibres around blood vessels, it has been suggested by a number of researchers that this tachykinin is involved in blood flow control and neurogenic inflammation (Hökfelt T. et al., 1975; Hökfelt T. et al., 1977; Polak J.M. and Bloom S.R., 1981; Furness J.B. et al., 1982). It is now well established that SP mediates vasodilatation and plasma extravasation (Pernow B., 1983; Chahl L.A., 1988; Holzer P., 1992; Donnerer J. and Amann R., 1993; Brain S.D., 1996; Holzer P., 1998). However, CGRP is a more potent vasodilator (Brain S.D., 1996). Thus SP's most prominent role, in neurogenic inflammation, is plasma protein extravasation which occurs as a result of the formations of gaps between the endothelial cells of post-capillary venules (Majno G. et al., 1969; Jancsó G., 1984; Kenins P. et al., 1984; Mendre C. et al., 1989; Kowalski M.L. et al., 1990; Gao G.C. et al., 1991). Dimitriadou et al. (1992) have shown that protein leakage is the result of increased numbers of endothelial pinocytic vesicles and not endothelial gap formation in vessels of the dura-mater. Therefore, the mechanism involved in mediating plasma protein extravasation probably differs with the vascular bed studied. Nonetheless, independently of the mechanism, the available data suggests that SP-IR terminals might preferentially innervate venules. Therefore, in this study we quantified the distance between SP-IR terminals and various blood vessel types. Our results demonstrate that SP-IR terminals innervated arterioles, capillaries and

venules. In fact, SP-IR terminals were located within 6.00 μm of the endothelial cell layer in 82.7% of arterioles, 90.2% of capillaries, and 86.9% of venules. Our data therefore suggests that SP-IR terminals are located more frequently around capillaries. A possible explanation is the fact that the microcirculation in the upper dermis is arranged into capillary loops that arise as extensions from terminal arterioles (Braverman I.M. and Yen A., 1977). Each dermal papilla is usually supplied by only one capillary. The loops allow for a high exchange of nutrients in the epidermis. This is essential, as the epidermis does not contain any blood vessels. By quantifying blood vessels in the superficial layers of the skin, where SP-IR terminals abound, we may be biasing our data towards the quantification of more capillaries with respect to other blood vessel types. Although more capillaries than venules are present in the upper dermis, SP-IR terminals tend to associate more closely with venules.

Contacts between mast cells and sensory nerve endings in humans have been observed using histochemical methods (Naukkarinen A. et al., 1991), however we did not detect any in the rat lower lip skin. This is probably the consequence of the higher resolution of our material due to excellent morphological preservation. Sensory nerves, mast cells and blood vessels have been identified close to one another (Eady R.A. et al., 1979; Wiesner-Henzel L. et al., 1981; Nawa H. et al., 1983; Skofitsch G. et al., 1985), similar to the triadic arrangements we have observed between SP-IR fibres, mast cells and blood vessels. With respect to neurogenic inflammation, mast cells are involved only in the later phases of inflammation when sufficient amounts of SP have been released and are able to diffuse and reach mast cells in the lower dermis (Kowalski M.L. and Kaliner M.A., 1988; Yano H. et al., 1989; Baraniuk J.N. et al., 1990). In fact, mast cells are

located deep within the skin (Kowalski M.L. et al., 1990), whereas SP-IR fibres are most abundant in the upper dermis (Hökfelt T. et al., 1975; Cuello A.C. et al., 1978; Hartschuh W. et al., 1983; Dalsgaard C.-J. et al., 1983; Gibbins I.L. et al., 1985; Gibbins I.L. et al., 1987; Wallengren J. et al., 1987). Furthermore, in mast cell deficient mice, the initial phase of plasma protein extravasation is unaltered, thus providing additional evidence that mast cells are involved in the later stages of neurogenic inflammation (Kowalski M.L. et al., 1990). However, some studies report neurogenic inflammation as being a mast cell-independent phenomena. Following electrical stimulation in rat skin, neurogenic inflammation developed while mast cells remained intact. Mast cell degranulation could only be achieved following prolonged stimulation, although by this point there were no more signs of plasma extravasation (Kowalski M.L. and Kaliner M.A., 1988). Another report suggested that SP had no vasodilatory actions if injected into the skin at doses lower than those required for mast cell degranulation (Brain S.D. and Edwardson J.A., 1987). In fact mast cell involvement has been observed only when high doses of exogenous SP (>10 μM) were administered (Tausk F. and Undem B., 1995) an observation that suggested that sensory fibres do not release sufficient amounts of endogenous SP to degranulate mast cells and led to the conclusion that a role for these cells in neurogenic inflammation was not justifiable. In our study, SP-IR terminals were associated with mast cells in both upper and lower dermis. It should be noted however that mast cells were more numerous in the lower dermis. Therefore, in the rat lower lip, mast cells may be involved in the early stages of plasma protein extravasation but they probably contribute more to later stages.

Neurokinin-1 receptors are expressed on blood vessel walls

In the periphery, at least some of SP's effects occur following SP binding to NK-1r (Stjärne P. et al., 1994). These receptors have been located on blood vessels and described on both endothelial and smooth muscle cells (Bowden J.J. et al., 1996; Kummer W. et al., 1999; Kido M.A. et al., 1999; Shimizu T. et al., 1999). Our light microscopy results revealed a close association between SP-IR terminals and NK-1r immunoreactive blood vessels. By electron microscopy, we determined that all blood vessels (arterioles, capillaries and venules) in the upper dermis of the skin possessed NK-1r. Although all blood vessel types express NK-1r, it is still unclear as to why SP is less potent than CGRP in mediating vasodilatation. By careful visual observation of the material we suggest that although NK-1r are present on arterioles, the intensity of labelling is less than on venules, suggesting the presence of fewer NK-1r on arterioles while CGRP receptors may be more abundant on arterioles. Our results are in accordance with those of other researchers that have identified NK-1r binding sites on blood vessel endothelial and smooth muscle cells (O'Flynn N.M. et al., 1989), with smooth muscle cell labelling being less intense than endothelial cell labelling. We also detected NK-1r on pericytic cells.

Substance P is capable of causing the release of vasoactive substances such as histamine and serotonin from mast cells [for review see (Holzer P., 1998)]. As SP's effects are mediate through NK-1r, it was thought that these receptors were expressed on the cell membrane of mast cells. We did not detect the presence of NK-1r on mast cells, in accordance with the results obtained by O'Flynn et al. (O'Flynn N.M. et al., 1989). This reinforces the observation that SP-induced mast cell activation is non-NK-1

receptor-mediated and occurs by direct interaction of SP's N-terminal basic residues with G-proteins on mast cell plasma membranes (Bueb J.L. et al., 1990).

Substance P and vascular blood flow

Our anatomical findings also suggest that SP may play a role in blood flow control. Studies have provided evidence that SP is involved in the control of vascular tone in humans (Crossman D.C. et al., 1989; Quyyumi A.A. et al., 1997). However, a recent study in human forearm skin suggests that endogenous SP is not involved in the maintenance of basal vascular tone (Newby D.E. et al., 1999). Indeed these researchers report no change in peripheral vascular tone and blood pressure following administration of NK-1r antagonists, although exogenous SP causes vasodilatation in the forearm skin through the activation of endothelial NK-1r. With respect to rat skin microcirculation, SP appears to exert tonic regulation of the vascular tone (Yonehara N. et al., 1992; Yonehara N. et al., 1993). This suggests that blood flow is differentially regulated in rat and human. However, as the results obtained in man are still inconclusive, further investigations are required. Holzer (1998) suggests that the role of peptidergic neurons in nociception must be considered when evaluating the participation of these neurons in vascular tone control. The microcirculatory changes observed usually occur in response to trauma or irritation of the skin because the peptidergic neurons' functions are to maintain tissue integrity and repair capability. When skin homeostasis is not maintained, disorders such as psoriasis, bullous pemphigoid, eczema, and photodermatoses may develop due to hyperreactive petidergic neurons (Geppetti P. and Holzer P., 1996). Therefore, under normal

conditions, peptidergic neurons may play a more significant role in the development of disease states than in the control of blood flow.

Conclusion

Substance P-IR fibres were associated with hair follicles, sebaceous glands, NK-1r immunopositive blood vessels and mast cells within the rat lower lip skin. The proximity of SP-IR fibres to blood vessels and mast cells is consistent with SP's role in neurogenic inflammation. The observation that SP-IR fibres equally innervate arterioles, capillaries and venules suggests that SP is as important in the generation of vasodilatation as it is in plasma protein extravasation in the skin of the rat lower lip. Furthermore, the proximity of SP-IR terminals to blood vessels in the upper dermis may suggest that these sensory fibres are directly involved in the regulation of cutaneous microcirculation. Lastly as SP-IR fibres are involved in nociception, their association with blood vessels may insure that proper homeostasis is maintained following trauma to the skin.

FIGURE 2.1: ***Pattern of SP-IR fibre innervation of the rat lower lip.*** Substance P-IR fibre bundles in cutaneous nerves of the lower dermis, and branching into smaller bundles as the fibres approach the upper dermis (**A & B** – larger arrows). Above the sebaceous gland level, these smaller bundles branch into individual fibres (**A & B** – smaller arrows) that are mainly directed towards the surface of the skin. Scale bar = 25 μm.

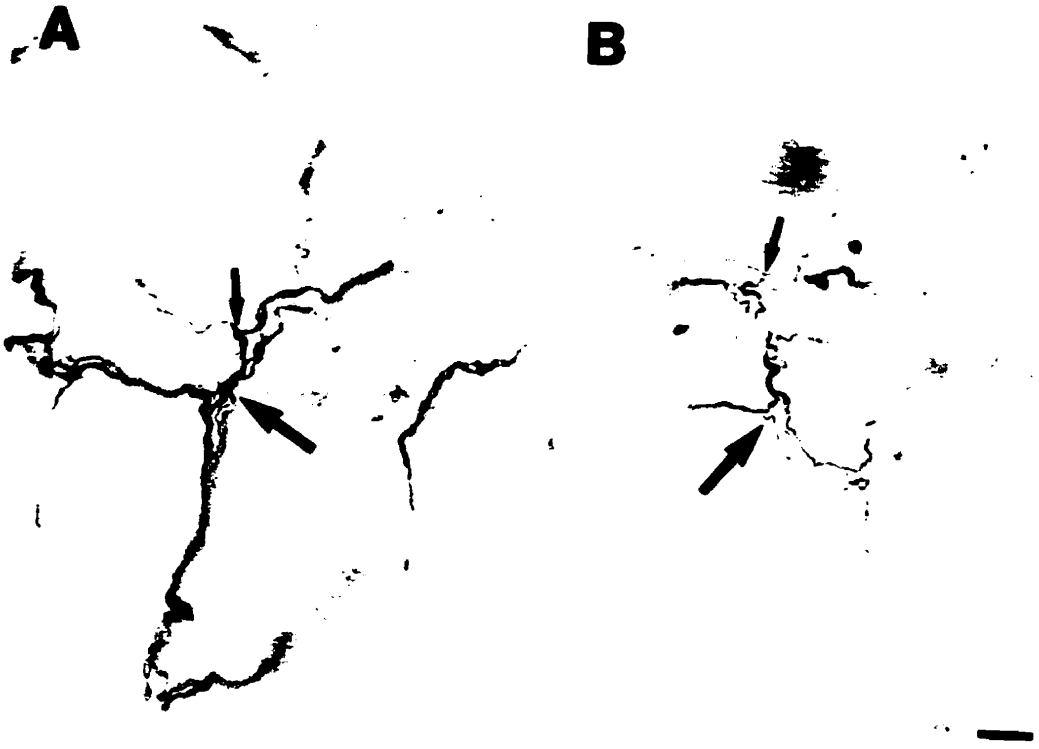
A
B

FIGURE 2.2: ***Substance P-IR fibres innervate the epidermis.*** The epidermis (e) is easily visualised in this preparation because the material has been counterstained with toluidine blue. Note that SP-IR fibres occasionally penetrate the epidermis (**A-C**). Upon entering the epidermis the SP-IR fibres branch (small arrows). The SP-IR fibres course through the epidermal layers up to the corneal layer (**A & B**), but never penetrate this layer. In panel **C** note that the SP-IR fibres run along the dermal epidermal junction before entering the epidermis at a 90^0 angle. Note the presence of numerous axonal varicosities on the SP-IR fibres in the epidermis. Scale bar = 25 μm.


A
B
C

FIGURE 2.3: ***Localisation of mast cells in the rat lower lip.*** The material for this figure was obtained from toluidine blue counterstained sections. Panels **A & B** represent fields of the upper and lower dermis respectively. Note the abundance of mast cells (arrows) in the lower dermis compared to the upper dermis. Panels **C & D** show the triadic arrangement between SP-IR fibres (curved arrows), mast cells (arrows) and blood vessels (L, blood vessel lumen). These triads occur more frequently in the lower dermis. Note the SP-IR fibres running along the outer borders of the blood vessel walls. These SP-IR fibres are studded with axonal varicosities. In panel **C** a mast cell can been seen almost making contact with the blood vessel wall. Scale bar = 25 μm.


A
B
C
L
D
L

FIGURE 2.4: ***Triadic arrangement between SP-IR terminals, mast cells and blood vessels in the rat skin.*** In panels **A & B** note that SP-IR terminals (arrows) can be found in the vicinity of blood vessels (L, vessel lumen) and mast cells (M). In this figure the SP-IR terminals are still wrapped by Schwann cells (S). The blood vessels in this figure appear to be venules. Scale bar = 1 μm.

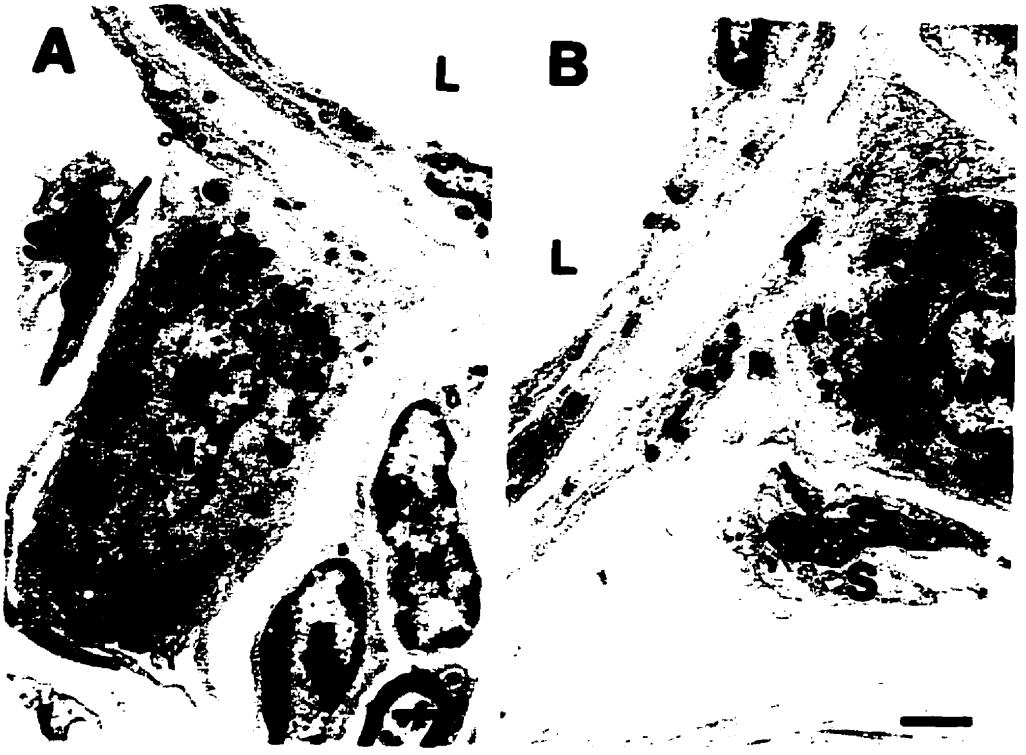
A
L
B
L
S

FIGURE 2.5: ***Substance P-IR fibres innervate hair follicles.*** For better visualisation of the layers in the hair follicles the sections were counterstained with toluidine blue. Substance P-IR fibres (arrows) are seen to run along the internal root sheath of hair follicles (F). The fibres never penetrate the internal root sheath. The SP-IR fibres associated with hair follicles are always very fine and few in number. These fibres also possess axonal varicosities (thin arrows). Scale bar = 25 μm.


A
F
B
F

FIGURE 2.6: ***Substance P-IR fibres innervate sebaceous glands.*** In panels **A & B** SP-IR fibres (arrows) are seen to run along the outer border of the sebacous glands (S). These fibres never penetrate the glands and contacts between the glands and the SP-IR fibres were never seen. Note the presence of axonal varicosities on the SP-IR fibres. Scale bars = 25 μm.


A
B
S
S

FIGURE 2.7: ***Proximity of SP-IR fibres to blood vessel endothelial cells.*** Substance P-IR fibre terminals (arrows) are seen close to blood vessel endothelial cells (e) of arterioles, capillaries and venules. The SP-IR fibres are wrapped by Schwann cells (s) (**A & C-E**). Note that in **E** two terminals are wrapped by the same Schwann cell. In **B** the SP-IR terminal has lost its association with its Schwann cell. L, blood vessel lumen. Scale bar = 0.5 μm.


A
S
L
B
L
C
L
S
D
L
S
E
L

FIGURE 2.8: ***High power magnification of a SP-IR varicosity.*** Substance P-IR varicosities resemble the one depicted in this figure. They contain both dense core (long arrows) and agranular (small arrows) synaptic vesicles. Note also the presence of numerous mitochondria (M) in the SP-IR varicosity. Scale bar = 0.5 μm

FIGURE 2.9: ***Quantification of the distance separating SP-IR terminals from blood vessel endothelial cells.*** All blood vessels were classified as arterioles, capillaries or venules. Larger calibre vessels were not observed. The distance of the SP-IR terminals to the blood vessel endothelial cells was obtained and tabulated as the number of terminals associated to each blood vessel type within each of four equal distance intervals. As the distance between the SP-IR terminals and the endothelial cells increased, the number of quantifiable SP-IR terminals decreased. Note that SP-IR terminals did not preferentially innervate any blood vessel type and that arterioles and venules were the blood vessel types encountered most frequently. The largest number of terminals was observed in the 0.23-2.99 μm range. Note also that at this range there was a trend towards the preferential innervation of venules, while in the 3.00-5.99 μm range the trend was towards the preferential innervation of arterioles, although in both cases the differences were not significant.

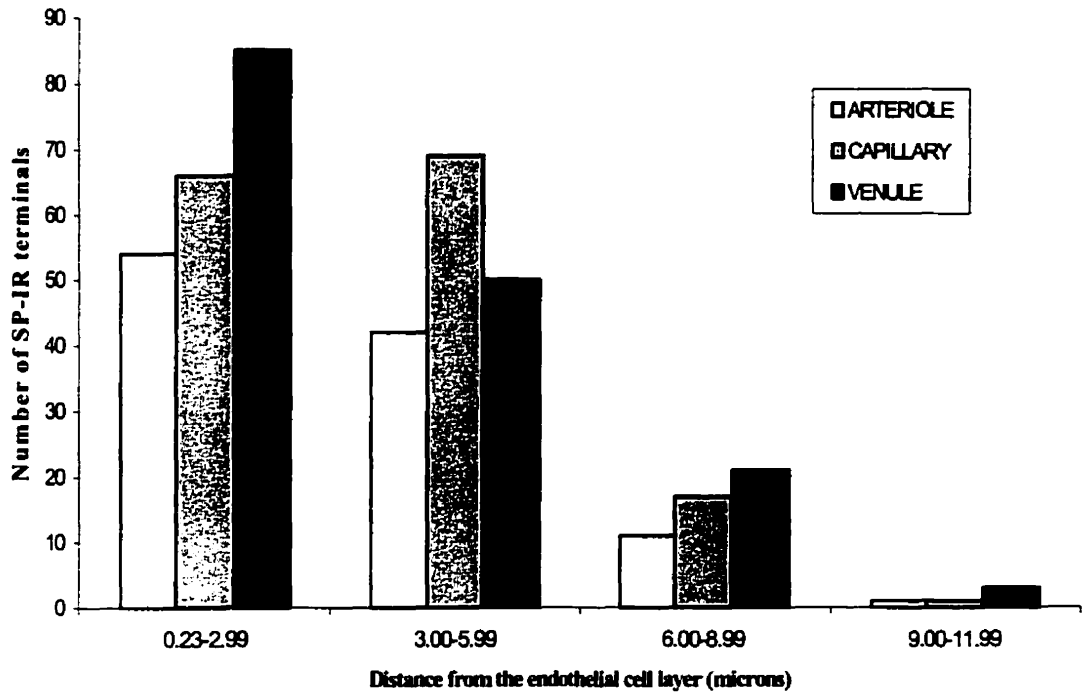
90
80
70
60
50
40
30
20
10
0
Number of SP-IR terminals
ARTERIOLE
CAPILLARY
VENULE
0.23-2.99
3.00-5.99
6.00-8.99
9.00-11.99
Distance from the endothelial cell layer (microns)

FIGURE 2.10: ***Double labelling light microscopy for SP and NK-1r.*** Substance P-IR fibres innervate NK-1r-IR blood vessels in the upper dermis of the rat lower lip, as depicted in this figure. Note in panels **A & B** SP-IR fibres running along the border of the blood vessel walls. In panel **C** note that the SP-IR fibre is seen closely wrapping itself around the NK-1r-IR blood vessel. In all cases single SP-IR fibres and not fibre bundles innervate NK-1r-IR blood vessels. V, blood vessel lumen. Scale bar = 20 μm.


A
SP
NK-1
B
SP
C
NK-1

FIGURE 2.11: ***Electron microscopy of immunostaining for the NK-1r.*** Neurokinin-1r-IR is mostly associated with the endothelial cell layer (E) of all blood vessels in the upper dermis of the rat lower lip. Panels **A, B & C** depict arterioles, capillaries and venules respectively. In some instances immunoreactivity could be observed on smooth muscle cells or pericytes (P). Panels D,E and F correspond to enlargements of the areas contained between the arrows in panels A,B and C respectively. In A & B scale bar = 1 μm. In C scale bar = 5 μm. In D & E scale bar = 0.5 μm. In F scale bar = 2 μm.

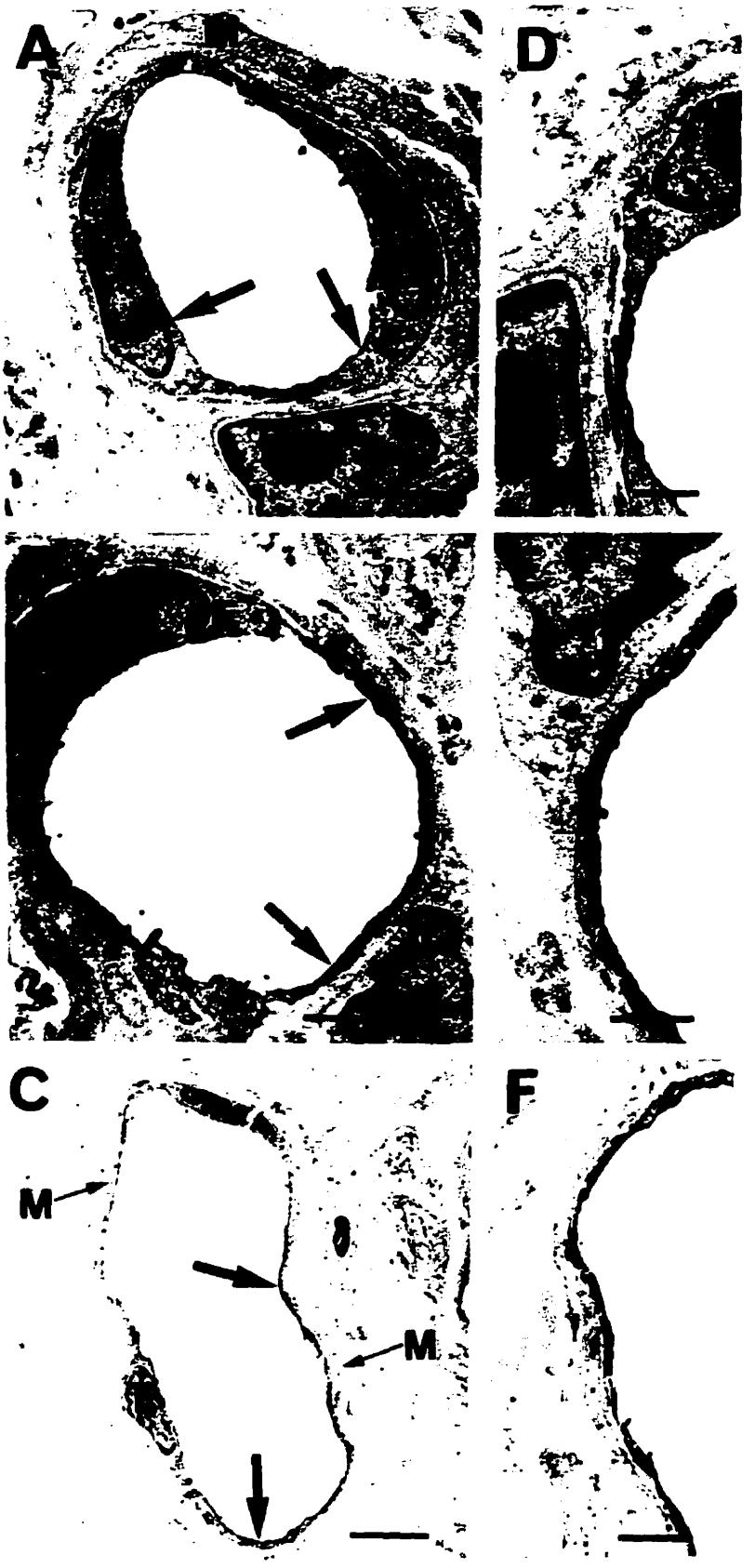
A
D
C
M
M
F

TABLE 2.1. Quantification of the distance between SP-IR terminals and the outer surface of the endothelium of blood vessels in the upper dermis[1]

Distance from endothelium	Arterioles	Capillaries	Venules
0.00-2.99 μm	44.23% (46)	46.60% (76)	54.20% (83)
3.00-5.99 μm	38.46% (40)	43.60% (71)	32.70% (50)
6.00-8.99 μm	16.35% (17)	8.60% (14)	11.80% (18)
9.00-11.99 μm	0.96% (1)	1.20% (2)	1.30% (2)

[1]Percentage of SP-IR terminals within each of four equal distance intervals from the endothelium of blood vessels. Numbers in brackets represent the number of terminals quantified. Note that at the shortest and longest ranges, SP-IR terminals preferentially innervate venules, although this difference is not significant. Note also that capillaries are the most abundant vessel type encountered in the upper dermis.

CONNECTING TEXT – CHAPTER 2 TO 3

In chapter 2, we investigated the pattern of SP fibre innervation of the rat lower lip skin. At the light microscopic level, SP immunoreactivity was found in the vicinity of blood vessels, hair follicles, sebaceous glands and mast cells. The ultrastructural quantification of the distance separating SP-IR terminals and blood vessel endothelial cells revealed that, contrary to common knowledge, SP did not preferentially innervate venules. Instead, immunoreactive terminals equally associated with arterioles, capillaries and venules. NK-1r immunoreactivity was also detected on the walls of these blood vessels. Thus SP appears to be capable of equally influencing all the blood vessels types of the microvasculature.

Despite the suggestion that SP plays a role in blood flow regulation, it is still unclear as to how this system interacts with the autonomic system. Therefore in the next chapter, we address this issue using antibodies against DβH and vAChT to label sympathetic and parasympathetic fibres, respectively. The relationships that SP-, DβH- and VAChT-IR fibres have with respect to one another and to their targets was investigated, at both the light and electron microscopic levels, in the skin of the rat lower lip.

CHAPTER 3

Skin Blood Vessels are Simultaneously Innervated by Sensory, Sympathetic and Parasympathetic Fibres

Isabella Ruocco, A. Claudio Cuello, A. Parent,
and Alfredo Ribeiro-da-Silva

Submitted to: The Journal of Comparative Neurology
(2001)

ABSTRACT

Despite the known major role of skin blood vessel innervation in blood flow control, particularly in disease, there is little information on co-innervation of blood vessels by sensory and autonomic fibres and the relationships of theses fibres to one another. To fill this gap in our knowledge, we performed a complete light and electron microscopic analysis of the innervation of skin vessels by sensory and autonomic fibres using the rat and monkey lower lips as a model. In rats, double-labelling immunocytochemistry revealed that combinations of fibres immunoreactive for substance P (SP) and dopamine-β-hydroxylase (DβH), SP and vesicular acetylcholine transporter (VAChT), as well as DβH and VAChT occurred in skin blood vessels of rats. All fibre types travelled in parallel and in close proximity to one another. Blood vessels immunoreactive for only one fibre-type were never observed. Although nerve terminals displayed synaptic vesicles, synaptic specializations were never observed, suggesting that, in this territory, these fibres do not establish synaptic contacts. Quantification of the distance between the various immunoreactive terminals and their presumptive targets (smooth muscle cells and endothelial cells) revealed that both sympathetic and parasympathetic fibres were significantly closer to the endothelial cell layer than sensory fibres, while only sympathetic fibres were significantly closer to smooth muscle cells compared to sensory fibres. In monkeys, double labelling immunocytochemistry was performed for SP-DβH and SP-VAChT only. The results obtained are similar to those in rats, however the intensity of the signals was more intense in monkeys. Our findings suggest that the regulation of skin microcirculation might be the result of the coordinated functions of sensory and autonomic fibres.

INTRODUCTION

It is well established that cutaneous substance P (SP)-containing sensory fibres are associated with blood vessels and are, at least in part, responsible for mediating antidromic phenomena such as vasodilatation and plasma extravasation (Lembeck F. and Holzer P., 1979; Couture R. et al., 1985). In cat gingiva, the use of SP and histamine H_1 receptor antagonists to block the effect of the trigeminal system and of mast cell activation, respectively, results in only a 20-30% decrease in the vasodilatory response (Izumi H. and Karita K., 1990; Izumi H. and Karita K., 1991), suggesting that other mediators or systems are involved in mediating the vasodilatation. It has been suggested that parasympathetic fibres may play a role in vasodilation (Couture R. et al., 1985), as it is well established that acetylcholine induces vasodilatation (Rang H.P. and Dale M.M., 1991). However, the parasympathetic fibre innervation of the skin is still not fully established, although there is sufficient evidence from the literature to state that it occurs at least in certain territories. For instance, there is immunohistochemical evidence using the indirect markers of parasympathetic fibres vasoactive intestinal polypeptide (VIP) and acetylcholinesterase (AChE), which, combined with a tracer, strongly suggested the presence of parasympathetic fibres around blood vessels in the rat lower lip skin (Kaji A. et al., 1988; Kaji A. et al., 1991). However, the precise relationship of these fibres to the blood vessel wall still remains unstudied.

In contrast with vasodilatation, which appears to result from sensory and parasympathetic fibre activation, vasoconstriction is controlled solely by sympathetic fibres, an effect that appears to be mediated via α-adrenergic receptors (Brown G.L. and Gillespie J.S., 1957; Ross G., 1971; Starke K., 1977; Izumi H. et al., 1990; Izumi H. and

Karita K., 1991; Hirst G.D.S. et al., 1996). The primary effect of sympathetic stimulation is determined by the number and distribution of α-adrenergic receptors (Ross G., 1971).

Although it is known that sensory and parasympathetic fibres mediate vasodilatation and that sympathetic fibres mediate vasoconstriction, it is still unclear as to how these fibre types relate to one another in a given vascular territory. In fact no study has ever attempted to compare all three fibre systems using both light and electron microscopy. Isolated studies in cats, dogs, guinea pigs and rats have reported minor differences in the organisation of the sensory and autonomic systems in these animals. Therefore, as the available data was obtained in different species, it is difficult to compare the results and formulate a comprehensive scheme of the interactions between sensory, sympathetic and parasympathetic fibres. An attempt has been made to compare all three systems and their distances to the blood vessels in the guinea pig, however no systematic quantification was performed and the results were based solely on visual observations (Edvinsson L. et al., 1989). Furthermore, Matsuyama et al. (1985) suggested that SP- and VIP-IR terminals were located within 100 nm from blood vessel smooth muscle cells, however no true quantification was performed in order to obtain the above value.

In short, there is only limited information on the relationships between sensory and autonomic fibres innervating blood vessels. In an attempt to fill this gap, we performed a thorough investigation of the innervation patterns by sensory, sympathetic and parasympathetic fibres of the rat lower lip skin, using antibodies against SP, dopamine-β-hydroxylase (DβH) and the vesicular acetylcholine transporter (VAChT). Furthermore we also studied the innervation patterns of blood vessels in monkeys as, to

our knowledge, no studies have ever been performed in this species. In this study we applied double-labelling immunocytochemistry to determine the fibre combinations associated with blood vessels and a quantitative analysis of some of these anatomical relationships in rat skin was performed.

MATERIALS AND METHODS

All rodent experiments were performed on male Wistar rats weighing 250-300 g. Animals were treated according to the guidelines provided by the Canadian Council on Animal Care and the McGill University Animal Care Committee. The animals were provided with food and water *ad libitum*, and kept under a twelve-hour day/night cycle. All efforts were made to minimise the number of animals used and animal suffering.

Primate tissue was obtained from two cynomolgus monkeys (*Macaca fascicularis*, 6-7 kg) and two squirrel monkeys (*Saimir sciureus*, 800-1000 g) of both sexes, which were used mainly for tract-tracing analysis of the basal ganglia circuitry. These animals received small, microiontophoretic injections of the antoregrade tracer biotinylated dextran amine in various components of the basal ganglia, as described in detail elsewhere (Sato F. et al., 2000). After a survival period of 8 to 10 days, the animals were processed as described below. All surgical and animal care procedures followed the guidelines of the Canadian Council on Animal Care and Laval University Animal Care Committee.

Light microscopy

A total of four rats were used for each immunostaining combination. Rats were anaesthetised with Equithesin (6.5 mg chloral hydrate - 3 mg sodium pentobarbital in a volume of 0.3 ml, i.p., per 100 g body weight) prior to transcardial perfusions for 30 minutes with 4% paraformaldehyde, 15% picric acid (v/v) and 0.1% glutaraldehyde in 0.1M phosphate buffer (PB), pH 7.4, and a subsequent 30 minutes with 4% paraformaldehyde and 15% picric acid in PB. The lower lips were collected and post-fixed in the latter fixative for one hour at 4^0C. The tissue was then infiltrated with 30% sucrose in PB for a minimum of 12 hours prior to being trimmed, snap frozen in liquid nitrogen, placed on a tissue holder and embedded in Tissue-Tek (OCT). Finally, 50-µm thick sections were obtained at -20^0C on a cryostat (Reichert-Jung 2800 Frigocut N). All sections were collected in phosphate buffered saline (PBS) containing 0.2% Triton X-100 (+T), pH 7.4. All washes and antibody dilutions were performed in PBS+T. Two 15-minute washes separated each treatment.

Double labelling for SP and DβH. The sections were pre-treated with 50% ethanol (v/v) (Llewellyn-Smith I.J. and Minson J.B., 1992) and 1% sodium borohydride in PBS for 30 minutes each, prior to an overnight incubation at 4^0C in a rat bi-specific anti-SP anti-horseradish peroxidase (HRP) monoclonal antibody (1:10) (Suresh M.R. et al., 1986) and a mouse monoclonal anti-DβH antibody (1:10: PharMingen, USA) (Mazzoni I.E. et al., 1991). Subsequently the sections were treated with HRP (Sigma type VI, 5µg/ml) and the SP antigenic sites were revealed by reacting the sections in 3,3'-diaminobenzidine tetrahydrochloride (DAB) and H_2O_2. The sections were then incubated

for one hour in a goat anti-mouse IgG (1:50; American Qualex), preabsorbed in fixed rat lip tissue for eight hours at 4^0C (Ruocco I. et al., 2000), and treated for one hour in a mouse monoclonal anti-HRP antibody (Seralab, UK) to which 5 μg/ml HRP had been previously added (Semenenko F.M. et al., 1985). In this case, the HRP was revealed using an SG chromogen labelling kit as instructed by the manufacturer (Vector Labs). Finally the sections were mounted on gelatin-subbed slides, dehydrated though ascending ethanol concentrations, cleared with xylene and cover-slipped with Permount (Fisher). A similar protocol was used for staining tissue from both cynomolgus and squirrel monkeys. These animals were anaesthetized with sodium pentobarbital and perfused transcardially with saline (NaCl, 0.9%), followed a fixative mixture of 4% paraformaldehyde and 0.1% glutaraldehyde in 0.1M PB, ph 7.4, for 30 minutes, followed by a final wash in 10% sucrose in PB. The monkey lower lips were collected, post-fixed in 4% paraformaldehyde in PB for 2 hours at 4^0C and cryoprotected with 30% sucrose in PB for a minimum of 12 hours. Following sectioning on the cryostat, the tissue was pre-treated with 50% ethanol, 0.3% H_2O_2 and 1% sodium borohydride. The sections were then incubated overnight at 4^0C in a rat bi-specific anti-SP anti-HRP monoclonal antibody and a rabbit serum against DβH (1:2000; Eugene Tech International Inc., NJ). SP antigenic sites were revealed as described above for the rat. The DβH antigenic sites were revealed by incubating the sections for one hour in goat anti-rabbit IgG (1:3000; ICN), which was preabsorbed in fixed rat lip for 8 hours at 4^0C, and one hour in an ABC complex (1:50; Vector Labs), prior to reacting the tissue with the SG chromogen.

Double labelling for SP and VAChT. The sections were pre-treated with 1% sodium borohydride and 5% normal goat serum (NGS). No ethanol was used for this staining. The sections were incubated overnight at 4^0C in a rat bi-specific anti-SP/anti-HRP monoclonal antibody and a rabbit polyclonal serum against VAChT (1:10 000) (Gilmor M.L. et al., 1996). The SP antigenic sites were revealed as indicated above. Following the reaction with DAB and H_2O_2, the sections were incubated for one hour in biotinylated goat anti-rabbit IgG (1:800 in 5% NGS; Vector Labs) and then for one hour in an ABC complex (1:400; Vector Labs). The VAChT antigenic sites were revealed as described above for DβH, using the SG chromogen. A similar protocol was used for staining tissue from both cynomolgus and squirrel monkeys, obtained as described above. Following sectioning on the cryostat, the tissue was pre-treated with 50% ethanol, 0.3% H_2O_2, 1% sodium borohydride and 5% NGS. The sections were then incubated overnight at 4^0C in a rat bi-specific anti-SP anti-HRP monoclonal antibody and a rabbit polyclonal serum against VAChT (1:3000). SP and VAChT antigenic sites were revealed as described above for the rat.

Double labelling for DβH and VAChT. Rat tissue sections were pre-treated in 50% ethanol, 1% sodium borohydride and 5% NGS prior to incubation in the mouse monoclonal anti-DβH antibody and the anti-VAChT rabbit serum overnight at 4^0C. Immunocytochemistry for DβH was performed as previously mentioned. However, the DβH antigenic sites were revealed by reacting the sections in DAB and H_2O_2. For VAChT staining the protocol was as described above. This double labelling was not performed in monkeys as these primary antibodies were both raised in rabbits. Attempts

at using a mouse anti-tyrosine hydroxylase or a mouse anti-DβH antibody were unsuccessful.

Sympathetic denervations. Sympathetic denervations were performed by the bilateral removal of the superior cervical ganglia (SCG) in four rats. This was done to confirm that the VAChT-IR fibres are of true parasympathetic origin. Following the surgery the rats were left to recover for one week. They were then perfused and single labelling immunocytochemistry for DβH and VAChT was performed (see above for the details of the experiment). In both cases, the antigenic sites were revealed by reacting the sections with DAB and H_2O_2.

Electron microscopy

A total of four rats were used. The animals were perfused as for light microscopy. However, all washes and incubations were performed in PBS instead of PBS+T. For electron microscopy, only single labelling experiments were performed. The protocols were identical to those described for light microscopy, although the antigenic sites were revealed differently. The DAB reaction was intensified using cobalt chloride and nickel-ammonium sulphate (Ribeiro-da-Silva A. et al., 1993). Following the double intensified DAB reaction, the sections were treated with OsO_4 for one hour and dehydrated in ascending alcohols and propylene oxide. The sections were flat-embedded in Epon [for details see (Ribeiro-da-Silva A. et al., 1993)], selected using light microscopic observation, the regions of interest re-embedded into Epon blocks from which ultrathin sections were cut and collected on formvar-coated one-slot copper grids using an

ultramicrotome. The sections were counterstained with uranyl acetate and lead citrate prior to observation using a Philips 410 LS electron microscope.

Quantification. For each antigenic site (SP, DβH and VAChT) under investigation, four re-embedded Epon blocks per rat (n=4) were trimmed. Ultrathin sections were then obtained as described above and observed under the electron microscope. Only one ultrathin section per block was chosen and only one blood vessel per ultrathin section was quantified. Photographs were taken of the blood vessels and their associated immunopositive terminals. The total number of terminals was counted and the distance of these terminals to the outermost smooth cells and to the adluminal surface of the endothelial cells was measured directly from the pictures, for each blood vessel, using a ruler. Therefore a total of 16 blood vessels per type of immunostaining were quantified. Statistical significance was assessed by performing an unpaired Student's t-test on the average values, per animal, of the distances of the immunopositive terminals to the surface of the endothelial cells and to smooth muscle cells. The following comparisons were performed: SP vs. DβH varicosities, SP vs. VAChT varicositiess and DβH vs. VAChT varicosities.

RESULTS

Light microscopy

Upper dermal blood vessels were innervated exclusively by SP-IR fibres. Dually innervated blood vessels were found only in the lower dermis in both rat and monkey. Furthermore, no significant differences were observed between Old World (cynomolgus

monkeys) and New World (squirrel monkeys) primates in regards to the pattern of blood vessel innervation.

Blood vessels are dually innervated by SP- and DβH-IR fibres

In the rat, SP-IR fibres were observed running along the blood vessel walls and displayed numerous varicosities at irregular intervals along the nerve fibres. DβH-IR fibres were seen innervating the same arterioles and venules as the SP-IR fibres. DβH-IR fibres innervated blood vessels, forming a mesh-like network around their wall (Fig. 3.1). These fibres possessed numerous varicosities located at regular intervals along the nerve fibre (Fig. 3.1-small arrows).

Dually innervated blood vessels were also observed in the monkeys' lower lip skin. SP- and DβH-IR fibres were located around small arteries and veins (Fig. 3.2) and around arterioles (data not shown). However, for both fibre types, a denser innervation pattern was observed in monkeys than in rats (Fig. 3.3). Furthermore, in monkeys, SP-IR fibres formed a mesh-like network around the blood vessel walls, an arrangement that did not occur in the rat.

Blood vessels are dually innervated by SP- and VAChT-IR fibres

In rat material processed for the demonstration of SP- and VAChT-IR fibres, the pattern of SP-IR fibre innervation is identical to the one described above. However, we detected that blood vessels were also innervated by VAChT-IR fibres (Fig. 3.4). The VAChT-IR fibres, like the SP-IR fibres, travelled along the walls of arterioles and venules, although never wrapping around them. The VAChT-IR fibres were studded with

numerous varicosities. Very often SP-IR and VAChT-IR fibres were seen coursing parallel and in close proximity to one another (Fig. 3.4 - curved arrows). In cross-sections (Fig. 3.4 C-D), both fibre types were intertwined as they coursed along the adventitial border of the blood vessel walls. To confirm that the VAChT-IR fibres were true parasympathetic fibres, sympathectomies were performed on a group of rats. One-week post-surgery, the DβH-IR fibres had completely disappeared in these animals while the VAChT-IR persisted.

In monkeys, we also observed this dual pattern of innervation of lower lip skin blood vessels. The SP- and VAChT-IR blood vessels were identified as small arteries and veins (Fig. 3.5), as well as arterioles (data not shown). The labelling intensity around these vessels was denser than in rats.

Blood vessels are dually innervated by DβH- and VAChT-IR fibres

In the rat, DβH- and VAChT-IR fibres were distributed around the same arterioles and venules (Fig. 3.6). The patterns of immunoreactivity for both fibre types were identical to those described in the previous sections. In some instances DβH- and VAChT-IR fibre labelling would perfectly overlay one another. For the reasons given in the Materials of Methods section, this double-labelling was not studied in monkey tissue.

Electron microscopy

Electron microscopic observations were performed only in the rat. SP-, DβH- and VAChT-IR terminals were all surrounded, at least in part, by Schwann cell cytoplasm (see Fig. 3.7-3.9). All terminals were filled with numerous synaptic vesicles, however

contacts between the terminals and the smooth muscle cells were never observed. In certain instances the terminals were very close to the smooth muscle cells and had lost part of their association with the Schwann cell (Fig. 3.8 A-B). Interestingly, VAChT-IR terminals were sometimes located between a blood vessel smooth muscle cell and a mast cell (Fig. 3.9B). On average, equal numbers of DβH-, SP- and VAChT-IR terminals were associated with blood vessels. Although VAChT-IR terminals were the least abundant, this difference was not significant (Table 3.1).

Our quantitative analysis revealed that DβH- and VAChT-IR terminals were located significantly closer to endothelial cells than SP-IR terminals (Fig. 3.10A). DβH-IR terminals were found within 2.3 μm from the endothelial cells while SP- and VAChT-IR terminals were within 4.3 μm and 2.6 μm respectively. However, DβH-IR terminals were the only ones to be significantly closer to smooth muscle cells when compared to SP-IR terminals (Fig. 3.10B). Although, VAChT-IR terminals tended to be located closer to smooth muscle cells when compared to SP-IR terminals, this difference was not significant (Fig. 3.10B). The distances separating the smooth muscle cells from the DBH-, SP- and VAChT-IR terminals were 1.1 μm, 3.0 μm and 1.5 μm respectively.

DISCUSSION

Sensory and autonomic innervation of lower lip blood vessels

To our knowledge, our study represents the first complete quantitative study demonstrating that the same skin blood vessels are innervated by both sensory and autonomic fibres. Our data suggest that SP-containing sensory, noradrenergic and cholinergic fibres possibly innervate the same blood vessels in the lower dermis of the rat

lower lip, since single-labelled blood vessels were not detected in this region. However, only SP-containing sensory fibres were found around upper dermal blood vessels (data not shown) in both rats and monkeys. An initial description of the possible innervation of vessels by sensory, sympathetic and parasympathetic was performed in the cerebral blood vessels (Edvinsson L., 1987).

Previous studies in our laboratory have demonstrated that sensory and sympathetic fibres enter the lower lip via independent pathways (Ruocco I. et al., 2000). In the present study we have shown this to also be true for the parasympathetic fibres since the bilateral removal of the SCG did not affect the staining intensity for VAChT, while it abolished any traces of DβH-IR fibre labelling. Kaji et al. (1988) provided evidence that, in the rat lower lip, VIP-IR fibres originate from the otic ganglion and are parasympathetic. Furthermore, they have shown that removing the SCG did not affect VIP-IR fibre labelling, eliminating the possibility that these fibres might be sympathetic fibres passing through the otic ganglion. In the skin, studies indicate that cholinergic fibres arise from parasympathetic fibres and a subset of postganglionic sympathetic fibres innervating sweat glands (Landis S.C. and Fredieu J.R., 1986; Schäfer M.K.-H. et al., 1997). However as there are no sweat glands in the rat lower lip skin, the cholinergic fibres in this tissue are strictly of parasympathetic origin.

No synaptic contacts or specializations were observed for any of the terminals studied. It has been suggested that the relationship between terminals and blood vessels cannot be accurately determined by randomly viewing single tissue sections (Hirst G.D.S. et al., 1996). However, as we observed blood vessels oriented in all three planes, we think that random sampling allows the detection of all possible profile scenarios. Therefore, if

one scenario is not observed, it probably does not occur or occurs at a very low frequency.

Autonomic terminals are located closer to blood vessel walls than sensory terminals

Our quantitative analysis revealed that SP-IR terminals occurred at a significantly greater distance from the surface of blood vessel endothelial cells compared to DβH- and VAChT-IR terminals. This data is in accordance with studies in which SP- and calcitonin gene-related peptide-IR varicosities were located farther from the adventitia or more superficially within the adventitia than tyrosine hydroxylase- and VIP-IR nerves (Morris J.L. et al., 1986; Edvinsson L. et al., 1989), although no quantification was performed in these studies. Therefore, our data provides the first true quantitative analysis of sensory and autonomic terminals and their spatial relationship to the blood vessel walls.

When comparing the distance between the immunoreactive terminals and the vessel smooth muscle cells, a significant difference was observed only between SP- and DβH-IR terminals, with the later lying closer to the blood vessel muscular layer. The observed differences cannot be attributed to variations in the number of terminals, as an equal number of all terminals types were located at various distances around the blood vessels. However, there was a non-significant trend for VAChT-IR terminals to be less abundant than DβH- and SP-IR terminals. Similar results have been reported for the superior mesenteric artery where NPY-IR terminals (sympathetic) are more abundant than VIP-IR terminals (Edvinsson L. et al., 1989). This suggests that cholinergic terminals may not play an important role in microcirculation, release more transmitter

upon stimulation or perhaps that ACh is a faster acting transmitter than SP and noradrenaline.

Quantification performed on randomly viewed sections of vascular smooth muscle preparations showed mean autonomic neuroeffector cleft widths ranging from 100 nm for the rat mesenteric arterioles to 1900 nm for the rabbit pulmonary artery [for references see (Hirst G.D.S. et al., 1996)]. Our results thus lie within and exceed the upper limit of these previously reported ranges with mean distances of 1.088, 1.538, and 2.983 μm for DβH-, VAChT- and SP-IR terminals respectively. Our data reinforces the concept that considerable regional variations exist in the patterns of blood vessel innervation.

Sensory-sympathetic interactions

SP-IR primary afferent fibres have been shown to frequently appose non-SP-IR fibres, suggesting that afferent and efferent fibres may directly interact with one another (Luff S.E. et al., 2000). Studies report that noradrenaline may modulate the release of peptide transmitters (Holzer P., 1992) and conversely that peptide transmitters may modulate noradrenaline release (Kawasaki H. et al., 1988; Ahluwalia A. and Vallance P., 1996). Activation of capsaicin sensitive sensory fibres within small rat mesenteric arteries has been shown to decrease sympathetic fibre activity (Ahluwalia A. and Vallance P., 1996). Body cooling, on the other hand, causes a decrease in vasodilatation, probably via the direct action of sympathetic fibres on sensory fibres in the periphery (Hornyak M.E. et al., 1990). Despite this knowledge, sympathetic activity is thought to have little effect, if any, on sensory fibres in the intact organism (Jänig W. and Koltzenburg M., 1991), as

suggested by studies in which sympathetic stimulation or injections of noradrenaline do not evoke activation of sensory fibres, nor do they enhance the activation of cutaneous nociceptive endings that had been previously activated by natural stimuli (Burchiel K.J., 1984; Barasi S. and Lynn B., 1986; Sato J. and Perl E.R., 1991; Bossut D.F. and Perl E.R., 1995; Michaelis M. et al., 1996). Thus interactions between sensory and sympathetic fibres may develop only following peripheral injuries, as many studies revealed that sympathetic fibres play a role in certain forms of neuropathic pain (McLachlan E.M. et al., 1993; Chung K. et al., 1993; Chung K. et al., 1996; Kim H.J. et al., 1996; McDougall A.J. and McLeod J.G., 1996a; McDougall A.J. and McLeod J.G., 1996b). *In vitro* studies revealed that it is possible for true sensory-sympathetic contacts to form, an observation that the authors interpret to mean that interactions between these two fibre systems may develop (Belenky M. and Devor M., 1997). Thus, nerve injury-induced stimuli may favour sensory-sympathetic interactions via the establishment of close appositions or contacts. However, in our tissue no true contacts between sensory and sympathetic fibres have been observed. Whether these contacts develop following trauma still remains to be investigated.

Sensory-parasympathetic interactions

In this study we observed perivascular SP- and VAChT-IR fibres coursing parallel to one another in the rat lower lip. However, this is not the case in other systems, such as in the anterior cerebral artery, where these two fibre-types appear to have different distribution patterns (Yamamoto K. et al., 1983; Matsuyama T. et al., 1983a; Matsuyama T. et al., 1983b; Matsuyama T. et al., 1985). This finding stresses the unique

nature of various vascular beds and the importance of understanding them fully in order to achieve proper blood flow control following tissue injury. In the rat lower lip skin sensory and parasympathetic fibres appear to have additive or complementary actions a notion that is supported by the fact that endothelium-derived nitric oxide, in rat skin, is released in response to VIP and SP (Ralevic V. et al., 1995). To date, the nature of the interaction between sensory and parasympathetic fibres remains unresolved.

Sympathetic-parasympathetic interactions

The close association between sympathetic and parasympathetic fibres reported in the present study provides the anatomical support for the long sought interactions between these fibre types. Cholinergic dilator fibres have been seen in association with sympathetic fibres (Uvnäs B., 1966; Uvnäs B., 2000) and many experiments suggest that acetylcholine inhibits sympathetic adrenergic transmission (Malik K.U. and Ling G.M., 1969; Rand M.J. and Varma B., 1970; Löffelholz K. and Muscholl E., 1970; Rand M.J. and Varma B., 1971; Malik K.U. and McGiff J.C., 1971; Levy M.N., 1971; Hume W.R. et al., 1972; Vanhoutte P.M. and Shepherd J.T., 1973). Furthermore, acetylcholine has been shown to have a dual mode of action on the saphenous vein of dogs (Vanhoutte P.M. and Shepherd J.T., 1973). In these animals, acetylcholine decreased the response of sympathetic fibres to electrical stimulation but it augmented the response of these same fibres to exogenous noradrenaline. The former vasodilatation is most probably mediated by the presynaptic inhibition of noradrenaline release, while the latter constriction would result from the direct action of acetylcholine on smooth muscle muscarinic receptors. The

dose of acetylcholine responsible for the smooth muscle relaxation is smaller than that necessary for its constriction.

Sensory and autonomic fibres innervate the same blood vessels in monkeys

In this study we have shown that sensory-sympathetic and sensory-parasympathetic fibre combinations are associated with blood vessels in monkey lower lips. To our knowledge this is the first direct demonstration that blood vessels in the primate skin are dually innervated. Since the sensory-sympathetic and sensory-parasympathetic patterns of innervation in monkeys are similar to those obtained in rats we propose that the same is probably true for the sympathetic-parasympathetic pattern of innervation, although we were unable to confirm this due to technical difficulties. Our monkey data also suggests that a similar pattern of innervation might exist in humans.

Conclusion

Our observations lend support to the hypothesis that blood flow in the skin is probably tightly regulated by the co-ordinated control of sensory, sympathetic and parasympathetic fibres. We have shown that, in the rat lower lip, these fibres are closely associated with one another, although in the absence of direct synaptic contacts between the various fibre types. Autonomic fibres establish a close relationship with smooth muscle and endothelial cells while sensory terminals lie more distant. This arrangement suggests that sensory transmitters must diffuse further than autonomic transmitters in order to reach targets on the blood vessel wall. Luff et al. (2000) also observed that SP-IR terminals were located farther from smooth muscle cells than non-SP-IR terminals, and

this was taken as an indication that peptides diffuse further than noradrenaline in order to reach blood vessel smooth muscle cells. In addition, our finding of the proximity of autonomic terminals to the blood vessel wall suggests that these fibres may mediate their effects upon blood vessels more rapidly compared to sensory fibres.

The rat lower lip skin provides a good model for further studies on blood flow in the skin because the three fibre systems in this model can be independently lesioned and manipulated. The present observations provide direct information on the innervation patterns of sensory and autonomic fibres by way of multiple labelling procedures. Thus studies of blood flow in this tissue following pharmacological or surgical manipulations of these fibre-systems should provide information on the nature of the fibre interactions and the possible mechanisms, which may develop following nerve injuries.

FIGURE 3.1: ***Substance P- and DβH-IR fibres innervate the same blood vessels in rats.*** Panels **A, B & C** depict blood vessels in longitudinal sections. Note the presence of both SP- (brown) and DβH-IR fibres (blue) around the blood vessel walls. DβH-IR fibres wrap around the blood vessel in a net-like fashion, while SP-IR fibres course along the blood vessel wall. Both fibre types possess numerous varicosities (SP-IR varicosities: double-headed arrows; DβH-IR varicosities: arrows). Scale bar = 50 μm.

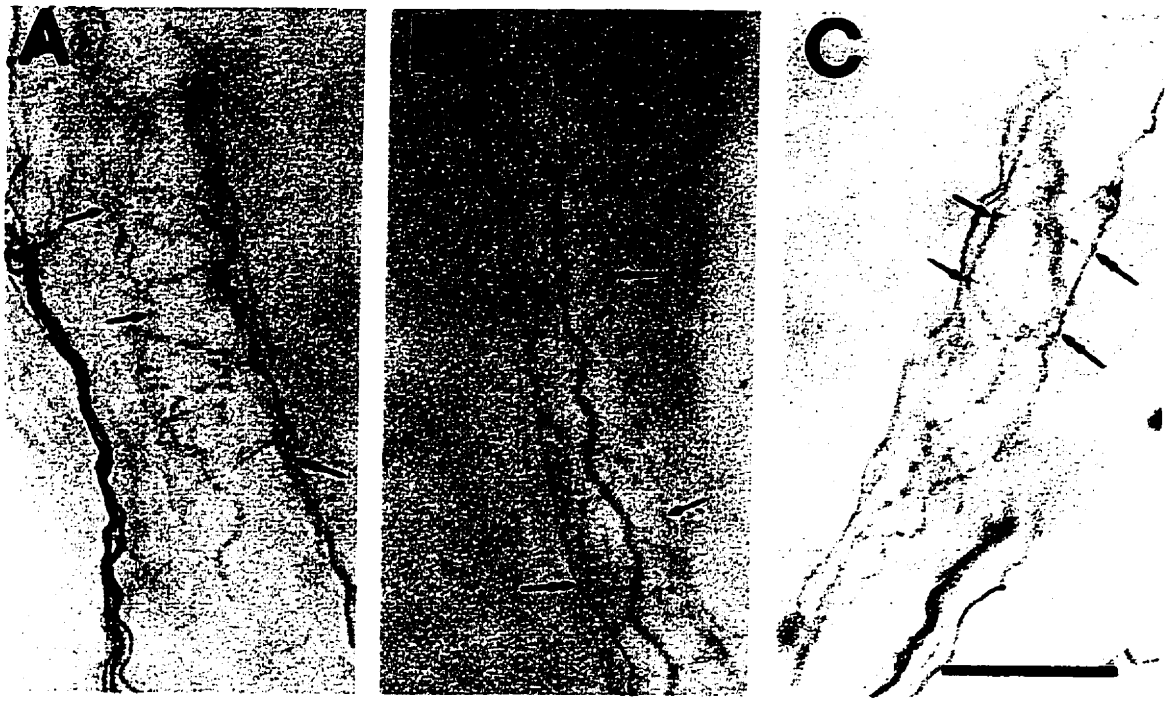
A
C

FIGURE 3.2: ***Substance P- and DβH-IR fibres innervate the same blood vessels in monkeys.*** All panels represent blood vessels in cross-section. SP- (brown) and DβH-IR fibres (blue) are seen around the adventitial layer of the blood vessel walls. These fibres are located around small arteries (**A&B**), small veins (**C**). A & B represent different focal planes of the same small artery. Small arteries were easily identified due to their internal elastic lamina (arrow). Arrowheads represent synaptic varicosities which are characteristic of both fibre types. e; endothelial layer. Scale bar = 50 μm.

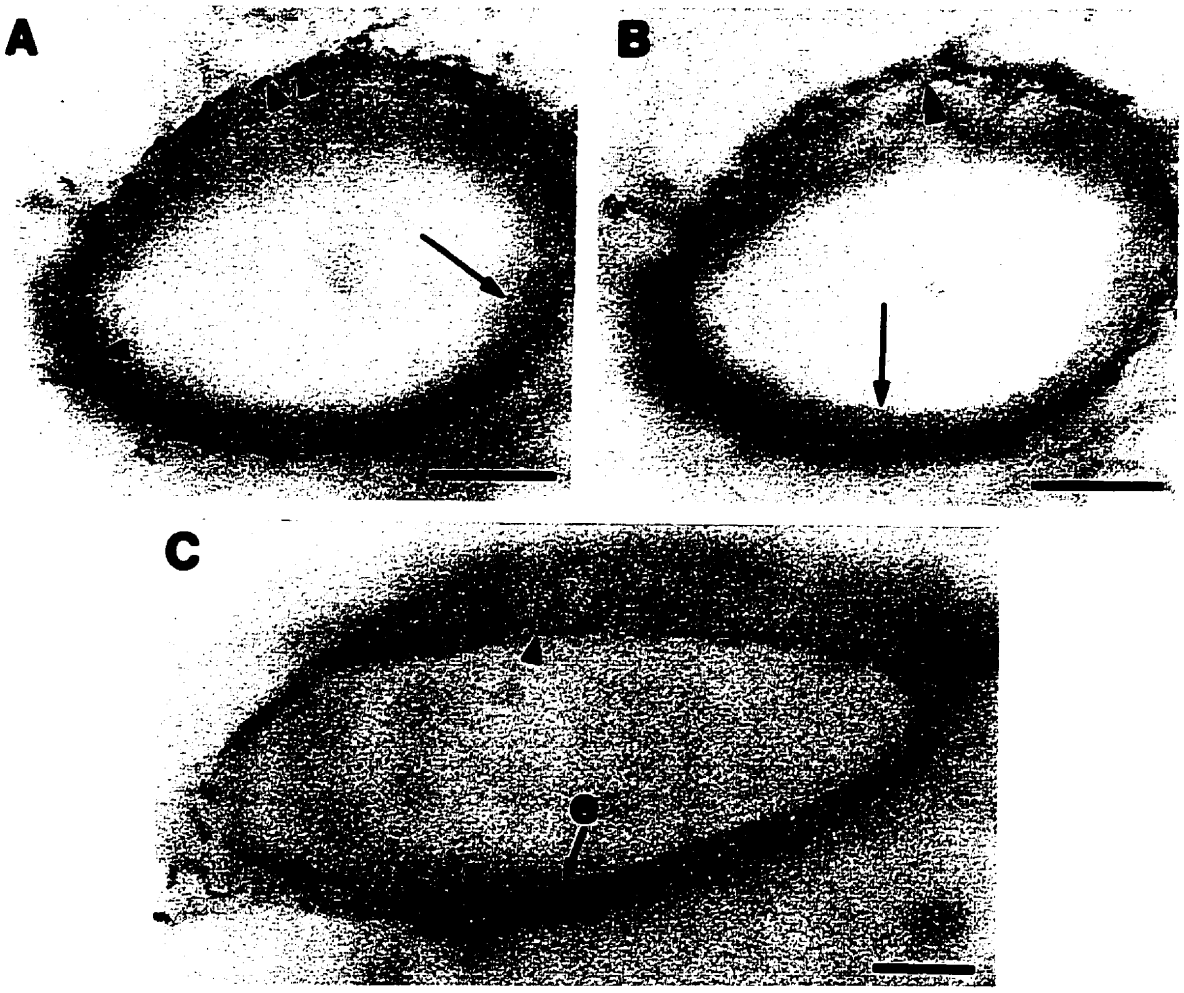
A
B
C

FIGURE 3.3: ***Substance P- and DβH-IR fibre labelling is more intense in monkeys.*** Panels **A-C** represent blood vessels cut longitudinally. Note that the labelling is far more intense than in the rat (compare with staining in Figure 3.1). Furthermore, in the monkey, SP-IR fibres (brown; double-headed arrows) form a mesh-like network around the blood vessel wall, as opposed to simply coursing along the wall. Arrows point to DβH-IR fibres. Scale bar = 50 μm.

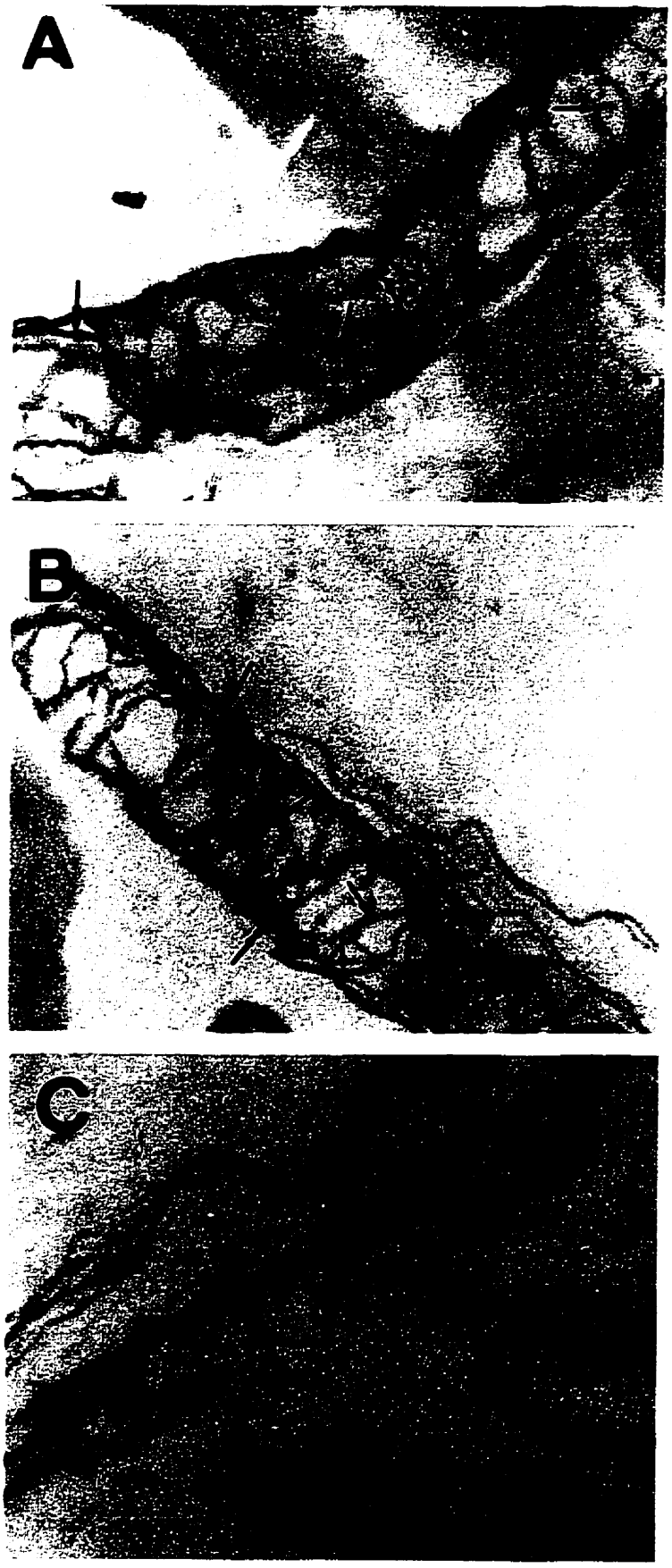
A
B
C

FIGURE 3.4: ***Substance P- and VAChT-IR fibres innervate the same blood vessels in rats.*** Panels **A&B** represent blood vessels cut longitudinally. Note that both SP- (brown) and VAChT-IR fibres (blue) course along the blood vessel walls without forming a mesh around them. In many instances both fibre types run parallel to one another as shown by the observation that both labels (brown and blue) are perfectly superimposed (curved arrows). Panels **C & D** depict cross-sectional views of blood vessels. SP- and VAChT-IR fibres run along the blood vessel adventitial layer. Small arrows represent synaptic varicosities (SP-IR varicosities: double-headed arrows; VAChT-IR varicosities: arrows). e; endothelial layer. Scale bar = 50 μm.

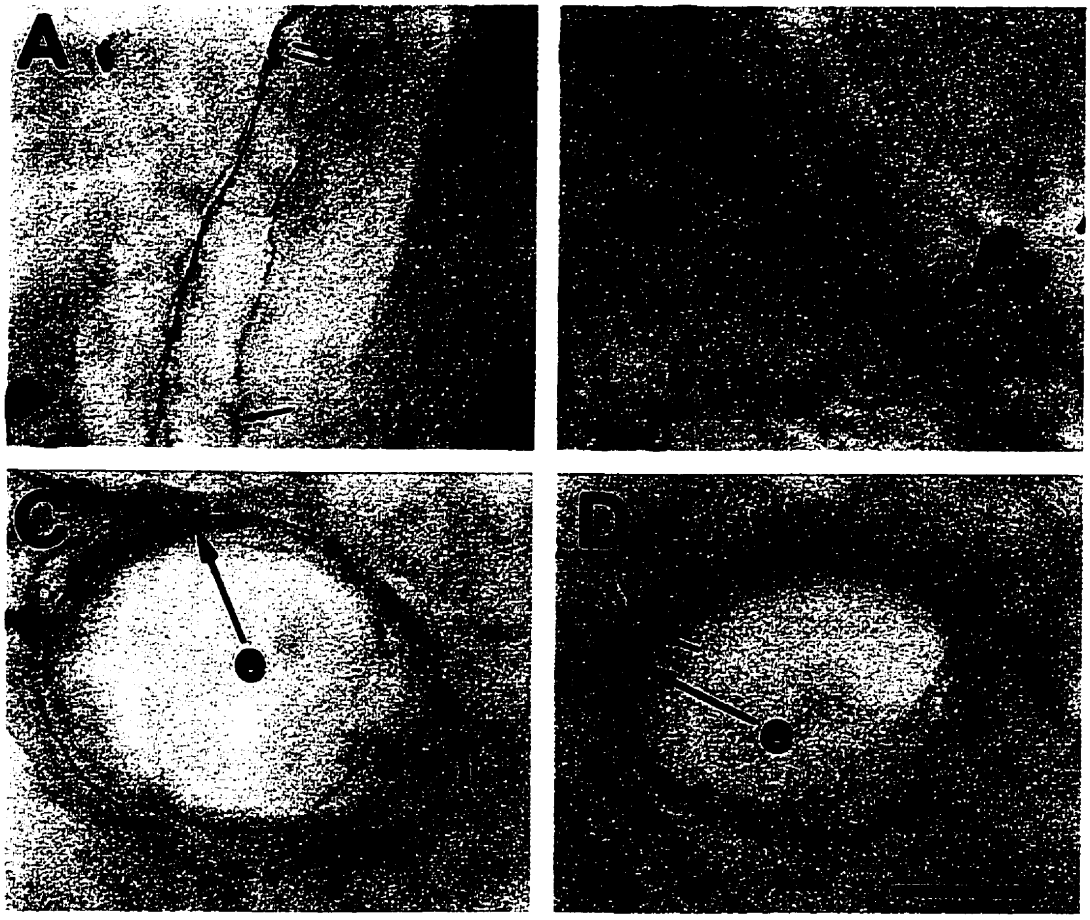
A
C
D

FIGURE 3.5: ***Substance P- and VAChT-IR fibres innervate the same blood vessels in monkeys.*** Panels **A&B** represent a small artery in longitudinal and cross-section respectively, while panels **C&D** represent a small vein in longitudinal and cross-section respectively. SP (brown) and VAChT-IR fibres (blue) are seen in association with both blood vessel types. In panel **D** SP- and VAChT-IR fibres are clearly seen coursing around the adventitial layer of the blood vessels. Both SP- and VAChT-IR fibres form extensive networks around the blood vessel walls. (SP-IR varicosities: arrowheads; VAChT-IR varicosities: arrows). Scale bar = 50 μm.

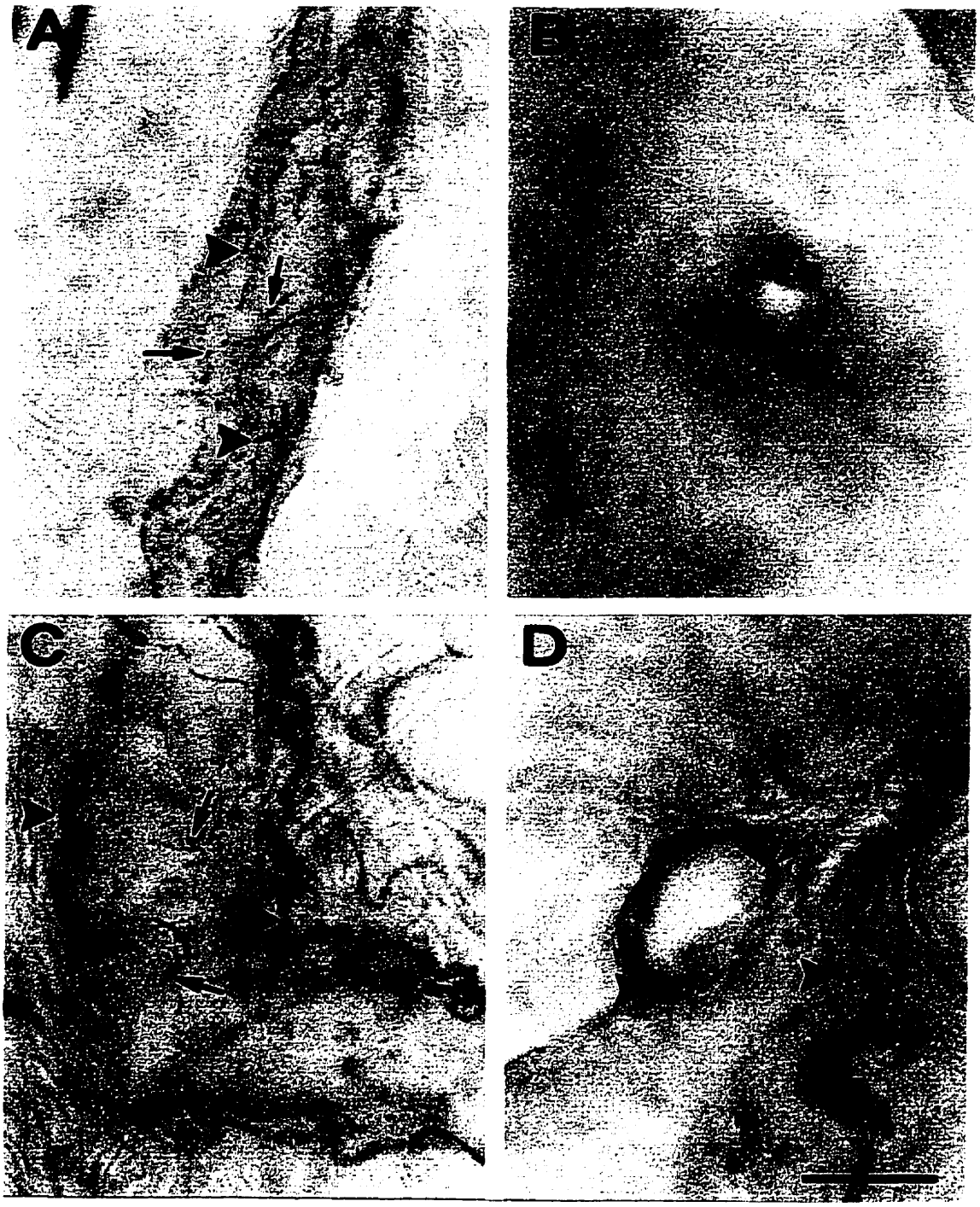
A
B
C
D

FIGURE 3.6: ***Dopamine-β-hydroxylase- and VAChT-IR fibres innervate the same blood vessels in rats.*** Panels **A-C** represent longitudinal sections of blood vessels innervated by both DβH- (brown) and VAChT-IR fibres (blue). Note that the DβH-IR fibres form a mesh around the blood vessel walls, while the VAChT-IR fibres simply run along the walls. DβH- and VAChT-IR fibres also run parallel to one another. Note the areas of perfect overlap between the two signals (curved arrow). Small arrows represent synaptic varicosities (DβH-IR varicosities: double-headed arrows; VAChT-IR varicosities: arrows). Scale bar = 50 μm.

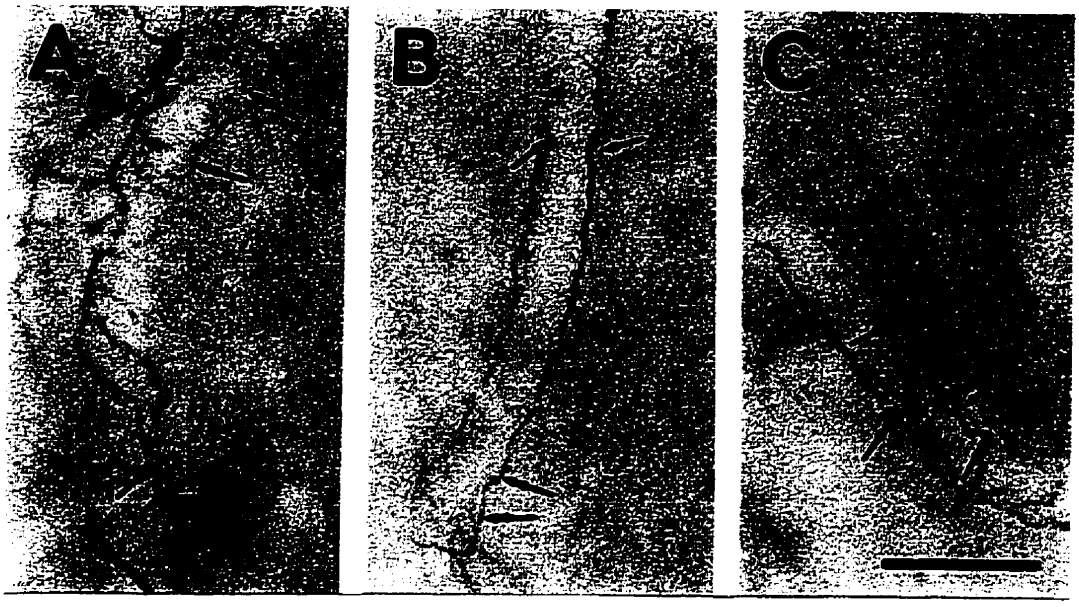
A
B
C

FIGURE 3.7: ***Electron micrographs of SP-IR terminals.*** SP-IR terminals abound around blood vessels in the rat lower lip. The synaptic varicosities are filled with dense-cored and agranular synaptic vesicles. Note the absence of Schwann cell (S) wrapping as some SP-IR terminals approach the blood vessel walls. Mitochondria (small arrows) are clearly seen within the synaptic varicosities. E; endothelial cell. L; blood vessel lumen. M; smooth muscle cell. Scale bar = 1μm.

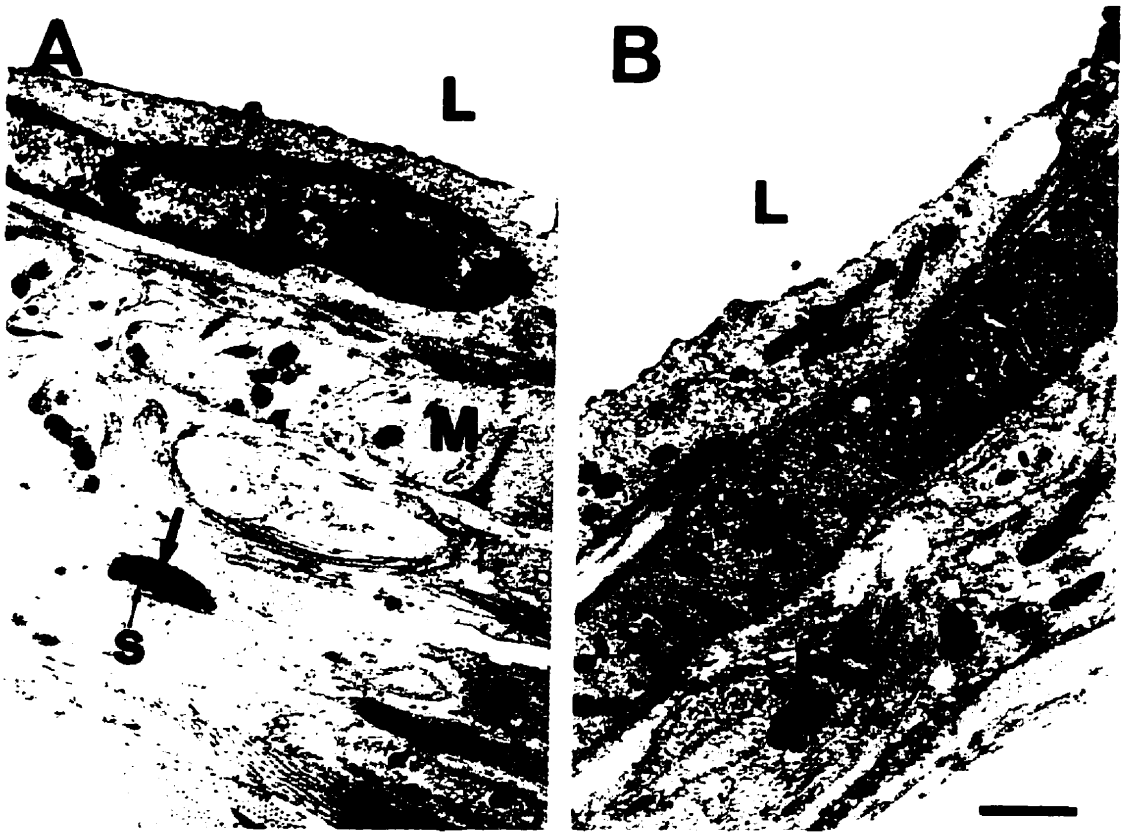
A
L
M
S
B
L

FIGURE 3.8: ***Electron micrographs of DβH-IR terminals.*** DβH-IR terminals in A-D are wrapped by Schwann cells (S). Note the proximity of these terminals to blood vessel smooth muscle cells (M). In **A & B** the portion of the DβH-IR terminals close to smooth muscle cells has lost its association with the Schwann cell. Note that the DβH-IR varicosities are filled with numerous densely packed granular vesicles. E; endothelial cell. L; blood vessel lumen. Scale bar in **D** applies to panels **B-D**. Scale bars = 1 μm.

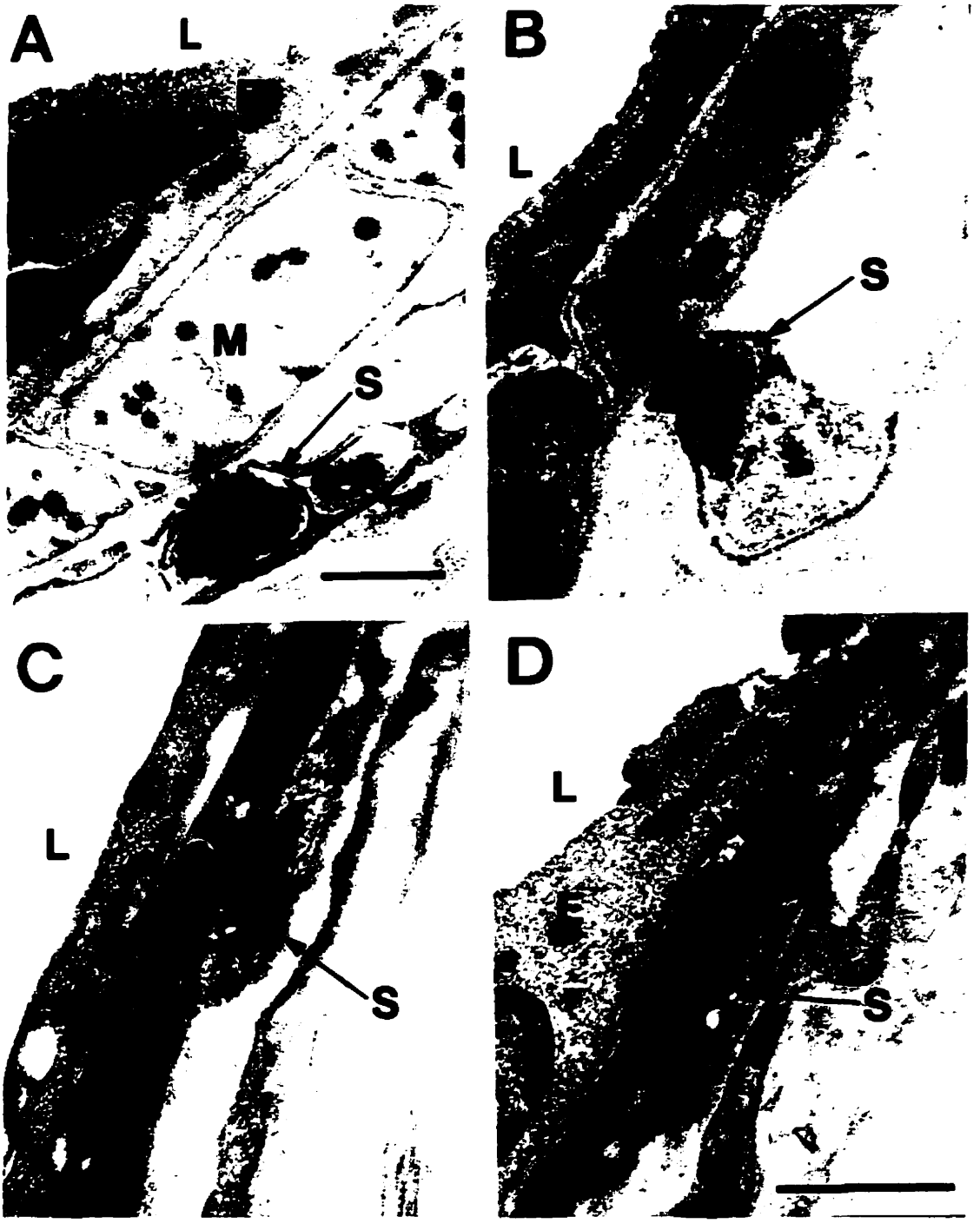
A
L
M
S
B
L
S
C
L
S
D
L
S

FIGURE 3.9: ***Electron micrographs of VAChT-IR terminals.*** VAChT-IR terminals are wrapped in Schwann cells (S) and located in the vicinity of blood vessel smooth muscle cells (M). Note that in **A** the VAChT-IR terminal is seen between a mast cell (m) and a blood vessel smooth muscle cell. Note the abundance of synaptic vesicles in the VAChT-IR varicosities. E; endothelial cell. L; blood vessel lumen. Scale bar = 1 μm.

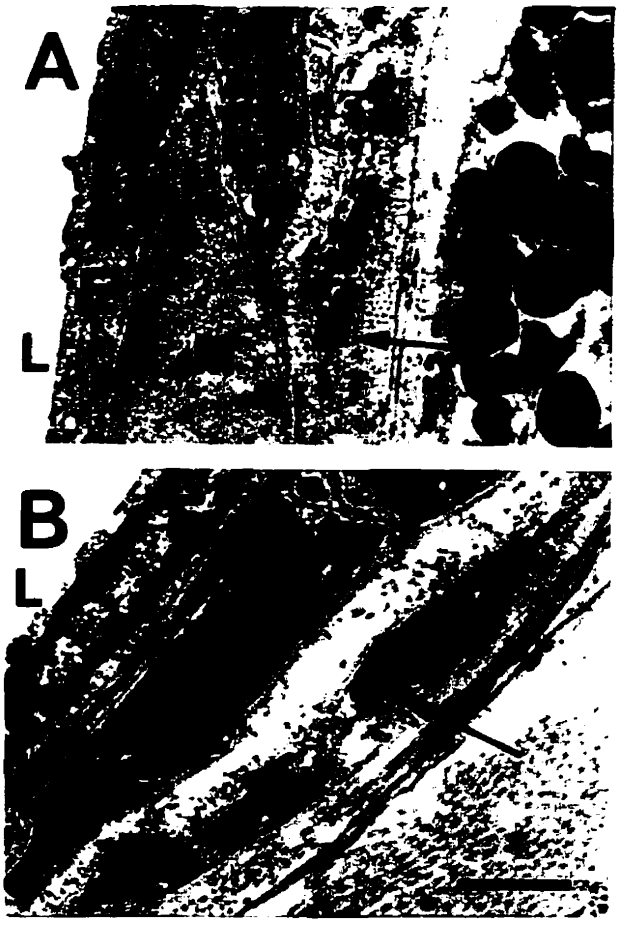
A
L
B
L

FIGURE 3.10: ***Quantification of the distance separating DβH-, SP, and VAChT-IR terminals from blood vessel endothelial cells and smooth muscle cells.*** Panel **A** shows the distance between the immunoreactive terminals and the outer surface of the blood vessel endothelial cells. Panel **B** shows the distance between the immunoreactive terminals and the outer surface of the blood vessel smooth muscle cells. *$p<0.05$, **$p<0.01$

A

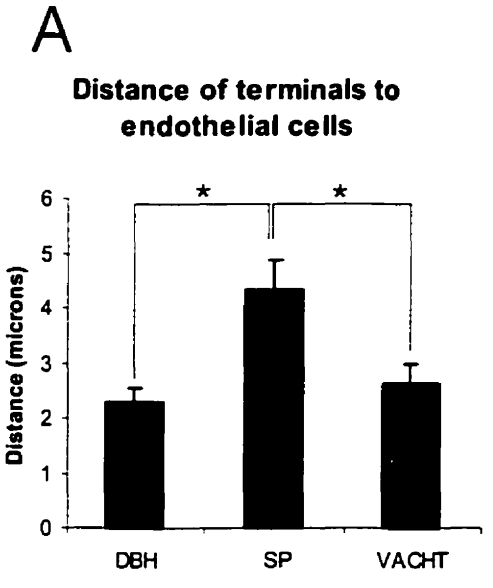
Distance of terminals to endothelial cells
Distance (microns)
0
1
2
3
4
5
6
*
*
DBH
SP
VACHT

B

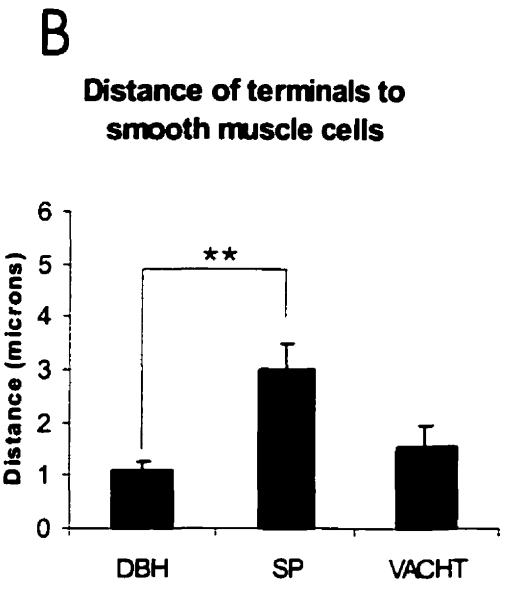
Distance of terminals to smooth muscle cells
Distance (microns)
0
1
2
3
4
5
6
**
DBH
SP
VACHT

Table 3.1. Quantification of the number of immunoreactive terminals associated with lower dermal blood vessels[1]

Terminal Type	Mean ± SEM
DBH	10.6 ± 1.7
SP	11.9 ± 2.0
VAChT	8.2 ± 1.4

[1]The mean number of DβH-, SP- and VAChT-IR terminals associated with blood vessels was obtained. Unpaired student *t-tests* were performed between DβH and SP, DβH and VAChT and VAChT and SP. The results show no significant difference in the number of terminals associated with lower dermal blood vessels amongst these three fibre-types. SEM; standard error of the mean.

CONNECTING TEXT – CHAPTER 3 TO 4

The previous chapters have focused on the sensory, sympathetic and parasympathetic patterns of innervation in the rat lower lip skin. In the next two chapters we focused on the changes in the sensory and sympathetic systems following nerve lesions. Investigations by other research groups have shown that lesions to peripheral nerves cause the sprouting of sympathetic fibres around dorsal root ganglion cells. This might suggest that these two fibre-types would interact with one another. Unfortunately, the physiological evidence does not favour an interaction at the sensory ganglia level, and the possibility remains that such interactions occur more peripherally.

Therefore, in Chapter 4, we investigated this possibility by studying the effects, over time, of bilaterally removing the mental nerves. We studied the changes in the innervation patterns of SP- and DβH-IR fibres in both the upper and lower dermis. One to eight weeks post-lesion, the rat lower lips were processed for immunocytochemistry at the light microscopic level.

CHAPTER 4

Peripheral Nerve Injury Leads to the Establishment of a Novel Pattern of Sympathetic Fibre Innervation in the Rat Skin

Isabella Ruocco, A. Claudio Cuello
and Alfredo Ribeiro-da-Silva

The Journal of Comparative Neurology
422:287-296 (2000)

ABSTRACT

Peripheral nerve injury has been shown to result in sympathetic fibre sprouting around dorsal root ganglia (DRG) neurons. It has been suggested that this anomalous sympathetic fibre innervation of the DRG plays a role in neuropathic pain. Other studies have suggested an interaction between sympathetic and sensory fibres more peripherally. To date, no anatomical study of these possible interactions in the terminal fields of sensory and sympathetic fibres has been performed, therefore we set out to study them in the rat lower lip following bilateral lesions of a sensory nerve, the mental nerve (MN). Immunocytochemistry for both substance P (SP) and dopamine-β-hydrohylase (DβH) was performed. Within the first week post-MN lesions, the SP-immunoreactive (IR) fibres had almost completely degenerated while DβH-IR fibres were found in the upper dermis, an area from which they are normally absent. These DβH-IR fibres were present in the upper dermis at all post-surgery times studied (1, 2, 3, 4, 6 and 8 weeks). Interestingly, although by the sixth week post-MN lesions SP-IR fibre reinnervation of the lower lip was occurring, the DβH-IR fibres were still present in the upper dermis. Quantification revealed that the migration and branching of the DβH-IR fibres into the upper dermis occurred gradually, and was most significant four weeks post-MN lesions as shown by the fact that the DβH-IR fibres were found 169.6±91.4 μm away from the surface of the skin as opposed to 407.1±78.4 μm away in sham operated animals. These findings suggest that the ectopic innervation of the upper dermis by sympathetic fibres may be important in the genesis of neuropathic pain through the interactions of sympathetic and SP-containing sensory fibres.

INTRODUCTION

Neuropathic pain frequently appears following peripheral nerve lesions. As the underlying mechanisms still remain unclear, it is very difficult to treat. Some patients can be relieved by the use of sympathetic blocking agents or following surgical sympathectomies [for review see (O'Halloran K.D. and Perl E.R., 1997)]. These patients are described as having sympathetically maintained pain (SMP). Although some neuropathic pain patients experience sympathetically independent pain (SIP) following peripheral nerve lesions, the number of patients suffering from SMP is considerable and is a major challenge in health research today.

Various animal nerve lesion models have been used in previous studies on the mechanisms of neuropathic origin. The three major models are: 1) the chronic constriction injury model (CCI) (Bennett G.J. and Xie Y.-K., 1988); 2) the partial sciatic nerve ligation injury model (PSL) (Seltzer Z. et al., 1990); and 3) the segmental spinal nerve ligation injury model (SNL) (Kim S.H. and Chung J.M., 1992). Although these animal models differ in the extent of pain behaviours that they produce, they all result in sympathetic sprouting in the dorsal root ganglia (DRG) at some point following the nerve injury (Lee B.H. et al., 1998). These observations led to the concept of a possible interaction between sensory and sympathetic neurons at the level of the DRG. Following nerve injuries, sympathetic fibres have been reported to sprout and form baskets or onions around DRG neurons (McLachlan E.M. et al., 1993; Chung K. et al., 1993; Chung K. et al., 1996; Ramer M.S. and Bisby M.A., 1997; Ramer M.S. and Bisby M.A., 1998; Lee B.H. et al., 1998). The sprouted sympathetic fibres displayed numerous varicose terminals around DRG neurons following SNL (Chung K. et al., 1997). Recently, it has

been shown that the source of the sprouting sympathetic fibres vary with the animal model used (Ramer M.S. and Bisby M.A., 1998). When comparing the CCI and SNL models, Ramer and Bisby (Ramer M.S. and Bisby M.A., 1998) observed that, in the CCI model, the sprouting fibres originated from perivascular axons, whereas in the SNL model they originated from a misdirection of regenerating sympathetic fibres. Sympathetic sprouting appears to be dependent upon the diameter of the injured fibres (Abbadie C. and Basbaum A.I., 1998), in that injury to larger diameter fibres leads to more abundant sympathetic sprouting onto DRG cell bodies. Curiously, sympathetic sprouting occurs more rapidly following CCI than following complete nerve transection, an observation that suggests that the degenerating neurons may interact with the spared sensory neurons to promote the DRG sprouting (Ramer M.S. and Bisby M.A., 1997).

It is still unclear what triggers sympathetic sprouting. There is, however, sufficient evidence to propose a role for nerve growth factor (NGF). In fact, sympathetic sprouting and basket formation in the DRG has been observed in mice that over-express NGF in the skin (Davis B.M. et al., 1994). Following sciatic nerve transections, NGF mRNA levels increased in the DRG (Serbert M.E. and Shooter E.M., 1993; Wells M.R. et al., 1994; Herzberg U. et al., 1997), suggesting that sprouting may occur due to a local source of NGF. Furthermore, mice over-expressing NGF in glial cells show more sympathetic sprouting in the DRG following CCI of the sciatic nerve than non-transgenic animals. These transgenic animals also experience increased neuropathic pain behaviours, such as thermal and mechanical allodynia (Ramer M.S. et al., 1998).

Surprisingly, few studies have looked distal to the DRG to investigate the possibility of more peripheral changes that may be crucial to understanding the etiology

of pain which follows peripheral nerve lesions. It has been shown that, following nerve damage, sympathetic stimulation or noradrenaline administration leads to the activation of C-fibre nociceptors in their receptive terminal region, an effect which was shown to be mediated by α_2-adrenergic receptors (Sato J. and Perl E.R., 1991; O'Halloran K.D. and Perl E.R., 1997). This indicates that nerve injury changed the responses of sensory neurons to the above-mentioned stimuli. Previous studies have tried to locate these α_2-adrenergic receptors. Following PSL, it was found that destroying the post-ganglionic sympathetic neuron (PGSN) terminals by means of 6-hydroxydopamine injections eliminated the noradrenaline-induced hyperalgesia, suggesting that the α_2-adrenergic receptors are located on the terminals of PGSNs and not on the nociceptors themselves (Tracey D.J. et al., 1995). Other studies have shown that the nociceptors are indirectly sensitized by noradrenaline-induced prostaglandin release from sympathetic terminals following their activation via the α_2-adrenergic receptors (Levine J.D. et al., 1986; Gonzales R. et al., 1989; Schaible H.-G. and Schmidt R.F., 1988; Cohen R.H. and Perl E.R., 1990; Gonzales R. et al., 1991; Birrell G.J. et al., 1991; Sherbourne C.D. et al., 1992). Despite this evidence, the anatomical localization of the α_2-adrenergic receptors has yet to be established. Therefore, it is still unclear whether the α_2-adrenergic receptors are located on the sensory or sympathetic terminal fields.

As there has been no anatomical study of the plastic changes that may occur in receptive fields following nerve lesion, we decided to address the issue by using the skin of the rat lower lip as our peripheral nervous system model. As the sensory innervation to this region originates from the mental nerve – a branch of the trigeminal nerve – and the sympathetic innervation originates from the superior cervical ganglion, we can thus

independently lesion one system or the other and observe the changes that occur in the terminal fields. The present study focuses on the changes that occurred in the innervation pattern of the rat lower lip skin following sensory denervation. Of the primary sensory fibres, we focussed on the substance P-immunoreactive (SP-IR) subset as they are of small diameter and are thought to play an important role in the transmission of pain-related information to the CNS and in neurogenic inflammation [for review see, e.g., (Cuello A.C., 1987; Otsuka M. and Yoshioka K., 1993)].

MATERIALS AND METHODS

Male Wistar rats weighing 250-300 g were used in all studies. The animal care guidelines described in "The Care and Use of Experimental Animals" of the Canadian Council on Animal Care, vols. I and II, were strictly followed. In addition, all experimental procedures were reviewed and approved by the McGill University Animal Care Committee before experiments started.

Surgical procedures. Prior to surgery, the animals were anaesthetised with acepromazine (0.2 ml/kg) subcutaneously, followed by an intramuscular injection of xylaxine (0.25 ml/kg) and ketamine (0.5 ml/kg). The anaesthetics were sequentially administered, with a ten-minute waiting period between each. Thirty-six rats underwent bilateral mental nerve (MN) transections, while another thirty-six rats were sham operated. The MN transections were performed with the aid of a surgical microscope (Leitz). The MN was freed from the surrounding connective tissue and a 1.0-2.0 mm segment of the nerve was removed at its exit point from the mental foramen. In sham operated animals, surgeries were performed as described above, except that the MN nerve

was not cut. The rats were then left to recover for one to eight weeks before being used for immunocytochemistry (ICC).

Five additional rats underwent MN transections as described above and were allowed to recover for four weeks. Then the animals had their superior cervical ganglia removed bilaterally under anaesthesia and were left to recover for a further four weeks before being used for immunocytochemical purposes.

Animal perfusions and tissue sectioning. At the appropriate time post-surgery (1, 2, 3, 4, 6 or 8 weeks), the rats were anaesthetised with 0.4 ml/kg of Equithesin and transcardially perfused with 4% paraformaldehyde, 15% picric acid (v/v) and 0.1% glutaraldehyde in 0.1M phosphate buffer (PB), pH 7.4, for 30 minutes, and subsequently with 4% paraformaldehyde and 15% picric acid (v/v) in 0.1M PB for an additional 30 minutes. Rat lower lips were collected and post-fixed at 4°C in the latter fixative for one hour. The tissue was then cryoprotected in 30% sucrose for a minimum of twelve hours. Subsequently, the tissue was trimmed, snap frozen in liquid nitrogen, thawed in 0.1M PB, placed on tissue holders and surrounded by Tissue-Tek (OCT). Fifty μm-thick cryostat sections were then obtained at -20°C.

Light microscopy. Sections were pre-treated with 50% ethanol (Llewellyn-Smith I.J. and Minson J.B., 1992), 0.3% H_2O_2 and 1% sodium borohydride in phosphate-buffered saline (PBS), pH 7.4, for 30 minutes each, followed by extensive washing in PBS containing 0.2% Triton X-100 (PBS+T), prior to incubation in the primary antibodies overnight at 4°C. PBS+T was used for all washes and for antibody dilutions. A rat bi-specific anti-substance P (SP) anti-horseradish peroxidase (HRP) monoclonal antibody (1:10; Medicorp, Canada) (Suresh M.R. et al., 1986) and a mouse monoclonal

anti-dopamine-β-hydroxylase (DβH) antibody (1:10; PharMingen, Canada) (Mazzoni I.E. et al., 1991) were used. Subsequently, sections were washed in PBS+T and treated with HRP (5 μg/ml) for one hour. After further washing, SP immunoreactive sites were revealed by incubating the sections in 3,3'-diaminobenzidine tetrahydrochloride (DAB) and H_2O_2. The sections were then washed in PBS+T, incubated for one hour in goat anti-mouse IgG (GAM) (American Qualex) (previously preabsorbed in fixed rat lip tissue for eight hours at 4^0C), washed again and treated for one hour in a mouse monoclonal PAP (Seralab, UK) (Semenenko F.M. et al., 1985). Finally, the sections were washed and the DβH labelling was revealed using SG chromogen (Vector Labs), following the instructions of the manufacturer. Lastly, the sections were dehydrated in ascending ethanol concentrations, cleared with xylene and mounted with Permount.

Quantification. The slides used for quantification were coded to ensure that the observer was blinded to all groups. The codes were broken only prior to statistical analyses. The number of DβH immunoreactive fibres located above the sebaceous gland level at all post-surgical time points were counted in order to establish a time course for fibre migration (see results). DβH fibres were counted in the sections processed for both SP and DβH using a Leitz Dialux 20 microscope. A graticule was placed in the microscope's eyepiece and three regions of 14.44 μm^2 each were counted per section. The regions were selected at random above the sebaceous glands. Data was collected from a total of 120 sections (four animals per time point and five sections per animal). The number of DβH fibres that crossed the inferior and right side borders of the quantification area were counted to establish the time course. In addition, the total number of DβH fibres within the area were counted to determine the extent of fibre

branching by direct observation. Statistical significance was assessed by one-way ANOVA followed by Dunnett's one-sided test.

The extent of fibre migration at the four-week time point was also quantified, using an M4 image analysis system (Imaging Research Inc., St. Catharines, ON, Canada). The distance between the closest point to the epidermis of the DβH fibres and the surface of the skin was measured in sham and MN transected rats. An unpaired Student's *t-test* was performed on the average of the distances obtained for the sham and operated animal groups in order to assess the statistical significance.

RESULTS

Patterns of innervation by SP and DβH in control animals

In naïve animals, SP-IR fibres were found throughout the lower lip, although fibre density was highest in the upper dermis (Fig. 4.1). The SP-IR fibres closest to the surface of the skin were studded with numerous varicosities (Fig. 4.1- curved arrows). These fibres represented terminal branches of larger fibres that were observed within nerves located in the dermis and hypodermis. Some SP-IR fibres were seen to penetrate the epidermis while other fibres were associated with blood vessels in the upper dermis. Furthermore some of the SP-IR fibres were located in the proximity of mast cells or in the vicinity of hair follicles.

DβH-IR fibres were located in the lower dermal region and hypodermis, but not in the upper dermis, and were associated with blood vessels (Fig. 4.2). The DβH-IR fibres were not seen to run in small bundles depicting autonomic nerves. Rather, we observed nerve branches in a net-like arrangement around blood vessels. These fibres

possessed numerous varicosities (Fig. 4.2- curved arrows) in their terminal branching network, which were rounder and packed closer together than those in SP-IR fibres.

Changes in SP- and DβH-immunoreactivity following bilateral MN transections

There were no differences in the fibre distribution pattern and density between sham operated and naive rats. Therefore, changes observed following MN transections were a consequence of cutting the MN and not of the surgical procedure itself.

One week post-surgery, the number of SP-IR fibres in the skin of the lower lip was greatly reduced, and only a few isolated fibres could be detected (Fig. 4.3A). Surprisingly, DβH-IR fibres were detected, although in limited number, in the upper dermis (Fig. 4.3B), a territory from which they were absent in sham-operated and naïve animals. By the second week post-surgery, SP-IR fibres were detected only occasionally (Fig. 4.3C). Furthermore these residual SP-IR fibres were very fine and weakly immunoreactive. At this point, DβH-IR fibres were detected closer to the surface of the epidermis than they were one week after the nerve was cut. These fibres were thus continuing their progression towards the surface of the skin. Furthermore, these DβH-IR fibres were thicker and more abundant (Figs. 4.3C & 4.3D) than at the previous time point. Three weeks post-surgery, the findings were very similar to those of the two week time point, however the DβH-IR fibres were observed even closer to the surface of the skin (Fig. 4.3F), while the SP-IR fibres had completely disappeared except for occasional very faint residual fibres. By four weeks post-surgery, some SP-IR fibres had reappeared in the upper dermis (Fig. 4.4B) and were seen to innervate the same structures as in naïve animals. As for the DβH-IR fibres, they were still present in the upper dermis and

remained closer to the surface of the skin (Fig. 4.4A) than in sham operated rats. At later time points (six weeks and eight weeks post-surgery), SP-IR fibres were more abundant in the upper dermis (Figs. 4.4C-D), although they were still not as abundant as in control animals. Interestingly, these fibres co-existed with the persisting DβH-IR fibres. It is also noteworthy that both SP- and DβH-IR fibres were oriented parallel to one another (Fig. 4.4B).

Quantification of DβH-IR fibre migration into the upper dermis of the rat lower lip

To further characterize the time-course of the DβH-IR fibre migration into the upper dermis after MN transections, we counted the number of DβH-IR fibres present in the upper dermis at all time points (see Materials and Methods for details). As shown in Table 4.1, there was a gradual, though significant, infiltration of the upper dermis by DβH-IR fibres, which reached its maximum by the fourth week post-MN lesions. Furthermore, it was at this latter time point that we observed the greatest level of fibre ramification. Although by the sixth and eighth week post-lesion the number of DβH-IR fibres in the upper dermis had decreased, the levels were still considerably higher than at the one-week time point.

The minimal distance between the DβH-IR fibres and the surface of the skin at the four-week time point was also measured (Fig. 4.5). We found that in MN transected animals the DβH-IR fibres were located within 169.6±91.4 μm from the surface of the skin whereas they were never closer than 407.1±78.4 μm from the surface of the skin in sham-operated rats. This difference was highly significant ($p<0.001$).

Finally, we performed bilateral MN transections on five rats and allowed the DβH-IR fibres to migrate. Four weeks post-surgery, the superior cervical ganglia (SCG) were bilaterally removed and the animals were then allowed to recover for 1 month. The above surgeries resulted in a total loss of DβH-IR fibres (Fig. 4.6) in the rat lower lip, thus confirming that the DβH-IR fibres which appeared *de novo* in the upper dermis arose from the sprouting and migration of sympathetic fibres in the lower dermis. As expected, one month post-MN surgery these animals displayed SP-IR fibres in the upper dermis as a result of the reinnervation of this previously denervated territory.

DISCUSSION

Sympathetic fibre migration

The present study examines the effect of sensory denervation on the rat lower lip skin in order to determine its effects upon the terminal fields of sympathetic and SP-IR sensory fibres. We found that there was a progressive degeneration of SP-IR fibres, which was noticeable by the first week post-MN lesion. By the end of the second week, there was an almost complete absence of sensory fibres in the skin. However, by the sixth week post-MN lesion, we observed a reinnervation by sensory fibres. It is interesting to note that some animals had residual sensory fibres remaining until the fourth week post-MN lesion. It is possible that, as there were individual variations amongst animals, these animals had an initially denser innervation pattern. Strikingly, we observed the appearance of sympathetic (DβH-IR) fibres in the upper dermis as early as one week post-lesion. These fibres do not normally innervate the upper dermis in naive rats.

Evidence from experiments using capsaicin, have shown that it is the loss of C-fibres and not damage to these fibres which promotes sympathetic sprouting in the DRG. This was shown by experiments in which sciatic nerve-transected animals displayed more sympathetic sprouts in the DRG than did the animals which did not receive the capsaicin pretreatment (Abbadie C. and Basbaum A.I., 1998). Furthermore, experiments using neonatal capsaicin treatments revealed that sympathetic sprouting and an increased number of noradrenergic contacts occur in the peripheral targets of the denervated tissue (Hill C.E. and Vidovic M., 1989; Luthman J. et al., 1989). One possible explanation for this invasion of sympathetic fibres into a territory from which they are normally absent is that these fibres are responding to a signal from the upper dermis. NGF may provide such a signal. In fact, as the sensory fibres degenerate, the NGF produced by peripheral targets such as keratinocytes (Tron V.A. et al., 1990; English K. et al., 1994), fibroblasts (Acheson A. et al., 1991) and Merkel cells (Vos P. et al., 1991) may become available and act as a chemotactic factor. Thus, sympathetic fibres respond by migrating towards the newly available source of NGF. In fact, it has been previously shown that NGF sensitive fibres will follow a concentration gradient of the neurotrophin (Campenot R.B., 1987). Furthermore, following a regional denervation, NGF-sensitive neurons can be induced to sprout from adjacent regions into the denervated area (Rich K.M. et al., 1984), a process which can be prevented by the administration of NGF antiserum (Diamond J. et al., 1992a; Diamond J. et al., 1992b).

As time progressed, the sympathetic fibres migrated closer to the surface of the epidermis. Even though sensory reinnervation of this territory occurred, they were still present at the last time point observed (8 weeks), suggesting that they may continue to

draw on the available NGF in the region. The new sensory fibres may originate from the cervical branch of the facial nerve, the lingual branch of the trigeminal nerve as well as from the cervical plexus. Although they are attempting to reestablish a seemingly normal pattern of innervation in the upper dermis, their fibre density does not return to that observed in control animals. Therefore, we postulate that the persisting sympathetic fibres may utilise part of the region's NGF supply, thus reducing the NGF available to restore the sensory innervation in the upper dermis to control levels.

Migrating sympathetic fibres originate from the lower dermis

To confirm the origin of the migrating sympathetic fibres, we allowed it to occur up until four weeks post-surgery – a point at which the migration was known to be significant – at which point we performed a SCG ganglionectomy on the animals. Four weeks later, we found that the newly arriving sensory fibres were still present but that the sympathetic fibres were not. This confirmed that the sympathetic fibres migrated from the lower dermis into the upper dermis, as the upper dermal fibres were no longer present following the sympathetic denervation of the lower dermis. Furthermore we were able to rule out the possibility that the reappearance of sensory fibres in the upper dermis was due to a phenotypic switch in the sympathetic fibres, since the former were still present despite the complete loss of sympathetic fibres.

It still is unclear how sympathetic fibres make their way through the connective tissue and into the upper dermis. After careful observation of the material, we found that the sensory and sympathetic fibres run parallel to one another. This suggests that the sympathetic fibres might use the tracts of the degenerating sensory fibres in order to gain

access into the upper dermis. Support for this comes from studies which have shown that, following nerve injuries, Schwann cells located around the degenerating neuron upregulate their synthesis of NGF and the p75 low-affinity NGF receptor, thus causing an increase in the local concentration of NGF (Taniuchi M. et al., 1986). Therefore, by responding to the available NGF, the sympathetic fibres would migrate along the sensory fibre tracts.

Peripheral mechanisms involved in sensory-sympathetic interactions

The relevance of looking at the terminal fields of sensory and sympathetic fibres following nerve lesions is supported by experiments in which lidocaine is applied at the site of injury (Gracely R.H. et al., 1992). In these experiments it was observed that, immediately following the lidocaine application, the neuropathic pain symptoms of patients diagnosed with reflex sympathetic dystrophy were relieved, suggesting that inputs coming from the periphery are important for the maintenance of the pain. Furthermore, blocking signals from entering into the spinal cord also alleviates neuropathic pain, pointing to the importance of signals originating from the site of injury and/or the DRG for maintenance of the pain (Sheen K. and Chung J.M., 1993; Yoon Y.W. et al., 1996). Therefore, although much evidence suggests that the interaction between sensory and sympathetic fibres occurs at the level of the DRG, some important signals may also arise from the terminal fields themselves. In fact, our results have shown that at later stages following MN lesions (8 weeks post-lesion), the sensory and sympathetic fibres run parallel to one another in the upper dermis, making it possible for interactions to occur at this level. It has been hypothesized that, following peripheral

nerve injuries, C-fibre axons begin to express adrenoceptors which may lead to catecholamine supersensitivity by binding the excess transmitter found in the systemic circulation or released from nerve terminals (McLachlan E.M. et al., 1993; Devor M. et al., 1994). α_2-adrenergic receptors have been postulated as the receptor subtype involved (Sato J. and Perl E.R., 1991; O'Halloran K.D. and Perl E.R., 1997). By expressing adrenoceptors, the C-fibres in our model would be directly stimulated by the release of noradrenaline from the sympathetic fibres running along with them. However prostaglandins, which have been shown to sensitize nociceptors (Martin H.A. et al., 1987; Schaible H.-G. and Schmidt R.F., 1988; Cohen R.H. and Perl E.R., 1990; Birrell G.J. et al., 1991), are produced and released upon noradrenaline binding to the α_2-adrenergic receptors on sympathetic fibres (Gonzales R. et al., 1991; Sherbourne C.D. et al., 1992) (Levine J.D. et al., 1986; Gonzales R. et al., 1989; Tracey D.J. et al., 1995) and thus in this way, the C-fibres in our model could be indirectly stimulated by the release of noradrenaline. Regardless of where the α_2-adrenergic receptors are located, our results support the idea of an aberrant interaction between sensory and sympathetic fibres, which may be one of the peripheral mechanisms underlying states such as sympathetically-maintained pain.

Conclusion

We have been able to show persistent plastic changes in sympathetic and SP-containing sensory fibre innervation of a region following denervation. These changes were observed in the terminal fields as opposed to those that have been described by other investigators at the level of the DRG. Therefore, it is probably important to consider

changes that occur peripherally to the DRG when trying to understand the mechanisms that underlie neuropathic pain syndromes. We suggest that sympathetic sprouting both at the level of the DRG and in the periphery are involved in sympathetically-related peripheral neuropathies.

FIGURE 4.1: ***Normal pattern of SP immunoreactivity in sham-operated animals.*** **A** -A dense network of SP-IR fibres can be seen in the upper dermis. There are also small fibre bundles present in the upper dermis. The curved open arrow indicates one such fibre bundle at one of its branching points. A fibre penetrating into the epidermis can also be seen (open arrow). **B** -These SP-IR fibres represent terminal branches as evidenced by the presence of numerous varicosities (curved arrows). The arrowheads indicate the surface of the skin. Scale bar = 20 μm.

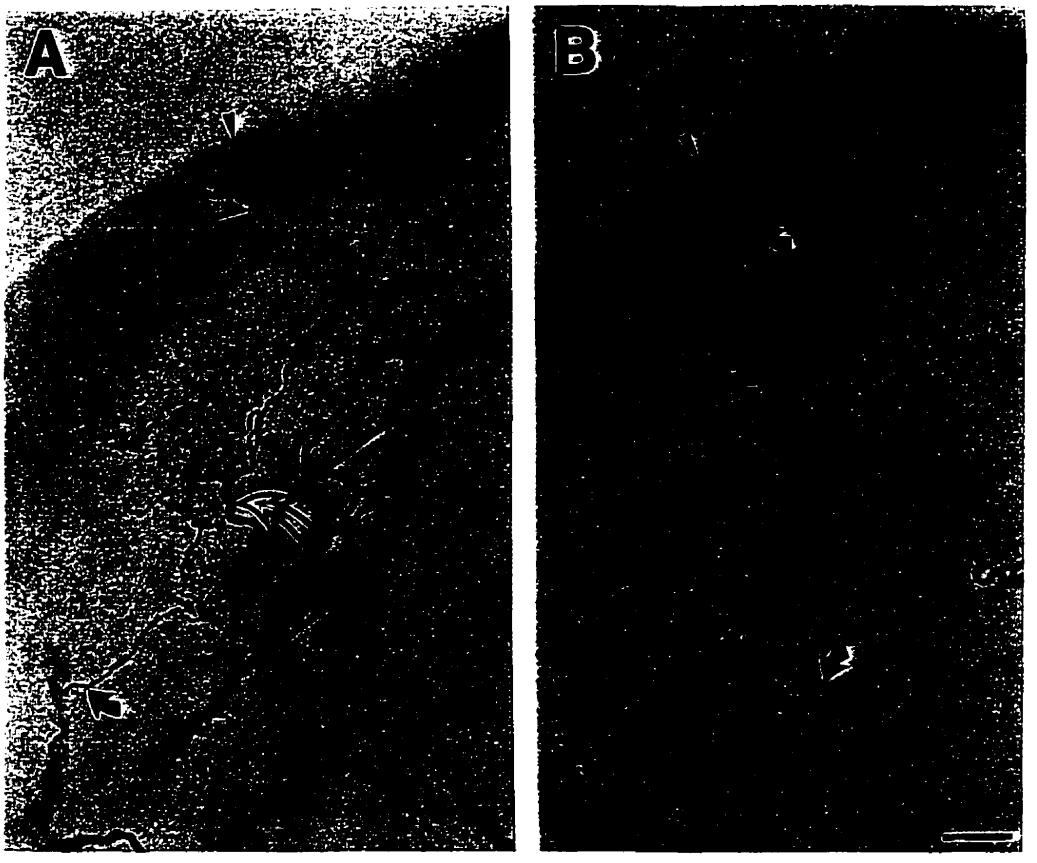
A
B

FIGURE 4.2: ***Normal pattern of DβH immunoreactivity in sham-operated animals.*** **A & B** -DβH-IR fibres are located in the lower dermis where they are associated with blood vessels (V). Like SP-IR fibres these DβH-IR fibres are also studded with numerous axonal varicosities (curved arrows). Note that these varicosities are larger and more regularly spaced along the axons than the varicosities on the SP-IR fibres. The DβH-IR fibres appear to form a mesh around the blood vessels. Note also that the DβH-IR blood vessels are also innervated by SP-IR fibres, which are seen to run along the blood vessel (especially in panel A), but these SP-IR fibres never wrap around the blood vessels as do the DβH-IR fibres. Scale bar = 20 μm.

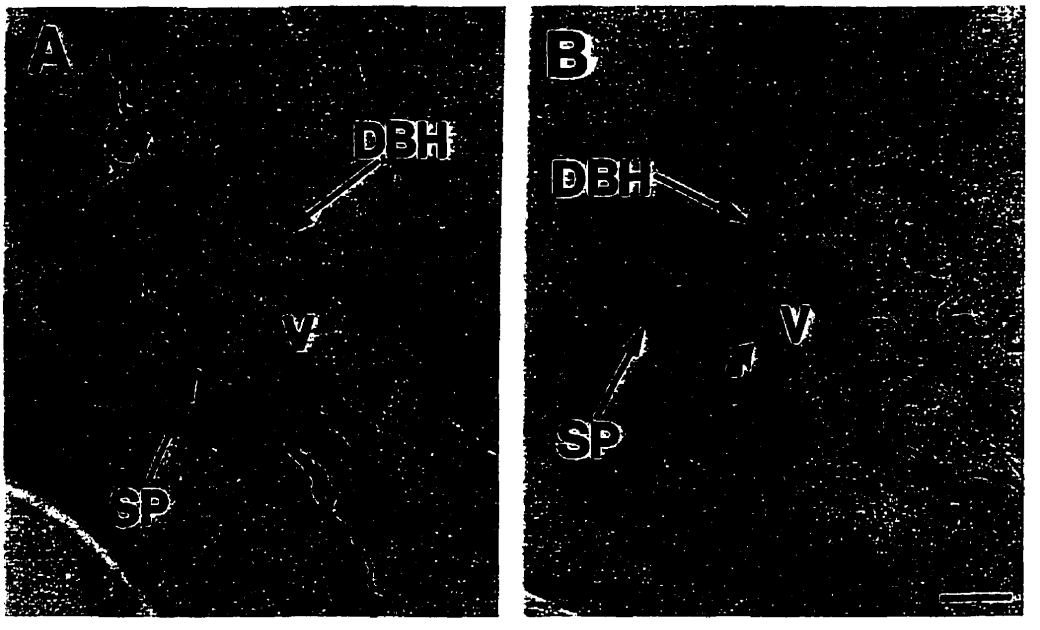
A
DBH
V
SP
B
DBH
V
SP

FIGURE 4.3: ***Substance P and DβH immunoreactivities one, two and three weeks following mental nerve lesions.*** **A & B** -One week post-MN lesion, DβH-IR fibres start to appear within the upper dermis. These fibres are fine and isolated and possess axonal varicosities (curved arrows). In some animals we can still note the presence of SP-IR fibres (**A**) which have not yet degenerated. **C & D** -Two weeks post-MN lesion, the DβH-IR fibres are more numerous in the upper dermis than at one week post-lesion. The DβH-IR fibres are seen to start branching within the upper dermis (open arrows). We can also clearly observe the presence of axonal varicosities (curved arrows). There are still some residual SP-IR fibres, but these are faint and few in number (in **C**). **E & F** -Three weeks post-MN lesion the DβH-IR fibres are even closer to the surface of the skin. These fibres appear to be arising from the DβH-IR fibres located in the lower dermis. This is suggested by the presence of very long DβH-IR fibres, which are seen to span both the upper and lower dermal regions. Some fibres can be seen to travel in bundles (double headed arrow). At this point SP-IR fibres have become virtually nonexistent. In all panels the arrowheads represent the surface of the skin. Scale bar = 20 μm.

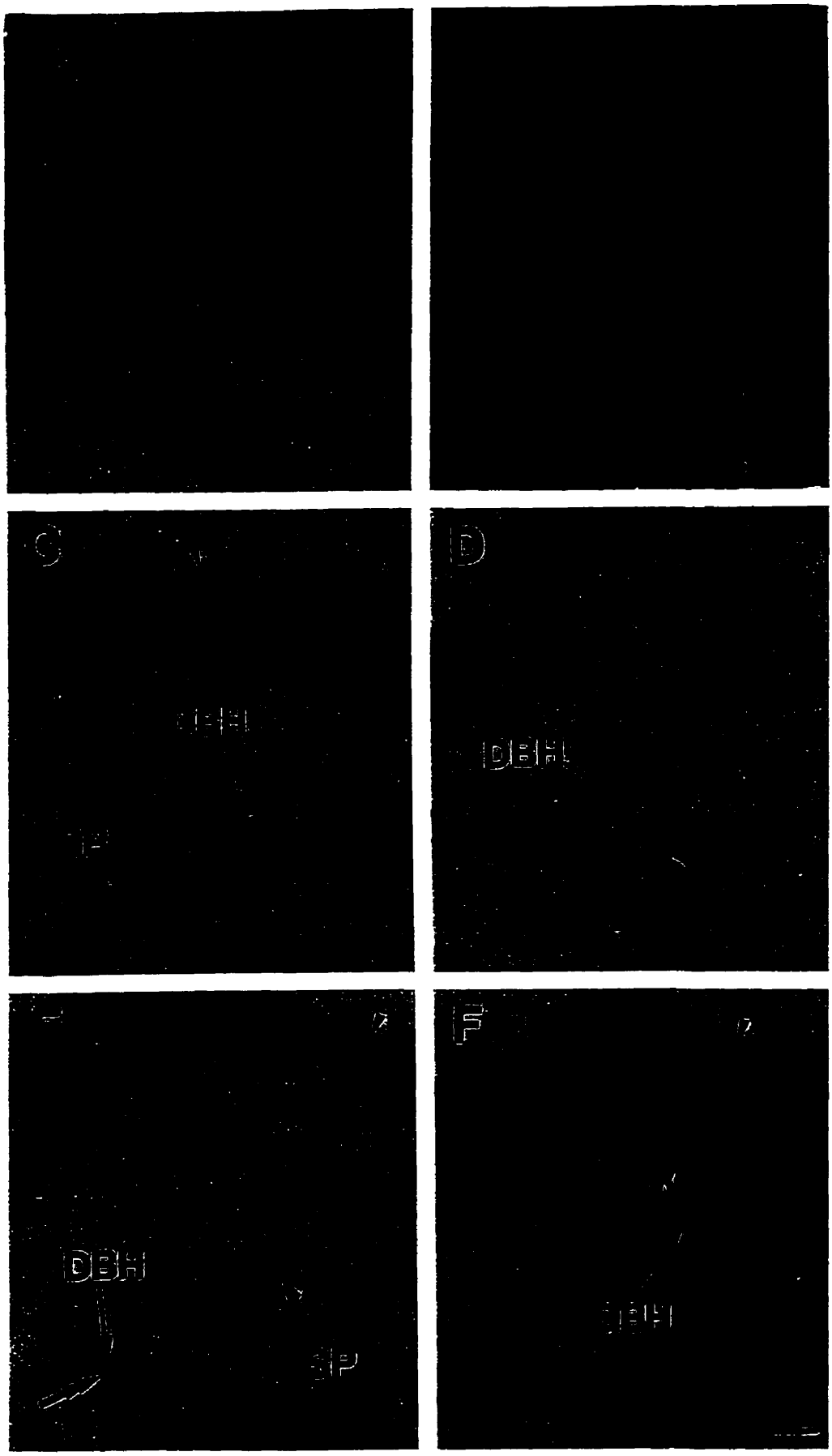
C
DBH
D
DBH
E
DBH
F
DBH

FIGURE 4.4: ***Substance P and DβH immunoreactivities four, six and eight weeks following mental nerve lesions.*** **A & B** -Four weeks post-MN lesion, the situation resembles that of the three weeks time point with the exception that SP-IR fibres have started to reinnervate the skin. The SP-IR fibres regain the upper dermis despite the presence of migrated DβH-IR fibres in this territory. Note that these fibres appear to be running parallel to one another (squared arrow). Six (**C & D**) and eight (**E & F**) weeks post-MN lesion a quasi normal pattern of SP immunoreactivity is achieved in the lower lip. The DβH-IR fibres persist in the upper dermis dispite SP reinnervation. Blood vessels (V) in the lower dermis appear to be innervated by both SP- and DβH-IR fibres once again. The arrowheads represent the surface of the skin. Scale bar = 20 μm.

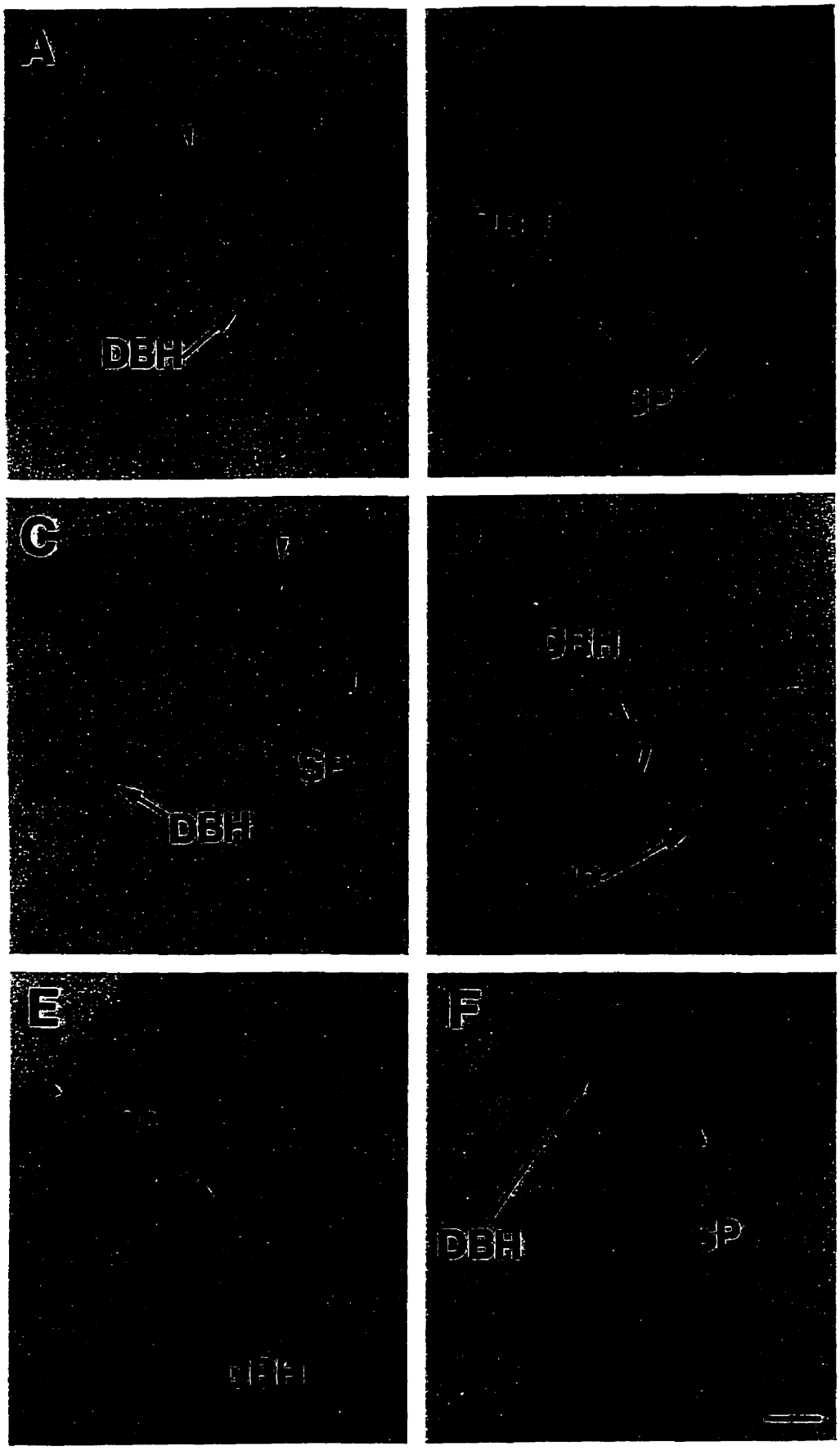
A
DBH
B
SP
C
SP
DBH
D
DBH
E
DBH
F
DBH
SP

FIGURE 4.5: ***Quantification of the extent of DβH-IR fibre migration into the upper dermis four weeks post-mental nerve lesions.*** Using an M4 image analysis system, we found that four weeks post-MN lesion, the DβH-IR fibres in lesioned animals are significantly closer to the surface of the skin when compared to sham operated animals. n=6 for each group. *$p < 0.001$

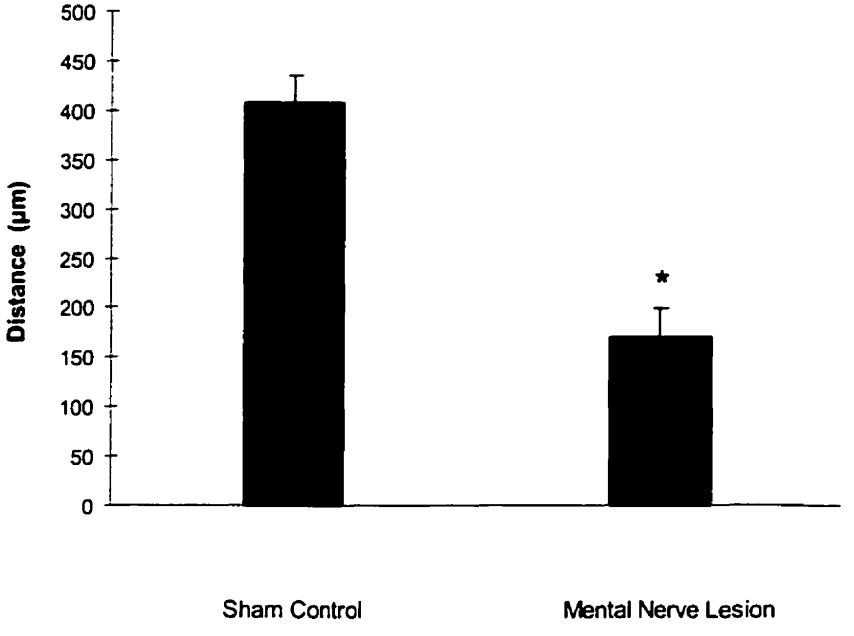
500
450
400
350
300
250
200
150
100
50
0
Distance (µm)
*
Sham Control
Mental Nerve Lesion

FIGURE 4.6: ***Substance P and DβH immunoreactivities following both mental nerve lesions and sympathectomies.*** **A** SP-IR fibres reinnervate the upper dermis following MN lesion and sympathectomy. Note that, as in sham operated animals, some of the SP-IR fibres are grouped in bundles (curved open arrows). **B** In the lower dermis note that DβH-IR fibres are no longer present. The SP-IR fibres however, reinnervate the lower dermal blood vessels (V). Curved arrows represent synaptic varicosities. The arrowhead represents the surface of the skin. Scale bar = 20 μm.

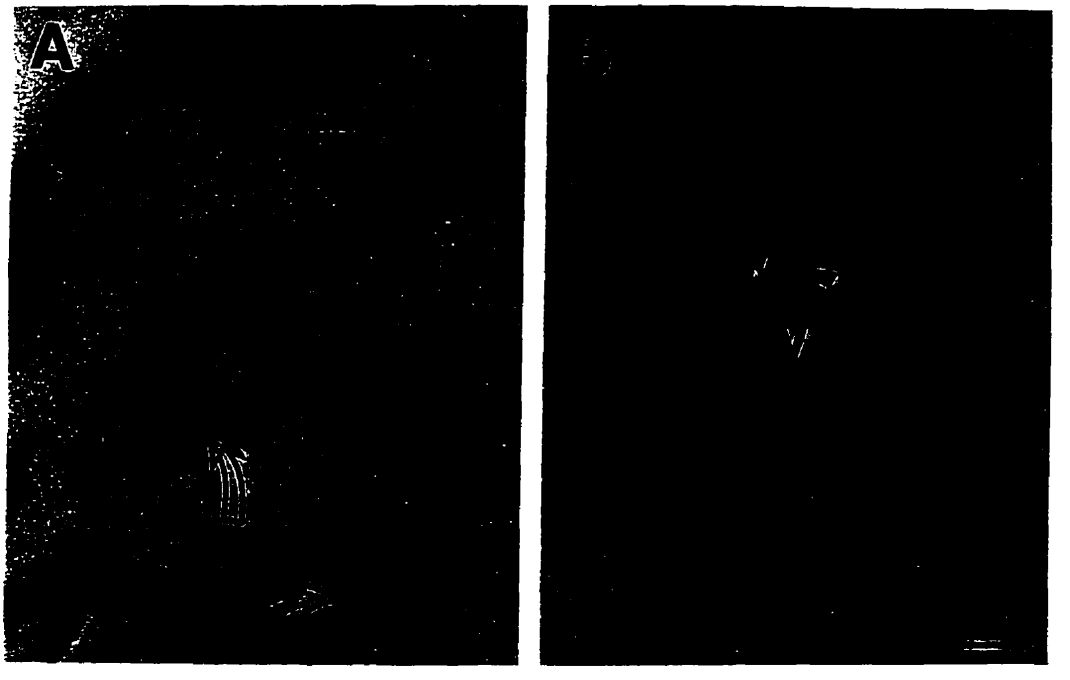
A

TABLE 4.1. Quantification of the migration of DβH-IR fibres into the upper dermis at all post-surgical time points[1]

post-surgical time points	fibres intersecting counting area	total number of fibres	total number of fibres including branches
1 week	3	19	19
2 weeks	18	29	33*
3 weeks	23	55	60**
4 weeks	87	125	192**
6 weeks	20	60	62**
8 weeks	17	47	53**

[1]Number of DβH-IR fibres in the upper dermis at various time points following mental nerve lesions. The DβH-IR fibres start to appear in the upper dermal region of the skin as early as one-week post-MN lesion. The migration into this territory is gradual and reaches maximal levels by the fourth week post-MN lesion. It is also at this latter time point that the extent of fibre branching reaches its maximum. After this point, the number of DβH-IR fibres and the number of fibre branches in the upper dermis begin to decline. However, the number of DβH-IR fibres and their branches are still higher than at the one-week time point. *$p<0.05$, **$p<0.001$ (one-way ANOVA followed by Dunnett's one-sided test)

CONNECTING TEXT – CHAPTER 4 TO 5

In the previous chapter, we demonstrated that bilateral mental nerve lesions led to the complete degeneration of SP-IR fibres and to the sprouting of DβH-IR fibres into the upper dermis, a territory from which these fibres are normally absent. Quantification of this fibre migration revealed that the DβH-IR fibres were significantly closer to the surface of the skin in lesioned animals than in controls, and that they displayed increasing numbers of branches over time. Furthermore, the sprouted DβH-IR fibres persisted in the upper dermis despite the re-innervation of the rat lower lip skin by SP-IR fibres. The novel pattern of innervation in the upper dermis consisted of SP- and DβH-IR fibres running parallel, and in close proximity, to one another.

Based on our findings, and those of others showing sensory fibre sprouting in the DRG following sciatic nerve lesions, we wanted to determine if, by lesioning the sympathetic system, we could induce sprouting of the sensory system. To test this, the superior cervical ganglia were bilaterally removed, and one to eight weeks post-surgery, SP, NK-1 and DβH immunoreactivities were assessed at the light microscopic level.

CHAPTER 5

Sympathectomies Lead to Transient Substance P-Immunoreactive Sensory Fibre Plasticity in the Rat Skin

Isabella Ruocco, A. Claudio Cuello, Ryuichi Shigemoto
and Alfredo Ribeiro-da-Silva

In press : Neuroscience (2001)
Reprinted with permission from Elsevier Science

ABSTRACT

Research using animal models of neuropathic pain has revealed sympathetic sprouting onto dorsal root ganglion cells. More recently, sensory fibre sprouting onto dorsal root ganglion cells has also been observed. Previous work in our laboratory demonstrated persistent sympathetic fibre sprouting in the skin of rat lower lip following sensory denervation of this region. Therefore, we applied immunocytochemistry to determine the effects of sympathectomies on the terminal fields of sensory fibres. The superior cervical ganglia were removed bilaterally and the effects on the innervation of the skin of rat lower lip were observed one, two, three, four, six and eight weeks post-surgery. Substance P and dopamine-β-hydroxylase immunoreactivities were used to identify a subset of sensory and sympathetic fibres respectively. We also assessed neurokinin-1 receptor immunoreactivity. Quantitative data was obtained with the aid of an image analysis system. In controls, the upper dermis was innervated by substance P-immunoreactive fibres only and possessed the highest density of neurokinin-1 receptor immunoreactivity, while blood vessels in the lower dermis were innervated by both substance P- and dopamine-β-hydroxylase-immunoreactive fibres. Following sympathectomies, substance P-immunoreactive fibres in the upper dermis were more intensely labelled only one and two weeks post-surgery when compared to sham controls. The length of substance P-immunoreactive fibres in this region was also increased only on the second week. Neurokinin-1 receptor immunoreactivity in the upper dermis was slightly decreased one and two weeks post-surgery. In the lower dermis, substance P-immunoreactive fibres associated with blood vessels were more intensely labelled only one and two weeks post-surgery, and at all post-surgical time points studied, blood

vessels in this region were devoid of dopamine-β-hydroxylase-immunoreactive fibres. The length of substance P-immunoreactive fibres was increased from the first to the third week post-surgery in the lower dermis.

These results indicate that sympathectomies lead to transient changes in substance P-immunoreactive fibre innervation and neurokinin-1 receptor expression in the upper and lower dermis of the rat lower lip skin. The effects are most prominent in the lower dermis probably due to a greater local concentration of nerve growth factor in this region.

INTRODUCTION

Several studies suggest a possible role of the sympathetic system in hyperalgesia following peripheral nerve injuries. Sympathetic sprouting in the dorsal root ganglion (DRG) was observed (McLachlan E.M. et al., 1993; Chung K. et al., 1996; Ramer M.S. and Bisby M.A., 1997) around large diameter DRG cells (Chung K. et al., 1993; Abbadie C. and Basbaum A.I., 1998). These sprouted fibres have been described as possessing varicose terminals that were observed in close proximity to the DRG cell bodies (Chung K. et al., 1997). It has also been demonstrated that the time course of the sympathetic sprouting (Lee B.H. et al., 1998) and the origin of the sprouted fibres (Ramer M.S. and Bisby M.A., 1998) varied according to the injury model used. Nonetheless, sympathetic sprouting onto DRG neurons appears to be a common feature of the injury models studied.

These findings indicate that the DRG is a site of anomalous interactions between the sensory and sympathetic systems. A previous study from our laboratory revealed that such aberrant interactions might also occur in the peripheral terminal field region of sensory and sympathetic fibres. In fact we found that sympathetic fibres are normally absent from the upper dermis of the skin of the rat lower lip. However, sensory denervation following bilateral transection of the rat mental nerves led to the migration of sympathetic fibres into the upper dermis. Although sensory re-innervation eventually occurred, the migrated sympathetic fibres remained in their new territory. Furthermore, these two fibre types were seen to run parallel to one another, suggesting that they interact in the re-innervated territory (Ruocco I. et al., 2000).

A recent study reported that, following a sciatic nerve transection, small sensory fibres form baskets around large diameter DRG neurons (McLachlan E.M. and Hu P., 1998). This provides evidence that changes in sensory fibre innervation patterns may occur following lesions, and that the changes are not restricted to the sympathetic system. Our objective in the present study was, therefore, to determine the effects of sympathectomies on the terminal fields of sensory and sympathetic fibres in the skin of the rat lower lip. The rat lower lip is a good model for this type of research as it allows for the independent manipulation of the sensory and sympathetic systems. The superior cervical ganglia (SCG) were surgically removed bilaterally and, at several post-surgical times, substance P (SP) and neurokinin-1 receptor (NK-1r) immunoreactivities were assessed as markers of changes in sensory innervation, while dopamine-β-hydroxylase (DβH) immunoreactivity was assessed for changes in sympathetic innervation.

MATERIALS AND METHODS

Male Wistar rats weighing 250-300 g were used in this study. The animals were provided with food and water *ad libitum* and kept under a twelve hour day/night cycle. All experimental procedures were performed in accordance with the guidelines from the Canadian Council on Animal Care. All efforts were made to minimise the number of animals used and animal suffering.

Animal preparation. A total of 60 rats were used. The animals were anaesthetised with acepromazine (0.2 ml/kg) subcutaneously, followed by intramuscular injections of xylazine (0.25 ml/kg) and ketamine (0.5 ml/kg). Each injection was followed by a 10 min waiting period. Half the animals had their SCG bilaterally removed. The remaining

animals were sham-operated and used as controls. All animals were left to recover for the appropriate post-surgical time (1, 2, 3, 4, 6, 8, weeks) prior to being perfused through the ascending aorta under Equithesin (0.4 ml/kg) anaesthesia. Sham-operated animals were perfused four weeks post-surgery. The fixation protocol used was 4% paraformaldehyde, 15% picric acid (v/v) and 0.1% glutaraldehyde in 0.1M phosphate buffer (PB) (pH 7.4) for 30 min, followed by 4% paraformaldehyde and 15% picric acid (v/v) in 0.1M PB for 30 min. The lower lips were collected and post-fixed at 4°C for 1 h in the latter fixative mixture. The lips were then immersed in 30% sucrose in 0.1M PB prior to being snap frozen in liquid nitrogen, thawed in 0.1M PB, placed on tissue holders and embedded in Tissue-Tek (OCT). Fifty-micrometer thick sections were cut on a cryostat at –20°C and collected in phosphate-buffered saline containing 0.2% Triton X-100 (PBS+T).

SP and DβH immunostaining. All washes and dilutions were performed in PBS+T unless otherwise mentioned. The sections were treated in 50% ethanol (v/v) (Llewellyn-Smith I.J. and Minson J.B., 1992), 0.3% H_2O_2 and 1% sodium borohydride in PBS for 30 min respectively. After extensive washing the sections were incubated with a mixture of rat bispecific anti-SP anti-horseradish peroxidase (HRP) monoclonal antibody (1:10) (Suresh M.R. et al., 1986) and a mouse monoclonal anti-DβH antibody (1:10) (Mazzoni I.E. et al., 1991) overnight at 4°C. Subsequent to washing, the sections were incubated with HRP (Sigma type VI, 5 μg/ml) for 1 h, washed and the SP antigenic sites revealed by 3,3'-diaminobenzidine tetrahydrochloride (DAB) and H_2O_2. After washing, DβH was demonstrated by incubating the sections for 1h in goat anti-mouse IgG (American Qualex, 1:50) preabsorbed for 8 h at 4°C in fixed rat lip tissue (Ruocco I. et al., 2000). Following washes and incubation in a mouse monoclonal peroxidase anti-peroxidase

antibody (Semenenko F.M. et al., 1985) for 1 h, the sections were washed and incubated with the SG chromogen (Vector Labs) for 15 min followed by 5 min in distilled water. Lastly, the sections were mounted on gelatin-subbed slides, dehydrated through ascending ethanol concentrations, cleared with xylene and cover slipped with Permount (Fisher).

NK-1r immunocytochemistry. For neurokinin-1 receptor (NK-1r) immunocytochemistry, the tissue sections were obtained as described above. Following the ethanol, H_2O_2 and sodium borohydride treatments (see above), the sections were pre-incubated in 5% normal goat serum followed by a polyclonal rabbit serum against the NK-1r (Shigemoto R. et al., 1993; Nakaya Y. et al., 1994) diluted 1:500 for 48 h at 4°C. The sections were then washed, incubated in a biotinylated goat-anti-rabbit IgG (1:3000; ICN) for 1 h, washed again and finally incubated in an ABC complex (1:50; Vector Labs) for 1 h. After further washing, the NK-1r signal was revealed by incubating the section in DAB and H_2O_2. The sections were mounted on gelatin-subbed slides, dehydrated through ascending ethanol concentrations, cleared through xylene and cover slipped with Entellan (BDH).

Quantification. SP immunoreactivity was quantified using an MCID-M4 image analysis system (Imaging Research Inc., St. Catharines, ON, Canada). Four animals per time point (sham, 1, 2, 3, and 4 weeks) and five 50 μm-thick sections per animal were quantified. Digital images of four regions (two from the upper and two from the lower dermis) per section were obtained and stored. Once all images were collected, they were subjected to a normalisation process in order to equalise the backgrounds across sections. Subsequently three adjacent fields of 0.1 mm^2 per region were quantified. We measured

the relative optical density (ROD) of SP-IR fibres as well as the total length of SP-IR fibres per 0.29 mm^2. ROD values were measured as they provide information on immunostaining intensity. The upper and lower dermal data were analysed separately and one-way ANOVA followed by Dunnett's one-sided test were used to assess statistical significance.

RESULTS

For the purpose of this study, we divided the dermis into upper and lower parts. The upper dermis is the area between the epidermis and the opening of the sebaceous glands into the hair follicles, while the lower dermis corresponds to the area between the sebaceous gland openings and the hypodermis.

Upper dermis

In controls, the upper dermis was innervated by SP-immunoreactive (SP-IR) fibres (Fig. 5.1D-F). These fibres formed an extensive branching network and possessed numerous axonal varicosities. Some SP-IR fibres in this region occurred as free nerve endings associated with blood vessels, the walls of which possessed NK-1r immunoreactivity (see below). Others were seen to run along the dermal-epidermal junction and these fibres occasionally penetrated into the epidermis. The upper dermis was devoid of DβH-IR fibres. Following sympathectomies, SP-IR fibre labelling was more intense one and two weeks post-surgery (Fig. 5.1A,B). However, this increase in staining intensity was short lasting and by the third week post-surgery (Fig. 5.1C) the

pattern of SP immunoreactivity did not differ from controls (Fig. 5.1D-F). There was also a slight increase in the length of SP-IR fibres in this region (Fig. 5.2).

An image analysis system was used to detect the relative intensity of immunostaining (ROD) for SP-IR fibres and their total length, as described in Experimental Procedures. This quantitative analysis revealed that the increase in fibre labelling intensity was significant one and two weeks post-sympathectomies (Fig. 5.3A). As for the length of SP-IR fibres, it was only significantly increased two weeks post-surgery (Fig. 5.3B). NK-1r immunoreactivity was considerably less than in controls one week post-surgery (Fig. 5.4A) and remained low up until the third week post-surgery (Fig. 5.4B), when the intensity of the staining was apparently identical to that of controls (Fig. 5.4D-F).

Lower dermis

Both SP- and DβH-IR fibres were associated with the same blood vessels in the lower dermis of controls (Fig. 5.5D-F). Both fibre types possessed numerous varicosities. However, DβH-IR fibres were seen in a net-like arrangement around the blood vessels, while SP-IR fibres ran mostly along the outer border of the blood vessel walls (Fig. 5.5). DβH-IR fibres were not detected one week post-surgery (Fig. 5.5A), and remained undetectable in all time points studied.

Quantitative analysis revealed that, one week post-surgery (Fig. 5.5A), SP-IR fibres associated with blood vessels were more intensely labelled than controls (Fig. 5.6A) and, as in the upper dermis, that this increase was transient. This increased labelling was observed until the second week post-surgery (Fig. 5.5B), and by the third

week SP-IR fibre labelling intensity did not differ from control (Fig. 5.5D-F). One to three weeks post-surgery, there was a dramatic and significant increase in the length of SP-IR fibres in the lower dermis (Fig. 5.5A-C and Fig. 5.6B). NK-1r are not normally detected in lower dermal blood vessels and no changes were observed post-surgery.

DISCUSSION

In this study we provide evidence that, unlike sensory denervations that lead to persistent sympathetic changes, sympathectomies induce transient changes in the sensory innervation of the skin of the rat lower lip (see Fig. 5.7). In fact, in the upper dermis, we observed more intense labelling which was accompanied by NK-1r down-regulation, one and two weeks post-sympathectomy. The NK-1r down-regulation appears to be a compensatory mechanism in response to the increased length and labelling intensity of SP-IR fibres. In fact, this type of compensatory mechanism has been observed in the spinal cord. Following inflammatory or nerve injury-induced pain, SP levels decreased in the spinal dorsal horn while NK-1r immunoreactivity was shown to increase (Abbadie C. et al., 1996; Malmberg A.B. et al., 1997). SP-IR fibre length was also increased one and two weeks post-surgery in the upper dermis. In the lower dermis, SP-IR fibre labelling was more intense only one and two weeks post-surgery. SP-IR fibre length however, was increased from one to three weeks post-surgery. In both the upper and lower dermis increases in labelling intensity and fibre length suggest increases in levels of SP expression and SP-IR fibre sprouting respectively.

The rat lower lip is innervated by both sensory and sympathetic fibres and these two fibre types appear to compete for target-derived nerve growth factor (NGF) for their

survival and maintenance (Otten N.U. et al., 1980; Kessler J.A. et al., 1983; Korsching S. and Thoenen H., 1985; Hill C.E. et al., 1988). Sensory fibre sprouting, following either surgical or chemical sympathectomy, has been observed (Kessler J.A. et al., 1983; Zhang S.Q. et al., 1984; Yodlowski M.L. et al., 1984; Hill C.E. et al., 1988) and this sprouting appears to occur as a result of the loss of sympathetic competition for NGF (Kessler J.A. et al., 1983). Indeed the sympathectomy-induced sensory sprouting is blocked when NGF anti-serum is administered (Kessler J.A. et al., 1983), further substantiating a role for NGF in the sprouting. Therefore this would explain how sensory fibre sprouting occurs in the rat lower lip following sympathectomies. SP-IR fibres in the rat lower lip skin are mostly associated with blood vessels. A view suggested in the past is that not all SP-IR fibres are NGF-responsive. Therefore, the fibres were then usually divided into two groups, NGF-sensitive and NGF-insensitive, with the latter thought to be responsive to an unidentified trophic factor (Rawdon B.B. and Dockray G.J., 1982). Amongst those thought to be NGF-insensitive were the SP-IR fibres which innervate blood vessels (Kessler J.A. et al., 1983; Kessler J.A. et al., 1983; Yodlowski M.L. et al., 1984). If this view were accurate, it would explain our results showing brief sensory changes, as these fibres are associated strictly with blood vessels.

Contrary to these findings, we believe that the literature provides significant evidence to support the view that SP-IR fibres associated with blood vessels in the lower dermis are NGF-responsive. For instance it has been shown that SP and calcitonin gene-related peptide (CGRP) are dependent upon the NGF produced by blood vessels (Donnerer J. et al., 1992; Lewin G.R. and Mendell L.M., 1993; Tuttle J.B. et al., 1993; Anand P. et al., 1997). Experiments using antibodies to NGF have resulted in a slight

decrease in immunoreactivity for SP and CGRP in the mesenteric artery and the femoral vein (Aberdeen J. et al., 1991). Furthermore, extracerebral blood vessels are innervated by nociceptive sensory axons which possess p75 and trkA receptors and are NGF-responsive (Kawaja M.D., 1998). Finally, evidence from diabetic patients shows that skin levels of NGF and substance P are decreased, and that the NGF depletion appears to correlate with a decrease in antidromic vasodilatation (Anand P., 1996). This evidence strongly indicates that blood vessel-associated sensory fibres, which are responsible for mediating vasodilatation, are NGF-sensitive. Therefore, we believe that the lack of long lasting changes in SP-IR fibre innervation of the rat lower lip skin is not due to the unresponsiveness of these fibres to NGF, but that it is due to a presently unknown reason. Furthermore, as the sympathetic fibres degenerate, the largest available pool of NGF becomes the lower dermis. Thus the most prominent effects are observed in the lower dermis. NGF is able to diffuse to the upper dermis and hence could be responsible for the upper dermal changes. The NGF concentration in this region may not be as elevated as in the lower dermis and this would explain the less striking results. It is clear, however, that the minimal changes observed are not due to unsuccessful sympathectomies, as the complete degeneration of the DβH-IR fibres occurred by the first week post-surgery and was maintained throughout this study.

Increases in SP-IR fibre detection may be due to an increased fibre number as a result of sprouting, increased expression of SP in each fibre or both. Previous studies have shown that sympathectomies can increase the expression of SP in C-fibres (Cole D.F. et al., 1983; Kessler J.A. et al., 1983; Carvalho T.L.L. et al., 1986; Nielsch U. and Keen P., 1987; Nelson D.K. et al., 1988) or the density of these fibres (Zhang S.Q. et al.,

1984; Yodlowski M.L. et al., 1984). NGF appears to play a role in increasing SP and CGRP fibre density (Kessler J.A. et al., 1983; Nielsch U. and Keen P., 1987; Aberdeen J. et al., 1990; Aberdeen J. et al., 1992), and mediating sensory fibre sprouting following sympathectomies (Kessler J.A. et al., 1983; Zhang S.Q. et al., 1984; Yodlowski M.L. et al., 1984; Hill C.E. et al., 1988). Systematic quantification of our material strongly suggested that in our model sympathectomies caused both an increase in SP-IR fibre number and SP content. No aberrant patterns of innervation by SP-IR fibres were observed. This is consistent with the observation that increasing the availability of NGF results in increased sensory fibre density in its normal target area, and in increased sympathetic fibre density in its normal and aberrant areas as well (Davis B.M. et al., 1997).

It has been reported that SP concentration, when measured by radioimmunoassay, is increased in the SCG following guanethidine-induced sympathectomies. The increase was observed six to eight weeks after cessation of drug treatment (Benarroch E.E. et al., 1992). At earlier stages (two weeks post-sympathectomy) increased levels of CGRP but not SP were observed (Benarroch E.E. et al., 1992). Examining later time points (beyond eight weeks post-sympathectomy) to determine if sensory changes would occur following a longer survival in our model might have some interest. However, this is unlikely as the effectiveness of chemical (in this case 6-hydroxydopamine) and, probably, surgical sympathectomy appears to be governed by the ratio of noradrenaline: SP in the tissue (Nielsch U. and Keen P., 1987). Based on these observations, we suggest that if this ratio is high, the competition for tissue-derived NGF by sympathetic fibres would be high. The removal of sympathetic fibres would result in the loss of competition for NGF and thus

favour sensory fibre sprouting. However if the ratio is small, the competition for NGF would be small (both sensory and sympathetic fibres successfully obtaining a substantial amount of NGF) and removing sympathetic fibres would not result in substantial sensory fibre sprouting. As both sensory and sympathetic fibres are abundant in the skin of the rat lower lip, the noradrenaline:SP ratio in our model is probably 1:1 and this could explain why sympathectomies did not lead to marked sensory changes.

A final consideration: the outcome of sympathectomies appears to depend on whether they were performed surgically or chemically (Ouyang A. et al., 1996). Furthermore, there appear to be discrepancies in the results obtained from researchers studying the same system. For instance, Aberdeen et al. (1992) show no increases in SP levels in the SCG, while Benarroch et al. (1992) show that they do occur. In both cases mature male Sprague-Dawley rats were treated with intraperitoneal injections of guanethidine. However, Aberdeen et al. (1992) treated the rats everyday for five weeks with 40 mg/kg, while Benarroch et al. (1992) treated the rats five days a week for 4 weeks with 80 mg/kg. In the later case, doubling the dose of guanethidine may have successfully removed more sympathetic fibres, thus allowing sprouting of the SP-IR fibres. Furthermore, Aberdeen et al. (1992) sacrificed the animals two weeks after the treatment ended, while Benarroch et al. (1992) sacrificed them six to eight weeks after the treatment ended. A longer post-treatment delay could allow SP-IR fibre sprouting into the SCG to occur and this effect could be missed in experiments with shorter delays.

In conclusion, we have shown transient sensory changes in the rat lower lip following sympathectomies. These changes include increased labelling intensity and sprouting of SP-IR fibres and were accompanied, only in the upper dermis, by the down-

regulation of NK-1r. However the majority of these changes were no longer observed three weeks post-sympathectomies. This data should be interpreted with caution, as previous studies have shown that the outcome of sympathectomies varies considerably depending on the target field studied and whether surgical and chemical sympathectomies are performed. However, our data revealed changes that may be related to the genesis of post-sympathectomy pain since plastic changes in sensory innervation of the rat lower lip were observed. The increased innervation of the rat lower lip by sensory fibres may result in anomalous patterns of innervation in this area, which in turn lead to increased pain sensation. These findings are of potential clinical relevance as post-sympathectomy pain is associated with such syndromes as sympathalgia, post-sympathectomy parotid pain and Raeder's paratrigeminal syndrome (Schon F., 1985).

FIGURE 5.1: ***Light microscopic distribution of SP-IR fibres in the epidermis and upper dermis of the skin of the rat lower lip in sympathectomized (A-C) and control (D-F) animals.*** Panels (**A-C**) were obtained from animals one (**A**), two (**B**) and three (**C**) weeks post-sympathectomy. Note the presence of thicker SP-IR fibre bundles (thick arrows) in (**A**) and (**B**). In (**C**), note that the appearance of SP-IR fibres did not differ from controls (**D-F**). The thin arrows in (**C-F**) point to SP-IR fibres with similar appearances. Note that these fibres are thinner than in (**A**) and (**B**). Note the complete absence of DβH-IR fibres in all panels. Scale bar = 25 μm.

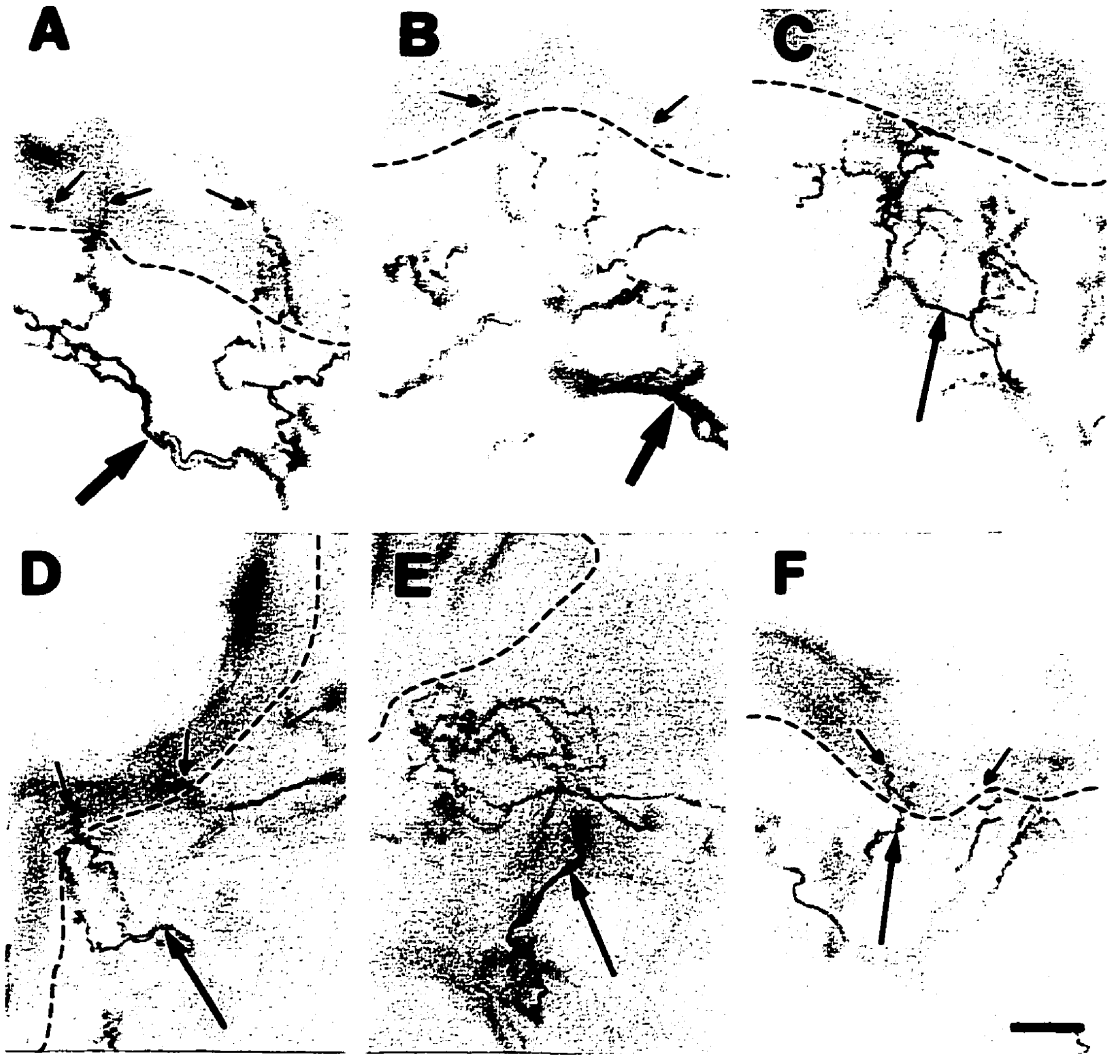
A
B
C
D
E
F

FIGURE 5.2: ***Light microscopic distribution of sprouting SP-IR fibres in the epidermis and upper dermis of the skin of the rat lower lip in control (A) and sympathectomized (B-C) animals.*** In (**A**), SP-IR fibres containing numerous varicosities (arrows) penetrate the epidermis and branch extensively. Note that following sympathectomies (**B**) the fibres branch more profusely in the epidermis. Panel (**C**) depicts the increase in SP-IR fibre density following sympathectomies, compared to controls (**A**) which possess less SP-IR fibres. Note the extensive branching network in (**B**) and (**C**) and its absence in (**A**). Scale bar = 25 μm.

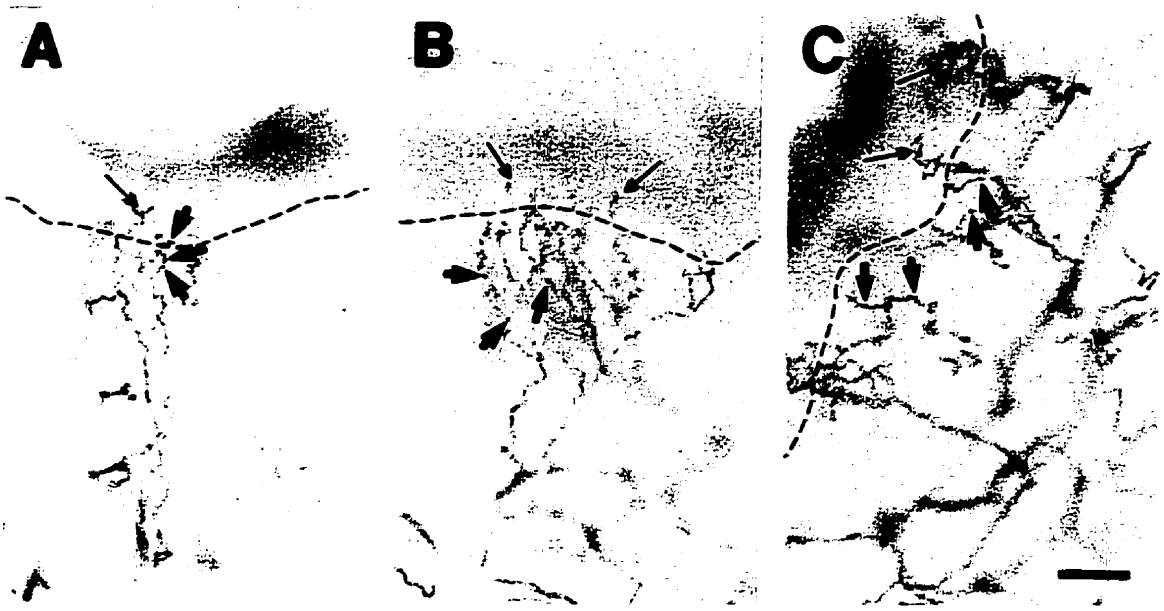
A
B
C

FIGURE 5.3: ***Quantitative analysis of the changes in SP-IR fibre labelling, in the epidermis and upper dermis of the rat lower lip skin at several time points following sympathectomies.*** Panel (**A**) shows the relative intensity of staining as relative optical density (ROD) of SP-IR fibres. Panel (**B**) shows the length in microns of the SP-IR fibres per 0.29 mm^2. s; sham-operated animals. *$p<0.05$

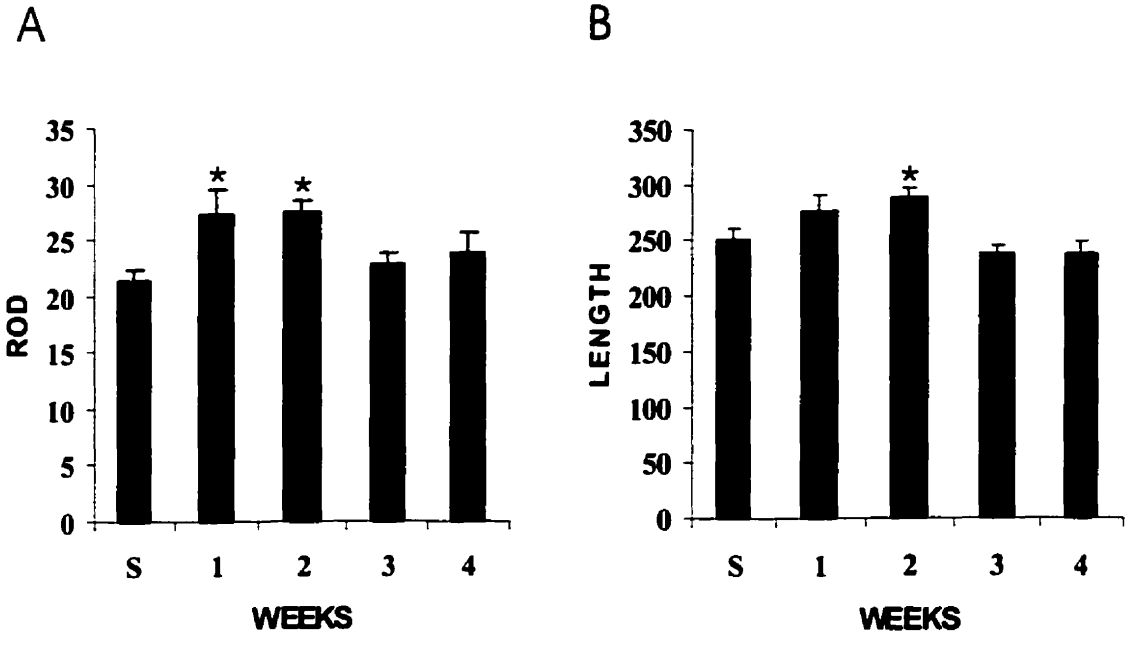
A
B
ROD
LENGTH
35
30
25
20
15
10
5
0
350
300
250
200
150
100
50
0
S
1
2
3
4
WEEKS
*

FIGURE 5.4: ***Light microscopic distribution of NK-1r immunoreactivity in the upper dermis of the skin of the rat lower lip in sympathectomized (A-C) and control (D-F) animals.*** Panels (A-C) were obtained from animals one (**A**), three (**B**) and six (**C**) weeks post-sympathectomy. NK-1r immunoreactivity is associated with the wall of blood vessels (v. blood vessel lumen). In (**A**) note the decrease in receptor immunoreactivity. In (**B**) and (**C**) NK-1r immunoreactivity did not differ from controls. Scale bar = 25 μm.

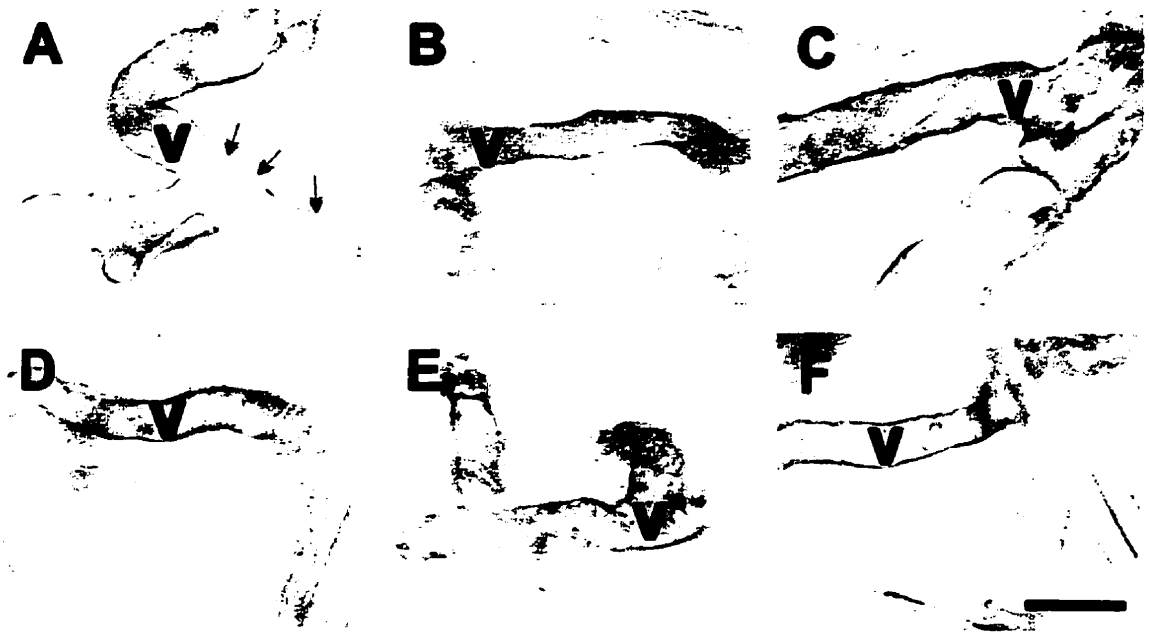
A
V
B
V
C
V
D
V
E
V
F
V

FIGURE 5.5: ***Light microscopic distribution of SP- and DβH-IR fibres in the lower dermis of the skin of the rat lower lip in sympathectomized (A-C) and control (D-F) animals.*** Panels (**A-C**) were obtained from animals one (**A**), two (**B**) and three (**C**) weeks post-sympathectomy. Note the absence of DβH-IR fibres (blue precipitate) in (**A-C**). In (**A**) note the presence of thicker SP-IR fibres (thick arrow) associated with the blood vessel wall. In (**B**) and (**C**), note that the SP-IR fibres (small arrows) did not appear different from controls (**D-F**). In panels (**D-F**), note the presence of DβH-IR fibres (curved arrows) associated with the wall of blood vessels. The blood vessels of the lower dermis received dual innervation from both SP- and DβH-IR fibres in sham controls. Scale bars = 25 μm.

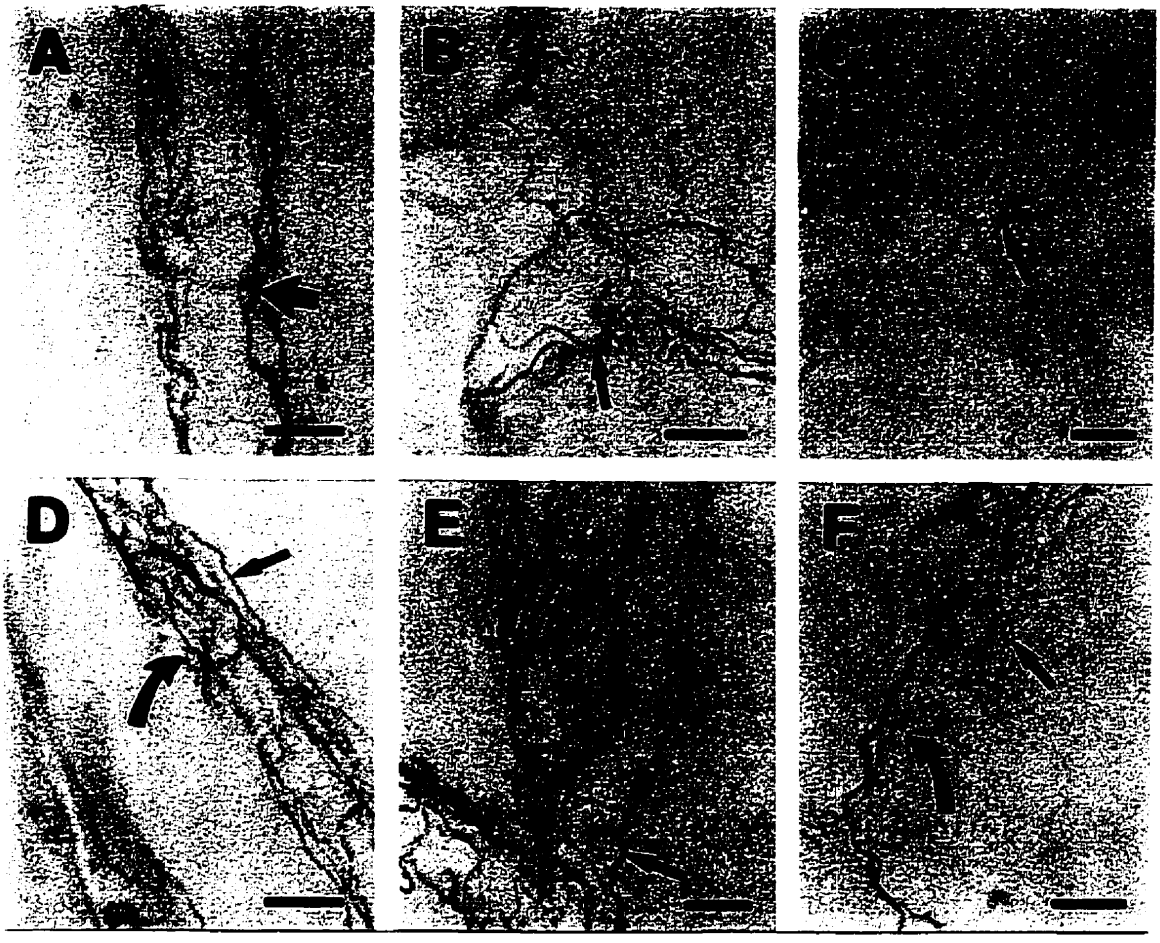
A
B
C
D
E
F

FIGURE 5.6: ***Quantitative analysis of the changes in SP-IR fibre labelling, in the lower dermis of the rat lower lip skin at several time points following sympathectomies.*** Panel (**A**) shows the relative intensity of staining as relative optical density (ROD) of SP-IR fibres. Panel (**B**) shows the length in microns of the SP-IR fibres per 0.29 mm^2. s; sham-operated animals. *$p<0.05$, **$p<0.001$

A

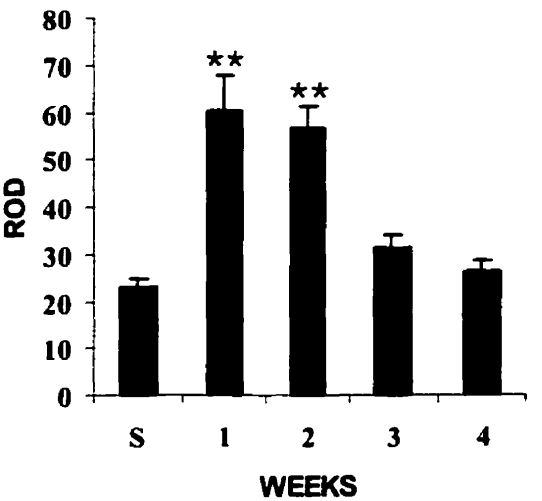
80
70
60
50
40
30
20
10
0
ROD
**
**
S
1
2
3
4
WEEKS

B

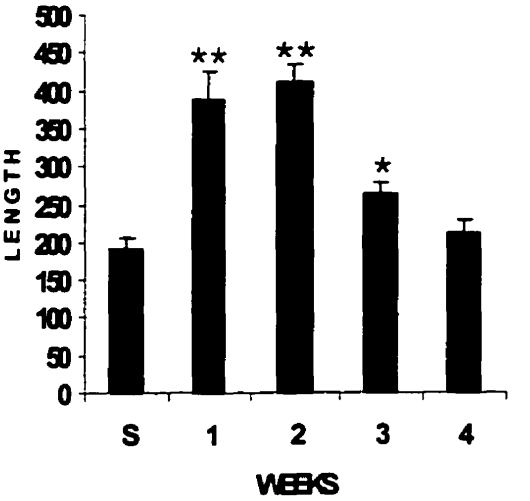
500
450
400
350
300
250
200
150
100
50
0
LENGTH
**
**
*
S
1
2
3
4
WEEKS

FIGURE 5.7: ***Schematic representation of the changes observed in the rat lower lip following symapthectomies.*** Under normal circumstances SP-IR fibres **(red)** are found throughout the lower lip. In short, they innervate blood vessels in the upper and lower dermis, while individual fibres penetrate the epidermis. In naïve animals NK-1r **(blue)** are observed on upper dermal blood vessels. As for DβH-IR fibres **(green),** they innervate only blood vessels in the lower dermis. One week post-sympathectomy, DβH-IR fibres degenerate and are no longer observed. In these animals NK-1r are down-regulated (note the reduced labelling –in blue- of the blood vessels. SP-IR fibres are more intensely labelled and have sprouted in the upper and lower dermis. Two weeks post-sympathectomy, the situation is identical to that of one-week post-sympathectomy. Three weeks post-sympathectomy, only SP-IR fibre sprouting is still present and this only in the lower dermis. DβH-IR fibres do not reinnervate the skin.

Normal

1 week

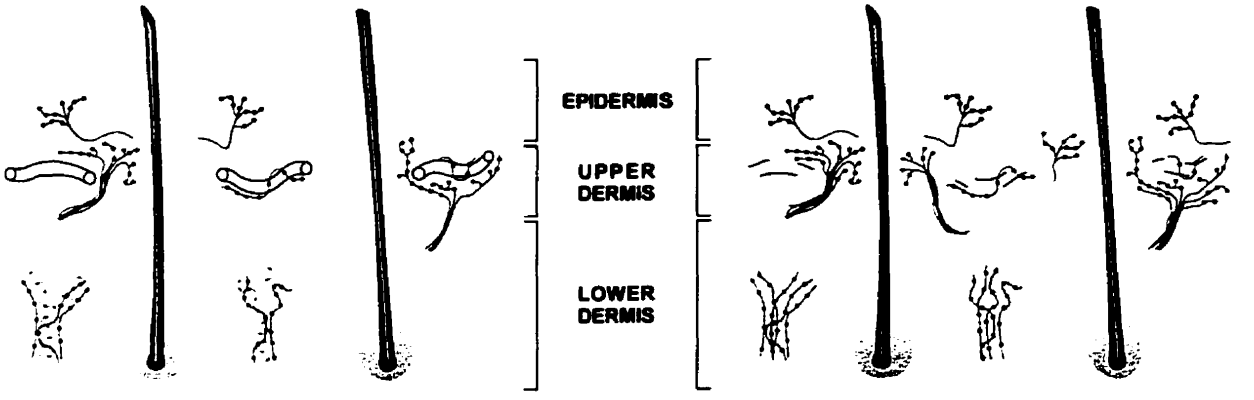

2 weeks

3 weeks

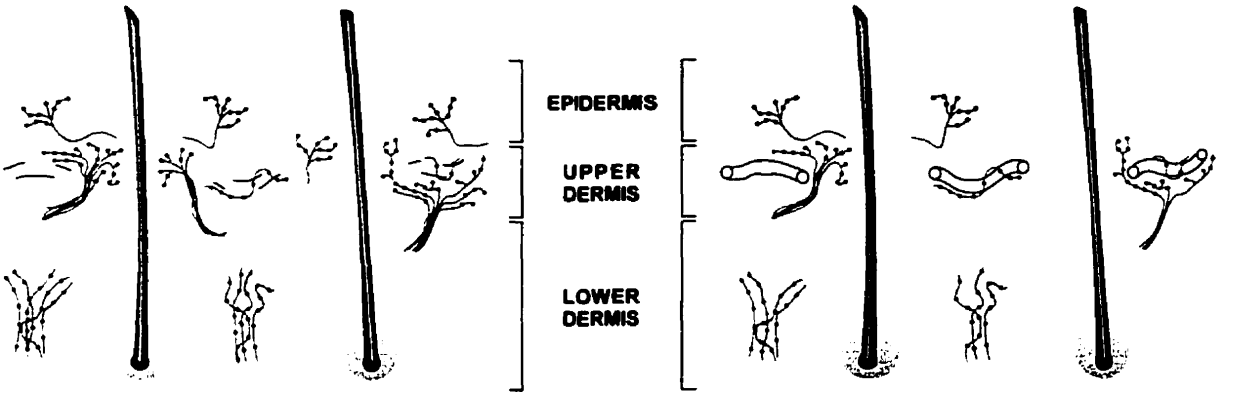

CHAPTER 6

GENERAL DISCUSSION

The main objective of this thesis was to study the changes that occur in the terminal fields following peripheral nerve injuries. Though evidence of changes occurring in the DRG had previously been published (McLachlan E.M. et al., 1993; Chung K. et al., 1993), information on more peripheral territories was still completely lacking. As the initial insult occurs in the nerve portion peripheral to the DRG, the extent of the changes may be relevant to the pain syndrome manifestation, since aberrant signals arising in the peripheral terminals may reach the spinal cord, and ultimately lead to the perception of pain.

In the following pages, the most significant results are summarized and discussed in the more general scheme of their putative involvement in neuropathic pain. Only the concepts that have not been addressed in the previous chapters' discussions will be presented herein. Initially we set forth to characterize the innervation patterns of the skin of the rat lower lip by sensory and autonomic fibres (Chapters 2 and 3). Although this model had been used in the study of neurogenic inflammation, a proper anatomical description of its innervation had yet to be published. This solid anatomical background was required for the studies involving peripheral nerve lesions (sensory and sympathetic). The objective of these experimental studies was to determine the extent of the changes incurred in the terminal field region following nerve injury (Chapters 4 and 5). Emphasis was given to sensory and sympathetic fibre interactions, as these are the ones that had been previously postulated to arise at the level of sensory ganglia (DRG).

6.1 Normal innervation of the rat lower lip skin

Our initial objective was to characterize the normal patterns of sensory and autonomic innervation in the rat lower lip skin.

6.1.1 **Sensory innervation**

Chapter 2 focussed mainly on the SP-IR subset of sensory fibres. We favoured the use of SP as a marker of peptidergic sensory fibres over CGRP, because SP in the skin is restricted to sensory fibres, while CGRP also occurs in some motor and autonomic fibres (Fundin B.T. et al., 1997). Although they do not label all peptidergic sensory fibres, anti-SP antibodies label the most uniform and abundant subpopulation. Using immunocytochemistry at both the light and electron microscopic level, we showed that SP fibres were found in the upper and lower dermis and that they innervated blood vessels, hair follicles and sebaceous glands. Importantly, the innervation patterns found in the rat lower lip skin resembled those observed in human skin (Dalsgaard C.-J. et al., 1983), thereby lending support to our use of this skin model. Examination of the relationship between mast cells, blood vessels and SP fibres revealed triadic arrangements, although no synaptic specializations or direct contacts were observed between these three structures. Interestingly, these triadic associations were present in both the upper and lower dermis, although the number of such profiles was lower in the upper dermis. One previous report described the absence of mast cells in the upper dermis of the skin of the rat innervated by the saphenous nerve (Kowalski M.L. et al., 1990). This might reflect differences in skin regions, although such variations have never been reported.

The association between blood vessels and SP fibres was quantified at the electron microscopic level by measuring the distance between the endothelial cells and the SP-IR terminals. SP-IR terminals were found within a distance of 0.23-5.99 μm from the endothelial cells in 82.7% of arterioles, 90.2% of capillaries and 86.9% of venules. There was no significant difference between these values, suggesting that SP fibres do not preferentially innervate any portion of the skin microvasculature, despite the notion that SP is thought to mainly act on venules (Holzer P., 1998).

Double labelling immunocytochemistry for SP and NK-1r revealed a close association between SP-IR fibres and NK-1r-IR blood vessels, in the upper dermis only. In fact, NK-1r labelling was very faint in the lower dermis, an observation suggesting that SP's effects on the microvasculature occur mainly in the upper dermis. Furthermore, NK-1r immunoreactivity equally occurred on arterioles, capillaries and venules. Visual observation of the material revealed that the intensity of labelling was not as strong on arterioles, although this data was not the result of a quantitative study. Despite this limitation, our data might lend support to the notion that SP acts preferential on venules.

The results of Chapter 2, initially obtained with the aim of characterizing the normal innervation patterns in our animal model, became important in light of SP's involvement in neurogenic inflammation. Various groups have reported that SP is the only tachykinin capable of producing both wheal and flare reactions following intradermal injections in rats and humans, while NKA and NKB produce only the former response (Hagermark O. et al., 1978; Foreman J.C. et al., 1983; Devillier P. et al., 1986). Using potent tachykinin receptor agonists, one study has provided evidence that all three tachykinins can produce neurogenic inflammation through the activation of NK-1r

(Andrews P.V. et al., 1989; Jacques L. et al., 1989).

SP binding sites, as demonstrated by using [^{125}I]-Bolton-Hunter SP, have been observed in rat lung tissue, as well as on capillary endothelial cells in rat and human skin (Carstairs J. and Barnes P., 1986; Hoover D. and Hancock J., 1987; Deguchi M. et al., 1989). These observations concur with our observation of NK-1r on capillaries. More recently, with the production of specific NK-1r antibodies, direct immunocytochemical evidence for these receptor sites on endothelial cells and arteriolar smooth muscle cells has been obtained (Bowden J.J. et al., 1994; Bowden J.J. et al., 1996; Kummer W. et al., 1999; Kido M.A. et al., 1999). Furthermore, SP induced NK-1r internalization has been demonstrated both *in vitro* and *in vivo* in endothelial cells, epithelial cells and spinal, striatal and enteric neurons (Bowden J.J. et al., 1994; Garland A.M. et al., 1994; Mantyh P.W. et al., 1995a; Mantyh P.W. et al., 1995b; Grady E.F. et al., 1996). Importantly for neurogenic inflammation, it appears that this receptor internalization might serve to limit the amount of plasma leakage during inflammation.

Changes in the patterns of skin innervation may lead to aberrant skin reactions to inflammatory mediators. The results presented in Chapter 2 might therefore be relevant to skin inflammatory reactions and blood flow regulation in normal and denervated skin.

6.1.2 **Autonomic innervation**

It is well known that sympathetic fibres innervate the skin. However, its innervation by parasympathetic fibres is still a matter of debate. In Chapter 3, we studied the innervation pattern of the rat lower lip skin by DβH- and VAChT-IR fibres, and their relationships to SP-containing sensory fibres. The use of DβH and VAChT as markers of

sympathetic and parasympathetic fibres, respectively, provides several advantages over many of the studies in the literature. DβH, the last enzyme in the conversion of tyrosine to noradrenaline, has been shown to be a better tool in the identification of both central and peripheral noradrenergic fibres than either catecholamine fluorescence or tyrosine hydroxylase immunoreactivity (Hartman B.K., 1973). Concerning the identification of cholinergic fibres, the use of choline acetyltransferase antibodies in peripheral tissue is usually not sensitive enough to allow for the proper detection of cell bodies and fibre terminals (Weihe E. et al., 1996). Also, acetylcholinesterase cytochemical or immunocytochemical approaches lack specificity. Consequently, experiments using anti-VAChT antibodies, resulted in a better, or more reliable, visualization of cholinergic terminal fields in the PNS, as well as the identification of new components of this cholinergic nervous system (Schäfer M.K.-H. et al., 1998).

With these tools, we have indirectly concluded that SP, DβH and VAChT fibres co-innervate the same blood vessels in the lower dermis. We also analyzed the lower lip skin of monkeys and found that the patterns of innervation by all three fibre-types in primates resembled those in rat. Thus, many of the results presented herein might be further extrapolated to the human species as well.

Importantly, we found that, under normal circumstances, upper dermal blood vessels were solely innervated by SP fibres, an indication that the superficial microcirculation is under sensory control or, alternatively, that sympathetic and parasympathetic fibre transmitters are capable of effects over great distances. Therefore, sensory-autonomic interactions most probably occur only in the lower dermis of the skin. The spatial relationship between these three fibre-types to one another, and with respect

to the blood vessel wall, needs to be resolved by confocal microscopy, which will allow for the simultaneous detection of the three signals.

The presence of sensory, sympathetic and parasympathetic fibres in lip skin has been reported by various groups (Kaji A. et al., 1988; Kaji A. et al., 1991; Kuchiiwa S. et al., 1992; Izumi H. and Karita K., 1992; Izumi H. and Karita K., 1993; Kuchiiwa S. and Kuchiiwa T., 1996), and validates our use of this model. These studies report that, in the head region, sensory fibres originate from the trigeminal ganglion, sympathetic fibres from the SCG and parasympathetic fibres from the otic, sphenopalatine and submandibular ganglia (Kuchiiwa S. and Kuchiiwa T., 1996; Zhu B.-S. et al., 1997). However, in the rat lower lip parasympathetic fibres originate from the otic ganglion exclusively (Kaji A. et al., 1988; Kaji A. et al., 1991). The findings of Kuchiiwa et al. (Kuchiiwa S. and Kuchiiwa T., 1996) in the cat molar organ and lower lip blood vessels, suggest that sensory, sympathetic and parasympathetic fibres all travel together within the mental nerve. However, the results of our studies, contrary to those reported in the cat, revealed the the MN is a purely sensory nerve, since lesioning of the MN did not decrease the density of sympathetic (Chapter 4) and/or parasympathetic (see Fig. 6.2) fibres in the lower lip skin of the rat. This discrepancy emphasizes the species differences underlying innervation patterns. In our hands, sensory and sympathetic lesions have been successfully performed, while parasympathetic fibre lesions were not attempted because of the extreme difficulty of surgically removing the parasympathetic ganglia in the head region.

In our study, quantification of the distance between the various terminals and the blood vessel wall, at the electron microscope level, led to the following conclusions in

rats: 1) DβH (2.3 μm) and VAChT (2.6 μm) terminals were significantly closer to endothelial cells than SP terminals (4.3 μm), 2) only DβH (1.1 μm) terminals were significantly closer to smooth muscle cells (VAChT 1.5 μm; SP 3.0 μm). Although, the distances separating VAChT and SP terminals from the smooth muscle cells were not statistically significantly different, it was clear that the parasympathetic terminals tended to be closer to their targets than the sensory terminals. These results are in accordance with those obtained in previous studies (Matsuyama T. et al., 1985; Luff S.E. et al., 2000). Importantly, our report is the first quantitative study to be performed.

6.1.2.1 *Blood flow regulation of the skin microcirculation*

Our results suggest that, at the level of the lower dermis, skin microcirculation is tightly regulated by sensory and autonomic fibres. However, anatomical findings are relevant only if they can be translated into functional terms. From our study, we can speculate that vasodilatation is controlled by both sensory and parasympathetic fibres, while vasoconstriction is the result of sympathetic activity only. Importantly, these mechanisms appear to operate only in the lower dermis of the rat lower lip skin, since the simultaneous localization of all three fibre-types around blood vessels is restricted to this region. In fact, all three systems have been shown to affect vascular tone (Burnstock G. and Ralevic V., 1994). In the skin of the territory of the rat saphenous nerve, vasoconstriction has been shown to be controlled strictly by sympathetic fibres via the release of noradrenaline and NPY (Pintér E. et al., 1997). Sympathetic fibres, however, have also been shown to have dilatory activity in the skin (Bell C., 1983). It is possible that in the event of a sensory nerve injury these fibres are capable of compensatory

dilatation, but this possibility has not been investigated. In the cat, gingival dilatation appears to be the result of both parasympathetic and sensory fibre activity (Izumi H. and Karita K., 1991).

Studies have shown that sympathetic tone is important in regulating blood flow at the level of the AVA when skin blood flow changes are mediated by thermally-induced reflexes, however, direct warming of the skin causes blood flow changes in the capillaries independently of sympathetic activity (Hales J.R.S. et al., 1978). Our anatomical findings lend support to these findings. Sympathetic fibres are abundant in the lower dermis, a region in which others have reported the presence of AVA (Hales J.R. et al., 1978). As for the capillaries, they are most abundant in the upper dermis (due to the presence of the capillary loops), which is devoid of sympathetic fibres and thus, not surprisingly, blood flow through these vessels could be independent of sympathetic activity. Furthermore, although sympathetic activity does not affect upper dermal blood flow directly, it does so indirectly by controlling the amount of blood that will gain access to the upper dermis through the AVA.

Transmitters released by sensory and autonomic fibres mediate their effects via the activation of specific receptors on the blood vessel wall (Burnstock G. and Ralevic V., 1994; Phillips J.K. et al., 1996; Phillips J.K. et al., 1998). These include neurokinin, muscarinic, α-adrenergic, purinergic (P2X), NPY, CGRP, VIP and serotonin receptors. The activation of sensory and autonomic fibres can lead to opposing signals being transmitted to the blood vessel wall at one time. Therefore, it is likely a combination of environmental factors and the emotional state of an individual which will determine whether vessel dilatation or constriction will prevail, although the exact control

mechanisms are still obscure (Johnson J.M. et al., 1986).

6.2 Autonomic fibre plasticity following peripheral nerve injuries

6.2.1 Sympathetic fibre sprouting

Chapters 2 and 3 of this thesis, although clearly not directly related to the understanding of the peripheral mechanisms underlying neuropathic pain, were essential in the characterization of our animal model. After providing an in depth description of the innervation patterns of the rat lower lip skin, we were able to perform sensory nerve lesions in an attempt to unravel the changes which may occur in the terminal field region of sensory and sympathetic fibres (Chapter 4). This study yielded very important and novel results.

Sensory denervations of the rat lower lip skin were achieved by the bilateral removal of 1-2 mm of mental nerve. One week post-surgery, immunocytochemical analysis of the rat lower lip revealed that sensory fibre denervation was almost complete, but the most fascinating observation was that DβH fibres started to migrate towards the upper dermis, from which they are normally absent. The migration was maximal four weeks post-surgery with the DβH fibres being within 169 ± 91.4 μm from the surface of the skin in lesioned animals, as opposed to 407.1 ± 78.4 μm in sham-operated animals. At the last time point studied (eight weeks post-surgery), the sprouted sympathetic fibres were still present in the upper dermis despite the reinnervation of the rat lower lip by SP fibres, and quantification revealed that the number of DβH fibres was still significantly higher than one week post-surgery. This study was the first to demonstrate that sensory nerve lesions lead to the establishment of novel patterns of innervation of the skin by

sympathetic fibres, a finding that had been previously reported only at the DRG level.

We observed that the migrating DβH fibres ran parallel to the degenerating SP fibres, a result that we interpret as strongly suggesting that the migrating fibres use the tracts of the degenerating fibres to access the upper dermis. Furthermore, it is known that degenerating fibres increase their production of NGF in Schwann cells. This NGF may act as a chemotactic factor guiding the DβH fibres through the degenerating tract and thus, contribute to the anatomical framework favouring the interaction of sensory and sympathetic fibres following peripheral nerve injuries (see discussion of Chapter 4). We hypothesize that this factor is NGF, based on the vast amount of literature supporting the growth of sympathetic fibres towards a source of NGF (Campenot R.B., 1987). However, this could be directly tested by injecting trkA-IgG fusion molecules (McMahon S.B. et al., 1995) into the lower lip prior to, and following, MN surgeries. These molecules have been shown to be able to sequester endogenous NGF. We would expect that if indeed NGF, alone, is responsible for the DβH fibre migration, this migration would be blocked following MN lesions if trkA-IgG fusion molecules had been injected. However, we could also expect a decrease in sympathetic fibre density in the lower dermis and a blockade of the late SP-IR fibre reinnervation, as both SP-IR and sympathetic fibres are NGF-dependent (Rice F.L. et al., 1998).

Our results are in accordance with other studies, which have reported that following complete nerve transections, as occur in the Chung model of neuropathic pain, sympathetic fibre sprouting occurs as early as two days post-surgery (Chung K. et al., 1996). Longer time points, beyond eight weeks post-MN lesion, should be examined because neuropathic pain has been described as a very dynamic syndrome with the pain

symptoms and underlying mechanisms varying over time (Woolf C.J. and Mannion R.J., 1999). Thus, eventually, the sprouted DβH fibres may either completely disappear from the upper dermis or persist indefinitely. Furthermore, the extent of the behavioural changes in these animals should be examined in order to determine if our anatomical changes translate into pain (see below for a description of mechanical and thermal hyperalgesia tests).

A recent study has provided evidence that the extent of sympathetic sprouting in the DRG is not related to sympathetically-dependent neuropathic pain (Kim H.J. et al., 1998), although previous reports had suggested otherwise (Chung K. et al., 1996; Lee D.H. et al., 1997). The focus of past research on the DRG has left more peripheral aspects uninvestigated. It is our opinion that peripheral mechanisms at the terminal field level, such as the ones suggested in Chapters 4 and 5, may, in fact, be more relevant to the pain generation than those which have been reported in the DRG. If the lack of patho-physiological relevance of DRG sympathetic sprouting is confirmed, it is likely that the sensory-sympathetic interactions occur more peripherally as our data suggest. This issue can be addressed by quantifying the extent of sympathetic fibre sprouting in one group of animals, and comparing it to the behavioural symptoms (see below) obtained in another group of animals at various intervals (e.g. every other day), to see if a correlation exists. In support of our hypothesis of a terminal field interaction, initial reports state that, in some patients, sympathetic fibre density in the periphery may contribute to neuropathic pain in the absence of autonomic disturbances (i.e. abnormal skin temperatures, sudomotor disturbances) (Bickel A. et al., 2000). Furthermore, in a different group of animals, thermal and mechanical thresholds could be assessed in the presence of the NK-

1r antagonist CP-96,345 (McLeod A.L. et al., 1999) or guanethidine (Benarroch E.E. et al., 1994), in order to determine the relative contribution of sensory and sympathetic fibres, respectively, to the pain generation.

Our data cannot be directly compared to that obtained with the other two commonly used animal models of neuropathic pain, which involve a partial ligation of the sciatic nerve (Bennett G.J. and Xie Y.-K., 1988; Seltzer Z. et al., 1990). For comparison purposes, we should perform partial lesions of the mental nerves. Preliminary results from our laboratory using a modified version of the Kruger model of chronic nerve constriction, consisting of applying a single polyethylene cuff to the mental nerve, demonstrate that, in fact, this type of lesion does lead to abnormal pain sensations in the rat lip skin (Fig. 6.1), as assessed by von Frey hair testing (Chaplan S.R. et al., 1994). This provides evidence that our model can be used in studies of neuropathic pain. Signs of pain-related behaviours were excessive licking of the lips, biting or jaw jerking. In more severe, cases the animals would hold the filament with their front paws and bite on it. The choice of the modified Kruger model better suits the rat lower lip, because the portion of nerve from its exit of the mental foramen to its entry in the lip skin is quite short and it would not be possible to place four polyethylene cuffs on that stretch of nerve. Alternatively, a modified version of the Bennett model could also be used. Thermal hyperalgesia should also be tested in these animals using an adaptation of the projector bulb system which is already used for the tail withdrawal reflex (Isabel G. et al., 1981; McLeod A.L. et al., 1999; McLeod A.L. et al., 2000). In addition, immunocytochemical studies need to be performed at various time points, in order to establish a time course of DβH fibre migration and SP fibre degeneration and

regeneration, if any.

A recent study reported that, following SNL, an α_2-adrenoceptor antagonist produced mechanical and cold allodynia in animals which had not developed neuropathic symptoms, but did not exacerbate these symptoms in the neuropathic animals (Xu M. et al., 1999). According to the authors, the endogenous noradrenergic tone is responsible for blocking the neuropathic symptoms in the non-neuropathic animals. The meaning of this study, that contradicts others, remains to be clarified. However, it is possible to speculate that inter-individual variability in the endogenous noradrenergic system may predispose to the development of neuropathic symptoms following peripheral nerve lesions. In agreement with this possibility, strain and gender variability have been reported in the development of neuropathic pain (Lee D.H. et al., 1997; Yoon Y.W. et al., 1999; DeLeo J.A. and Rutkowski M.D., 2000). The issue of the individual variability of the noradrenergic system could be experimentally addressed. If in fact, the development of neuropathic pain symptoms is dependent upon the extent of sympathetic innervation in the rat lower lip skin, we would expect that the animals with the lowest thresholds to mechanical stimulation by Von Frey hair testing would display the greatest extent of sympathetic fibre sprouting. As the sympathetic sprouting is greatest four weeks post-MN lesions, animals should be tested every other day during the fourth week post-lesion. The animals would be perfused on the last day of testing and their lower lips processed for immunocytochemistry using a mouse anti-DβH antibody, as described in Chapter 4. Averages of the behavioural thresholds for each animal would be obtained and compared to the respective DβH fibre migration quantitative data. A correlation showing decreased thresholds with increased DβH fibre migration would confirm the sympathetic

dependency of neuropathic pain symptoms.

6.2.2 **Parasympathetic fibre sprouting**

As the skin innervation by parasympathetic fibres was still not well established previous to our investigation, it is not surprising that the changes these fibres undergo following peripheral nerve injuries have not been studied. We have shown that the rat lower lip skin innervation by parasympathetic fibres is as abundant as its innervation by sympathetic fibres (see Chapter 3). Therefore, MN lesions should be performed and the parasympathetic fibre changes, if any, should be determined. Preliminary results obtained in our laboratory show that, surprisingly, VAChT fibres migrate into the upper dermis, a territory from which they are normally absent, within one week post-surgery, and are still present in the upper dermis at the eight-week time point (Fig. 6.2) (Ruocco I. et al., 2001). A complete quantitative study must be performed in order to determine the significance and the extent of these results. Furthermore, behavioural studies (thermal and mechanical hyperalgesia testing) should be performed in order to determine if parasympathetic fibres play a role in the hyperalgesia. As sensory fibres possess both nicotinic and muscarinic receptors (Coggeshall R.E. and Carlton S.M., 1997), the release of ACh in the close proximity of upper dermal sensory fibres, once sensory reinnervation of the rat lower lip is achieved, may cause sensory fibre activation and thus, contribute to the nociceptive behaviours. Behavioural studies should be performed in the presence of the NK-1r antagonist and guanethidine, in order to determine the contribution of the parasympathetic fibre component. Whether these results can be extrapolated to other skin regions requires a complete anatomical characterization of the parasympathetic

innervation patterns of other skin regions such as the scalp, abdomen, hindpaws, and back, since it is commonly thought that parasympathetic innervation in the skin is scarce or absent, despite some evidence to the contrary as that presented in this thesis. Even if our results prove to be specific to the head and neck region, they will still contribute significantly to our knowledge of the possible mechanisms underlying disorders such as Postsympathectomy parotid pain and Raeder's paratrigeminal syndrome (Schon F., 1985). These represent conditions in which there is considerable suffering and which are difficult to treat.

6.3 Sensory fibre regeneration and recovery of function following peripheral nerve injury

Following peripheral nerve injuries, sensory reinnervation of the denervated skin can be restored by means of regeneration of damaged axons, and/or collateral sprouting of spared axons [for review see (Diamond J. and Foerster A., 1992)]. Regardless of the mechanism underlying the reinnervation, the most important parameter is the return to normal function. Crushing of the sciatic nerve, using forceps, produced a rapid degeneration of protein gene product (PGP) 9.5, CGRP, SP and VIP fibres in the mouse footpad skin (Navarro X. et al., 1997; Verdú E. and Navarro X., 1997). In these animals, sweat gland function returned to 88% of control 16 days post-crush and nociceptive responses to 100% of control 17 days post-crush (Verdú E. and Navarro X., 1997). However, the fibre density in the mouse footpad skin did not return to normal levels, although small fibre function was completely restored. This is an indication that the density of reinnervation is not proportional to functional recovery, and that as long as some level of reinnervation is achieved there will be a considerable, or complete, return

of normal functions. In our system, SP fibre reinnervation of the rat lower lip occurred by the fourth week post-MN lesions (Chapter 4). This is in agreement with studies that have shown that SP fibre reinnervation of the mouse footpad skin occurred 35 days post-sciatic nerve sectioning (Navarro X. et al., 1997). The functional state of the sprouted SP fibres in the rat lower lip skin remains unknown, but could be determined by comparing von Frey hair testing results in the presence of the NK-1r antagonist CP-96,345 or its inactive enantiomer CP-96-344, to the reinnervation time course of the SP fibres. If the sprouted SP fibres are functional, as expected, we should observe a decrease in nociceptive thresholds as reinnervation progressed and a reversal of this decrease in the presence of NK-1r antagonists.

As discussed in Chapter 4, in our model, the sympathetic fibres invading the upper dermis might not use all of the available NGF. As the collateral sprouting of cutaneous nociceptors is dependent on NGF, while their regeneration is not (Diamond J. et al., 1987), it is most likely that, in our model, the reinnervation of the rat lower lip is the result of NGF mediated collateral sprouting, since the MN was completely severed and thus, regeneration of the fibres could not occur.

Studies in the rat lower lip have revealed that growth-associated protein 43 (GAP-43) is expressed in the mature trigeminal system (Verzé L. et al., 1999). GAP-43, which is associated with axonal elongation and synaptic plasticity (Benowitz L.I. and Routtemberg A., 1997; Oestreicher A.B. et al., 1997), may play a role in remodelling, regeneration, and sprouting in the lower lip skin. Changes in GAP-43 immunoreactivity should be assessed following peripheral nerve lesions. Fluctuations in GAP-43 levels may reflect the changes in the innervation status of peripheral tissues, such as the lower

lip and footpad skin, following peripheral nerve injuries.

6.4 Sensory fibre plasticity following peripheral nerve injuries

The interaction between sensory and sympathetic fibres following peripheral nerve lesions has always been described in terms of sympathetic fibre sprouting onto the sensory system. However the inverse situation – sensory fibre sprouting onto sympathetic fibres - has not received much attention. In Chapter 5, we addressed this issue by proceeding to the bilateral removal of the SCG and observing the effects on sensory and sympathetic fibre terminal fields. The effects were much less dramatic than those of sensory denervation, and were most significant in the lower dermis. There, DβH fibre degeneration was complete by one week post-surgery and reinnervation of this territory by these fibres never occurred. In the lower dermis, a significant increase in SP fibre immunostaining intensity one and two weeks post-surgery, and in SP fibre length one, two and three weeks post-surgery were observed. In the upper dermis, significant changes in SP fibre length and labelling intensity were observed one and two weeks post-surgery for the former, and only at the two weeks time point for the latter. As for NK-1r in the upper dermis, based on visual observation only, we found the labelling intensity to be decreased one week post-surgery and still low by the second week, although by week three the levels were identical to those of controls. As mentioned in Chapter 5, we were unable to quantify the levels of receptor expression due to the relatively low levels of immunoreactivity. Another problem with NK-1r labelling came from the ABC protocol used, which produced unspecific labelling at the level of the sebaceous glands. As the sebaceous gland staining was much stronger than that of the NK-1r, the image analysis

system would not allow the quantification of the NK-1r, which it considered as being the unspecific labelling. Attempts were made to only select the NK-1r-IR blood vessels, but this did not produce very reliable measurements, as most vessels were very close to the sebaceous glands and it was impossible to accurately select the blood vessels only. We also tried to preabsorb the secondary antibody, as we did for DβH fibre labelling (see materials and methods in Chapter 3), however, we were unable to achieve proper results without compromising the labelling intensity of NK-1r-positive structures. We do not know if this transient upregulation of SP fibres in the rat lower lip translates into a small window of increased or aberrant pain sensations. To address this the animals could be tested for nociceptive response thresholds following the application of mechanical and/or thermal stimuli.

Parasympathetic fibre plasticity in the rat lower lip skin should also be investigated following the bilateral removal of the SCG, to determine if collateral sprouting of parasympathetic fibres occurs in the lower dermis of the rat lower lip skin in the absence of sympathetic fibres. Research has shown that sympathetic denervation can block the decrease in choline acetyltransferase enzymatic activity observed following the parasympathetic denervation of the submaxillary gland in rats (Ekström J., 1981). This suggests that the parasympathetic fibres are responding, possibly in a compensatory manner, to the loss of sympathetic fibres. The above study however, does not provide any information as to the mechanisms underlying the increased enzyme activity. An increase in enzymatic activity may originate from an increase in activity within the existing fibres or as a result of extra fibres derived from the sprouted fibres.

6.5 Blood flow changes and neuropathic pain

Neuropathic pain sufferers often experience abnormal skin temperature in the symptomatic part of the body (most often the extremities). Initially, these patients experience increases in skin temperature, which over time change to decreases in skin temperature [for review see (Schwartzman R.J., 1992)]. The initial loss of sympathetic fibres, caused by the peripheral nerve injury, results in the loss of the sympathetic constrictor tone and thus, the unopposed vasodilatation causes a rise in skin temperature. However, over time, the denervation leads to catecholamine supersensitivity of the vascular smooth muscle cells and, thus, the ensuing chronic vasoconstriction leads to decreases in skin temperatures (Kurvers H.A.J.M. et al., 1997). The idea that the changes in skin temperature is a reflection of the sympathetic vasomotor activity has been challenged. Studies have shown that vasomotor changes may occur in the absence of sympathetic fibres (Wakisaka S. et al., 1991). In this study it was shown that following a CCI of the sciatic nerve, some animals displayed abnormally cold paws in the absence of noradrenergic fibres, whereas other animals had abnormally high paw temperatures with normal levels of noradrenergic fibres. Despite these findings, the majority of studies suggest that changes in blood flow, and thus in skin temperature, are the direct result of changes in sympathetic fibres activity, or proportion, in the territory of the peripheral nerve lesion.

We have not addressed the possible changes in skin blood flow and temperature brought about by our MN or SCG lesions. We could study changes in blood flow and skin temperature by laser Doppler flowmetry (Pintér E. et al., 1997) and by infrared thermography, respectively (Bennett G.J. and Ochoa J.L., 1991). More relevant to our

system, we could collect venous blood from the anterior facial veins in lesioned animals and compare the output to that of naïve animals, a technique which has been used to study antidromic vasodilatation (Couture R. and Cuello A.C., 1984).

Based on the above information, we would expect the venous output of the MN lesioned animals to be significantly less than that of the naïve animals in the initial time points. Once sensory reinnervation of the rat lower lip occurs, one of two possible scenarios may come into play. The first one is that blood flow might return to normal, the sensory fibres being able to oppose the excessive sympathetic constrictor tone. The second is that blood flow in the rat lower lip might increase. Sympathetic fibre activation may lead to the release of sensory neuropeptides via the stimulation of α_2-adrenoreceptors on sensory fibres, which would result in vasodilatation that could not be fully opposed by the sympathetic fibres. In fact, under normal conditions, peptidergic afferents have been postulated to counterbalance the spontaneous release of adrenergic mediators from sympathetic afferents (Sann H. et al., 1988), and it has been suggested that this balance is disrupted, at least in patients suffering from CRPS I (Schwartzman R.J. and McLellan T.L., 1987). Should our assumptions prove to be true, our animal model would produce, contrary to what has been published in other commonly used animal models, an initial cooling followed by warming or a return to normal temperature of the skin.

Following the removal of the SCG we would expect an increase in blood flow at all post-surgical time points, since the loss of the sympathetic fibres would result in unopposed vasodilatation. Furthermore, sympathetic fibre regeneration was not observed in the rat lower lip skin.

6.6 Non-peptidergic sensory fibres and neuropathic pain

Of the seven cloned P2X receptors, the P2X3 subtype appears to be predominantly expressed by small diameter non-peptidergic sensory neurons, although low levels have also been detected in the superior cervical and coeliac sympathetic ganglia (Xiang Z. et al., 1998). Plastic changes in this receptor level, although transient, have been observed following inferior alveolar nerve injury, therefore in the same territory we have investigated (Eriksson J. et al., 1998), as well as following a CCI injury to the sciatic nerve (Novakovic S.D. et al., 1999). More recently, experiments performed in P2X3-deficient mice have revealed that these animals display increased thermal hyperalgesia and are unable of coding the intensity of non-noxious heat stimuli, as evidenced by the fact that neurons did not fire until the noxious heat stimulus range was reached (Souslova V. et al., 2000). In the P2X3-deficient mice, decreased pain responses to the injection of ATP and formalin, decreased bladder contraction and decreased voiding frequency, but normal bladder pressures were also reported (Cockayne D.A. et al., 2000).

Unfortunately, the distribution of the non-peptidergic small diameter sensory fibres has been studied mostly by means of the binding of the lectin GSA-IB4 in conditions that enhanced the binding, i.e. in the presence of divalent cations, and this results in the labelling of a variable number of peptidergic fibres as well (Streit W.J. et al., 1986; Fundin B.T. et al., 1997; Alvarez F.J. and Fyffe R.E.W., 2000). Furthermore, the only detailed analysis in rat was performed in the skin of the mystacial pad (Fundin B.T. et al., 1997), which is essentially a sensory organ and not standard skin. However, there is indirect evidence suggesting that the non-peptidergic small diameter afferents are

abundant, outnumbering the peptidergic. This evidence was obtained by comparing the immunostaining of small diameter fibres obtained with an antibody against an overall marker of axons, PGP 9.5, to the labelling obtained with antibodies against CGRP (Rice F.L. and Rasmusson D.D., 2000). Based on this comparative study, non-peptidergic fibres seem to abundantly penetrate the epidermis and are seen around hair follicles, but were seldom observed in the wall of blood vessels (Maricq H.R., 1972; Couture R. et al., 1993).

Considering the abundance of non-peptidergic fibres in the skin and their possible involvement in inflammatory or neuropathic conditions, the experiments performed for the peptide-containing sensory fibres need to be expanded to the non-peptidergic fibre population. Since, in this thesis, the conditions for the generation of optimal results have been worked out, it is just a question of time before a comparative study between these two fibre populations and their respective contribution to neuropathic pain can be completed. These studies should include double labelling for SP and GSA-IB4 in order to determine the differential innervation pattern of these two fibre types. The relation of DβH (sympathetic) and VAChT (parasympathetic) fibres to the non-peptidergic sensory fibres should also be determined. As the relative role of peptidergic and non-peptidergic fibres in skin nociception is still unclear at present, we will take advantage of the unique characteristics of the skin of the lower lip to address this issue. For this, some rats will receive bilateral injections, directly into the mental nerves, of the toxin saporin conjugated to the lectin GSA-IB4. This treatment leads to the elimination of the GSA-IB4-binding fibres through cellular death and is highly specific (Tarpley J.W. et al., 2000). After 2 weeks, the animals will be tested for thresholds of mechanical and thermal

noxious stimuli. Other animals will receive, instead, an injection of the non-peptide NK-1 receptor antagonist CP-96,345 prior to behavioural testing. These investigations should provide clues on the relative participation in skin nociceptive mechanisms of the two different classes of small diameter sensory fibres. Once this is established, complete or partial MN lesions should be performed, as mentioned above, and the time course of the reinnervation of the rat lower lip by non-peptidergic sensory fibres should be determined and compared to that of the peptidergic sensory fibres. Based on the published data, we expect that the non-peptidergic fibres may be relevant for the establishment of thermal hyperalgesia, but that these fibres will not contribute significantly to the mechanical hyperalgesia (Cockayne D.A. et al., 2000). In fact VR1 receptors have been detected on peptidergic and non-peptidergic sensory fibres, suggesting that both populations include heat nociceptors (Tominaga M. et al., 1998).

6.7 Implications of terminal field changes for neuropathic pain

In Chapters 4 to 6 we provide, for the first time, evidence that, following peripheral nerve lesions, changes occur in the peripheral terminal fields of sensory, sympathetic and parasympathetic fibres. The sprouting of these three fibre-types may be involved in the reported decrease in nociceptive thresholds in animal models of neuropathic pain (Bennett G.J. and Xie Y.-K., 1988; Seltzer Z. et al., 1990; Kim S.H. and Chung J.M., 1992). Furthermore, we believe that the considerable expansion of the terminal fields in the periphery, due to extensive sprouting of fibres into a new territory (the upper dermis in our case), allows for a greater receptive area, whereby external inputs will be received and possibly misinterpreted. It is possible that, in the upper dermis

of the rat lower lip skin, novel interactions between sensory, sympathetic and parasympathetic fibres develop. For instance, sympathetic excitation of sensory fibres has been reported following peripheral nerve lesions, and appears to result from the upregulation of a specific subset of adrenergic receptors on sensory fibres (Sato J. and Perl E.R., 1991; Shi T.-J.S. et al., 2000). Receptor upregulation might also occur on sympathetic and parasympathetic fibres. Whether such mechanisms occur in our model remains to be tested. Importantly, the dynamic aspects of the changes reported in this thesis should be investigated, since different systems may operate at various time points following peripheral nerve lesions. These results will provide valuable information concerning the proper timing for treatment following a peripheral nerve lesion. A better understanding of the time frame during which innervation patterns are altered will allow for proper targeting of the mechanisms involved in the pain generation.

FIGURE 6.1: ***Graphic representing tactile hyperalgesia as assessed by von Frey hair testing.*** Polyethylene cuffs, 1-2 mm long, were bilaterally placed around the mental nerves. The animals were first tested on day 3 post-surgery and subsequently every third day. Unpaired Student's t-tests were used to determine the significance of these results. n=7 ** $p<0.01$, *$p<0.05$

Von Frey hair testing in cuffed and control animals

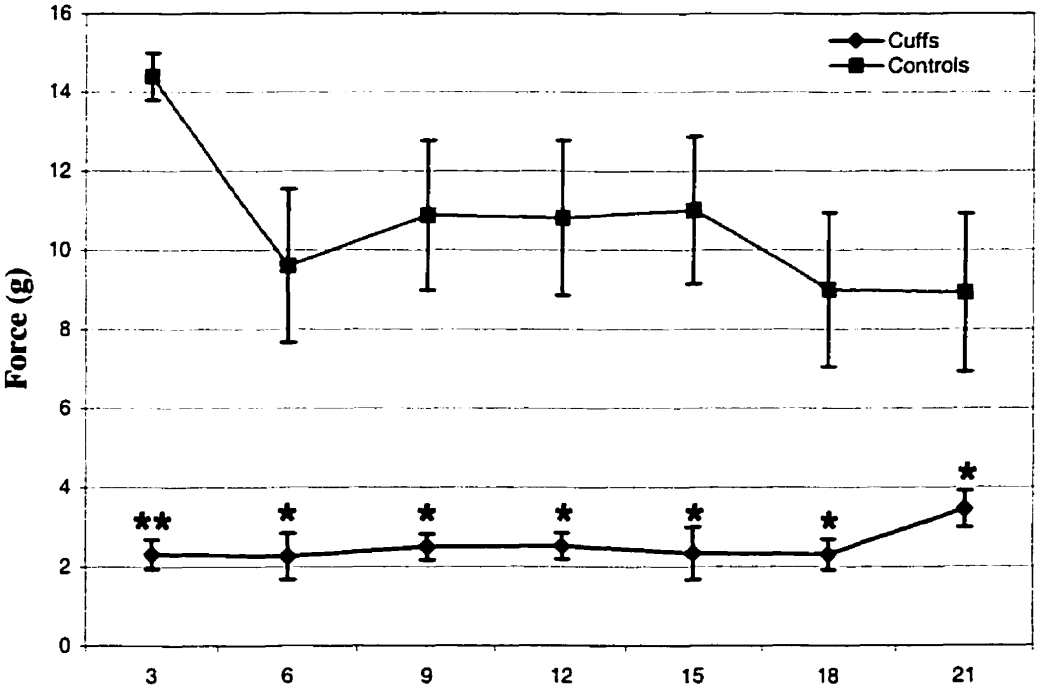

FIGURE 6.2: ***Parasympathetic fibre migration into the upper dermis of the rat lower lip skin, eight weeks following mental nerve lesions.*** Following MN lesions, VAChT-IR fibres (green arrows) migrate into the upper dermis of the rat lower lip skin, a territory from which they are normally absent. These sprouted fibres are still present in the upper dermis eight weeks post-lesions. SP-IR fibres (black arrows) reinnervate the upper dermis despite the presence of migrated VAChT-IR fibres in this territory. Note that these fibres appear to be running parallel and in close proximity to one another. Scale bar = 50 μm.

epidermis

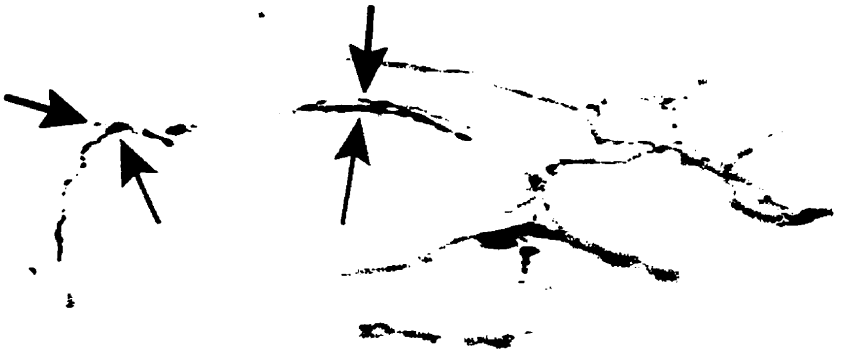

upper dermis

CONCLUSIONS

The observations and results presented in this thesis lend support to the following conclusions:

1. Terminals of SP-IR fibres are observed throughout the rat lower lip skin in association with blood vessels, mast cells, hair follicles and sebaceous glands.
2. SP-IR fibres equally innervate arterioles, capillaries and venules, thus indicating that they do not preferentially innervate any vessel types of the skin microvasculature.
3. NK-1r are located on the walls of arterioles, capillaries and venules of the skin microvasculature, suggesting that SP is capable of acting at all levels of the microcirculation. However, most receptors are located in the upper dermis, suggesting that the lower dermis is less affected by SP.
4. Blood vessels in the lower dermis are, most likely, simultaneously innervated by SP-, DβH- and VAChT-IR fibres.
5. DβH- and VAChT-IR fibres lie closer to their targets than SP-IR fibres.
6. Mental nerve lesions lead to the complete degeneration of SP-IR fibres, and to the sprouting of DβH-IR fibres into the upper dermis, where they branch extensively over time.
7. SP-IR fibre reinnervation of the rat lower lip does not cause the regression of the sprouted upper dermal DβH-IR fibres. Instead, SP- and DβH-IR fibres run parallel and in close proximity to one another in this territory.

8. Sympathectomies only lead to the transient sprouting and downregulation of SP-IR fibres and NK-1r, respectively. SP-IR fibre sprouting was most abundant in the lower dermis.
9. Preliminary data indicate that parasympathetic cholinergic fibres sprout into the upper dermis following mental nerve lesions. Following sensory reinnervation, sensory and parasympathetic fibres are observed in close proximity in the upper dermis.

ORIGINAL CONTRIBUTIONS

1. SP immunoreactivity was abundant in the rat lower lip skin. It was associated with blood vessels, mast cells, hair follicles and sebaceous glands. Mast cells were observed both in the upper and lower dermis, contrary to previous studies suggesting that they are only located deep within the skin. SP fibres, mast cells and blood vessels were observed in triadic arrangements in the upper and lower dermis of the rat lower lip skin, supporting their role in neurogenic inflammation.

2. Quantification at the ultrastructural level revealed that SP terminals did not preferentially innervate venules. In fact, SP terminals were encountered most frequently close to capillaries, less frequently close to venules and least frequently close to arterioles, however these differences were not statistically significant. Contacts between SP terminals and blood vessel smooth muscle or endothelial cells were never observed.

3. NK-1r immunoreactivity was most prominent around upper dermal blood vessels. These receptors were located on endothelial cells, smooth muscle cells and pericytes. SP fibres were seen to wrap around NK-1r positive blood vessels. Arterioles, capillaries and venules were shown to possess NK-1r on their walls.

4. For the first time, blood vessels in the lower dermis were shown to be innervated by SP sensory-sympathetic, SP sensory-parasympathetic and sympathetic-

parasympathetic fibre combinations, suggesting that all three fibre-systems are simultaneously present around lower dermal blood vessels. Blood vessels in the upper dermis were only innervated by SP fibres. The ultrastructural quantification of these terminals within the same tissue revealed that sympathetic and parasympathetic terminals lie closer to their targets than the SP-sensory terminals. Synaptic specializations between these terminals and blood vessel walls were never observed.

5. Mental nerve lesions caused the complete degeneration of SP fibres in the rat lower lip skin, with a progressive, although not complete, regeneration over time. Following the lesion DβH fibres gradually migrated into the upper dermis, where fibre branching was observed. DβH fibres were maintained in the upper dermis despite SP fibre reinnervation of the territory. In fact, the aberrant innervation of the upper dermis consisted of SP and DβH fibres running in close proximity and parallel to one another. This provides the first anatomical evidence that sensory-sympathetic interactions may occur at the level of the terminal fields in the periphery, following peripheral nerve lesions.

6. Superior cervical ganglia removal led to transient SP fibre changes, consisting of increased labelling intensity and fibre density. These effects were greater in the lower dermis. Sympathetic fibres disappeared completely from the rat lower lip skin and reinnervation did not occur. A transient NK-1r downregulation was also observed.

7. Following mental nerve lesions, VAChT fibres gradually migrated into the upper dermis, where fibre branching was observed. VAChT fibres were maintained in the upper dermis despite SP fibre reinnervation of the territory. In fact, the aberrant innervation of the upper dermis consisted of SP and VAChT fibres running in close proximity and parallel to one another. This provides the first anatomical evidence that sensory-parasympathetic interactions may occur at the level of the terminal fields in the periphery, following peripheral nerve lesions.

REFERENCES

Anonymous (1988) Cell and Tissue Biology: A Textbook of Histology. Baltimore: Urban & Schwarzenberg Inc.

Anonymous (1992) Pharmacology of the Skin. Boca Raton: CRC Press Inc.

Abbadie C. and Basbaum A.I. (1998) The contribution of capsaicin-sensitive afferents to the dorsal root ganglion sprouting of sympathetic axons after peripheral nerve injury in the rat. Neurosci Lett *253* :143-146.

Abbadie C., Brown J.L., Mantyh P.W., and Basbaum A.I. (1996) Spinal cord substance P receptor immunoreactivity increases in both inflammatory and nerve injury models of persistent pain. Neuroscience *70*:201-209.

Abboud F.M. and Weinberg S.M. (1965) Post-stimulation vasodilatation in the perfused foreleg of dog. Federation Proc *24*:270-277.

Aberdeen J., Corr L., Milner P., Lincoln J., and Burnstock G. (1990) Marked increases in calcitonin gene-related peptide-containing nerves in the developing rat following long-term sympathectomy with guanethidine. Neuroscience *35*:175-184.

Aberdeen J., Milner P., Lincoln J., and Burnstock G. (1992) Guanethidine sympathectomy of mature rats leads to increases in calcitonin gene-related peptide and vasoactive intestinal polypeptide-containing nerves. Neuroscience *47*:453-461.

Aberdeen J., Moffitt D., and Burnstock G. (1991) Increases in NPY in non-sympathetic nerve fibres supplying rat mesenteric vessels after immunosympathectomy. Regul Pep *34*:43-54.

Acheson A., Barker P.A., Alderson R.F., Miller F.D., and Murphy R.A. (1991) Detection of brain derived neurotrophic factor-like activity in fibroblasts and Schwann cells : Inhibition by antibodies to NGF. Neuron *7*:265-275.

Ahluwalia A. and Vallance P. (1996) Interaction between sympathetic and sensory nerves in rat small arteries: involvement of nitric oxide. Am J Physiol *271*:H969-H976.

Allen T.D. and Potten C.S. (1975) Desmosomal form, fate and function in mammalian epidermis. J Ultrastruct Res *51*:94-105.

Alvarez F.J. and Fyffe R.E.W. (2000) Nociceptors for the 21st century. Current Rev Pain *4*:451-458.

Alvarez F.J., Rodrigo J., Jessell T.M., Dodd J., and Priestley J.V. (1989a) Morphology and distribution of primary afferent fibres expressing alpha-galactose extended oligosaccharides in the spinal cord and brainstem of the rat. Light microscopy. J Neurocytol *18*:611-629.

Alvarez F.J., Rodrigo J., Jessell T.M., Dodd J., and Priestley J.V. (1989b) Ultrastructure of primary afferent fibres and terminals expressing alpha-galactose extended oligosaccharides in the spinal cord and brainstem of the rat. J Neurocytol *18*:631-645.

Amara S.G., Jonas V., Rosenfeld M.G., Ong E.S., and Evans R.M. (1982) Alternative RNA processing in calcitonin gene expression generates mRNAs encoding different polypeptide products. Nature *298*:240-244.

Anand P. (1996) Neurotrophins and peripheral neuropathy. Philos Trans R Soc Lond B: Biol Sci *351*:449-454.

Anand P., Parrett A., Chadwick L., and Hamlyn P. (1997) Nerve growth factor concentrations in human cerebral blood vessels [letter]. J Neurol Neurosurg Psychiatry *62*:199-200.

Andrews P.V., Helme R.D., and Thomas K.L. (1989) NK-1 receptor mediation of neurogenic plasma extravasation in rat skin. Br J Pharmacol *97*:1232-1238.

Arbuckle J.B. and Docherty R.J. (1995) Expression of tetrodotoxin-resistant sodium channels in capsaicin-sensitive dorsal root ganglion neurons of adult rats. Neurosci Lett *185*:70-73.

Attal N., Neil A., Chen L., and Guilbaud G. (1990) Effects of adrenergic depletion with guanethidine before and after the induction of a peripheral neuropathy on subsequent mechanical-, heat- and cold sensitivities in rats. Pain *Suppl 5*:S464.

Baluk P. (1997) Neurogenic inflammation in skin and airways. J Invest Dermatol *2*:76-81.

Baraniuk J.N., Kowalski M.L., and Kaliner M.A. (1990) Relationships between permeable vessels, nerves, and mast cells in rat cutaneous neurogenic inflammation. J Appl Physiol *68*:2305-2311.

Barasi S. and Lynn B. (1986) Effect of sympathetic stimulation on mechano-receptive and nociceptive afferent units from the rabbit pinna. Brain Res *378*:21-27.

Barnes P.J., Belvisi M.G., and Rogers D.F. (1991) Modulation of neurogenic inflammation: novel approaches to inflammatory diseases. Trends Pharmacol Sci *11*:185-189.

Basbaum A.I. (1999) Distinct neurochemical features of acute and persistent pain. Proc Natl Acad Sci USA *96*:7739-7743.

Basbaum A.I. and Woolf C.J. (1998) Pain. Current Bio *9*:R429-R431.

Battaglia G. and Rustioni A. (1988) Coexistence of glutamate and substance P in dorsal root ganglion neurons of the rat and monkey. J Comp Neurol *277*:302-312.

Beitz A.J. (1990) Relationship of glutamate and aspartate to the periaqueductal gray-raphe magnus projection: Analysis using immunocytochemistry and microdialysis. J Histochem Cytochem *38*:1755-1765.

Belenky M. and Devor M. (1997) Association of postganglionic sympathetic neurons with primary afferents in sympathetic-sensory co-cultures. J Neurocytol *26*:715-731.

Bell C. (1983) Vasodilator neurons supplying skin and skeletal muscle of the limbs. J Autonom Nerv Sys *7*:257-262.

Benarroch E.E., Zollman P.J., Schmelzer J.D., Nelson D.K., and Low P.A. (1992) Guanethidine sympathectomy increases substance P concentration in the superior sympathetic ganglion of adult rats. Brain Res *584*:305-308.

Benarroch E.E., Zollman P.J., Smithson I.L., Schmelzer J.D., and Low P.A. (1994) Different reinnervation patterns in the celiac/mesenteric and superior cervical ganglia following guanethidine sympathectomy in adult rats. Brain Res *644*:322-326.

Bennett D.L.H., Micheal, G.J., Ramachandran N., Munson J.B., Averill S., Yan Q., McMahon S.B., and Priestley J.V. (1998) A distinct subgroup of small DRG cells express GDNF receptor components and GDNF is protective for these neurons after nerve injury. J Neurosci *18*:3059-3072.

Bennett G.J. (1998) Neuropathic pain: new insights, new interventions. Hosp Prac *33*:95-110.

Bennett G.J. and Ochoa J.L. (1991) Thermographic observations on rats with experimental neuropathic pain. Pain *45*:61-67.

Bennett G.J. and Xie Y.-K. (1988) A peripheral mononeuropathy in rat that produces disorders of pain sensation like those seen in man. Pain *33*:87-107.

Bennett H.S., Luft J.H., and Hampton J.C. (1959) Morphological classification of vertebrate capillaries. Am J Physiol *196*:381-390.

Benowitz L.I. and Routtemberg A. (1997) GAP-43: an intrinsic determinant of neural development and plasticity. Trends Neurosci *20*:84-91.

Bevan S. (1999) Nociceptive peripheral neurons: cellular properties. In Wall P.D. and Melzack R. (eds): Textbook of Pain. London: Churchill Livingstone, pp. 85-103.

Bickel A., Butz M., Schmelz M., Handwerker H.O., and Neundörfer B. (2000) Density of sympathetic axons in sural nerve biopsies of neuropathy patients is related to painfulness. Pain *84*:413-419.

Billingham R.E. and Silvers W.K. (1960) The melanocytes of mammals. Qt Rev Biol *35*:1-13.

Birder L.A. and Perl E.R. (1999) Expression of α_2-adrenergic receptors in rat primary afferent neurones after peripheral nerve injury or inflammation. J Physiol (London) *515*:533-542.

Birrell G.J., McQueen D.S., Iggo A., Coleman R.A., and Grubb B.D. (1991) PGI2-induced activation and sensitization of articular mechanonociceptors. Neurosci Lett *124*:5-8.

Bloom S.R. and Polak J.M. (1983) Regulatory peptides and the skin. Clin Exp Dermatol *8*:3-18.

Bossut D.F. and Perl E.R. (1995) Effects of peripheral nerve injury on sympathetic excitation of A-delta mechanical nociceptors. J Neurophysiol *73*:1721-1723.

Bowden J.J., Baluk P., Lefevre P, Vigna S.R., and McDonald D.M. (1996) Substance P (NK_1) receptor immunoreactivity on endothelial cells of the rat tracheal mucosa. Am J Physiol *270*:L404-L414.

Bowden J.J., Garland A.M., Baluk P., Lefevre P, Grady E.F., Vigna S.R., Bunnett N.W., and McDonald D.M. (1994) Direct observation of substance P-induced internalization of neurokinin 1 (NK_1) receptors at sites of inflammation. Proc Natl Acad Sci USA *91*:8964-8968.

Bowsher D. (1991) Neurogenic pain syndromes and their management. Br Med Bull *47*:644-666.

Bradbury E.J., Burnstock G., and McMahon S.B. (1998) The expression of $P2X_3$ purinoreceptors in sensory neurons: Effects of axotomy and glial-derived neurotrophic factor. Mol Cell Neurosci *12*:256-268.

Brain S.D. (1996) Sensory neuropeptides in the skin. In Geppetti P. and Holzer P. (eds): Neurogenic inflammation. Boca Raton: CRC Press, pp. 229-244.

Brain S.D. , and Edwardson J.A. (1987) Neuropeptides and skin. In Greaves M.W. and Shuster S. (eds): Pharmacology of the Skin, Vol. 1, Handbook of Experimental Pharmacology. Berlin: Springer-Verlag, pp. 89-113

Brain S.D. and Williams T.J. (1988) Substance P regulates the vasodilator activity of calcitonin gene-related peptide. Nature *335*:73-75.

Braverman I.M. and Yen A. (1977) Ultrastructure of the human dermal microcirculation. II. The capillary loops of the dermal papillae. J Invest Dermatol *68*:44-52.

Briggaman R.A. and Wheeler C.E.Jr. (1975) The epidermal-dermal junction. J Invest Dermatol *65*:71-84.

Brock J.A., McLachlan E.M., and Belmonte C. (1998) Tetrodotoxin-resistant impulses in single nociceptor nerve terminals in guinea-pig cornea. J Physiol (London) *512*:211-217.

Brown G.L. and Gillespie J.S. (1957) The output of sympathetic transmitter from the spleen of the cat. J Physiol (London) *138*:81-102.

Bueb J.L., Mousli M., Bronner C., Rouot B., and Landry Y. (1990) Activation of G_i-like proteins, a receptor-independent effect of kinins in mast cells. Mol Pharmacol *38*:816-822.

Burchiel K.J. (1984) Spontaneous impulse generation in normal and denervated dorsal root ganglia: sensitivity to alpha-adrenergic stimulation and hypoxia. Exp Neurol *85*:257-272.

Burnstock G. (2000) P2X receptors in sensory neurons. Br J Anaesth *84*:476-488.

Burnstock G. and Ralevic V. (1994) New insights into the local regulation of blood flow by perivascular nerves and endothlium. Br J Plast Surg *47*:527-543.

Caffrey J.M., Eng D.L., Black J.A., Waxman S.G., and Kocsis J.D. (1992) Three types of sodium channels in adult rat dorsal root ganglion neurons. Brain Res *592*:283-297.

Campenot R.B. (1987) Local control of neurite sprouting in cultured sympathetic neurons by nerve growth factor. Dev Brain Res *37*:293-301.

Carlton S.M. and Coggeshall R.E. (1999) Inflammation-induced changes in peripheral glutamate receptor populations. Brain Res *820*:63-70.

Carlton S.M., Hargett G.L., and Coggeshall R.E. (1995) Localization and activation of glutamate receptors in unmyelinated axons of rat glabrous skin. Neurosci Lett *197*:25-28.

Carr P.A., Yamamoto T., and Nagy J.I. (1990) Calcitonin gene-related peptide in primary afferent neurons of rat: co-existance with fluoride-resistant acid phosphatase and depletion by neonatal capsaicin. Neuroscience *36*:751-760.

Carraway R., Cochrane D.E., Lansman J.B., Leeman S.E., Paterson B.M., and Welch H.J. (1982) Neurotensin stimulates exocytotic histamine secretion from rat mast cells and elevates plasma histamine levels. J Physiol (London) *323*:403-414.

Carstairs J. and Barnes P. (1986) Autoradiographic mapping of substance P receptors in lung. Eur J Pharmacol *127*:295-296.

Carter M.S. and Krause J.E. (1990) Structure, expression, and some regulatory mechanisms of the rat preprotachykinin gene encoding substance P, neurokinin A, neuropeptide K, and neuropeptide γ. J Neurosci *10*:2203-2214.

Carvalho T.L.L., Hodson N.P., Blank M.A., Wilson P.F., Mulderry P.K., Bishop A.E., Gu J., Bloom S.R., and Polak J.M. (1986) Occurrence, distribution and origin of peptide-containing nerves of guinea-pig and rat male genitalia and the effects of denervation on sperm characteristics. J Anat *149*:121-141.

Caterina M.J., Schumacher M.A., Tominaga M., Rosen T.A., Levine J.D., and Julius D. (1997) The capsaicin receptor: a heat-activated ion channel in the pain pathway. Nature *389*:816-824.

Cauna N. (1970) The fine structure of the arteriovenous anastomosis and its nerve supply in the human nasal respiratory mucosa. Anat Record *168*:9-21.

Cauna N. and Mannan G. (1958) The structure of the human digital Pacinian corpuscles (corpuscula lamellosa) and its functinal significance. J Anat *92*:1-11.

Celander O. and Folkow B. (1953) The nature and the distribution of afferent fibres provided with the axon reflex arrangement. Acta Physiol Scand *29*:359-370.

Cesare P. and McNaughton P. (1997) Peripheral pain mechanisms. Curr Opin Neurobiol *7*:493-499.

Chahl L.A. (1979) The effect of putative peptide neurotransmitters on cutaneous vasculature permeability in the rat. Naunyn-Schmied Arch Pharmacol *309*:159-163.

Chahl L.A. (1988) Antidromic vasodilatation and neurogenic inflammation. Pharmac Ther *37*:275-300.

Chaplan S.R., Bach F.W., Pogrel J.W., Chung J.M., and Yaksh T.L. (1994) Quantitative assessment of tactile allodynia in the rat paw. J Neurosci Methods *53*:55-63.

Chiba T., Yamaguchi A., Yamatani T., Nakamura A., Morishita T., Inui T., Fukase M., Noda T., and Fujita T. (1989) CGRP receptor antagonist hCGRP, 8-37. Am J Physiol *256*:E331-E335.

Cho H.-J., Kim D.-S., Lee N.-H., Kim J.-K., Lee K.-M., Han K.-S., Kang Y.-N., and Kim K.-J. (1997) Changes in the α_2-adrenergic receptor subtypes gene expression in rat dorsal root ganglion in an experimental model of neuropathic pain. NeuroReport *8*:3119-3122.

Chung K., Kim H.J., Na H.S., Park M.J., and Chung J.M. (1993) Abnormalities of sympathetic innervation in the area of an injured peripheral nerve in a rat model of neuropathic pain. Neurosci Lett *162*:85-88.

Chung K., Lee B.H., Yoon Y.W., and Chung J.M. (1996) Sympathetic sprouting in the dorsal root ganglion of the injured peripheral nerve in a rat neuropathic pain model. J Comp Neurol *376*:241-252.

Chung K., Yoon Y.W., and Chung J.M. (1997) Sprouting sympathetic fibers form synaptic varicosities in the dorsal root ganglion of the rat with neuropathic injury. Brain Res *751*:275-280.

Clements J.R., Magnusson K.R., and Beitz A.J. (1990) Ultrastructural description of glutamate-, aspartate-, taurine-, and glycine-like immunoreactive terminals from five rat brain regions. J Electron Microsc Tech *15*:49-66.

Cockayne D.A., Hamilton S.G., Zhu Q.-M., Dunn P.M., Zhong Y., Novakovic S., Malmberg A.B., Cain G., Berson A., Kassotakis L., Hedley L., Lachnit W.G., Burnstock G., McMahon S.B., and Ford A.P.D.W. (2000) Urinary bladder hyporeflexia and reduced pain-related behaviour in $P2X_3$-deficient mice. Nature *407*:1011-1015.

Coggeshall R.E. and Carlton S.M. (1997) Receptor localization in the mammalian dorsal horn and primary afferent neurons. Brain Res Rev *24*:28-66.

Cohen R.H. and Perl E.R. (1990) Contributions of arachidonic acid derivatives and substance P to the sensitization of cutaneous nociceptors. J Neurophysiol *64*:457-464.

Coimbra A., Magalhaes M.M., and Sodré-Borges B.P. (1970) Ultrastructural localization of acid phosphatase in synaptic terminals of the substantia gelatinosa Rolandi. Brain Res *22*:142-146.

Coimbra A., Sodré-Borges B.P., and Magalhaes M.M. (1974) The substantia gelatinosa Rolandi of the rat. Fine structure, cytochemistry (acid phosphatatse) and changes after dorsal root section. J Neurocytol *3*:199-217.

Cole D.F., Bloom S.R., Burnstock G., Butler J.M., McGregor G.P., Saffrey M.J., Unger W.G., and Zhang S.Q. (1983) Increase in SP-like immunoreactivity in nerve fibres of rabbit iris and ciliary body one to four months following sympathetic denervation. Exp Eye Res *37*:191-197.

Couture R., Boucher S., Picard P., and Regoli D. (1993) Receptor characterization of the spinal action of neurokinins on nociception: a three receptor hypothesis. Regul Pep *46*:426-429.

Couture R. and Cuello A.C. (1984) Studies on the trigeminal antidromic vasodilatation and plasma extravasation in the rat. J Physiol (London) *346*:273-285.

Couture R., Cuello A.C., and Henry J.L. (1985) Trigeminal antidromic vasodilatation and plasma extravasation in the rat: effects of acetylcholine antagonists and cholinesterase inhibitors. Br J Pharmacol *84*:637-643.

Couture R., Cuello A.C., and Henry J.L. (1985) Trigeminal antidromic vasodilatation and plasma extravasation in the rat: effects of sensory, autonomic and motor denervation. Brain Res *346*:108-114.

Crossman D.C., Larkin S.W., Fuller R.W., and Davies G.J. (1989) Substance P dilates epicardial coronary arteries and increases coronary blood flow in humans. Circulation *80*:475-484.

Cuello A.C. (1987) Central and peripheral ends of substance P-containing neurons: relevance to nociceptive mechanisms. In F.Sicuteri (ed): Trends in cluster headache. Amsterdam: Elsevier Science Publishers B.V., pp. 3-12.

Cuello A.C., Del Fiacco M., and Paxinos G. (1978) The central and peripheral ends of the substance-P-containing sensory neurones in the rat trigeminal system. Brain Res *152*:499-509.

Dalsgaard C.-J., Jernbeck J., Stains W., Kjartansson J., Hægerstrand A., Hökfelt T., Brodin E., Cuello A.C., and Brown J.C. (1989) Calcitonin gene-related peptide-like immunoreactivity in nerve fibres in human skin. Relation to fibres containing substance P-, somatostatin- and vasoactive intestinal polypeptide-like immunoreactivity. Histochemistry *91*:35-38.

Dalsgaard C.-J., Jonsson C.-E., Hökfelt T., and Cuello A.C. (1983) Localization of substance P-immunoreactive fibers in the human digital skin. Experientia *39*:1018-1020.

Davis B.M., Albers K.M., Seroogy K.B., and Katz D.M. (1994) Overexpression of nerve growth factor in transgenic mice induces novel sympathetic projections to primary sensory neurons. J Comp Neurol *349*:464-474.

Davis B.M., Fundin B.T., Albers K.M., Goodness T.P., Cronk K.M., and Rice F.L. (1997) Overexpression of nerve growth factor in skin causes preferential increases among innervation to specific sensory targets. J Comp Neurol *387*:489-506.

De Biasi S. and Rustioni A. (1990) Ultrastructural immunocytochemical localization of excitatory amino acids in the somatosensory system. J Histochem Cytochem *38*:1745-1754.

De Koninck Y., Ribeiro-da-Silva A., Henry J.L. , and Cuello A.C. (1993) Ultrastructural immunocytochemistry combined with intracellular marking of physiologically identified neurons *in vivo*. In Cuello A.C. (ed): Immunohistochemistry II. Chichester: John Wiley & Sons, pp. 369-393.

Deguchi M., Niwa M., Shigematsu K., Fujii T., Namba K., and Ozaki M. (1989) Specific [^{125}I]Bolton-Hunter substance P binding sites in human and rat skin. Neurosci Lett *99*:287-292.

DeLeo J.A. and Rutkowski M.D. (2000) Gender differrences in rat neuropathic pain sensitivity is dependent on strain. Neurosci Lett *282*:197-199.

Dellemijn P. (1999) Are opioids effective in relieving neuropathic pain. Pain *80*:453-462.

Dennis T., Fournier A., Cadieux A., Pomerleau F., Jolicoeur F.B., St.Pierre S., and Quirion R. (1990) $hCGRP_{8-37}$, a calcitonin gene-related peptide antagonist revealing calcitonin gene-related peptide receptor heterogeneity in brain and periphery. J Pharm Exp Therap *254*:123-128.

Devillier P., Drapeau G., Renoux M., and Regoli D. (1989) Role of the N-terminal arginine in the histamine-releasing activity of substance P, bradykinin and related peptides. Eur J Pharmacol *168*:53-60.

Devillier P., Regoli D., Asseraf A., Descurs B., Marsac J., and Renoux M. (1986) Histamine release and local responses of rat and human skin to substance P and other mammalian tachykinins. Pharmacology *32*:340-347.

Devor M., Jänig W., and Michaelis M. (1994) Modulation of activity in dorsal root ganglion neurons by sympathetic activity in nerve-injured rats. J Neurophysiol *71*:38-47.

Diamond J., Coughlin M., MacIntyre I., Holmes M., and Visheau B. (1987) Evidence that endogenous β-nerve growth factor is responsible for the collateral sprouting but not the regeneration of nociceptive axons in adult rats. Proc Natl Acad Sci USA *84*:6956-6600.

Diamond J. and Foerster A. (1992) Recovery of sensory function in skin deprived of its innervation by lesion of the peripheral nerve. Exp Neurol *115*:100-103.

Diamond J., Foerster A., Holmes M., and Coughlin M. (1992a) Sensory nerves in adult rats regenerate and restore sensory function to the skin independently of endogenous NGF. J Neurosci *12*:1467-1476.

Diamond J., Holmes M., and Coughlin M. (1992b) Endogenous NGF and nerve impulses regulate the collateral sprouting of sensory axons in the skin of the adult rat. J Neurosci *12*:1454-1466.

Dimitriadou V., Buzzi M.G., Theoharidess T.C., and Moskowitz M.A. (1992) Ultrastructural evidence for neurogenically mediated changes in blood vessels of the rat dura mater and tongue following antidromic trigeminal stimulation. Neuroscience *48*:187-203.

Ding Y., Cesare P., Drew L., Nikitaki D., and Wood J.N. (2000) ATP, P2X receptors and pain pathways. J Autonom Nerv Sys *81*:289-294.

Dodd J. and Jessell T.M. (1985) Lactoseries carbohydrates specify subsets of dorsal root ganglion neurons projecting to the superficial dorsal horn of rat spinal cord. J Neurosci *5*:3278-3294.

Donnerer J. and Amann R. (1993) The inhibition of neurogenic inflammation. Gen Pharmac *24*:519-529.

Donnerer J., Schuligoi R., and Stein C. (1992) Increased content and transport of substance P and calcitonin gene-related peptide in sensory nerves innervating inflamed tissue: evidence for a regulatory function of nerve growth factor in vivo. Neuroscience *49*:693-698.

Du J., Koltzenburg M., and Carlton S.M. (2001) Glutamate-induced excitation and sensitization of nociceptors in rat glabrous skin. Pain *89*:187-198.

Eady R.A., Cowen T., Marshall T.F., Plummer V., and Greaves M.W. (1979) Mast cell population density, blood vessel density and histamine content of normal human skin. Br J Dermatol *100*:623-633.

Edelson R.L. and Fink J.M. (1985) The immunologic function of skin. Scientific American *252*:46-53.

Edvinsson L. (1987) Innervation of the cerebral circulation. Annals New York Acad Sci *519*:334-348.

Edvinsson L., Gulbenkian S., Jansen I., Wharton J., Cervantes C., and Polak J.M. (1989) Comparison of peptidergic mechanisms in different parts of the guinea-pig superior mesenteric artery: immunocytochemistry at the light and ultrastructural levels and responses in vitro of large and small arteries. J Autonom Nerv Sys *28*:141-154.

Ekström J. (1981) Sympathetic denervation affects the choline acetyltransferase activity in decentralized parasympathetic neurones of the submaxillary gland of the rat. Acta Physiol Scand *112*:71-75.

Elias P.M. (1983) Epidermal lipds, barrier function and desquamation. J Invest Dermatol *80*:S44-S49.

Elliott A.A. and Elliott J.R. (1993) Characterization of TTX-sensitive and TTX-resistant sodium currents in small cells from adult rat dorsal root ganglia. J Physiol (London) *463*:39-56.

Emeson R.B. (1996) Posttranscriptional regulation of calcitonin gene-related peptide (CGRP) mRNA production. In Geppetti P. and Holzer P. (eds): Neurogenic inflammation. Boca Raton: Crc Press, pp. 15-30.

English K., Harper S., Stayner N., Wang Z.-M., and Davies A.M. (1994) Localization of nerve growth factor (NGF) and low-affinity NGF receptors in touch domes and quantification of NGF mRNA in keratinocytes of adult rats. J Comp Neurol *344*:470-480.

Eriksson J., Bongenhielm U., Kidd E., Matthews B., and Fried K. (1998) Distribution of $P2X_3$ receptors in the rat trigeminal ganglion after inferior alveolar nerve injury. Neurosci Lett *254*:37-40.

Eroschenko V.P. (1993) di Fiore's Altlas of Histology with Functional Correlations. Philadelphia, London: Lea & Febiger.

Evans J.A. (1946) Reflex sympathetic dystrophy. Surg Clin *26*:780-790.

Fawcett D.W. (1986) Bloom and Fawcett a Textbook of Histology. Philadelphia: W.B. Saunders Company.

Fewtrell C.M., Foreman J.C., and Jordan C.C. (1982) The effects of substance P on histamine and 5-hydroxytryptamine release in the rat. J Physiol (London) *230*:393-411.

Fitzpatrick T.B., Szabo G., Seiji M. , and Quevedo W.C. (1979) Biology of the melanin pigmentary system. In Fitzpatrick T.B. (ed): Dermatology in General Medicine. New York: McGraw-Hill Book Co., pp. 131-163.

Fjellner B. and Hagermark O. (1981) Studies on puritogenic and histamine-releasing effects of some putative peptide neurotransmitters. Acta Derma Venereal (Stockholm) *61*:245-250.

Flores C.M., DeCamp R.M., Kilo S., Rogers S.W., and Hargreaves K.M. (1996) Neuronal nicotinic receptor expression in sensory neurons of the rat trigeminal ganglion: Demonstration of $\alpha 3\beta 4$, a novel subtype in the mammalian nervous system. J Neurosci *16*:7892-7901.

Florey H. (1961) Exchange of substances between the blood and tissues. Nature *192*:908-921.

Fong T.M. (1996) Molecular biology of tachykinins. In Geppetti P. and Holzer P. (eds): Neurogenic inflammation. Boca Raton: CRC Press, pp. 3-14.

Foreman J.C., Jordan C.C., Oehme P., and Renner H. (1983) Structure-activity relationships for some substance P-related peptides that cause wheal and flare reactions in human skin. J Physiol (London) *335* :449-465.

Fuller R.W., Conradson T.-B., Dixon C.M.S., Crossman D.C., and Barnes P.J. (1987) Sensory neuropeptide effects in human skin. Br J Pharmacol *92*:781-788.

Fundin B.T., Pfaller K., and Rice F.L. (1997) Different distributions of the sensory and autonomic innervation among the microvasculature of the rat mystacial pad. J Comp Neurol *389*:545-568.

Furness J.B., Papka R.E., Della N.G., Costa M., and Eskay R.L. (1982) Substance P-like immunoreactivity in nerves associated with the vascular system of guinea-pigs. Neuroscience *7*:447-459.

Gao G.C., Dashwood M.R., and Wei E.T. (1991) Corticotropin-releasing factor inhibition of substance P-induced vascular leakage in rats: possible sites of action. Peptides *12*:639-644.

Garland A.M., Grady E.F., Payan S.R., Vigna S.R., and Bunnett N.W. (1994) Agonist-induced internalization of the substance P (NK_1) receptor expressed in epithelial cells. Biochem J *303*:177-186.

Garret C., Carruette A., Fardin V., Moussaoui S., Peyronel J.F., Blanchard J.C., and Laduron P.M. (1991) Pharmacological properties of a potent and selective nonpeptide substance-P antagonist. Proc Natl Acad Sci USA *88*:10208-10212.

Gartner L.P. , and Hiatt J.L. (1997) Color Textbook of Histology. Philadelphia: W.B. Saunders Company.

Gartner L.P. , and Hiatt J.L. (2000) Color Atlas of Histology. Baltimore, Philadelphia: Lippincott Williams & Wilkins.

Geppetti P. , and Holzer P. (1996) Neurogenic inflammation. Boca Raton: CRC Press.

Gibbins I.L., Furnes J.B., Costa M., MacIntyre I., Hillyard C.J., and Girgis S. (1985) Co-localization of calcitonin gene-related peptide-like immunoreactivity with substance P in cutaneous, vascular and visceral sensory neurons of guinea-pigs. Neurosci Lett *57*:125-130.

Gibbins I.L., Wattchow D., and Coventry B. (1987) Two immunohistochemically identified populations of calcitonin gene-related peptide (CGRP)-immunoreactive axons in human skin. Brain Res *414*:143-148.

Gilmor M.L., Nash N.R., Roghani A., Edwards R.H., Yi H., Hersh S.M., and Levey A.I. (1996) Expression of the putative vesicular acetylcholine transporter in rat brain and localization in cholinergic synaptic vesicles. J Neurosci *16*:2179-2190.

Gold M.S., Reichling D.B., Shuster M.J., and Levine J.D. (1996) Hyperalgesic agents increase a tetrodotoxin-resistant Na^+ current in nociceptors. Proc Natl Acad Sci USA *93*:1108-1112.

Gonzales R., Goldyne M.E., Taiwo Y.O., and Levine J.D. (1989) Production of hyperalgesic prostaglandins by sympathetic postganglionic neurons. J Neurochem *53*:1595-1598.

Gonzales R., Sherbourne C.D., Goldyne M.E., and Levine J.D. (1991) Noradrenaline-induced prostaglandin production by sympathetic postganglionic neurons is mediated by α_2-adrenergic receptors. J Neurochem *57*:1145-1150.

Gracely R.H., Lynch S.A., and Bennett G.J. (1992) Painful neuropathy: altered central processing maintained dynamically by peripheral input. Pain *51*:175-194.

Grady E.F., Gamp P.D., Jones E., Baluk P., McDonald D.M., Payan D.G., and Bunnett N.W. (1996) Endocytosis and recycling of neurokinin-1 receptors in enteric neurons. Neuroscience *79*:1239-1254.

Grant G. (1995) Primary afferent projections to the spinal cord. In Paxinos G. (ed): The rat nervous system. Sydney: Academic Press, pp. 61-66.

Guo A., Vulchanova L., Wang J., Li X., and Elde R. (1999) Immunocytochemical localization of the vanilloid receptor 1 (VR1): relationship to neuropeptides, the $P2X_3$ purinoceptor and IB4 binding sites. Eur J Neurosci *11*:946-958.

Haberberger R., Henrich M., Couraud J.Y., and Kummer W. (1999) Muscarinic M2-receptors in rat thoracic dorsal root ganglia. Neurosci Lett *266*:177-180.

Hagermark O., Hökfelt T., and Pernow B. (1978) Flare and itch induced by SP in human skin. J Invest Dermatol *71*:233-235.

Halata Z. (1975) The mechanoreceptors of the mammalian skin: Ultrastructure and morphological classification. In Brodal A. (ed): Advances in Anatomy, Embryology and Cell biology. New York: Springer-Verlag, pp. 1-23.

Hales J.R., Fawcett A.A., Bennett J.W., and Needham A.D. (1978) Thermal control of blood flow through capillaries and arteriovenous anastomoses in skin of sheep. Pflügers Arch *378*:55-63.

Hales J.R.S., Iriki M., Tsuchiya K., and Kozawa E. (1978) Thermally-induced cutaneous sympathetic activity related to blood flow through capillaries and arteriovenous anastomoses. Pflügers Archiv-Eur J Physiol *375*:17-24.

Hall J.M. , and Brain S.D. (1996) Pharmacology of calcitonin gene-related peptide. In Geppetti P. and Holzer P. (eds): Neurogenic inflammation. Boca Raton: CRC Press, pp. 101-114.

Hartman B.K. (1973) Immunofluorescence of dopamine-β-hydroxylase: application of improved methodology to the localization of the peripheral and central noradrenergic nervous system. J Histochem Cytochem *21*:312-332.

Hartschuh W., Weihe E., and Reinecke M. (1983) Peptidergic (neurotensin, VIP, substance P) nerve fibres in the skin. Immunohistochemical evidence of an involvement of neuropeptides in nociception, pruritus and inflammation. Br J Dermatol *109*:14-17.

Hassan A.A.K., Rayman G., and Tooke J.E. (1986) Effect of indirect heating on the postural control of skin blood flow in the human foot. Clin Sci *70*:577-582.

Häbler H.-J., Eschenfelder S., Liu X.-G., and Jänig W. (2000) Sympathetic-sensory coupling after L5 spinal nerve lesion in the rat and its relation to changes in dorsal root ganglion blood flow. Pain *87*:335-345.

Helfert R.H., Juiz J.M., Bledsoe Jr.S.C., Bonneau J.M., Wenthold R.J., and Altschuler R.A. (1992) Patterns of glutamate, glycine, and GABA immunolabeling in four synaptic terminal classes in the lateral superior olive of the guinea pig. J Comp Neurol *323*:305-325.

Hemingway A. and Price W.M. (1968) The autonomic nervous system and regulation of body temperature. Anesthesiology *20*:693-701.

Herzberg U., Eliav E., Dorsey J.M., Gracely R.H., and Kopin I.J. (1997) NGF involvement in pain induced by chronic constriction injury of the rat sciatic nerve. NeuroReport *8*:1613-1618.

Hill C.E., Jelinek H., Hendry I.A., McLennan I.S., and Rush R.A. (1988) Destruction by anti-NGF of autonomic, sudomotor neurones and subsequent hyperinnervation of the foot pad by sensory fibres. J Neurosci Res *19*:474-482.

Hill C.E. and Vidovic M. (1989) The role of competition in the refinement of the projections of the sympathetic neurons to the rat eye during development. Int J Dev Neurosci *7*:539-551.

Hinsey J.C. and Gasser H.S. (1930) The component of the dorsal root mediating vasodilatation and the Sherrington contracture. Am J Physiol *92*:679-689.

Hirst G.D.S., Choate J.K., Cousins H.M., Edwards F.R., and Klemm M.F. (1996) Transmission by post-ganglionic axons of the autonomic nervous system: the importance of the specialized neuroeffector junction. Neuroscience *73*:7-23.

Holbrook K.A. , and Wolff K. (1987) The structure and development of skin. In Fitzpatrick T.B., Eisen A.Z., Wolff K., Freedberg I.M., and Austen K.F. (eds): Dermatology in General Medicine. New York: McGraw-Hill, pp. 93-120.

Holzer P. (1992) Peptidergic sensory neurons in the control of vascular functions: mechanisms and significance in the cutaneous and splanchnic vascular beds. Rev Physiol, Biochem & Pharmacol *121*:49-146.

Holzer P. (1998) Neurogenic vasodilatation and plasma leakage in the skin. Gen Pharmac *30*:5-11.

Hoover D. and Hancock J. (1987) Autoradiographic localization of substance P binding sites in guinea-pig airways. J Autonom Nerv Sys *19*:171-174.

Hornyak M.E., Naver H.K., Rydenhag B., and Wallin B.G. (1990) Sympathetic activity influences the vascular axon reflex in the skin. Acta Physiol Scand *139*:77-84.

Hökfelt T., Elde R., Johansson O., Luft R., Nilsson G., and Arimura A. (1976) Immunohistochemical evidence for separate populations of somatostatin-containing substance P-containing primary afferent neurons in the rat. Neuroscience *1*:131-136.

Hökfelt T., Elfvin L.G., Schultzberg M., Goldstein M., and Nilsson G. (1977) On the occurrence of substance P-containing fibres in sympathetic ganglia: immunohistochemical evidence. Brain Res *132*:29-41.

Hökfelt T., Johansson O., Kellerth J.-O., Ljungdahl Å., Nilsson G., Nygårds A. , and Pernow B. (1977) Immunohistochemical distribution of substance P. In von Euler U.S. and Pernow B. (eds): Substance P. New York: Raven Press, pp. 117-145.

Hökfelt T., Kellerth J.-O., Nilsson G., and Pernow B. (1975) Experimental immunohistochemical studies on the localization and distribution of substance P in cat primary sensory neurons. Brain Res *100*:235-252.

Hökfelt T., Kellerth J.O., Nilsson G., and Pernow B. (1975) Substance P: localization in the central nervous system and in some primary sensory neurons. Science *190*:889-890.

Hökfelt T., Ljungdahl Å., Terenius L., Elde R., and Nilsson G. (1977) Immunohistochemical analysis of peptide pathways possibly related to pain and analgesia: enkephalin and substance P. Proc Natl Acad Sci USA *74*:3081-3085.

Hua X.-Y., Theodorsson-Norheim E., Brodin E., Lundberg J.M., and Hökfelt T. (1985) Multiple tachykinins (neurokinin A, neuropetide K and substance P) in capsaicin-sensitive sensory neurons in the guinea-pig. Regul Pep *13*:1-19.

Hume W.R., De La Lande I.S., and Waterson J.G. (1972) Effect of acetylcholine on the response of the isolated rabbit ear artery to stimulation of the perivascular sympathetic nerves. Eur J Pharmacol *17*:227-233.

Hunt S.P. and Rossi J. (1985) Peptide- and non-peptide-containing unmyelinated primary sensory afferents: the parallel processing of nociceptive information. Philos Trans R Soc Lond B: Biol Sci *308*:283-289.

Iggo A. and Andres K.H. (1982) Morphology of cutaneous receptors. Annual Rev Neurosci *5*:1-31.

Isabel G., Wright D.M., and Henry J.L. (1981) Design for an inexpensive unit for measuring tail flick latencies. J Pharmac Meth *5*:241-247.

Iversen L.L., Watling K.J., McKnight A.T., Williams B.J. , and Lee C.M. (1987) Multiple receptors for substance P and related tachykinins. In Leeming P.R. (ed): Topics in Medicinal Chemistry. London: Royal Society of Chemists, pp. 1-25.

Izumi H. and Karita K. (1990) The effects of capsaicin applied topically to inferior alveolar nerve on antidromic vasodilatation in cat gingiva. Neurosci Lett *112*:65-69.

Izumi H. and Karita K. (1991) Vasodilator responses following intracranial stimulation of the trigeminal, facial and glossopharyngeal nerves in the cat gingiva. Brain Res *560*:71-75.

Izumi H. and Karita K. (1992) Selective excitation of parasympathetic nerve fibres to elicit the vasodilatation in cat lip. J Autonom Nerv Sys *37*:99-108.

Izumi H. and Karita K. (1993) Innervation of the cat lip by two groups of parasympathetic vasodilator fibres. J Physiol (London) *465*:501-512.

Izumi H., Kuriwada S., Karita K., Sasano T., and Sanjo D. (1990) The nervous control of gingival blood flow. Microvasc Res *39*:94-104.

Jacques L., Couture R., Drapeau G., and Regoli D. (1989) Capillary permeability induced by intravenous neurokinins, receptor characterization and mechanism of action. Naunyn-Schmied Arch Pharmacol *340*:170-179.

Jancsó G. (1984) Sensory nerves as modulators of inflammatory reactions. In Chahl L.A., Szolcsányi J., and Lembeck F. (eds): Antidromic vasodilatation and neurogenic inflammation. Budapest: Akadémiai Kiadò, pp. 207-222.

Jancsó N., Jancsó-Gábor A., and Szolcsányi J. (1967) Direct evidence for neurogenic inflammation and its prevention by denervation and by pretreatment with capsaicin. Br J Pharmacol Chemother *31*:138-151.

Jänig W. , and Koltzenburg M. (1991) What is the interaction between the sympathetic terminal and the primary afferent fibre? In Basbaum A.I. and Besson J.-M. (eds): Towards a new pharmacotherapy of pain. New York: Wiley, pp. 331-352.

Jessell T.M. and Dodd J. (1985) Structure and expression of differentiation antigens on functional subclasses of primary sensory neurons. Philos Trans R Soc Lond B: Biol Sci *19*:271-281.

Jessell T.M. , and Dodd J. (1989) Functional chemistry of primary afferent neurons. In Wall P.D. and Melzack R. (eds): Textbook of pain. Edinburg, London, Melbourne and New York: Churchill Livingstone, pp. 82-99.

Johnson J.M., Brengelmann G.L., Hales J.R.S., Vanhoutte P.M., and Wenger C.B. (1986) Regulation of the cutaneous circulation. Federation Proc *45*:2841-2850.

Jones E.G. (1988) The nervous tissue. In Weiss L. (ed): Cell and tissue biology. A textbook of histology. Baltimore: Urban & Schwarzenberg, pp. 277-351.

Ju G., Hökfelt T., Brodin E., Fahrenkrug J., Fischer J.A., Frey P., Elde R.P., and Brown J.C. (1987) Primary sensory neurons of the rat showing calcitonin gene-related peptide immunoreactivity and their relation to substance-P-, somatostatin-, galanin-, vasoactive intestinal polypeptide- and cholecystokinin-immunoreactive ganglion cells. Cell Tissue Res *247*:417-431.

Junqueira L.C., Carneiro J. , and Kelley R.O. (1998) Basic Histology. East Norwalk: Appleton & Lange.

Kaji A., Maeda T., and Watanabe S. (1991) Parasympathetic innervation of cutaneous blood vessels examined by retrograde tracing in the rat lower lip. J Autonom Nerv Sys *32*:153-158.

Kaji A., Shigematsu H., Fujita K., Maeda T., and Watanabe S. (1988) Parasympathetic innervation of cutaneous blood vessels by vasoactive intestinal polypeptide-immunoreactive and acetylcholinesterase-positive nerves: histochemical and experimental study on rat lower lip. Neuroscience *25*:353-362.

Katzung B.G. (2001) Introduction to autonomic pharmacology. In Katzung B.G. (ed): Basic & Clinical Pharmacology. New york: Lange Medical Books/McGraw-Hill, pp. 75-91.

Kawaja M.D. (1998) Sympathetic and sensory innervation of the extracerebral vasculature: role for p75NTR neuronal expression and nerve growth factor. J Neurosci Res *52*:295-306.

Kawasaki H., Takasaki K., Saito A., and Goto K. (1988) Calcitonin gene-related peptide acts as a novel vasodilator neurotransmitter in mesenteric resistance vessels of the rat. Nature *335*:164-167.

Kenins P. (1981) Identification of the unmyelinated sensory nerves which evoke plasma extravasation in response to antidromic stimulation. Neurosci Lett *25*:137-141.

Kenins P. (1982) Responses of single nerve fibres to capsaicin applied to the skin. Neurosci Lett *29*:83-88.

Kenins P., Hurley J.V., and Bell C. (1984) The role of substance P in the axon reflex in the rat. Br J Dermatol *111*:551-559.

Kessler J.A., Bell W.O., and Black I.B. (1983) Interactions between the sympathetic and sensory innervation of the iris. J Neurosci *3*:1301-1307.

Kessler J.A., Bell W.O., and Black I.B. (1983) Substance P levels differ in sympathetic target organ terminals and ganglion perikarya. Brain Res *258*:144-146.

Kido M.A., Yamaza T., Goto T., and Tanaka T. (1999) Immunocytochemical localization of substance P neurokinin-1 receptors in rat gingeval tissue. Cell Tissue Res *297*:213-222.

Kim H.J., Na H.S., Nam H.J., Park K.A., Hong S.K., and Kang B.S. (1996) Sprouting of sympathetic nerve fibers into the dorsal root ganglion following peripheral nerve injury dependes on the injury site. Neurosci Lett *212*:191-194.

Kim H.J., Na H.S., Sung B., and Hong S.K. (1998) Amount of sympathetic sprouting in the dorsal root ganglia is not correlated to the level of sympathetic dependence of neuropathic pain in a rat model. Neurosci Lett *245*:21-24.

Kim S.H. and Chung J.M. (1991) Sympathectomy alleviates mechanical allodynia in an experimental animal model for neuropathy in the rat. Neurosci Lett *134*:131-134.

Kim S.H. and Chung J.M. (1992) An experimental model for peripheral neuropathy produced by segmental spinal nerve ligation in the rat. Pain *50*:355-363.

Kinnman E., Nygårds E.-B., and Hansson P. (1997) Peripheral α-adrenoreceptors are involved in the development of capsaicin induced ongoing and stimulus evoked pain in humans. Pain *69*:79-85.

Knyihár E. (1971) Fluoride-resistant acid phosphatase system of nociceptive dorsal root afferents. Experientia *27*:1205-1207.

Knyihár E. and Gerebtzoff M.A. (1973) Extra-lysosomal localization of acid phosphatase in the spinal cord of the rat. Exp Brain Res *18*:383-395.

Korsching S. and Thoenen H. (1985) Nerve growth factor supply for sensory neurons: site of origin and competition with the sympathetic nervous system. Neurosci Lett *54*:201-205.

Kowalski M.L. and Kaliner M.A. (1988) Neurogenic inflammation, vascular permeability, and mast cells. J Immunol *140*:3905-3911.

Kowalski M.L., Sliwinska-Kowalska M., and Kaliner M.A. (1990) Neurogenic inflammation, vascular permeability, and mast cells. 2. Additional evidence indicating mast cells are not involved in neurogenic inflammation. J Immunol *145*:1214-1221.

Krause J.E., Chirgwin J.M., Carter M.S., Xu Z.S., and Hershey A.D. (1987) Three rat preprotachykinin mRNAs encode the neuropeptides substance P and neurokinin A. Proc Natl Acad Sci USA *84*:881-885.

Kuchiiwa S., Izumi H., Karita K., and Nakagawa S. (1992) Origins of parasympathetic postganglionic vasodilator fibres supplying the lips and gingivae; an WGA-HRP study in the cat. Neurosci Lett *142*:237-240.

Kuchiiwa S. and Kuchiiwa T. (1996) Autonomic and sensory innervation of cat molar gland and blood vessels in the lower lip, gingiva and cheek. J Autonom Nerv Sys *61*:227-234.

Kummer W., Shigemoto R., and Haberberger R. (1999) Smooth muscle cells are the site of neurokinin-1 receptor localization in the arterial supply of the rat sciatic nerve. Neurosci Lett *259*:119-122.

Kurvers H.A.J.M., Hofstra L., Jacobs M.J.H.M., Daemen M.A.R.C., van den Wildenberg F.A.J.M., Kitslaar P.J.E.H.M., Slaaf D.W., and Reneman R.S. (1996) Reflex sympathetic dystrophy: Does sympathetic dysfunction originate from peripheral neuropathy. Surgery *119*:288-296.

Kurvers H.A.J.M., Tangelder G.-J., De Mey J.G.R., Slaaf D.W., Beuk R.J., van den Wildenberg F.A.J.M., Kitslaar P.J.E.H.M., Reneman R.S., and Jacobs M.J.H.M. (1997) Skin blood flow abnormalities in a rat model of neuropathic pain: Result of decreased sympathetic vasoconsctrictor outflow? J Autonom Nerv Sys *63*:19-29.

Landis S.C. and Fredieu J.R. (1986) Coexistence of calcitonin gene-related peptide and vasoactive intestinal peptide in cholinergic sympathetic innervation of rat sweat glands. Brain Res *377*:177-181.

Lavker R.M. and Sun T.-T. (1982) Heterogeneity in basal keratinocytes: morphological and functional correlations. Science *215*:1239-1241.

Lee B.H., Yoon Y.W., Chung K., and Chung J.M. (1998) Comparison of sympathetic sprouting in sensory ganglia in three animal models of neuropathic pain. Exp Brain Res *120*:432-438.

Lee D.H., Chung K., and Chung J.M. (1997) Strain differences in adrenergic sensitivity of neuropathic pain behaviors in an experimental rat model. NeuroReport *8*:3453-3456.

Lee Y., Kawai Y., Shiosaka S., Takami K., Kiyama H., Hillyard C.J., Girgis S., MacIntyre I., Emson P.C., and Tohyama M. (1985) Coexistence of calcitonin gene-related peptide and substance P-like peptide in single cells of the trigeminal ganglion of the rat: immunohistochemical analysis. Brain Res *330*:194-196.

Lee Y., Takami K., Kawai Y., Girgis S., Hillyard C.J., MacIntyre I., Emson P.C., and Tohyama M. (1985) Distribution of calcitonin gene-related peptide in the rat peripheral nervous system with reference to its coexistence with substance P. Neuroscience *15*:1227-1237.

Lei Y.-H., Barnes P.J., and Rogers D.F. (1992) Inhibition of neurogenic plasma exudation in guinea-pig airways by CP-96,345, a new non-peptide NK1 receptor antagonist. Br J Pharmacol *105*:261-262.

Lembeck F. (1983) Sir Thomas Lewis' nocifensor system, histamine and substance-P-containing primary afferent nerves. Trends Neurosci *6*:106.

Lembeck F., Donnerer J., and Barthò L. (1982) Inhibition of neurogenic vasodilatation and plasma extravasation by substance P antagonists, somatostatin, and D-met^2,Pro^5-enkephalinamide. Eur J Pharmacol *85*:171-176.

Lembeck F., Donnerer J., Tsuchiya M., and Nagahisa A. (1992) The non-peptide tachykinin antagonist, CP-96,345, is a potent inhibitor of neurogenic inflammation. Br J Pharmacol *105*:527-530.

Lembeck F. and Holzer P. (1979) Substance P as neurogenic mediator of antidromic vasodilatation and neurogenic plasma extravasation. Naunyn-Schmied Arch Pharmacol *310*:175-183.

Levine J.D., Dardick S.J., Basbaum A.I., and Scipio E. (1985) Reflex neurogenic inflammatiom I. Contribution of the peripheral nervous system to spatially remote inflammatory responses that follow injury. J Neurosci *5*:1380-1386.

Levine J.D. , and Reichling D.B. (1999) Peripheral mechanisms of inflammatory pain. In Wall P.D. and Melzack R. (eds): Textbook of Pain. London: Churchill Livingstone, pp. 59-84.

Levine J.D., Taiwo Y.O., Collins S.D., and Tam J.K. (1986) Noradrenaline hyperalgesia is mediated through interaction with sympathetic postganglionic neurone terminals rather than activation of primary afferent nociceptors. Nature *323*:158-160.

Levy M.N. (1971) Sympathetic-parasympathetic interactions in the heart. Circ Res *29*:437-445.

Lewin G.R. and Mendell L.M. (1993) Nerve growth factor and nociception. Trends Neurosci *16*:353-359.

Lewis T. (1927) The blood vessels of the human skin and their responses. London: Shaw & Sons.

Li H.-S. and Zhao Z.-Q. (1998) Small sensory neurons in the rat dorsal root ganglia express functional NK-1 tachykinin receptor. Eur J Neurosci *10*:1292-1299.

Litwin M.S. (1962) Postsympathectomy neuralgia. Arch Surg *84*:121-125.

Llewellyn-Smith I.J. and Minson J.B. (1992) Complete penetration of antibodies into vibratome sections after glutaraldehyde fixation and ethanol treatment: light and electron microscopy for neuropeptides. J Histochem Cytochem *40*:1741-1749.

Lowman M.A., Benyon R.C., and Church M.K. (1988) Characterization of neuropeptide-induced histamine released from human dispersed skin mast cells. Br J Pharmacol *95*:121-130.

Löffelholz K. and Muscholl E. (1970) Inhibition by parasympathetic nerve stimulation of the release of the adrenergic transmitter. Naunyn-Schmied Arch Pharmacol *267*:181-184.

Luff S.E., Young S.B., and McLachlan E.M. (2000) Ultrastructure of substance P-immunoreactive terminals and their relation to vascular smooth muscle cells of rat small mesenteric arteries. J Comp Neurol *416*:277-290.

Lundberg J.M. (1996) Pharmacology of cotransmission in the autonomic nervous system: integrative aspects on amines, neuropeptides, adenosine triphosphate, amino acids and nitric oxide. Pharmacol Rev *48*:113-178.

Luthman J., Stromberg I., Brodin E., and Jonsson G. (1989) Capsaicin treatment to developing rats induces increase of noradrenaline levels in the iris without affecting the adrenergic terminal density. Int J Dev Neurosci *7*:613-622.

MacFarlane B.V., Wright A., O'Callaghan J., and Benson H.A.E. (1997) Chronic neuropathic pain and its control by drugs. Pharmac Ther *75*:1-19.

MacKenzie I.L. (1972) The ordered structure of the mammalian epidermis. In Maibach H.I. and Rovee D.T. (eds): Epidermal Wound Healing. New york: Year Book Medical Publication, pp. 5-25.

Maggi C.A. and Meli A. (1988) The sensory-efferent function of capsaicin-sensitive sensory neurons-. Gen Pharmac *19*:1-43.

Majno G., Shea S.M., and Leventhal M. (1969) Endothelial contraction induced by histamine-type mediators. An electron microscopic study. J Cell Biol *42*:647-670.

Malik K.U. and Ling G.M. (1969) Modification by acetylcholine of the response of rat mesenteric arteries to sympathetic stimulation. Circ Res *25*:1-9.

Malik K.U. and McGiff J.C. (1971) Modification by choline of adrenergic transmission in rat mesenteric arteries. Br J Pharmacol *43*:776-783.

Malmberg A.B., Chen C., Tonegawa S., and Basbaum A.I. (1997) Preserved acute pain and reduced neuropathic pain in mice lacking PKCγ. Science *278*:279-283.

Mannion R.J., Doubell T.P., Coggeshall R.E., and Woolf C.J. (1996) Collateral sprouting of uninjured primary afferent A-fibres into the superficial dorsal horn of the adult rat spinal cord after topical capsaicin treatment to the sciatic nerve. J Neurosci *16*:5189-5195.

Mantyh P.W., DeMaster E., Malhotra A., Ghilardi J.R., Rogers S.D., Mantyh C.R., Liu H., Basbaum A.I., Vigna S.R., Maggio J.E., and Simone D.A. (1995a) Receptor endocytosis and dendrite reshaping in spinal neurons after somatosensory stimulation. Science *268*:1629-1632.

Mantyh P.W., Allen C.J., Ghilardi J.R., Rogers S.D., Mantyh C.R., Liu H., Basbaum A.I., Vigna S.R., and Maggio J.E. (1995b) Rapid endocytosis of a G protein-coupled receptor: Substance P-evoked internalization of its receptor in the rat striatum *in vivo*. Proc Natl Acad Sci USA *92*:2622-2626.

Mantyh P.W., Rogers S.D., Honore P., Allen B.J., Ghilardi J.R., Li J., Daughters R.S., Lappi D.A., Wiley R.G., and Simone D.A. (1997) Inhibition of hyperalgesia by ablation of lamina I spinal neurons expressing the substance P receptor. Science *278*:275-279.

Maricq H.R. (1972) Local effect of serotonin on blood vessels of human skin. Microvasc Res *4*:258-263.

Martin-Schild S., Gerall A.A., Kastin A.J., and Zadina J.E. (1998) Endomorphine-2 is an endogenous opioid in primary sensory afferent fibres. Peptides *19*:1783-1789.

Martin H.A., Basbaum A.I., Kwait G.C., Goetzl E.J., and Levine J.D. (1987) Leukotriene and prostaglandin sensitization of cutaneous high-threshold C- and A-delta mechanonociceptors in the hairy skin of rat hindlimbs. Neuroscience *22*:651-659.

Matsuyama T., Matsumoto M., Shiosaka S., Fujisawa A., Yoneda S., Kimura K., Abe H., and Tohyama M. (1983a) Overall distribution of substance P and vasoactive intestinal polypeptide in the cerebral arteries: an immunohistochemical study using whole-mount. J Cereb Blood Flow Metabol *3* :S208-S209.

Matsuyama T., Shiosaka S., Matsumoto M., Yoneda S., Kimura K., Abe H., Hayakawa T., Inoue H., and Tohyama M. (1983b) Overall distribution of vasoactive intestinal polypeptide-containing nerves on the wall of cerebral arteries: an immunohistochemical study using whole-mounts. Neuroscience *10*:89-96.

Matsuyama T., Shiosaka S., Wanaka A., Yoneda S., Kimura K., Hayakawa T., Emson P.C., and Tohyama M. (1985) Fine structure of peptidergic and catecholaminergic nerve fibers in the anterior cerebral artery and their interrelationship: an immunoelectron microscopic study. J Comp Neurol *235*:268-276.

Mayer D.J., Mao J., Holt J., and Price D.D. (1999) Cellular mechanisms of neuropathic pain, morphine tolerance, and their interactions. Proc Natl Acad Sci USA *96*:7731-7736.

Mazzoni I.E., Jaffe E., and Cuello A.C. (1991) Production and immunocytochemical application of a highly sensitive and specific monoclonal antibody against rat dopamine-β-hydroxylase. Histochemistry *96*:45-50.

McDougall A.J. and McLeod J.G. (1996a) Autonomic neuropathy, I. Clinical features, investigation, pathophysiology, and treatment. J Neurol Sci *137*:79-88.

McDougall A.J. and McLeod J.G. (1996b) Autonomic neuropathy, II: Specific peripheral neuropathies. J Neurol Sci *138*:1-13.

McLachlan E.M. and Hu P. (1998) Axonal sprouts containing calcitonin gene-related peptide and substance P form pericellular baskets around large diameter neurons after sciatic nerve transection in the rat. Neuroscience *84*:961-965.

McLachlan E.M., Jänig W., Devor M., and Michaelis M. (1993) Peripheral nerve injury triggers noradrenergic sprouting within dorsal root ganglia. Nature *363*:543-546.

McLeod A.L., Ritchie J., Cuello A.C., Julien J.-P., Henry J.L., and Ribeiro-da-Silva A. (2000) Upregulation of an opioid-mediated antinociceptive mechanism in transgenic mice overexpressing substance P in the spinal cord. Neuroscience *96*:785-789.

McLeod A.L., Ritchie J., Cuello A.C., Julien J.-P., Ribeiro-da-Silva A., and Henry J.L. (1999) Transgenic mice over-expressing substance P exhibit allodynia and hyperalgesia which are reversed by substance P and *N*-methyl-D-aspartate receptor antagonists. Neuroscience *89*:891-899.

McMahon S.B. (1991) Mechanisms of sympathetic pain. Br Med Bull *47*:584-600.

McMahon S.B., Bennett D.L.H., Priestley J.V., and Shelton D.L. (1995) The biological effect of endogenous nerve growth factor on adult sensory neurons revealed by a trkA-IgG fusion molecule. Nature Med *1* :774-780.

Mendre C., Ribeiro-da-Silva A., and Cuello A.C. (1989) Utrastructural demonstration of plasma extravasation and mast cell degranulation after antidromic nerve stimulation in the skin of the rat hindlimb. Eur J Neurosci *Suppl. 2*:114(Abstract).

Michaelis M., Devor M., and Jänig W. (1996) Sympathetic modulation of activity in rat dorsal root ganglion neurons changes over time following peripheral nerve injury. J Neurophysiol *76*:753-763.

Mihara M., Hashimoto K., Ueda K., and Kumakiri M. (1979) The specialized juntions between Merkel cell and neurite: an electron microscopic study. J Invest Dermatol *73*:325-334.

Miki K., Fukuoka T., Tokunaga A., and Noguchi K. (1998) Calcitonin gene-relatead peptide increase in the rat spinal horn and dorsal horn column nucleus following peripheral nerve injury: up-regulation in a subpopulation of primary afferent sensory neurons. Neuroscience *82*:1243-1252.

Minami M., Maekawa K., Yabuuchi K., and Satoh M. (1995) Double in situ hybridization study on coexistence of μ-, δ- and kappa-opioid receptor mRNAs with preprotachykinin A mRNA in the rat dorsal root ganglia. Mol Brain Res *30*:203-210.

Mitchell S.W., Morehouse C.R. , and Keen W.W. (1864) Gunshot wounds and other injuries of the nerves. Philadelphia: J.B. Lippincott.

Montagna W., Bentley J.P., and Dobson R.L. (1970) The dermis. Adv Biol Skin *10*:1-302.

Montagna W. , and Lobitz W.C.Jr. (1964) The Epidermis. New York: Academic Press.

Montagna W.W. , and Parakkal P.F. (1974) The structure and function of skin. New York: Academic Press.

Morris J.L., Gibbins I.L., Campbell G., Murphy R., Furness J.B., and Costa M. (1986) Innervation of the large arteries and heart of the toad (*Bufo marinus*) by adrenergic and peptide-containing neurons. Cell Tissue Res *243*:171-184.

Mosconi T. and Kruger L. (1996) Fixed-diameter polyethylene cuffs applied to the rat sciatic nerve induce a painful neuropathy: ultrastructural morphometric analysis of axonal alterations. Pain *64*:37-57.

Mousli M., Bronner C., Landry Y., Bockaert J., and Rouot B. (1990) Direct activation of GTP-binding regulatory proteins (G-proteins) by substance P and compound 48/80. FEBS Lett *259*:260-262.

Movat H.Z. and Pernando N.V.P. (1964) The fine structure of the terminal vascular bed. IV. Venules and their perivascular cells. Exp Mol Pathol *3*:98-115.

Mulderry P.K., Ghatei M.A., Spokes R.A., Jones P.M., Pierson A.M., Hamid Q.A., Kanse S., Amara S.G., Burrin J.M., Legon S., Polak J.M., and Bloom S.R. (1988) Differential expression of α-CGRP and β–CGRP by primary sensory neurons and enteric autonomic neurons of the rat. Neuroscience *25*:195-205.

Nakanishi S. (1987) Substance P precursor and kininogen: their structures, gene organizations, and regulation. Physiol Rev *67*:1117-1142.

Nakaya Y., Kaneko T., Shigemoto R., Nakanishi S., and Mizuno N. (1994) Immunohistochemical localization of substance P receptor in the central nervous system of the adult rat. J Comp Neurol *347*:249-274.

Naukkarinen A., Harvima I.T., Aalto M.L., Harvima R.J., and Horsmanheimo M. (1991) Quantitative analysis of contact sites between mast cells and sensory nerves in cutaneous psoriasis and lichen planus based on a histochemical double staining technique. Arch Dermatol Res *283*:433-437.

Navarro X., Verdú E., Wendelschafer-Crabb G., and Kennedy W.R. (1997) Immunohistochemical study of skin reinnervation by regenerative axons. J Comp Neurol *380*:164-174.

Nawa H., Hirose R., Takashima H., Inayama S., and Nakanishi S. (1983) Nucleotide sequence of cloned cDNAs for two types of bovine brain substance P precursor. Nature *306*:32-36.

Nawa H., Kotani H., and Nakanishi S. (1984) Tissue-specific generation of two preprotachykinin mRNAs from one gene by alternative RNA splicing. Nature *312*:729-734.

Nelson D.K., Service J.E., Studelska D.R., Brimijoin S., and Go V.L.W. (1988) Gastrointestinal neuropeptide concentrations following guanethidine sympathectomy. J Autonom Nerv Sys *22*:203-210.

Newby D.E., Sciberras D.G., Ferro C.J., Gertz B.J., Sommerville D., Majumdar A., Lowry R.C., and Webb D.J. (1999) Substance P-induced vasodilatation is mediated by the neurokinin type I receptor but does not contribute to basal vascular tone in man. Br J Clin Pharmacol *48*:336-344.

Newson B., Dahlström A., Enerbäck L., and Ahlman H. (1983) Suggestive evidence for a direct innervation of mucosal mast cells. An electron microscopic study. Neuroscience *10*:565-570.

Nielsch U. and Keen P. (1987) Effects of neonatal 6-hydroxydopamine administration on different substance P-containing sensory neurones. Eur J Pharmacol *138*:192-197.

Nishiyama K., Brighton B.W., Bossut D.F., and Perl E.R. (1993) Peripheral nerve injury enhances α_2-adrenergic receptor expression by some DRG neurons. Soc Neurosci Abstr *19*:207.

Novakovic S.D., Kassotakis L.C., Oglesby I.B., Smith J.A.M., Eglen R.M., Ford A.P.D.W., and Hunter J.C. (1999) Immunocytochemical localization of P_{2X3} purinoceptors in sensory neurons in naive rats and following neuropathic injury. Pain *80*:273-282.

Novakovic S.D., Tzoumaka E., McGivern J.G., Haraguchi M., Sangameswaran L., Gogas K.R., Eglen R.M., and Hunter J.C. (1998) Distribution of the tetrodotoxin-resistant sodium channel PN3 in rat sensory neurons in normal and neuropathic conditions. J Neurosci *18*:2174-2187.

O'Flynn N.M., Helme R.D., Watkins D.J., and Burcher E. (1989) Autoradiographic localization of substance P binding sites in rat footpad skin. Neurosci Lett *106*:43-48.

O'Halloran K.D. and Perl E.R. (1997) Effects of partial nerve injury on the responses of C-fiber polymodal nociceptors to adrenergic agonists. Brain Res *759*:233-240.

Oestreicher A.B., De Graan P.N.E., Gispen W.H., Verhaagen J., and Schrama L.H. (1997) B-50, the growth associated protein-43: modulation of cell morphology and communication in the nervous system. Prog Neurobiol *53*:627-686.

Otsuka M. and Yoshioka K. (1993) Neurotransmitter functions of mammalian tachykinins. Physiol Rev *73*:229-308.

Otten N.U., Goedert M., Mayer N., and Lembeck F. (1980) Requirement of nerve growth factor for development of substance P-containing sensory neurons. Nature *287*:158-159.

Ouyang A., Zimmerman K., Wong K.-L., Sharp D., and Reynolds J.C. (1996) Effect of ciliac ganglionectomy on tachykinin innervation, receptor distribution and intestinal responses in the rat. J Autonom Nerv Sys *61*:292-300.

Palade G. (1953) Fine structure of blood capillaries. J Appl Physiol *24*:1424-1431.

Perl E.R. (1993) Causalgia:sympathetically-aggravated chronic pain from damaged nerves. Pain: Clin Updates *I*:1-4.

Perl E.R. (1999) Causalgia, pathological pain, and adrenergic receptors. Proc Natl Acad Sci USA *96*:7664-7667.

Pernow B. (1983) Substance P. Pharmacol Rev *35*:85-141.

Petersen M., Zhang J., Zhang J.-M., and LaMotte R.H. (1996) Abnormal spontaneous activity and responses to norepinephrine in dissociated dorsal root ganglion cells after chronic nerve constriction. Pain *67*:391-397.

Phillips J.K., McLean A.J., and Hill C.E. (1998) Receptors involved in nerve-mediated vasoconstriction in small arteries of the rat hepatic mesentery. Br J Pharmacol *124*:1403-1412.

Phillips J.K., Vidovic M., and Hill C.E. (1996) α-adrenergic, neurokinin and muscarininc receptors in rat mesenteric artery; an mRNA study during postnatal development. Mech Ageing Dev *92*:235-246.

Pintér E., Helyes Z., Pethö G., and Szolcsányi J. (1997) Noradrenergic and peptidergic sympathetic regulation of cutaneous microcirculation in the rat. Eur J Pharmacol *325*:57-64.

Pitcher G.M., Ritchie J., and Henry J.L. (1999) Nerve constriction in the rat: model of neuropathic, surgical and central pain. Pain *83*:37-46.

Polak J.M. and Bloom S.R. (1981) The peripheral substance P-ergic system. Peptides *Suppl 2*:133-148.

Pollard A.A. and Beck L. (1971) The distinct nature of the sustained dilator system: evidence against the pseudo transmitter hypothesis. J Pharm Exp Therap *179*:132-143.

Porreca F., Lai J., Bian D., Wegert S., Ossipov M.H., Eglen R.M., Kassotakis L., Novakovic S., Rabert D.K., Sangameswaran L., and Hunter J.C. (1999) A comparison of the potential role of the tetrodotoxin-insensitive sodium channels, PN3/SNS and NaN/SNS2, in rat models of chronic pain. Proc Natl Acad Sci USA *96*:7640-7644.

Quyyumi A.A., Mulcahy D., Andrews N.P., Husain S., Panza J.A., and Cannon R.O. (1997) Coronary vascular nitric oxide activity in hypertension and hypercholesterolemia. Circulation *95*:104-110.

Ralevic V., Khalil Z., Helme R.D., and Dusting G.J. (1995) Role of nitric oxide in the actions of substance P and other mediators of inflammation in rat skin microvasculature. Eur J Pharmacol *284*:231-239.

Ramer M.S. and Bisby M.A. (1997) Rapid sprouting of sympathetic axons in dorsal root ganglia of rats with a chronic constriction injury. Pain *70*:237-244.

Ramer M.S. and Bisby M.A. (1998) Differences in sympathetic innervation of mouse DRG following proximal or distal nerve lesions. Exp Neurol *152*:197-207.

Ramer M.S., French G.D., and Bisby M.A. (1997) Wallerian degeneration is required for both neuropathic pain and sympathetic sprouting. Pain *72*:71-78.

Ramer M.S., Kawaja M.D., Henderson J.T., Roder J.C., and Bisby M.A. (1998) Glial overexpression of NGF enhances neuropathic pain and adrenergic sprouting into DRG following chronic sciatic constriction in mice. Neurosci Lett *251*:53-56.

Ramer M.S., Thompson S.W.N., and McMahon S.B. (1999) Causes and consequences of sympathetic basket formation in dorsal root ganglia. Pain *suppl 6*:S111-S120.

Rand M.J. and Varma B. (1970) Effects of cholinomimetic drugs on responses to sympathetic nerve stimulation and noradrenaline in the the rabbit ear artery. Br J Pharmacol *38*:758-770.

Rand M.J. and Varma B. (1971) Effects of muscarinic agonist McN-A-343 on responses to sympathetic nerve stimulation in the rabbit ear artery. Br J Pharmacol *43*:536-542.

Rang H.P. , and Dale M.M. (1991) Pharmacology. New York: Churchill Livingstone.

Rawdon B.B. and Dockray G.J. (1982) Effects of conditioned media on extension and substance P-immunoreactive neurites from cultured mouse sensory ganglia. Neurosci Lett *34*:159-164.

Rhodin J.A. (1967) The ultrastructure of mammalian arterioles and precapillary sphincters. J Ultrastruct Res *18*:181-223.

Rhodin J.A. (1968) Ultrastructure of mammalian venous capillaries, venules and small collecting venules. J Ultrastruct Res *25*:452-500.

Rhodin J.A.G. (1974) Histology; a textbook and atlas. New York: Oxford University Press.

Riaz S.S. and Tomlinson D.R. (1996) Neurotrophic factors in peripheral neuropathies: pharmacological strategies. Prog Neurobiol *49*:125-143.

Ribeiro-da-Silva A. (1995) Substantia gelatinosa of spinal cord. In Anonymous (ed): The rat nervous system. Sydney: Academic Press, pp. 47-59.

Ribeiro-da-Silva A., Kenigsberg R.L., and Cuello A.C. (1991) Light and electron microscopic distribution of nerve growth factor receptor-like immunoreactivity in the skin of the rat lower lip. Neuroscience *43*:631-646.

Ribeiro-da-Silva A., Priestley J.V. , and Cuello A.C. (1993) Pre-embedding ultrastructural immunocytochemistry. In Cuello A.C. (ed): Immunohistochemistry II. Chichester: John Wiley & Sons, pp. 181-227.

Rice F.L., Albers K.M., Davis B.M., Silos-Santiago I., Wilkinson G.A., LeMaster A.M., Ernfors P., Smeyne R.J., Aldskogius H., Phillips H.S., Barbacid M., DeChiara T.M, Yancopoulos G.D., Dunne C.E., and Fundin B.T. (1998) Differential dependency of unmyelinated and Aδ epidermal and upper dermal innervation on neurotrophins, trk receptors, and $p75^{LNGFR}$. Dev Biol *198*:57-81.

Rice F.L. and Rasmusson D.D. (2000) Innervation of the digit on the forepaw of the racoon. J Comp Neurol *417*:467-490.

Rich K.M., Yip H.K., Osborne P.A., Schmidt R.E., and Johnson Jr.E.M. (1984) Role of nerve growth factor in the adult dorsal root ganglia neuron and its response to injury. J Comp Neurol *230*:110-118.

Roberts W.J. (1986) A hypothesis on the physiological basis for causalgia and related pains. Pain *24*:297-311.

Rolewicz T.F. and Zimmerman B.G. (1972) Peripheral distribution of cutaneous sympathetic vasodilator system. Am J Physiol *223*:939-944.

Ross G. (1971) The regional circulation. Annual Rev Physiol *33*:445-478.

Rowden G. (1977) Immunoelectron microscopic studies of surface receptors and antigens of human Langerhans cells. Br J Dermatol *97*:593-608.

Rowell L.B. (1977) Reflex control of the cutaneous vasculature. J Invest Dermatol *69*:154-166.

Ruocco I., Cuello A.C., and Ribeiro-da-Silva A. (2000) Peripheral nerve injury leads to the establishment of a novel pattern of sympathetic fibre innervation in the rat skin. J Comp Neurol *422*:287-296.

Ruocco I., Ramien M., St.Louis M., Cuello A.C., and Ribeiro-da-Silva A. (2001) Parasympathetic nerve fibres invade the upper dermis following sensory denervation of rat lower lip skin. Soc Neurosci Abstr *27*:In press.

Sann H., Pintér E., Szolcsányi J., and Pieraw Fr.K. (1988) Peptidergic afferents might contribute to the regulation of skin blood flow. Agents Actions *3*:14-15.

Saria A. (1984) Substance P in sensory nerve fibres contribute to the development of oedema in the rat hind paw after thermal injury. Br J Pharmacol *82*:217-222.

Saria A., Lundberg J.M., Skofitsch G., and Lembeck F. (1983) Vascular protein leakage in various tissues induced by substance P, capsaicin, bradykinin, serotonin, histamine and by antigen challenge. Naunyn-Schmied Arch Pharmacol *324*:212-218.

Sato F., Lavallée P., Lévesque M., and Parent A. (2000) Single-axon tracing study of neurons of the external segment of the globus pallidus in primate. J Comp Neurol *417*:17-31.

Sato J. and Perl E.R. (1991) Adrenergic excitation of cutaneous pain receptors induced by peripheral nerve injury. Science *251*:1608-1610.

Schaible H.-G. and Schmidt R.F. (1988) Excitation and sensitization of fine articular afferents from cat's knee joint by prostaglandin E2. J Physiol (London) *403*:91-104.

Schäfer M.K.-H., Eiden L.E., and Weihe E. (1998) Cholinergic neurons and terminal fields revealed by immunohistochemistry for the vesicular acetylcholine transporter. II. The peripheral nervous system. Neuroscience *84*:361-376.

Schäfer M.K.-H., Schütz B., Weihe E., and Eiden L.E. (1997) Target-independent cholinergic differentiation in the rat sympathetic nervous system. Proc Natl Acad Sci USA *94*:4149-4154.

Schon F. (1985) Postsympathectomy pain and changes in sensory neuropeptides: towards an animal model. Lancet *2*:1158-1160.

Schwartzman R.J. (1992) Reflex sympathetic dystrophy and causalgia. Neurologic Clin *10*:953-973.

Schwartzman R.J. (1993) Reflex sympathetic dystrophy. Curr Opin Neurol Neurosurg *6*:531-536.

Schwartzman R.J. and McLellan T.L. (1987) Reflex sympathetic dystrophy: a review. Arch Neurol *44*:555-561.

Scofitch G., Donnerer J., Petronijevic S., Saria A., and Lembeck F. (1983) Release of histamine by neuropeptides from the perfused rat hindquarter. Naunyn-Schmied Arch Pharmacol *322*:153-157.

Seltzer Z., Dubner R., and Shir Y. (1990) A novel behavioral model of neuropathic pain disorders produced in rats by partial sciatic nerve injury. Pain *43*:205-218.

Semenenko F.M., Bramwell S., Sidebottom E., and Cuello A.C. (1985) Development of a mouse antiperoxidase secreting hybridoma for use in the production of a mouse PAP complex for immunocytochemistry and as a parent cell line in the development of hybrid hybridomas. Histochemistry *83*:405-408.

Serbert M.E. and Shooter E.M. (1993) Expression of mRNA for neurotrophic factors and their receptors in the rat dorsal root ganglion and sciatic nerve following nerve injury. J Neurosci Res *36*:357-367.

Sheen K. and Chung J.M. (1993) Signs of neuropathic pain depend on signals from injured nerve fibers in a rat model. Brain Res *610*:62-68.

Sherbourne C.D., Gonzales R., Goldyne M.E., and Levine J.D. (1992) Norepinephrine-induced increase in sympathetic neuron-derived prostaglandins is independent of neuronal release mechanisms. Neurosci Lett *139*:188-190.

Shi T.-J.S., Winzer-Serhan U., Leslie F., and Hökfelt T. (2000) Distribution and regulation of α_2-adrenoceptors in rat dorsal root ganglia. Pain *84*:319-330.

Shigemoto R., Nakaya Y., Nomura S., Ogawa-Meguro R., Ohishi H., Kaneko T., Nakanishi S., and Mizuno N. (1993) Immunocytochemical localization of rat substance P receptor in the striatum. Neurosci Lett *153*:157-160.

Shimizu T., Koto A., Suzuki N., Morita Y., Takao M., Otomo S., and Fukuuchi Y. (1999) Occurrence and distribution of substance P receptors in the cerebral blood vessels of the rat. Brain Res *830*:372-378.

Shir Y. and Seltzer Z. (1991) Effects of sympathectomy in a model of causalgiform pain produced by partial sciatic nerve injury in rats. Pain *45*:309-320.

Skofitsch G. and Jacobowtiz D.M. (1985) Calcitonin gene-related peptide coexists with substance P in capsaicin sensitive neurons and sensory ganglia of the rat. Peptides *6*:747-754.

Skofitsch G., Savitt J.M., and Jacobowtiz D.M. (1985) Suggestive evidence for a functional unit between mast cells and substance P fibres in the rat diaphragm and mesentery. Histochemistry *2*:5-8.

Snider W.D. and McMahon S.B. (1998) Tackling pain at the source: new ideas about nociceptors. Neuron *20*:629-632.

Somogyi P., Halasy K., Somogyi J., Storm-Mathisen J., and Ottersen O.P. (1986) Quantification of immunogold labelling reveals enrichment of glutamate in mossy and parallel fiber terminals in cat cerebellum. Neuroscience *19*:1045-1050.

Souslova V., Cesare P., Ding Y., Akopian A.N., Stanfa L., Suzuki R., Carpenter K.Dickenson A., Boyce S., Hill R., Nebenius- Oosthuizen D., Smith A.J.H., Kidd E.J., and Wood J.N. (2000) Warm-coding deficits and aberrant inflammatory pain in mice lacking $P2X_3$ receptors. Nature *407*:1015-1017.

Stanton-Hicks M., Jänig W., Hassenbusch S., Haddox J.D., Boas R., and Wilson P. (1995) Reflex sympathetic dystrophy: changing concepts and taxonomy. Pain *63*:127-133.

Starke K. (1977) Regulation of noradrenaline release by presynaptic receptor systems. Rev Physiol, Biochem & Pharmacol *77*:1-124.

Stjärne P., Rinder J., and Delay-Goyet P. (1994) Effects of NK_1 receptor antagonists on vasodilation induced by chemical and electrical activation of sensory C-fibre afferents in different organs. Acta Physiol Scand *152*:153-161.

Streit W.J., Schulte B.A., Balentine J.D., and Spicer S.S. (1986) Evidence for glycoconjugate in nociceptive primary sensory neurons and its origin from the Golgi complex. Brain Res *377*:1-17.

Suresh M.R., Cuello A.C., and Milstein C. (1986) Advantages of bispecific hybridomas in one-step immunocytochemistry and immunoassays. Proc Natl Acad Sci USA *83*:7989-7993.

Szolcsányi J. (1988) Antidromic vasodilatation and neurogenic inflammation. Agents Actions *23*:4-11.

Szolcsányi J. (1991) Perspectives of capsaicin-type agents in pain therapy and research. In Parris W.C.V. (ed): Contemporary Issues in Chronic Pain Management. Norwell: Kluwer Academic, pp. 97-122.

Szolcsányi J., Pintér E. , and Pethö G. (1992) Role of unmyelinated afferents in regulation of microcirculation and its chronic distortion after trauma and damage. In Jänig W. and Schmidt R.F. (eds): Reflex sympathetic dystrophy pathophysiological mechanisms and clinical implications. Weinheim: VCH Verlaggesellschaft, pp. 245-273.

Tainio H., Vaalasti A., and Rechardt L. (1987) The distribution of substance P-, CGRP-, galanin- and ANP-like immunoreactive nerves in human sweat glands. Histochem J *19*:375-380.

Taniuchi M., Clark H.B., and Johnson E.M. (1986) Induction of nerve growth factor receptor in Schwann cells after axotomy. Proc Natl Acad Sci USA *83*:4094-4098.

Tarpley J.W., Martin W.J., Baldwin B.S., Forrest M.J., and MacIntyre D.E. (2000) Contribution of IB4-positive sensory neurons to NGF-induced hyperalgesia in the rat. Soc Neurosci Abstr *26*:1693.

Tausk F. and Undem B. (1995) Exogenous but not endogenous substance P releases histamine from isolated human skin fragments. Neuropeptides *29*:351-355.

Thomas P.K. (1999) Diabetic peripheral neuropathies: their cost to patient and society and the value of knowledge of risk factors for development of interventions. Eur Neurol *41*:35-43.

Tominaga M., Caterina M.J., Malmberg A.B., Rosen T.A., Gilbert H., Skinner K., Raumann B.E., Basbaum A.I., and Julius D. (1998) The cloned capsaicin receptor integrates multiple pain-producing stimuli. Neuron *21*:531-543.

Tracey D.J., Cunningham J.E., and Romm M.A. (1995) Peripheral hyperalgesia in experimental neuropathy: mediation by α2-adrenoreceptors on post-ganglionic sympathetic terminals. Pain *60*:317-327.

Tron V.A., Coughlin M.D., Jang D.E., Stanisz J., and Saunder D.N. (1990) Expression and modulation of nerve growth factor in murine keratinocytes (PAM 212). J Clin Invest *85*:1085-1089.

Tuttle J.B., Etheridge R., and Creedon D.J. (1993) Receptor-mediated stimulation and inhibition of nerve growth factor secretion by vascular smooth muscle. Exp Cell Res *208*:350-361.

Uvnäs B. (1966) Cholinergic vasodilator nerves. Federation Proc *25*:1618-1622.

Uvnäs B. (2000) Cholinergic muscle vasodilatation. In Bartorelli C. and Zanchetti A. (eds): Cardiovascular regulation in health and disease: recent advances in physiology, diagnosis and treatment of cardiovascular diseases. Milan: Instituto di Ricerche Cardiovascolari, pp. 63-70.

Vanhoutte P.M. and Shepherd J.T. (1973) Venous relaxation caused by acetylcholine acting on the sympathetic nerves. Circ Res *XXXII*:259-267.

Verdú E. and Navarro X. (1997) Comparison of immunohistochemical and functional reinnervation of skin and muscle after peripheral nerve injury. Exp Neurol *146*:187-198.

Verzé L., Paraninfo A., Ramieri G., Viglietti-Panzica C., and Panzica G.C. (1999) Immunocytochemical evidence of plasticity in the nervous structures of the rat lower lip. Cell Tissue Res *297*:203-211.

Von Banchet G.S. and Schaible H.G. (1999) Localization of neurokinin 1 receptors on a subset of substance P-positive and isolectin B4-negative dorsal root ganglion neurons of the rat. Neurosci Lett *274*:175-178.

von Euler U.S. and Gaddum J.H. (1931) An unidentified depressor substance in certain tissue extracts. J Physiol (London) *72* :74-86.

Vos P., Stark F., and Pittman R.N. (1991) Merkel cells *in vitro*: production of nerve growth factor and selective interactions with sensory neurons. Dev Biol *144*:281-300.

Wakisaka S., Kajander K.C., and Bennett G.J. (1991) Abnormal skin temperature and abnormal sympathetic vasomotor innervation in an experimental painful peripheral neuropathy. Pain *46*:299-313.

Wallengren J., Ekman R., and Sundler F. (1987) Occurrence and distribution of neuropeptides in the human skin. An immunochemical and immunocytochemical study on normal skin and blister fluid from inflammed skin. Acta Derma Venereal (Stockholm) *67*:185-192.

Waxman S.G., Dib-Hajj S., Cummins T.R., and Black J.A. (1999) Sodium channels and pain. Proc Natl Acad Sci USA *96*:7635-7639.

Weihe E., Tao-Cheng J.-H., Schäfer M.K.-H., Erickson J.D., and Eiden L.E. (1996) Visualization of the vesicular acetylcholine transporter in cholinergic nerve terminals and its targeting to a specific population of small synaptic vesicle. Proc Natl Acad Sci USA *93*:3547-3552.

Wells M.R., Vaidya U., and Schwartz J.P. (1994) Bilateral phasic increases in dorsal root ganglia nerve growth factor synthesis after unilateral sciatic nerve crush. Exp Brain Res *101*:53-58.

Wiesenfeld-Hallin Z., Hökfelt T., Lundberg J.M., Forssmann W.G., Reinecke M., Tschopp F.A., and Fischer J.A. (1984) Immunoreactive calcitonin gene-related peptide and substance P co-exist in sensory neurons to the spinal cord and interact in spinal behavioral responses of the rat. Neurosci Lett *52*:199-204.

Wiesner-Henzel L., Schulz B., Vakilzadeh F., and Czarnetzki B.M. (1981) Electron microscopical evidence for a direct contact between nerve fibres and mast cells. Acta Derma Venereal (Stockholm) *61*:465-469.

Williams M. (1984) The dynamics of desquamation. Lessons to be learned from ichthyoses. Am J Dematopath *6*:381-385.

Winkelmann R.K., Sheen S.R., and Pyka R.A.Jr. (1961) Cutaneous vascular patterns in studies with injection preparations and alkaline phosphatase reactions. Adv Biol Skin *2*:1-19.

Wolff K. and Stingl G. (1983) The Langerhans cell. J Invest Dermatol *80*:S17-S21

Wong G.Y. and Wilson P. (1997) Classification of complex regional pain syndromes. Hand Clinics *13*:319-325.

Woolf C.J. and Doubell T.P. (1994) The pathophysiology of chronic pain - increased sensitivity to low threshold A beta-fibre inputs. Curr Opin Neurobiol *4*:525-534.

Woolf C.J. and Mannion R.J. (1999) Neuropathic pain: aetiology, symptoms, mechanisms, and management. Lancet *353*:1959-1964.

Woolf C.J., Shortland P., and Coggeshall R.E. (1992) Peripheral nerve injury triggers sprouting of myelinated afferents. Nature *355*:75-78.

Xiang Z., Bo X., and Burnstock G. (1998) Localization of ATP-gated P2X receptor immunoreactivity in rat sensory and sympathetic ganglia. Neurosci Lett *256*:105-108.

Xu M., Kontinen V.K., and Kalso E. (1999) Endogenous noradrenergic tone controls symptoms of allodynia in the spinal nerve ligation model of neuropathic pain. Eur J Pharmacol *366*:41-45.

Yaksh T.L., Hua X.-Y., Kalcheva I., Nozaki-Taguchi N., and Marsala M. (1999) The spinal biology in humans and animals of pain states generated by persistent small afferent input. Proc Natl Acad Sci USA *96*:7680-7686.

Yamamoto K., Matsuyama T., Shiosaka S., Inagaki S., Senba E., Shimizu Y., Ishimoto I., Hayakawa T., Matsumoto M., and Tohyama M. (1983) Overall distribution of substance P-containing nerves in the wall of the cerebral arteries of the guinea pig and its origins. J Comp Neurol *215*:421-426.

Yano H., Wershil B.K., Arizono N., and Galli S.J. (1989) Substance P-induced augmentation of cutaneous vascular permeability and granulocyte infiltration in mice is mast cell dependent. J Clin Invest *84*:1276-1286.

Yodlowski M.L., Fredieu J.R., and Landis S.C. (1984) Neonatal 6-hydroxydopamine treatment eliminates cholinergic sympathetic innervtaion and induces sensory sprouting in rat sweat glands. J Neurosci *4*:1535-1548.

Yonehara N., Chen J.-Q., Imai Y., and Inoki R. (1992) Involvement of substance P present in primary afferent neurons in modulation of cutaneous blood flow in the instep of rat hind paw. Br J Pharmacol *106*:256-262.

Yonehara N., Takiuchi S., Imai Y., Tang F.-D., and Inoki R. (1993) Involvement of substance P in small-diameter afferent fibres in microcirculatory hemodynamics of the rat hind instep. Regul Pep *46*:220-222.

Yoon Y.W., Lee D.H., Lee B.H., Chung K., and Chung J.M. (1999) Different strains and substrains of rats show different levels of neuropathic pain behaviors. Exp Brain Res *129*:167-171.

Yoon Y.W., Na H.S., and Chung J.M. (1996) Contributions of injured and intact afferents to neuropathic pain in an experimental rat model. Pain *64*:27-36.

Zhang S.Q., Terenghi G., Unger W.G., Ennis K.W., and Polak J. (1984) Changes in substance P- and neuropeptide Y-immunoreactive fibres in rat and guinea-pig irides following unilateral sympathectomy. Exp Eye Res *39*:365-372.

Zhou L., Zhang Q., Stein C., and Schäfer M. (1998) Contribution of opioid receptors on primary afferent versus sympathetic neurons to peripheral opioid analgesia. J Pharm Exp Therap *286*:1000-1006.

Zhu B.-S., Blessing W.W., and Gibbins I.L. (1997) Parasympathetic innervation of cephalic arteries in rabbits: comparison with sympathetic and sensory innervation. J Comp Neurol *389*:484-495.

Zimmerman B.G. and Whitmore L (1967) Transmitter release in skin and muscle blood vessels during sympathetic stimulation. Am J Physiol *212*:1043-1054.

NQ

75678

INFORMATION TO USERS

This manuscript has been reproduced from the microfilm master. UMI films the text directly from the original or copy submitted. Thus, some thesis and dissertation copies are in typewriter face, while others may be from any type of computer printer.

The quality of this reproduction is dependent upon the quality of the copy submitted. Broken or indistinct print, colored or poor quality illustrations and photographs, print bleedthrough, substandard margins, and improper alignment can adversely affect reproduction.

In the unlikely event that the author did not send UMI a complete manuscript and there are missing pages, these will be noted. Also, if unauthorized copyright material had to be removed, a note will indicate the deletion.

Oversize materials (e.g., maps, drawings, charts) are reproduced by sectioning the original, beginning at the upper left-hand corner and continuing from left to right in equal sections with small overlaps.

ProQuest Information and Learning
300 North Zeeb Road, Ann Arbor, MI 48106-1346 USA
800-521-0600

ELECTRODE EROSION AND ARC STABILITY IN TRANSFERRED ARCS WITH GRAPHITE ELECTRODES

A Thesis by Hongsun Seon

Department of Chemical Engineering
McGill University

Under the Supervision of Prof. R.J. Munz

A thesis submitted to the Faculty of Graduate Studies and Research
of McGill University in partial fulfillment of the requirements
for the degree of Doctor of Philosophy

McGill University
Montreal, Canada

April 2001

ABSTRACT

Arc stability and erosion behavior were studied on a hollow graphite DC cathode in an argon atmosphere at atmospheric pressure. It was found that the arc stability is associated with the electron emission mode transition of the cathode operation. Estimation of current densities, SEM pictures, Fast Fourier Transform (FFT) of total voltage, and measurement of cathode surface temperature supported this. Stable arcs are in the thermionic emission regime while unstable arcs in the thermofield emission regime. Higher argon gas flow rate is believed to cause the shift of the mode from the thermofield emission to the thermionic emission by increasing the arc root temperature through steepening the thermal gradient at the arc root and increasing ionization phenomena inside the arc. Sharp cathode tip geometry usually leads to the thermionic emission while a rounded tip geometry encourages the thermofield emission. For the unstable arcs, the high voltage fluctuation resulted from the jumping of the arc root between different cathode spots and changes in the arc length. In the stable arcs, however, the voltage was almost constant because of the absence of arc jumping. The standard deviation of the voltage was used as the arc stability indicator and was less than 3 V for the stable arc in this transferred arc system.

The erosion rate of the cathode in this work ranged from 0.41 to 2.61 μg/C. At 150 A runs the arc stability strongly influenced the erosion rate; as the arc stability increased, the erosion rate decreased. Higher currents runs (300 and 400 A), however, showed the opposite trend because of the carbon vapor redeposition. The total erosion rates of 150 A runs were separated into the stable (E_s) and the unstable (E_u) erosion rate. The E_u was more than 3 times higher in this work. It is believed that the thermofield emission of the

unstable arcs produced more erosion because of the higher local heat flux to the cathode spots.

Résumé

La stabilité d'un arc électrique en courant continu et son comportement quand à l'érosion des électrodes est étudié sur une cathode creuse de graphite à pression atmosphérique fonctionnant en mode d'arc transféré. Dans notre étude, la stabilité de l'arc est associée à une transition du régime d'émission électronique à la cathode. Ces résultats sont en accord avec les estimations de la densité de courant à la cathode et avec une série de données expérimentales telles les observations par microscopie électronique (SEM), les signaux de tension et leur transformée de Fourrier (FFT), et les mesures de température de surface de la cathode. Les arcs stables fonctionnent en régime d'émission thermionique à la cathode alors que les arcs instables fonctionnent en régime thermo-champ. Un changement du mode d'émission passant du mode thermo-champ vers une émission thermionique est observé pour des débits d'argon plus élevé. Ce changement de régime est attribué à une augmentation de température au pied cathodique de l'arc suite au gradient thermique plus important induits dans cette région, et à une augmentation du phénomène d'ionisation dans la colonne d'arc. Habituellement, une cathode à tige pointue mène vers une émission thermionique, alors qu'un bout à géométrie hémisphérique favorise un régime thermo-champ. Les fluctuations importantes de la tension d'arc dans le cas des arcs instables sont attribués aux sauts du pied d'arc vers différents spots cathodiques d'émission et à des changements dans la longueur de l'arc. La tension d'arc reste cependant essentiellement constante dans le cas d'arcs stables et aucun saut d'arc n'est alors observé. L'écart type sur les fluctuations de tension est utilisé comme indicateur de stabilité de l'arc électrique. Cette écart type est moins de 3 V pour les arcs stables dans le présent système à arc transféré.

Les taux d'érosion de la cathode dans cette étude varient entre 0.41 et 2.61 μg/C. Pour des essais

à 150 A, la stabilité de l'arc influence grandement le taux d'érosion. Le taux d'érosion observé décroit alors lorsque la stabilité de l'arc augmente. Les essais à plus forts courants (300 et 400 A) montrent cependants une tendance inverse attribuée à une re-déposition des vapeurs de carbone. Le taux d'érosion des essais effectués à 150 A sont séparés en taux d'érosion en mode stable (E_s) et instables (E_u). Les valeurs observées durant la période instable (E_u) sont plus du triple des valeurs observées en période stable E_s. L'érosion élevée observé pour les arcs instables opérant en mode thermo-champ est attribué aux flux thermique locaux plus importants au niveau des spots cathodiques.

ACKNOWLEDGMENTS

To Professor R.J. Munz for giving an opportunity to study thermal plasma technology and his supervision with patience.

To Professor J.-L. Meunier for his good introduction course of arc physics and many comments.

To the members of the Chemical Engineering staff: P. Fong, A. Prihoda, J. Terrasi, L. Miller-Aspin, B. Hanley, L. Cusmich, A. Gagnon, W. Greenland, C. Dolan, E. Siliauskaus, B. Habib, and F. Caporuscio.

To the members of the plasma group: Tony Addona, Antonio Carlos da Cruz, Julie Filion, Patrice Nadeau, Munther Kandah, Jorg Oberste-Berghaus, Karen Sum, Sylvain Coulombe, Harbec David, Jun Yu, Alison Hanstead, Honqin Liu, Felipe Aristzabal, and Sakamon Devahastin for the useful discussions.

To summer student Arash Hooshangi for help with the experiments, the SEM analysis, and arc pictures.

To Helen Campbell for help with the SEM analysis.

To Saverio Biunno for help with the oscilloscope analysis.

To the Natural Sciences and Engineering Research Council of Canada for the financial support.

To my father for the love and the support.

To my wife Mihyune for her understanding and caring Minji and Minho.

TABLE OF CONTENTS

LIST OF FIGURES

LIST OF TABLES

CHAPTER I

GENERAL INTRODUCTION

The selection of the right thermal plasma torch is very important for the commercial viability of plasma processes. The designer of thermal plasma furnaces should deal not only with torch efficiency and electrode life but also consider the best combination of torches and furnaces for an application.

This study focuses on hollow graphite DC cathodes which are believed to be one of the most promising torch systems for the treatment of many solid wastes as well metallurgical processing. Their potential advantages include safety, high energy efficiency, compact design, and ease of scale-up.

This work was designed to study the behavior of hollow graphite cathodes including the arc electrical behavior, erosion rate, and the spontaneous transition between thermionic and thermofield electron emission. Although previous work on hollow AC electrodes has been done regarding applications in the metallurgical industries, it was believed that further study of these phenomena is needed for better understanding. The previous work concentrated on overall electrode consumption but did not examine the effects of mode transition. The erosion in at least some of those studies was the result of a combination of chemical reaction and erosion due to arc effects and was complicated by the presence of a metal bath and poorly controlled atmosphere. The present work uses graphite electrodes in a well-controlled atmosphere.

This thesis starts with a literature review on arc cathodic phenomena, considerations of arc stability of hollow graphite electrodes and erosion of graphite electrodes. Industrial

applications of hollow graphite electrodes are also included. This is followed by the research objectives and the experimental methods used in this study. Chapter V presents brief thermodynamic study to identify the carbon species expected to be found in the arc atmosphere. Chapter VI on results and discussion first characterizes the arc and examines the emission mode transition. This is followed by an examination of the erosion rates of the cathode and finally the development of a correlation for erosion as a function of operating conditions under stable conditions. The last chapter gives conclusions, recommendations for further work, and contributions to knowledge.

CHAPTER II

LITERATURE REVIEW

2.1. INTRODUCTION

The term "arc stability" here means the absence or the disappearance of acoustical and electrical noise of hollow graphite electrodes used in this work. The disappearance of both types of noise indicates stable arcs, and the appearance of both types of noise means unstable arcs. The arc stability is a cathodic phenomenon and is related to mode transition in arc cathode operation. Maddever et al. (1976) and Sommerville et al. (1987) reported that for hollow graphite electrodes, the arc stability as well as the consumption rate could be controlled by the argon gas flow rate. Higher argon gas flow rate provided stable arcs and lower consumption rates.

Recently Roth (1995) stated that mode transitions, from non-thermal to thermal arcs and spontaneous mode transitions of thermal arcs, is one of the present issues of arc physics and that "the industrial uses of arcs will not be well understood until such time as the physical processes responsible for mode transitions are identified, and the criteria for the onset of mode transitions are understood in a quantitative manner". Thus this work was designed to further study the mode transitions of thermal arcs using hollow graphite DC cathodes for better understanding of the arc stability. The arc stability is associated with the spontaneous mode transitions. It was also planned to study erosion behavior as a function of the arc stability. The difference between erosion and consumption is that erosion excludes the oxidation and the breakage of graphite electrodes.

In this section, hollow graphite electrodes and their related studies are reviewed. Firstly considerations for arc cathode phenomena connected with this work is introduced. In the

next part, typical use of graphite electrodes in electric arc furnaces (EAFs) is given. This is followed by previous work on the arc stability of hollow graphite electrodes. In addition, erosion of graphite electrodes is also included. Finally some industrial applications of hollow graphite DC cathodes are introduced.

2.2. ARC CATHODE PHENOMENA

2.2.1. Modes of High Pressure Arc Cathodes

In this part, characteristics of modes of cathode operation of high pressure arcs, as opposed to vacuum arcs, are introduced because this work has been performed at atmospheric pressure. Guile (1971), Anders et al. (1991), and Coulombe (1997) reviewed the operation modes of high pressure arcs, and a summary, based on their data, about some features of the modes of high pressure arcs is presented in Table 2-1. Coulombe (1997) defined high pressure arcs as arcs in which "the medium is composed of the ambient gas filling the chamber and to some extent, the electrode erosion products".

According to the review of Anders et al. (1991), the modes of high pressure arcs can be separated into the stationary and the nonstationary mode. The electron emission mechanism of the stationary mode is thermionic emission while that of the nonstationary mode is thermofield or field emission. The cathode electrode materials used for the stationary mode are high boiling point refractory materials, and for the nonstationary mode low-boiling point metals, such as copper and nickel, are used. They are also known as "hot cathode" and "cold cathode", respectively. Current density of the stationary mode ranges from $10^7 \sim 10^8$ A/m^2 while that of the nonstationary mode ranges from $10^{10} \sim 10^{11}$

Table 2-1: A summary of cathode operation modes of high pressure arcs.

Mode[2]	Stationary	Nonstationary
Mechanism of electron emission [1,2,3]	Thermionic emission	Thermofield or field emission
Type of cathode[1]	Refractory	Low boiling points metals
Typical materials[1]	W, C	Cu
Operating temperature [1]	> 3500 K	Wide range, generally below 3000 K
Current Density[1]	$10^7 \sim 10^8$ A/m^2	$10^{10} \sim 10^{11}$ A/m^2
Number of arc attachment points[3]	One and diffuse over a diameter of some mm	Several and constricted over diameters of 5 ~ 20 μm
Movement of the arc attachment[3]	Fixed or slow	Rapid
Voltage characteristics[2]	No fluctuation	Great fluctuation

Data Sources;

1. Guile (1971), 2. Anders et al. (1991), 3. Coulombe (1997)

A/m^2. For the stationary mode the number of arc attachment points is one, and it is diffuse over a diameter of some mm; however, for the nonstationary mode there are several arc attachment points constricted over diameters of 5 ~ 20 μm. The arc movement in the stationary mode is slow or nonexistent, but in the nonstationary mode the movement is rapid.

Conceptually, the arc attachment points introduced by Coulombe (1997) are the same as the arc roots on arc cathodes. In thermionic emission, the single arc attachment point is

the arc root. This is also termed "thermionic spot" by Anders et al. (1991). Hereafter the term "thermionic spot" is used to indicate the arc root in the thermionic emission. Otherwise, in the thermofield emission, the arc attachment points are made of macrospots, and these macrospots are composed of several cathode spots. Due to the different internal structure of the arc attachment points, different behaviors of the arc attachment points are observed. Hereafter the term "cathode spots" is used to point to the spots inside the macrospot in the thermofield emission.

The mode separation is basically related to electron emission mechanisms. In general arc cathodes can emit electrons through thermionic, thermofield, or field emission. Thermionic emission, which occurs when the cathode temperature is high and the field is low, is described by the Richardson-Dushman equation; the effects of intermediate fields on the thermionic emission are known as the Schottky effect which enhances electron emission from the cathode. Field emission occurs when the field is high and the cathode temperature is low, and is described by the Fowler-Nordheim equation. Dolan et al. (1954) reported that when both the cathode temperature and the field are high, the emission process is termed thermofield emission which is an intermediate state between the thermionic and the field emission. Most arcs have been recognized to be in the thermofield emission regime. In thermionic emission, electrons can escape from the electrode surface if they acquire sufficient energy to overcome the energy barrier. The energy is known as the work function. In field emission, electrons can tunnel the barrier because of the higher electric field.

Murphy and Good (1956) developed the generalized electron emission equation, which can be applied to the entire electron emission regimes. The equation shows that electron current density (J_e) is related to temperature, electric field strength and work function as follows:

$$J_e = e\int_{-W_a}^{\infty} D(E_c, W)N(T_c, W)dW \qquad (2\text{-}1)$$

where $D(E_c, W)$ is the emission probability for an electron with energy W, from the cathode surface material submitted to an electric field E_c and the cathode surface temperature T_c . $N(T_c, W)dW$ represents the number of electrons reaching the potential barrier per second and per unit area with energy between W and W+dW. W_a represents potential barrier energy. The Richardson-Dushman equation for the thermionic emission is a limit of the equation (2-1) when the temperature is high and the electric field is low while the Fowler-Nordheim equation for the field emission is also the limit when the temperature is low and the electric field is high. Coulombe et al. (1997) reported that the Murphy and Good equation should be used for the calculation of the thermofield emission current densities in order to increase the accuracy of numerical prediction for the arc-cathode interactions.

Anders and Jütter (1990) studied transition of the cathode mode in high pressure discharge lamps during the starting period. They used tungsten AC electrodes activated by $Ba_2CaW_3O_6$. The transition from the thermofield to the thermionic emission and vice versa is only expected to occur for hot cathodes. Guile (1971) also mentioned this mode

transition. Anders and Jütter (1990) reported that the arc of the high pressure discharge lamp was usually in the thermofield emission regime immediately after the glow-to-arc transition in each half-cycle after the initial breakdown as shown in Figure 2-1. The "vapor arc mode" in the figure means the thermofield emission regime. After a time of the order of one second, however, the electrodes were sufficiently heated and thus were operated in the thermionic emission regime. This transition was detected by the sudden disappearance of the burning voltage and the barium line emission noise. The great fluctuations of the arc voltage meant that the electrodes were in the thermofield emission regime.

2.2.2. THE CATHODE REGION

Figure 2-2 shows a schematic representation of the regions of an arc. Roth (1995) defined the cathode region as a region of "potential and density gradients, with an axial extent of perhaps $d_c \approx 1$ mm". This means that the cathode region is not in the local thermodynamic equilibrium (LTE) and is characterized by steep gradients of temperatures, particle densities, and electric field in a very thin layer between the cathode and the arc. In this figure, before the arc column region, Roth (1995) presents three regions, the cathode sheath, the cathode region, and the cathode flow zone. That could be different according to researchers. Some researchers like Zhou et al. (1994) and Coulombe (1997) who performed the modeling work in the cathode region considered the cathode region as the connection region between the cathode and the arc column. For the detailed description of this region, Coulombe (1997) subdivided the cathode region into the cathode sheath zone (or the space charge zone) and the ionization zone (or the

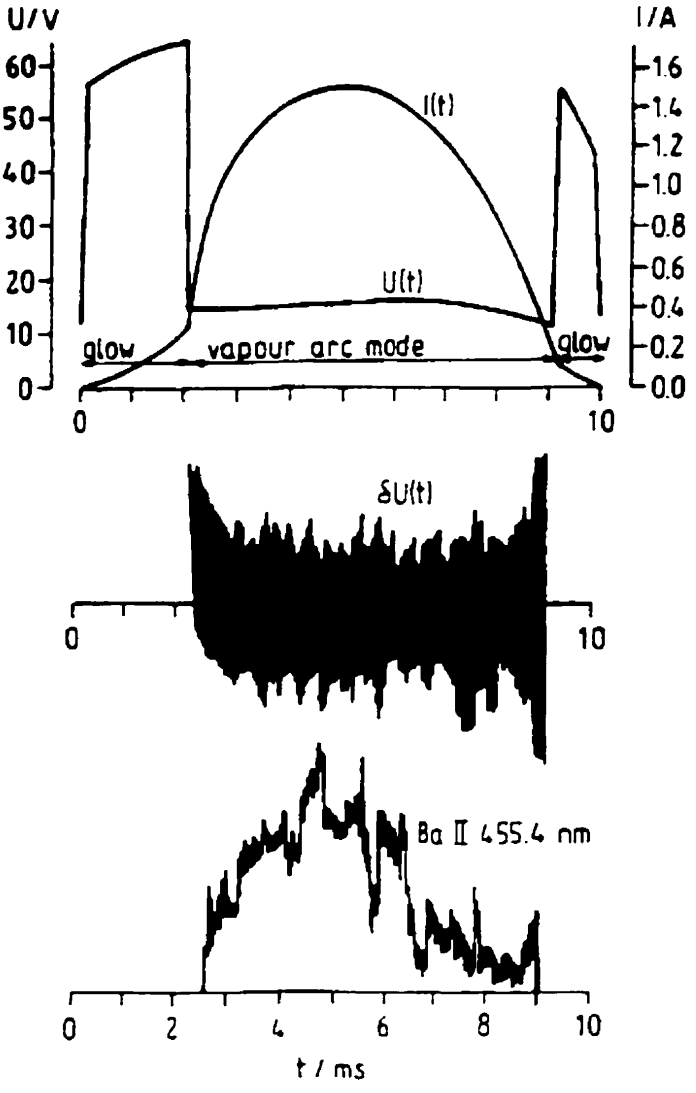

Figure 2-1: Sixth half-cycle of the current I(t), burning voltage U(t), noisy component δU(t) and barium line intensity of an electrode of a 70 W high-pressure sodium discharge lamp after the initial breakdown (Anders and Jütter 1990).

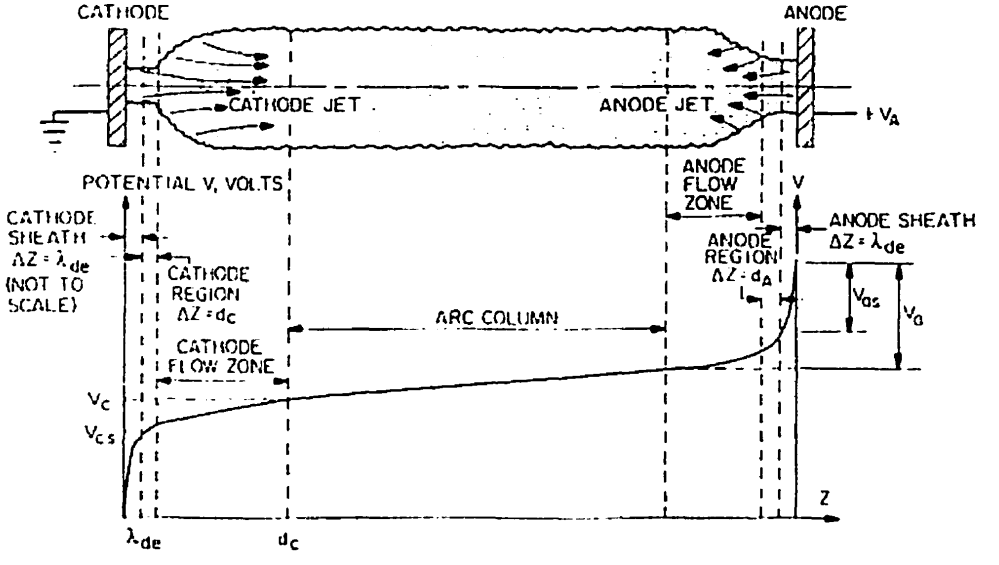

Figure 2-2: A schematic diagram of the regions of an arc (Roth 1995).

presheath zone). The cathode sheath zone can be thought as a collisionless zone, and the density of the positive ions is much greater than that of the emitted electrons because of faster movement of electrons. The positive space charge zone is, therefore, established and produces an electric field. The electric field strengths as well as the positive ion bombardment in the cathode region are recognized to be responsible for electron emission from arc cathodes.

In the cathode region, there are cathode jets which may exert a strong influence on the cathode region and sometimes on the entire arc. The cathode jets have been observed in hot as well as cold cathodes, particularly at higher current levels. Choi (1981) stated that these cathode jets might be attributed to four different sources: electromagnetically induced jets, vaporization of cathode material and/or surface impurities, ablation and explosive release of cathode material, and chemical reactions on the cathode surface producing gases. The interaction of the arc current with its own magnetic field leads to the phenomena of induced plasma jets in an arc section of variable cross section. These phenomena are not restricted to the cathode or anode region of an arc; they may also occur in other parts of the arc column where the conditions of variable column cross section are met. The induced cathode jet may serve as a stabilizing mechanism for a free-burning arc.

2.2.3. RANGES OF PHYSICAL PROPERTIES OF THE SPOTS

Even though numerous researches on thermionic and cathode spots have been reported, it is still difficult to find general agreement. This part, therefore, focuses on the ranges of

physical properties of the spots; these are size, current density, and lifetime of the spots. The properties are dynamic and based on experimental results through arc tracks.

1) Size of the spots

Generally the size of the thermionic spot is bigger. According to Anders et al.'s (1991) survey on arcs in a pressure range from ultrahigh vacuum (UHV) to 10^7 Pa and in a current range from 0.1 to 10^5 A, for high pressure arcs in the thermionic regime, the thermionic spot area is between 0.1 and 10 mm^2. By assuming the thermionic spot is a circle, the diameter of the thermionic spot may be estimated to be between 0.4 and 3.6 mm. For low pressure arcs in the thermionic emission regime, they reported the range of the thermionic spot area of 0.01 ~ 1 cm^2 ; this range corresponds to a circle diameter of 1.1 ~ 11.3 mm.

For high pressure arcs in the thermofield emission regime, Coulombe (1997) reported the craters of 5 ~10 μm-diameter and some of up to 25 μm-diameter uniformly distributed along the arc trace on the copper electrode. For vacuum arcs believed in the thermofield emission regime, Kandah (1997) reported the general range of the cathode spot diameter of 0.01 ~ 100 μm. Siemroth et al. (1995) provided more detailed information about the size in vacuum arcs. They reported that in a pressure range from 10^{-4} ~ 10^{-3} Pa, the size of a macrospot on the copper electrode is 100 μm and that of the cathode spots inside the macrospot is 10μm.

2) Current density of the spots

In the thermionic emission regime, Anders et al. (1991) gave the range of current density of $10^4 \sim 10^8$ A/m^2 for both low and high pressure arcs. For high pressure arcs the current density is between $10^7 \sim 10^8$ A/m^2 which is the same range as Guile (1971). For low pressure arcs the current density is between $10^4 \sim 10^7$ A/m^2.

For high pressure arcs in the thermofield emission regime, Guile (1971) reported the range of current density of $10^{10} \sim 10^{11}$ A/m^2 as introduced in Table 2-1. For vacuum arcs, Kandah (1997) gave the general range of current density of $10^6 \sim 10^{12}$ A/m^2.

Generally the current density in the thermofield emission regime is higher than that in the thermionic emission regime. In the thermionic emission regime, the current density can be estimated through total current divided by the thermionic spot area. For the thermofield emission regime, however, several cathode spots are in the arc attachment area, resulting in the splitting of the arc. Therefore, the current density in the thermofield emission regime is based on the individual spot area and the current delivered to each spot.

3) Lifetime scale of the spots

It is especially difficult to determine general lifetime scale of the spots, but the lifetime scale may be inferred through the arc movement. As mentioned earlier for the thermionic emission regime the arc movement is slow or fixed; however, for the thermofield emission regime the arc movement is rapid. These different types of arc movement are related to the lifetime scale of the spots because the spots are the sites of electron

emission.

For the thermionic emission regime, Anders et al. (1991) reported that for high pressure arcs, hopping of the thermionic spot may occur and the hopping frequency is about several Hertz. It can be inferred from the frequency that the lifetime scale of the thermionic spot may be a time of the order of decisecond. This time scale may be rough, but it can be seen that this scale is much bigger than the lifetime scale of the cathode spots in the thermofield emission regime, which is introduced in the next paragraph.

For the thermofield emission regime, the faster movement of arcs is associated with the cathode spots' extinction and reignition at new sites. This is one of the reasons for the voltage fluctuations of cold cathodes. Because arcs move irregularly, this is also referred to as "random walk". For the spots in the thermofield emission regime, two different lifetime scales are reported. One is the lifetime scale of the macrospots and the other is that of the cathode spots inside the macrospot spot. The lifetime scale of the macrospot in this regime, according to Coulombe's (1997) review, is much less than 1 ms scale and probably of the order of 1 μs. Meanwhile, Jütter (1997, 1999) reported the lifetime scale of the cathode spots is of the order of nanoseconds.

2.2.4. EROSION OF ARC CATHODES

Arc cathode erosion can be simply defined as vaporization of the cathode material and ejection of particles and molten cathode material mainly due to the localized excess heat which cannot be dissipated either by conduction through the cathode or radiation and

convection from the cathode surface. In general, arc cathode erosion is considered as a necessary physical phenomenon to maintain an arc for the thermofield emission and as a consequence of the strong heat load for the thermionic emission.

In the following part previous work related to the heat transfer at the cathode spot surface, performed at Plasma Technology Research Center (CRTP), McGill University is introduced. The heat transfer as well as the current transport is very important for erosion studies because it is related to the localized heat flux. In addition, Benilov's review (1999) about the heating of hot cathodes of high pressure arcs is also mentioned.

Szente et al. (1992), who studied the erosion of copper cathodes, noted that the arc heats the cathode in four different ways: radiation, convection (from the plasma), joule heating, and ion bombardment. Among them, the joule heating and the ion bombardment have been recognized as the main source of the heat input to the cathode. The positive ions directly transport their energy to the cathode spot as shown in Figure 2-3. The transported energy is lost by vaporization of the cathode material, electron emission cooling, and conduction within the cathode. Joule heating may be appreciable with a low conductivity cathode and in the very high current density regions near the emitting areas. The radiation and convection terms are too diffuse to cause erosion and can in general be neglected for most erosion studies.

Coulombe et al. (1997) calculated the magnitude of the different source of the heat flux at the cathode spot surface on a cold copper cathode. In their calculation, for the current

transport in the cathode sheath, they described that three charge carriers are related to the current transport to the cathode spot, respectively j_{ion} for the ions, j_{bde} for the back-diffusing electrons, and $j_{T\text{-}F}$ for the electrons emitted by the thermofield emission from the cathode as shown in Figure 2-3. For the energy balance on the cathode spot surface, they described that energy is transported to the cathode spot by the positive ions (q_{ion}) and back-diffusing electrons (q_{bde}); energy is lost by vaporization of the cathode material (q_{vap}), by electron emission cooling (q_{not}), and by conduction within the cathode (q_{cond}). Radiative heat exchanges from the cathode spot surface with the surroundings are ignored in comparison with the other heat fluxes. The results are presented in Table 2-2. It can be seen that the heat input to the cathode spot surface (q_{in}) is increased as the total current density (j_{tot}) is increased, and the ion bombardment is the dominant component of the heat input. For the heat loss, as the total current is increased, the electron emission cooling (q_{not}) is more important than the other heat fluxes of the heat loss. The vaporization of the cathode material (q_{vap}) is also increased, and this means increase of the erosion rate. Meanwhile, the importance of the conduction within the cathode (q_{cond}) is decreased as the total current increased.

For the heating of hot cathodes of high pressure arcs, Benilov (1999) stated that presently there is no general agreement on the dominating mechanism of the heat transfer to the thermionic spot. According to his review, for the main component of the heat input, some researchers believe that the hot cathode is mainly heated by the ion bombardment, while others consider that the thermal conduction from the arc is greater than the contribution of the ion bombardment. In any case it appears that further research about that is needed.

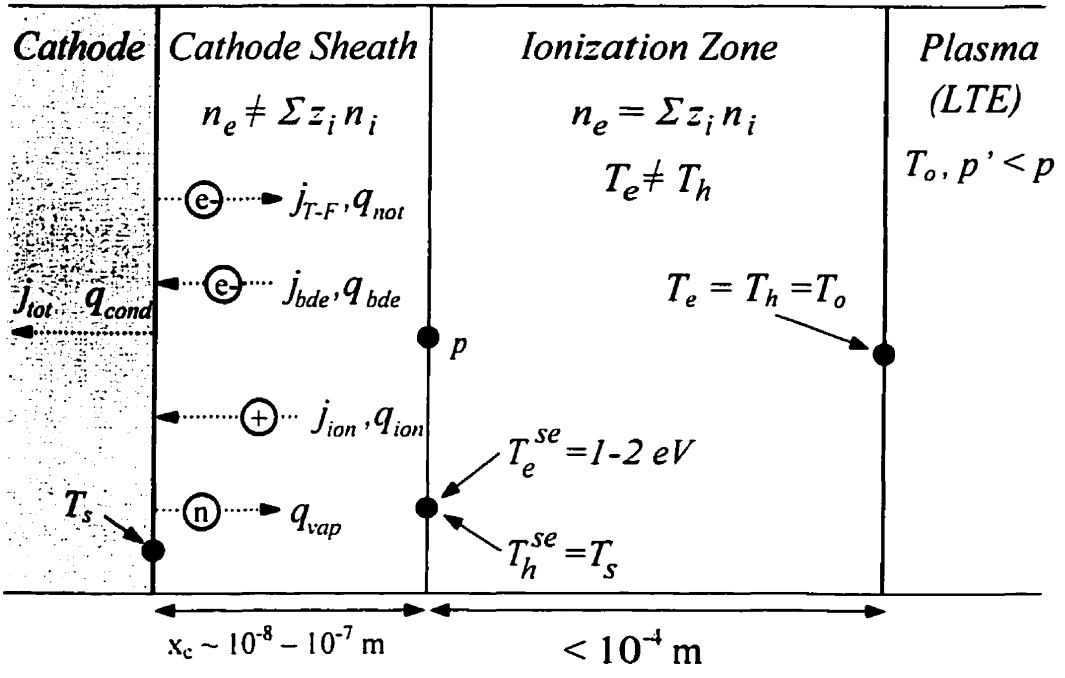

Figure 2-3: The cathode region prepared by Coulombe et al. for their modeling work (Coulombe et al. 1997).

Table 2-2: Distribution of the total heat flux to a single cathode spot on a cold Cu cathode for T_e at the cathode sheath edge = 1 eV (Coulombe et al. 1997).

V_c (V)	J_{tot} ($x10^9$ Am^{-2})	q_{in} ($x10^{10}$ Wm^{-2})	q_{ion}/q_{in}	q_{not}/q_{in}	q_{vap}/q_{in}	q_{cond}/q_{in}
7	1	1.18	0.95	0.07	0.27	0.66
7	5	3.48	0.95	0.31	0.30	0.39
7	10	5.28	0.95	0.46	0.31	0.23
15	1	1.54	~1	0.06	0.17	0.77
15	5	4.28	~1	0.26	0.18	0.56
15	10	5.93	~1	0.45	0.20	0.35

The erosion mechanism of arc cathodes is not yet understood perfectly because many physical phenomena occur in the very thin cathode region at the same time. The erosion phenomenon, however, may be explained by the following well-known three considerations: 1) evaporation of cathode material, 2) ejection of particles and droplets of molten cathode material, and 3) redeposition. Evaporation can be explained as being caused by the localized excess heat fluxes over the spot surface. Coulombe (1997) stated that ejection is mainly due to the ion pressure release upon the spot extinction and the onset of important thermo-capillary flows within the molten bath. Redeposition reduces the erosion rate of cathodes and may come from 1) by the condensation of vaporized cathode atoms existing in the vicinity of the arc root and 2) by the neutralization of the positive ions of cathode materials on the cathode spot surface. In case of the condensation, Zhou et al. (1994) mentioned tungsten redeposition in the form of whiskers and Meunier et al. (1987) reported copper redeposition. For copper redeposition, it was

believed that the copper redeposited was part of the bulk of the cathode structure and could carry the current because no weakly bounded structure was found through their microscopic observation. Also, for fullerence synthesis the carbon redeposition, i.e. the deposition of vaporized graphite material from the anode on the graphite cathode surface, has been reported. Lefort et al. (1993) used the redeposition by the neutralization of the positive ions of cathode materials in their modeling work.

2.3. GRAPHITE ELECTRODES

Graphite electrodes are widely used in thermal plasma processing. Typically graphite electrodes have been reliably used in EAFs. Recently in case of recycling or treatment of solid wastes, graphite electrodes have been considered possibly superior to metal torches. Finally graphite arc discharges in a helium atmosphere are the one of the present methods for fullerene production.

2.3.1. General Characteristics of Graphite

Graphite is one of the four allotropes of carbon; the others are amorphous carbon, diamond, and fullerenes. Graphite is based on sp^2 structure and its structure is described as layers of carbon atoms with an interatomic distance of 0.142 nm and with an interplanar distance of 0.335 nm as shown in Figure 2-4 (Encyclopedia of Chemical Technology 1992). Each carbon atom within the layers is bonded only to three carbon atoms in a trigonal planar arrangement with 120° angles (Kandah 1997). Because each atom is formally bonded to only three neighboring atoms, the remaining valence electron (one in each atom) is free to circulate within each plane of atoms; therefore, graphite is an

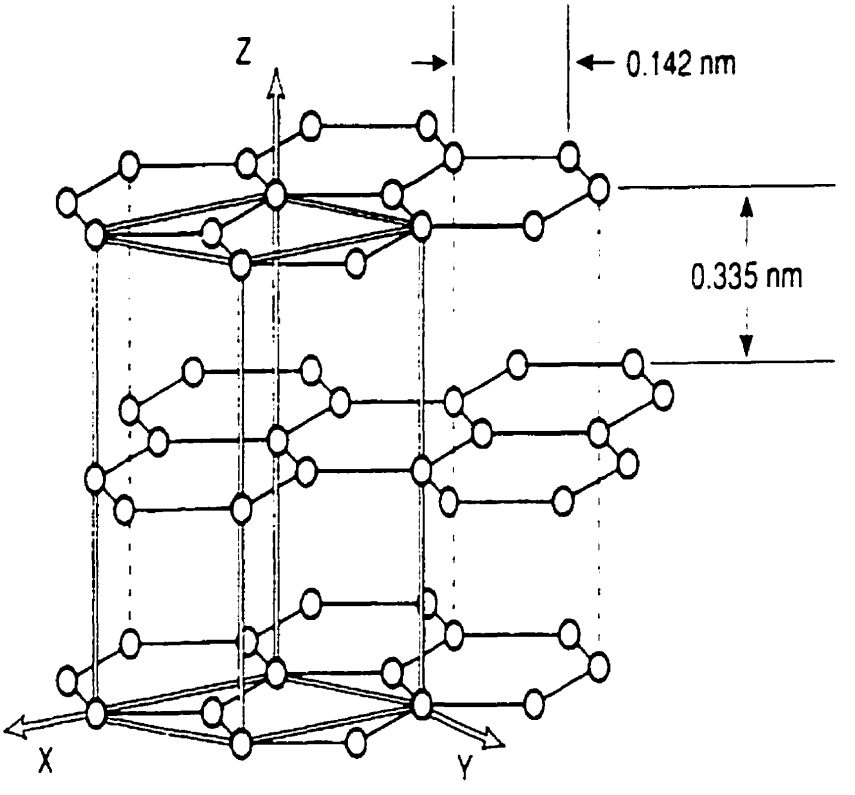

Figure 2-4: Structure of graphite (Encyclopedia of Chemical Technology 1992).

electrical conductor. In addition, separation of each layer represents a non-bonding situation, and thus graphite can be used as a lubricant.

In this work polycrystalline graphite, which is a blend of amorphous carbon and very small graphite crystals, has been used for electrodes and its general production process, provided by POCO Graphite INC., USA, is as follows. Polycrystaline graphite is made by the calcination of the raw material, i.e. petroleum coke, in large kilns to shrink it and drive out the volatile content. It is then crushed into a very fine powder and sized into different particle sizes through screens. The crushed raw material is mixed with a binder, compressed into a block, and fired at very high temperature to remove any volatile materials and to assure homogeneity. Because the coke does not melt during processing, the resultant structure is much like sand that is stuck together by a thin layer of glue. Generally polycrystalline graphite has some anisotropy; however, POCO graphite, used in this work, is isotropic.

2.3.2. Graphite Electrodes in Arc Furnaces

In this part several features of graphite electrodes in arc furnaces are introduced because graphite electrodes are typically used in EAFs. In many arc furnaces it seems that water-cooled metal electrodes may not be needed. A simple graphite electrode will be sufficient although the improvement of the arc stability is required. Barcza (1986) has reported that the arc stability can be realized if the graphite electrode is made in the form of a hollow electrode to introduce plasma gas through a small hole and the end of the graphite electrode is shaped to improve the directionality of an arc to an open bath in arc furnaces.

Compared with water-cooled metal electrodes, graphite electrodes have some advantages. Graphite electrodes are generally more massive than water-cooled metallic electrodes so that they can carry higher electrical currents. Moreover, because they are refractory, heavy water-cooling is not necessary. Sometimes water leaks of water-cooled metallic electrodes result in explosions in arc furnaces.

As is well known, graphite electrodes are consumed during the operation of arc furnaces. Through field tests, it has been reported that the consumption of the graphite electrodes in EAFs can be divided into three broad categories: tip consumption, sidewall consumption, and breakage (Lefrank et al. 1983, Schwabe 1971, Encyclopedia of Chemical Technology 1980). Figure 2-5 shows the longitudinal loss resulting from the tip consumption and the transverse loss because of the sidewall consumption in case of graphite electrodes of AC EAFs. Roughly half of the observed consumption occurs at the graphite electrode tip where the intensely hot and rapidly moving arc root produces both vaporization of the graphite and some ejection of small graphite particles. In addition, the graphite electrode tip can be eroded by contact with the liquid metal and slag. The rate of incremental tip consumption generally increases when operating current or power is increased. The sidewall of hot graphite electrodes is consumed by reaction with oxidizing atmospheres both inside and outside the EAFs, resulting in a tapering of the graphite electrode toward the arc tip. The sidewall consumption is increased by the use of many fume removal systems and by the use of oxygen in the EAFs for assisting melting or refining. Kaltenhauser et al. (1983) mentioned that since the sidewall consumption may account for 40 % or more of the total graphite electrode consumption, extensive efforts have been

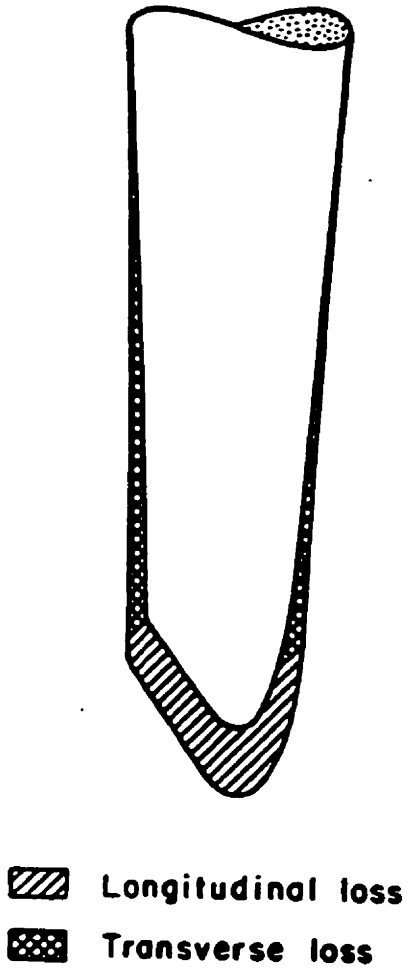

Figure 2-5: Typical consumption patterns of a graphite electrode in AC EAFs (Jurewicz 1997).

made to reduce this component of consumption through the use of oxidation retardants and electrode coating. Such efforts have had little success to date, primarily because of the extreme thermal and chemical environment to which the graphite electrode is exposed. A third form of consumption consists primarily of graphite electrode breakage resulting from excessive movement of large masses of scarp during melting or the presence of nonconductors in the charge. Although such breakage usually accounts for less than 10 % of the total graphite electrode consumption, excessive thermal shock, improper joining practice, and incorrect phase rotation may magnify this form of electrode consumption.

Owing to the development of solid state diodes and high current thyristor controlled rectifiers in the recent past, interest in DC EAFs has strongly been stimulated. As the main advantages of DC EAFs over AC EAFs, Jurewicz (1997) mentioned 1) lower graphite electrode consumption, 2) higher electrode current carrying capability, 3) reduced disturbances in electrical supply systems (less flicker), 4) uniform heat distribution, 5) the stirring effect, and 6) lower noise emission. Besides less wear on flexible power cables (less electrode movement), reduced maintenance on electrode arm of furnaces, less electrode breakage, and lower energy consumption have been mentioned. On the other hand the requirement of the bottom (bath) electrode and relatively difficult arc starting have been recognized as the disadvantages of DC EAFs. The bottom electrode may not be easily cooled and increases maintenance problems. Also, in case of insufficient electrical contact between the cathode and the bottom electrode, it may be difficult to ignite an arc. In that case a metal or a graphite rod may be

used as an auxiliary electrode in the bath to establish the electrical contact between the cathode and the anode.

2.4. THE ARC STABILITY OF HOLLOW GRAPHITE ELECTRODES

Maddever et al. (1976) studied the effect of the gas injection on the arc stabilization and the consumption rate of hollow graphite AC electrodes on the laboratory and the industrial scale. For the laboratory scale the diameter of the graphite electrode was 7/8 inches and that of the hole in the graphite electrode for the gas injection was 1/8 inches. Various gases such as argon, nitrogen, carbon dioxide, and several hydrocarbons were investigated. The gas flow rates were approximately 2 ~ 3 ft^3 per hour. Among the gases, the argon gas was preferred because it provided the uniform and sinusoidal waveforms of the current, the voltage, and the power without the operating problems. Nitrogen gas enhanced pickup of that gas into the melt by a considerable degree, and hydrocarbon gases caused the blocking of the hole by the carbon deposition. The uniform and sinusoidal waveforms meant the increase of the arc stability. Experiments performed with the argon gas injection also showed the decrease of the consumption rate of the electrodes. For the plant scale the diameter of the graphite electrodes was 7 inches and that of the hole was 1/4 inches. In case of the argon gas flow rate of 40 ft^3 per hour, enhancement of the arc stability was reported as in the results of the laboratory experiments.

Sommerville et al. (1987) further studied the work of Maddever et al. (1976) and reported several general characteristics of the improvement of the arc stability of the

hollow graphite AC electrodes. The characteristics are as following: 1) the waveforms of the current and the voltage are considerably smoother for stable arcs, 2) the arc can be extended easily and is less apt to be self-extinguished, 3) the arc shows the strong directional component, and follows a more confined path with less tendency to flare, 4) the acoustical and the electrical noise is decreased, and 5) the consumption rate of the graphite electrodes decreased; in their study the consumption rate was decreased from 9.99 to 8.62 lb/ton of product.

Ochs et al. (1989) studied the improvement of the arc stability of hollow graphite AC electrodes in an EAF. The power was supplied to the electrodes through two single-phase AC welders connected in parallel and rated at 1500 A, thus providing the maximum operating current of 3000 A. The structure of their hollow graphite electrodes was quite different from that of the electrodes used by Maddever et al. (1976) and Sommerville et al. (1987). Ochs et al. (1989) made multiple holes in the graphite electrode for the gas injection. The 12 holes of 1/32 inches diameter were located on the 1 inch diameter circle encompassing the electrode tip (see Figure 2-6). This tip was connected to 3 inch graphite electrodes. The inert gases of helium and argon were injected into these holes as well as windows of the EAF. The inert gases shrouded the arc, thus maintaining the arc in a vertical direction and allowing more of the heat to be directed to the melt. The gases also helped to confine the arc to the tip section while it cooled the outer portion of the electrode and decreased the consumption rate by reducing the oxidation of the graphite electrode.

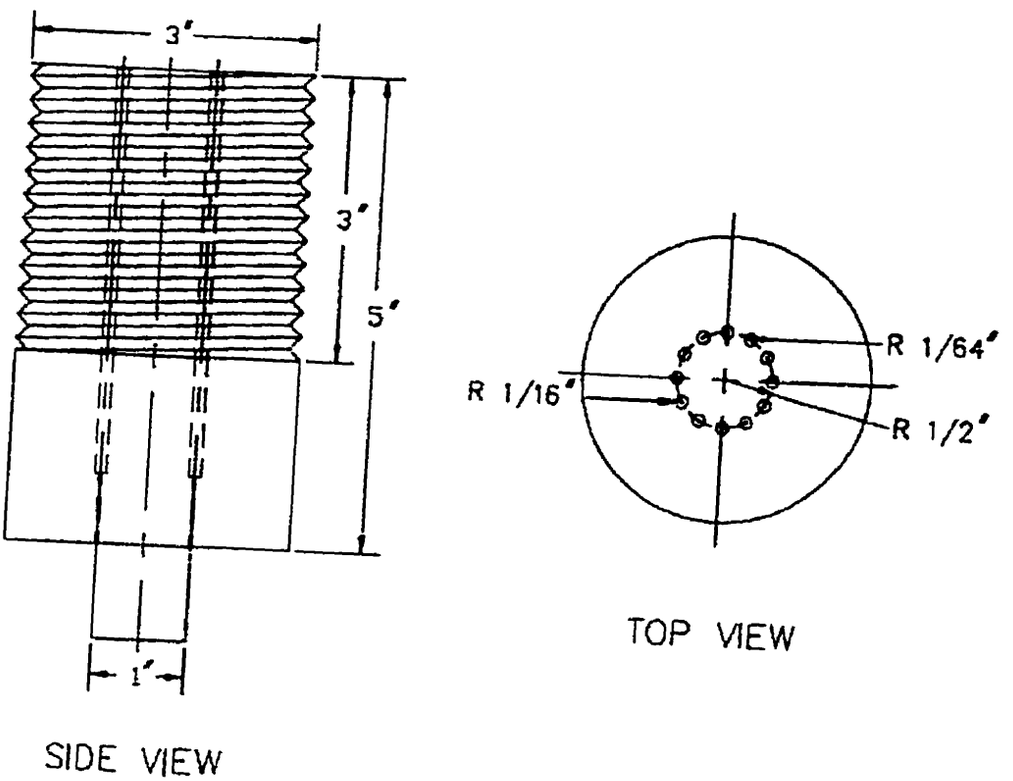

Figure 2-6: Schematic drawings of the electrode tip with the holes (Ochs et al. 1989).

2.5. EROSION OF GRAPHITE ELECTRODES

Holm (1949) proposed an energy balance at the cathode spot to provide an explanation of the vaporization of metal and carbon cathodes, i.e. the cathode erosion. He assumed that the total energy produced in the cathode region was transferred to the cathode and neglected the relatively small radiation from the cathode. Although Holm's study is simple and has several oversimplifications, it has produced significant results, which are well-accepted today. The results are that the high vaporization from the cathode is inevitable and as the current density increases, the heat loss by vaporization is much more important than the heat loss by conduction. Later, Holm (1967) modified this energy balance by replacing the total current term with the ion current term since the main component of the input energy to the cathode spot is the positive ion bombardment.

Mentel (1977, 1977, 1978) studied the influence of vaporization upon the arc roots of high current arcs using graphite rod DC cathodes. His study provides a range of erosion rate of a graphite cathode measured in an argon atmosphere at atmospheric pressure and the temperature of graphite vapor jets. The diameters of the graphite DC cathodes were 3, 4.6, and 6.15 mm. High-speed photography of the arc roots at 1000 A in argon atmosphere showed that the cooling of the electrodes could affect the appearance of the arc roots. By changing the height of the cathode above the water-cooled collar, the cooling rate of the electrodes was controlled. The height variation was from 2 mm to 10 mm. For the strong cooling of the cathode (2 mm above the collar) the arc roots remained stable. In contrast, for the weaker cooling of the cathode (6 and 10 mm above the collar), the separation of the arc and the graphite vapor jet could be seen at the arc roots. The

vapor was observed as a trail or jet and was relatively cold. The spectroscopic measurements of the C_2 molecular bands gave the vapor jet temperature was between 4000 and 5000 K. For the strong cooling, the erosion rate of the graphite cathode was increased slowly as the current density was increased; however, the erosion rate for the weaker cooling was increased greatly as shown in Figure 2-7. In addition, for the weaker cooling, it was reported that a large cathode spot developed as the current increased. It seems that the cathode spot he mentioned is a thermionic spot because his operating conditions are believed in the thermionic emission regime. The erosion rate for the height of 10 mm in Figure 2-7 was further analyzed because generally graphite electrodes are used without water-cooling. The unit of the erosion rate in Figure 2-7 is mg/(cm^2 s). This unit is converted into the μg/C unit used in this work and the results are presented in Table 2-3. The μg/C unit is the common unit in erosion studies and is independent of the arc duration. The estimated current range of his experiments in Figure 2-7 was between about 300 and 1040 A. The estimation of the erosion rate ranges from about 3.0 μg/C at 300 A to 85.7 μg/C at 1040 A. His equipment was designed to prevent the carbon redeposition from the graphite anode; therefore, these erosion rates may be thought as the erosion rate of the graphite cathode.

Lefort et al. (1993) proposed a model for graphite electrode erosion. They studied the cathode surface and its interaction with the space charge region to derive governing equations at the cathode. At the anode the equations were similar to those at the cathode. To estimate the erosion rate for the graphite cathode they assumed the cathode spot was one dimensional and was single, circular, and practically motionless. In addition, the

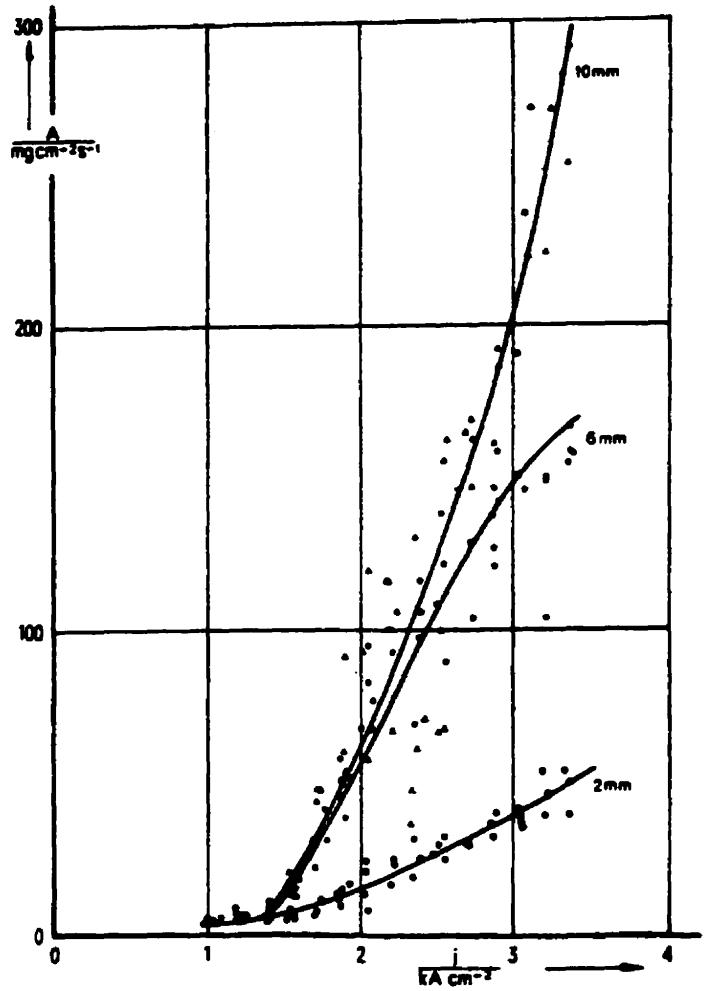

Figure 2-7: Erosion of the graphite cathodes with a diameter of 6.15 mm for different heights, h, of the electrode above the cooled collar (Mentel 1977).

Table 2-3: Conversion of the erosion rates of Mentel's work (1977).

Current density in Figure 2-7 (kA/cm^2)	Estimated current (A)[1)]	Erosion rate for h = 10 mm in Figure 2-7 (mg/cm^2s)	Estimated erosion rate (mg/s)[2)]	Estimated erosion rate ($\mu g/C$)[3)]
1	297	3	0.9	3.0
2	594	63	18.8	31.7
3	891	200	59.4	66.7
3.5	1040	300	89.1	85.7

1) Conversion: the current density in Figure 2-7 (kA/cm^2) x the cross-sectional area of the graphite cathode (cm^2)

2) Conversion: the erosion rate in Figure 2-7 (mg/cm^2 s) x the cross-sectional area of the graphite cathode (cm^2)

3) Conversion: the erosion rate (mg/s) x 1000 / the estimated current (A)

cathode material was homogeneous with a perfect surface state and only cathode material evaporation was considered for erosion. The unique feature of their theoretical work is the introduction of the redeposition by the neutralization of the positive ion current. When calculating the erosion rate with considering the redeposition, they assumed all the positive ionic flux coming from the ionization region was captured and neutralized on the cathode surface. In addition, they introduced a general empirical model of the erosion rates of the graphite electrodes in AC arc furnaces as follows:

$$G = K I^{\alpha} \qquad (2\text{-}2)$$

where G is the mass loss in kg/second; K is a constant; I is the arc current in A; α is a constant between 1 and 2. The Research Institute of French Iron and Steel Metallurgy (IRSID) modified this model for the mass losses (G) of graphite electrodes in DC arc furnaces as follows:

$$G = 6.6 \times 10^{-9} I_m^2 \quad (2\text{-}3)$$

where I_m is the mean current calculated over a half period in A; G is in 10^{-3} kg/second. Lefort et al. (1993) compared their erosion rate estimation including the anode erosion with the IRSID model and found out their estimation was greater. They concluded that one of the reasons of the over-estimation was the lack of the information about the mechanism of the redeposition.

2.6. Applications of Hollow Graphite DC Cathode

In this part, industrial applications of hollow graphite DC cathodes have been reviewed. The tundish heating at the BGH, The Electro-Pyrolysis Inc. (EPI) Arc Furnace, the Exide High Temperature Metals Recovery (EHTMR) process of the Exide Co., the Arc Technology Company process, and the DROSCAR process of the Hydro-Quebec are introduced.

Some processes using the graphite cathodes for treatment of solid wastes are introduced because of the recent interest of the transferred arc treatment of solid wastes. In the arc treatment, graphite electrodes have been proposed for the electrodes of the transferred arc plasma and may be expected to replace water-cooled metallic electrodes because of the advantages mentioned in the earlier part. (Wittle et al. 1994, Drouet et al. 1995, Schumacher et al. 1995, Rozelle et al. 1995, Neuschutz 1996, Eddy 1999). The historical perspective and up-to-date trends of plasma technology for these applications are well reviewed by Cohn(1997), Fauchais et al. (1997), and Counts et al. (1999).

2.6.1 The Tundish Heating at the BGH

Neuschütz et al. (1996) investigated the arc heating in the tundish with a hollow graphite DC cathode in comparison with a metallic plasma torch. This study was performed at the BGH Edelstahl Siegen GmbH, a steelmaker located at Siegen, Germany. The length of the DC graphite cathode they used was 1250 mm and the diameter was 100 mm. Argon was blown at a rate of 3.6 m^3 per hour through a 20 mm hole into the arc for stabilization. The average arc voltage was 100 V and the maximum arc current was 3300 A. The electrode position was continuously adapted to keep the arc voltage constant. They reported the consumption rate of the graphite electrode by both the tip and side wear was 0.46 kg/hour after 6 months of the operation. The average current of the operation was 2000 A. Also, they reported another tip and side consumption rates of a different hollow graphite electrode of the BGH. The side wear was 0.04 kg/hour and the tip wear was 0.78 kg/hour. They analyzed that the lower side consumption rate was due to the argon gas injection, which caused the reduction of the oxygen partial pressure around the graphite electrode. Compared to metallic torches, they concluded that except for sensitive steel grades, the hollow graphite DC cathode appeared to be recommendable for all steel grades operations because the running costs were lower than with metallic torches because of less water cooling, less wear of parts like nozzles and starting electrodes, and less personnel for maintenance.

2.6.2. The EPI Arc Furnace

Wittle et al. (1994) reported that Electro-Pyrolysis Inc. (EPI), Massachusettes Institute of Technology (MIT), and Pacific Northwest Laboratory (PNL) developed DC graphite arc

furnaces named EPI's Mark I and Mark II to the processing of Subsurface Disposal Area (SDA) wastes. According to their report the graphite electrode DC arc furnace is attractive because it provides the advantages of simplicity, high availability, safety, high processing rate, easy of scale-up, and versatility and thus the furnace is well suited for treating high melting point wastes containing metals. The Mark I furnace (see Figure 2-8) includes a graphite crucible with a capacity of one hundred pounds of material. A movable two-inch diameter graphite electrode is located in the center of the graphite crucible. The entire system is contained in a square carbon steel box with hot face brick and insulating brick surrounding the crucible. The Mark I furnace is capable of operating at DC power levels of 300 kW. The furnace has operated under an inert atmosphere by purging 3 ~ 4 ft^3 per minute of N_2 through the furnace chamber. The Mark II furnace is approximately 23 feet in height and 7 feet in diameter. The furnace is a refractory lined carbon steel vessel as shown in Figure 2-9. The graphite electrode in the Mark II furnace incorporates a unique coaxial arrangement within an outer graphite electrode that is 16 inches in outside diameter and 10 inches inside diameter. The inner graphite electrode is a solid 6 inches piece of graphite. This electrode assembly has the capability to operate in the transferred arc mode or the non-transferred mode. This allowed the furnace to be easily started by operating the torch in the non-transferred mode to melt the material in the crucible. When the molten material becomes electrically conductive, the operation of the electrode can then be changed to the transferred mode of operation. The transferred mode which is a more efficient method of providing heat-energy to the material being melted.

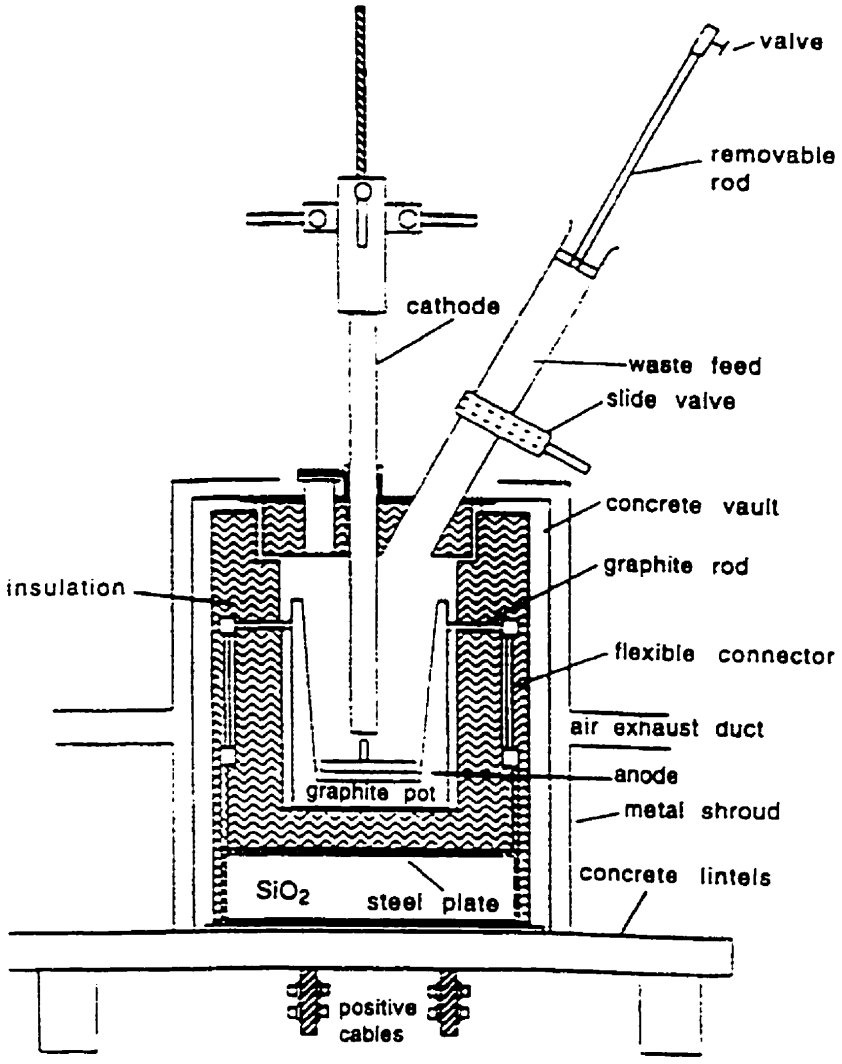

Figure 2-8: The schematic diagram of the EPI's Mark I furnace (Wittle et al. 1994).

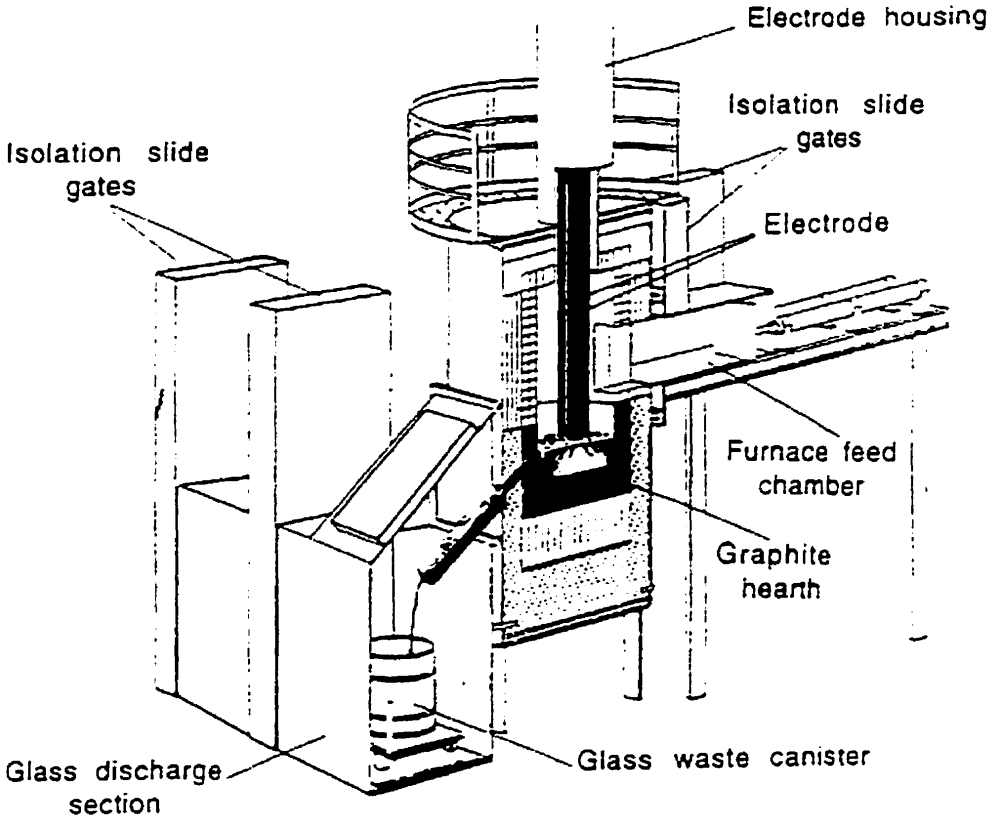

Figure 2-9: The schematic diagram of the EPI's MarkII furnace (Wittle et al. 1994).

2.6.3. The EHTMR Process

The Exide Corportion (Rozelle et al. 1995) developed the Exide High Temperature Metals Recovery (EHTMR) process to treat a variety of solid wastes and by-products containing metals by using a submerged transferred arc plasma. The process is designed to recover the valuable metals in the solid wastes for reuse and to produce a metals-depleted slag that can be marketable. The heart of the EHTMR process is a DC transferred arc plasma furnace (see Figure 2-10). This furnace features a hollow graphite DC cathode through which the solid wastes can be fed. In order to assist in solid waste feeding and to provide arc stabilization, the process is equipped with a system to feed inert plasma gas (argon) through the electrode. Solid wastes requiring fuming through the electrode were fed through the zone of maximum energy density at the arc which enhances volatilization of metals in the solid wastes. This is an inherent advantage in transferred plasma arc operations with a hollow electrode feed, which is not possible in non-transferred plasma arc operations.

2.6.4. The Arc Technology Company Process

The Arc Technology Company (UIE, 1988) developed a DC arc furnace (see Figure 2-11) for the destruction of PCB filled condensers. The furnace is a chamber, with walls made of refractory graphite, where an electric arc is initiated between a hollow graphite DC electrode and a bath of molten metals. The entire condenser is brought into the bath of metals at 1650 °C located at the bottom of the furnace (area 1). The condenser melts and releases its PCBs which are subjected to ultraviolet radiation from the plasma arc and

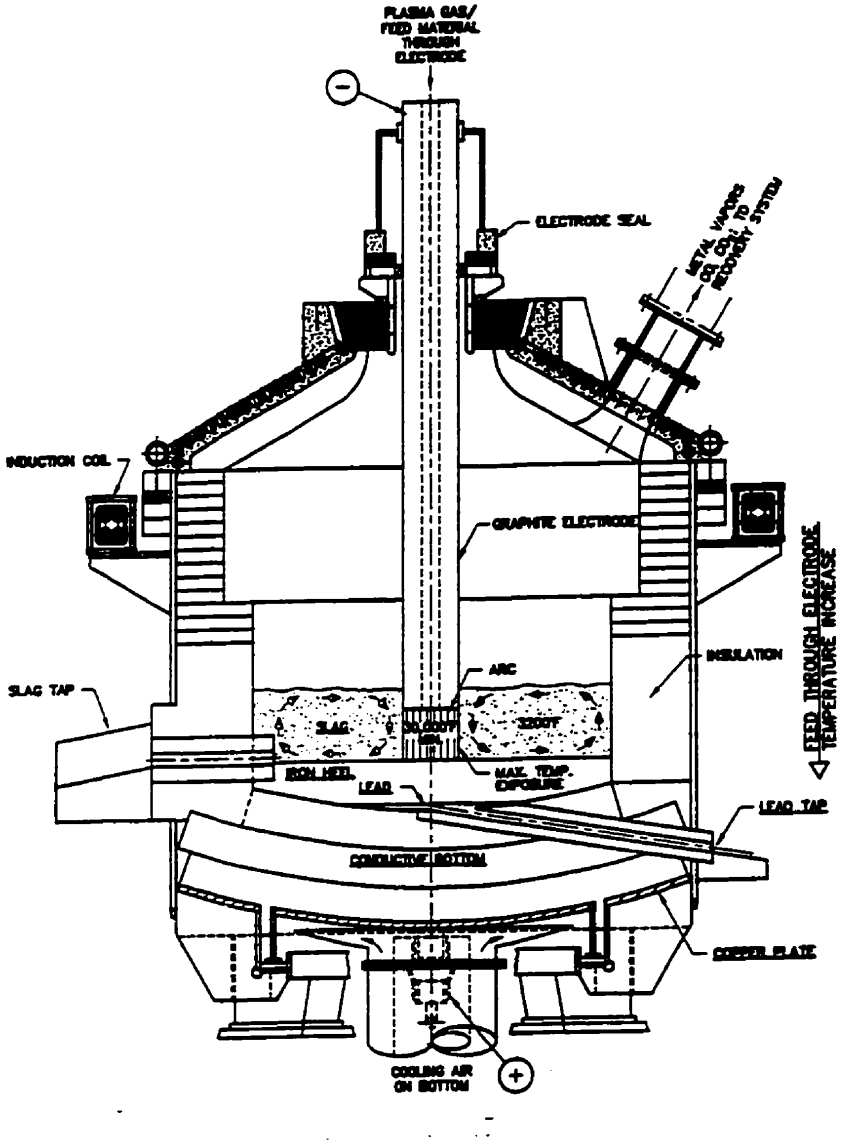

Figure 2-10: The transferred arc furnace of the EHTMR process (Rozelle et al. 1995).

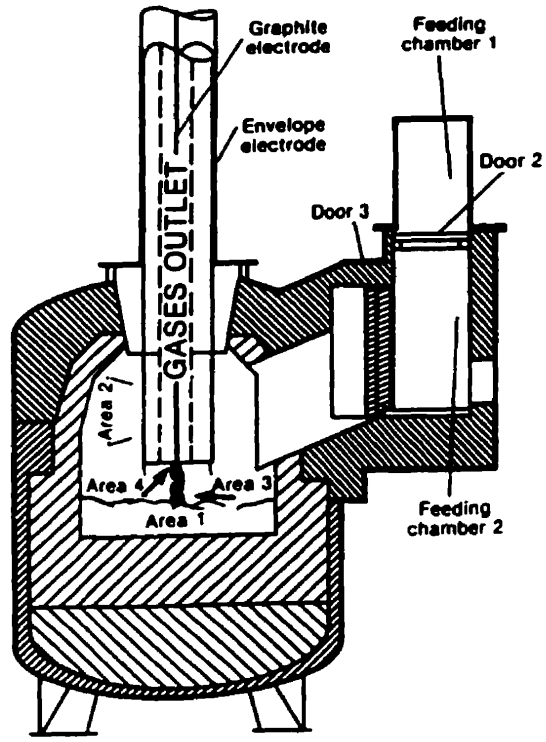

Area 1 : molten metals 1650°C
Area 2 : furnace 1650°C t_s = 1.77 s
Area 3 : gas envelope # 6100°C
Area 4 : electric arc 6100°C t_s = 3 ms
N_2 gas, noise 50 dB — Height 8 m

Figure 2-11: The transferred arc furnace of the Arc Technology Company process (UIM 1988).

to the heat from the molten metal. As a result, the PCBs are pyrolysed. The pyrolysis gases are extracted by the inside of the electrode after going through the electric arc (area 4) and its gaseous envelope (area 3). This installation has a treatment capacity of 1500 kg/hour; it produces 750 kg/hour of molten metals and 882 Nm^3/hour gases containing CO, H_2, and HCl. The gases are purified in two successive washing venturi scrubbers. The destruction efficiency of the system is 99.9999%.

2.6.5. The DROSCAR Process

Hydro-Quebec has developed a rotary DC graphite arc furnace for aluminum dross treatment. Aluminum dross occurs as an unavoidable by-product of all aluminum melting operations. Generally, depending on the operations, it represents 1 to 5 weight % of the melt and may contain as much as 75 weight % of free aluminum in the form of very small droplets entrapped in aluminum oxides. Since aluminum production is highly energy-intensive, aluminum dross recycling is very attractive. The conventional recycling process uses rotary salt furnaces heated with a fuel or a gas burner but the process is thermally inefficient and environmentally unacceptable because of salt slags. Plasma recycling treatment of the aluminum dross is thus being developed. Neuschutz (1996) and Burkhard et al. (1994) reviewed the existing aluminum dross recycling processes: the Alcan process, the Hydro-Quebec process, the BOC process, and the MGC process. Among them, only the Hydro-Quebec process named the DROSCAR process has been introduced here because the process uses graphite DC electrodes.

The DROSCAR process employs a new salt-free technology for the treatment of the

aluminum dross which uses a rotary furnace heated by a DC electric arc between two graphite electrodes as shown in Figure 2-12 (Drouet et al. 1994, 1995). In Table 2-4 the optimal operating parameters of the 600 kW DROSCAR pilot plant are presented. An electric arc stretched and maintained between two graphite electrodes is used to heat the charge above the aluminum melting point. The energy transfer mechanism in the furnace is mainly radiation from the arc to the refractories and the charge. Heat transfer by conduction between the refractories and the charge also plays an important role. The furnace rotates as the dross is heated to provide mechanical stirring, which breaks the oxide film on the droplets of aluminum present in the dross and promotes agglomeration of the molten metal. Rotation also prevents formation of hot spots on the charge or refractories and improves energy transfer. On completion of the heating, the metal is tapped from the furnace through a hole in the side. The solid residues remaining in the furnace form a greyish powder which is removed by tilting the furnace forward while slowly rotating it. Gaseous and particulate emissions are significantly reduced in this technology; only 3 m^3 gas is used per tonne of the dross treated compared to 30 m^3 per tonne the dross for the air plasma torch of the Alcan process and as much as 300 m^3 per tonne of the dross for the gas or fuel burner. Argon is used, especially for arc stabilization, and helps to create an inert atmosphere inside the furnace, thereby minimizing reactions between the molten aluminum and the furnace atmosphere. The oxidation and nitrification of the aluminum can be an important source of heat but should be avoided. No salt is added to improve recovery, so the charge is not increased, additional heating energy is not required, and the amount of residues is kept as low as

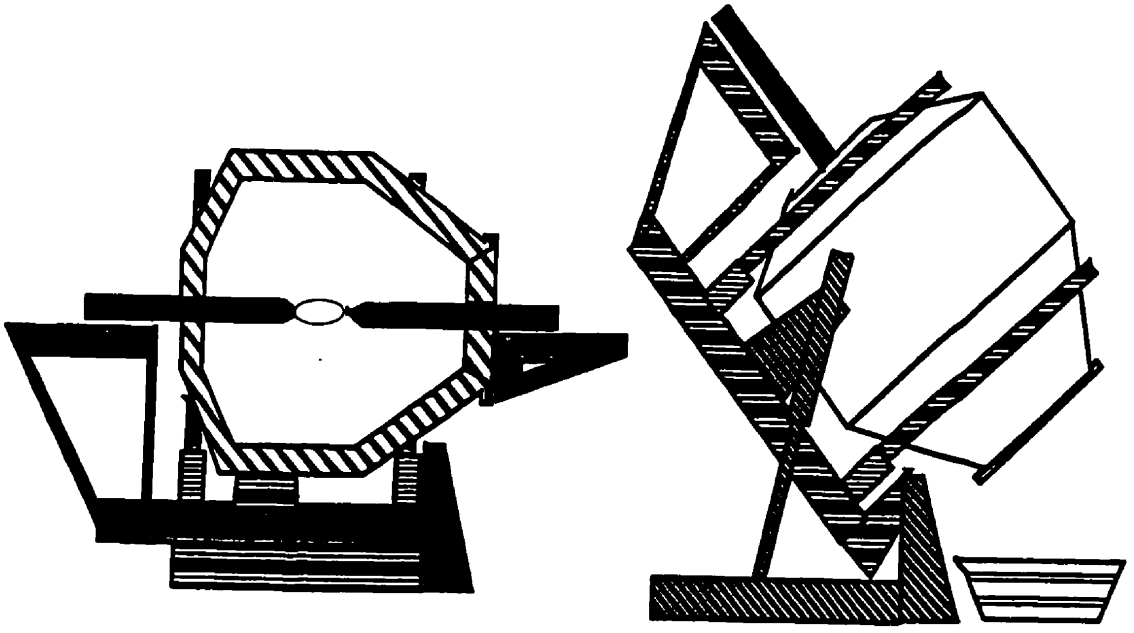

Normal Operation Discharge

Figure 2-12: The rotary furnace of the Hydro-Quebec process (Drouet et al. 1995).

Table 2-4: The optimal operating parameters of the 600 kW DROSCAR process (Drouet et al. 1995).

Parameters	Mean
Total cycle time	70 minutes
Charging time	10 minutes
Heating time	36 minutes
Dross tumbling time	13 minutes
Aluminum (Al)tapping time	6 minutes
Residue discharge time	5 minutes
Dross treatment capacity	0.87 ton/hour
Energy consumption	371 kWh/ton-dross
Energy efficiency	74.9 %
Al recovery rate (for a 50 % Al dross)	94.7 %
Electrode consumption	0.88 kg/ton-dross

possible. Furthermore since the process uses a graphite arc, there are no-water cooled parts in the furnace, which eliminates the hazard created by possible water leaks over the molten metal.

CHAPTER III

RESEARCH OBJECTIVES

The two main objectives of this study were to examine the arc stability and erosion behavior of a DC hollow graphite cathode struck to a graphite anode in argon at atmospheric pressure. The detailed research objectives and the methodologies used are given below:

1. Arc Stability at a DC Hollow Graphite Cathode

This objective was focused on identifying the electron emission mode transition of graphite arc cathode operation by studying the characteristics of the thermionic and thermofield emission modes. Firstly, total voltage patterns, arc movement and acoustic noise were examined as a function of operating parameters. The chosen parameters were argon gas flow rate, initial interelectrode gap, arc current, and cathode tip geometry. Secondly, the characteristics of each mode were examined through the estimation of current densities, Fast Fourier Transform (FFT) of the total voltage, measurement of the cathode surface temperature, and examination of the cathode surface using scanning electron microscopy.

2. Erosion Behavior of a DC Hollow Graphite Cathode

This objective concentrated on analyzing the erosion behavior of the graphite cathode when arcing to a graphite anode in argon at atmospheric pressure. The erosion rate was measured as a function of argon flow rate, initial interelectrode gap, and arc current.

These parameters were associated with the emission mode transition and the arc stability. Erosion rates were separated into rates for stable and unstable operation.

CHAPTER IV

EXPERIMENTAL METHODS

4.1. EXPERIMENTAL APPARATUS

The schematic diagram of the transferred arc system for this work is shown in Figure 4-1. The main components of the experimental system were a power supply, a hollow graphite DC cathode, a graphite anode, a data acquisition system to record total voltage and arc current, a gas-tight water-cooled chamber to house the graphite electrodes, an oxygen meter, and a thermohygrometer. All equipment was electrically grounded except the graphite cathode which operated at an elevated negative potential. Argon was used as the plasma gas and its rate was measured in liters per minutes (lpm) at 293 K and 1 atm.

4.1.1. Power Supply

Eight Miller SRH-444 rectifiers (Miller Electric Mfg. Co., Appleton, Wisconsin, USA) connected in series supplied the power to the graphite cathode. Because of this series connection, the arc current was limited to 400 A. Each rectifier had an open circuit voltage of 75 V and a power rating of 19.6 kW. The input voltage was three phases, 575 V at 60 Hz and the total open circuit voltage was 600 V. The rectifier was connected to a control console, which controlled the plasma gas flow rate and the power to the cathode. The console also contained a high frequency starter (HF 2000 High Frequency Arc Starter, Miller Electric Mfg. Co.) and a safety shut-off system which could be deployed in case of an emergency.

4.1.2. The Chamber

The chamber consisted of the roof, the upper chamber, the lower chamber, and the bottom. The inside diameter of the chamber was 29.5 cm, and the height was 29.0 cm.

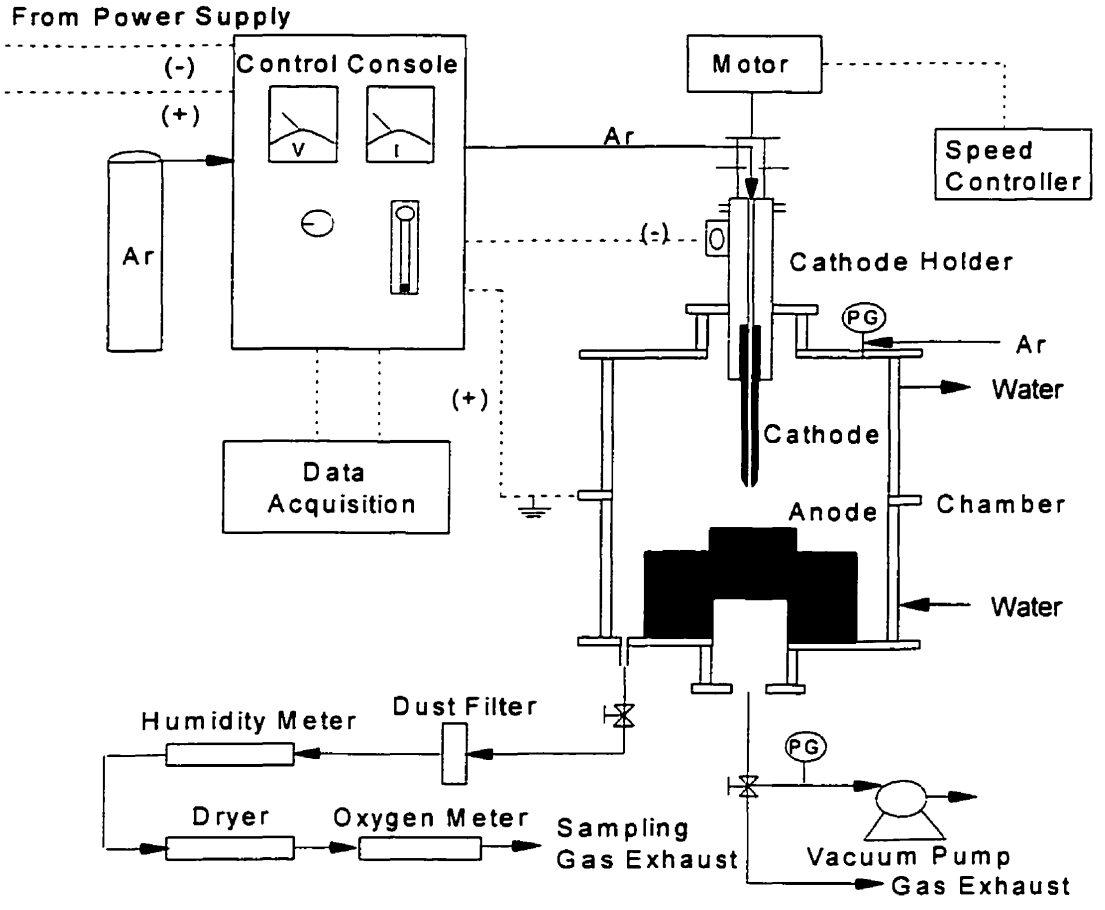

Figure 4-1: The schematic diagram of the transferred arc experimental system.

Two cooling water circuits were connected to the chamber. One was for the roof and the upper chamber, and the other was for the lower chamber and the bottom. The cooling water rate was fixed at 15.6 slpm for the upper part and 7.2 slpm for the lower part.

4.1.3. Hollow Graphite DC Cathodes

Two types of hollow graphite DC cathodes, named cathode I and cathode II, were used in this study. Schematic drawings of the graphite cathodes are presented in Figure 4-2. The length of each graphite cathode was 27.94 cm. The inner diameter of each cathode was 0.32 cm. The only difference between the two cathodes was the size of the outer diameter. The outer diameter of cathode I was 1.91 cm, and that of cathode II was 1.07 cm.

The determination of the outer diameter of cathode II was based on apparent current density. This is defined as ratio of arc current to the cross-sectional area of each cathode. Cathode II was planned to simulate a 1000 A run at real 300 A because of the current limitation of the power supply. The cross-sectional area of cathode I is 2.77 cm^2 and the apparent current density of cathode I at 1000 A is 360 A per cm^2. The outer diameter of cathode II was sized to give this apparent current density at 300 A.

Cathode II was designed to confirm that arcs in the thermionic emission regime do not show the electrical and acoustical noise. The influence of the reduction of the outer diameter of cathode I for the preparation of cathode II may be explained by considering the energy balance on the cathode spot surface. The energy balance, in general, is described by the following equation:

(a) Cathode I

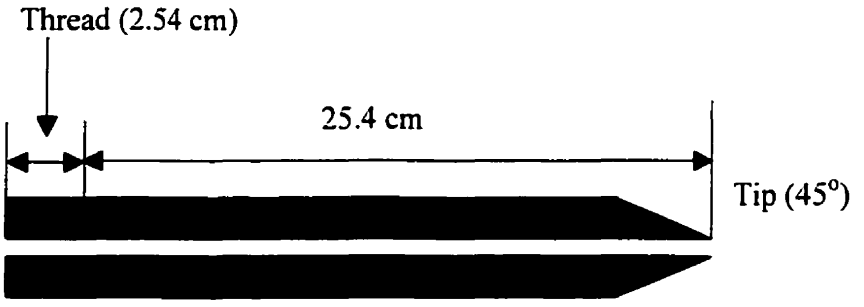

(b) Cathode II

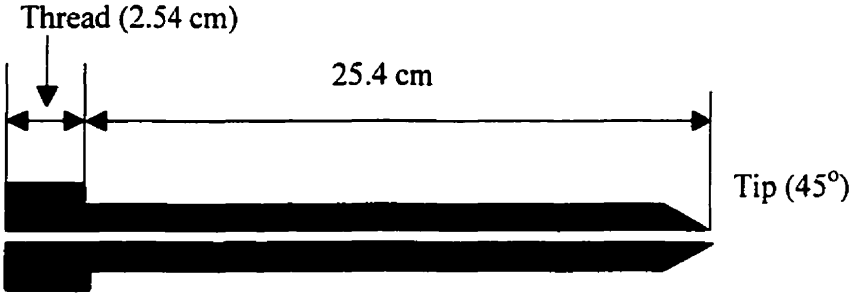

Figure 4-2: The schematic drawing of cathode I and cathode II.

$$q_{\text{ion bombardment}} = q_{\text{vaporization}} + q_{\text{conduction}} + q_{\text{electron emission}} \quad (4\text{-}1)$$

where q is the heat flux at the cathode spot surface. As discussed in chapter II, the ion bombardment is the main component of the energy input; the vaporization of the cathode material, the conduction heat loss through the cathode, and electron emission are the major components of the energy output. Among the energy output components, only the conduction heat loss depends on the geometry of a cathode. Therefore, reduction of the diameter of a cathode can decrease the conduction heat loss, thus providing a higher temperature at the arc root.

The tip of both cathodes was machined to a contained angle of 45°. Both cathodes were connected with the brass water-cooled cathode holder through a 2.54 cm long threaded section. This cathode holder was water-cooled to avoid the melting of the teflon electrical insulator, located in the roof of the chamber. The cooling water rate of the holder was fixed at 4.8 slpm. The length of the both cathodes below the water-cooled holder was 25.4 cm. Argon was injected through the hole of the cathode at flow rates of 0, 4.5, 10, and 15 slpm.

XT grade graphite, produced by POCO GRAPHITE INC., was used in this study as the material for the cathodes and the anode. The graphite is isotropic and has uniform pore size distribution. Physical properties of the graphite at room temperature, provided by POCO GRAPHITE INC., are presented in Table 4-1.

Table 4-1: Physical properties of XT grade graphite at room temperature.

Physical properties	Units	Values
Particle size	microns	20
Total porosity	(% volume)	26
Apparent density	g/cc	1.71
Compressive strength	N/mm^2	86
Flexural strength	N/mm^2	45
Electrical resistivity	μ.ohm.cm	1250
Coefficient of thermal expansion	microns/m °C	7.5
Thermal conductivity	W/m K	115

4.1.4. The Anode

The anode was a graphite disc as shown in Figure 4-3. The XT grade of the POCO Graphite Inc. was used for the anode material. The diameter was 5.72 cm, and the height was 3.18 cm.

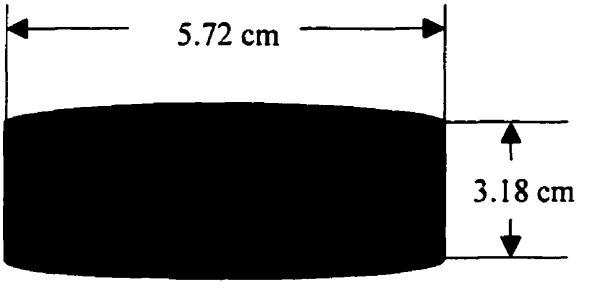

Figure 4-3: The schematic drawing of the anode.

4.1.5. Data Acquisition System

The data acquisition system consisted of a DAS-1401 data acquisition board and a standard personal computer. Control of the data acquisition system was done using a computer program written in BASIC. The sampling time of the data acquisition system was programmed as 8 seconds. The system was used to record total voltage and arc current. The data acquired were saved to an ASCII text file for later processing.

4.1.6. Oxygen Meter

Before each experiment, oxygen (O_2) concentration, relative humidity (RH), and temperature in the chamber were measured to check the purity of an argon atmosphere of the chamber. The GC-502 model of GC Industries located Fremont, California, USA was used to measure the O_2 concentration in the chamber. The measuring range of the O_2 meter is from 0 to 25 volume percent in 0.1 volume percent increments, and at constant ambient temperature the accuracy of the O_2 meter is $\pm$ 0.5 volume percent.

4.1.7. Thermohygrometer

With the O_2 meter, the 37950-10 model thermohygrometer of Cole-Parmer was used to measure the RH and temperature in the chamber. The thermohygrometer measures RH from 0 to 99.9% and temperature from 0^{o} to 199.9 ^{o}F.

4.1.8. Optical Pyrometers

For the measurement of the graphite cathode surface temperature, two types of optical pyrometers were used: single wavelength and two-wavelength pyrometers. The single

wavelength pyrometer is a model of the Pyrometer Instrument Co., Inc., located in New Jersey, USA. This pyrometer is designed to adjust the filament current to match the color of the filament to that of the object, i.e. it used the disappearing filament principle of temperature measurement. The single wavelength is 0.65μm. Holman (1989) gives the schematic diagram of this type of the pyrometer as presented in Figure 4-4. The radiation from the object is viewed through the lens and filter arrangement. An absorption filter at the front of the pyrometer reduces the intensity of the incoming radiation. Figure 4-5 illustrates the disappearance of the lamp filament for the match as viewed from the eyepiece. If the filament is too cold, it needs an increase of the current; if the filament is too hot, it needs a decrease of the current. The temperature measurement is performed for the null condition.

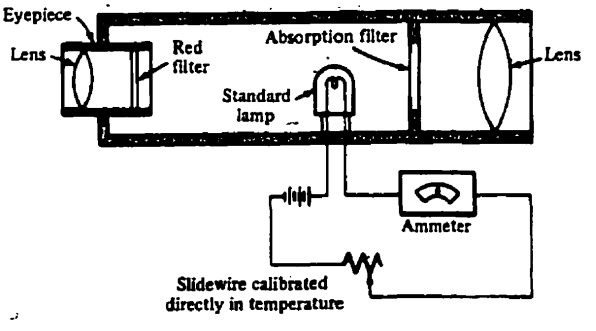

Figure 4-4: The schematic diagram of the single wavelength pyrometer (Holman 1989).

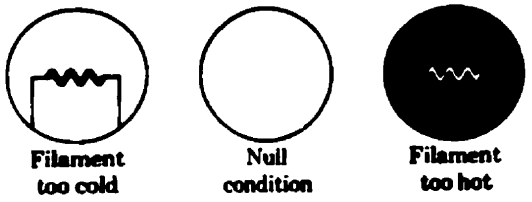

Figure 4-5: Appearance of the lamp filament in eyepiece of the single wavelength pyrometer (Holman 1989).

For the two-wavelength pyrometer, a ROS-8 model pyrometer of Capintec Instruments, Inc., located in Pittsburgh, USA, was used. It detects radiation in the near infrared region of the spectrum at 0.78 and 0.83 μm. The temperature reading of this pyrometer depends on the ratio of the intensities of the object radiation at the two selected wavelengths unlike the single wavelength pyrometer. In addition, for a gray body, knowledge of the absolute values of spectral emissivities is not needed because the emissivity of the gray body is not affected by the wavelength. In that case, Themelis et al. (1962) gave the relevant equation to determine the temperature of the gray body as follows:

$$\ln\frac{W_{\lambda 1}}{W_{\lambda 2}} = \ln[(\frac{\varepsilon_{\lambda 1}}{\varepsilon_{\lambda 2}})(\frac{\lambda_2}{\lambda_1})^5] - [(\frac{1}{T})(\frac{C_2}{\lambda_1} - \frac{C_2}{\lambda_2})] \qquad (4\text{-}2)$$

where W_λ is intensity of non-black body radiation at wavelength λ, ε_λ is emissivity of body at wavelength λ, C_2 (=1.4387 cm · K) is a constant, and T is absolute temperature, K. Equation (4-2) indicates that there should be a linear relationship between the

logarithmic ratio of the monochromatic intensities and the reciprocal of the absolute temperature of the object.

4.1.9. Oscilloscope

A TDS 200-series digital storage oscilloscope, produced by Tektronix Incorporation located in Oregon, USA, was used to measure total voltage and to perform its Fast Fourier Transform (FFT) in the order of the ms and μs time scale. This oscilloscope is capable of converting a time-domain signal into its frequency components, thus allowing the FFT analysis of the total voltage measured in the time domain. The single triggering mode was used for the measurement of the total voltage and the FFT to avoid the uncertainties caused by the signal overlapping. The signals and the frequency components captured in this mode were sent to a Hewlett-Packard laser jet printer for hardcopies.

4.2. PARAMETER RANGES

In this study arc current, arc duration, argon gas flow rate, and initial interelectrode gap were used as operating variables. The ranges of these parameters are presented in Table 4-2. The actual interelectrode gap increased as the electrodes eroded and this depended on the operating conditions. The maximum length change of the electrodes was measured to examine the gap change. The maximum length change for the cathode was 0.8 cm. For the graphite anode, the maximum length change was 0.5 cm and this occurred as a hole at the anodic arc root. The plasma gas flow rate greatly influenced length change of the anode since the argon gas cooled the surface. For a flow rate of 0 slpm, the depth of the hole reached a maximum of 0.5 cm, while for a gas flow rate of 15 slpm, the anode

remained flat and did not change measurably in length. The final interelectrode gap was determined by these maximun length changes as shown in Table 4-3.

Table 4-2: Parameter ranges of this work.

Operation variables	Units	Ranges
Arc current*	A	150, 300, 400
Arc duration	minutes	10, 30, 60, 90, 120
Argon gas flow rate	slpm	0, 4.5, 10, 15
Initial interelectrode gap	cm	0.5, 1.5, 3.0

*) Standard deviations: 6 A for 150 A, 8 A for 300 A, and 11 A for 400 A.

Table 4-3: The ranges of the final interelectrode gap.

Initial interelectrode gap	Final interelectrode gap
0.5 cm	1.3 ~ 1.8 cm
1.5 cm	2.3 ~ 2.8 cm
3.0 cm	3.8 ~ 4.3 cm

4.3. THE ARGON ATMOSPHERE

Before erosion measurements, the chamber was repeatly filled with pure argon (33 slpm) and evacuated to – 20 in Hg while maintaining a lower argon flow rate (3 slpm). The cycle was repeated five times after which argon was fed at a flow rate of 3 slpm and the chamber pressure was kept slightly above atmospheric pressure. Normally, the oxygen concentration was at the lower limit of the meter 0.1 % and the RH at 1.0 % at 20 °C. The argon gas was high purity (99.999 %) from PRAXAIR Technology Inc., located

Danbury, Connecticut, USA. Estimation of the graphite consumption mass loss because of the oxygen and the humidity in this argon atmosphere was performed and the procedure is given in Appendix 1. The estimated consumption mass loss was $4.60 \times 10^{-3} \sim 4.54 \times 10^{-2}$ g and was neglected; therefore, the mass change of a graphite cathode before and after a run was directly used for the calculation of erosion rate.

4.4. ARC OBSERVATION

A white screen and lens were used to produce an image of the arc and a digital video camera was employed to record the arc. The bi-convex lens (focal length = 20 cm and diameter = 5 cm) and the screen were installed in front of the window of the upper chamber. The lens produced an inverse image of the arc on the screen. The digital camera was TV 203 model of SONY and had special digital effects that enabled to focus very sharply on the image regardless of the surrounding lighting, etc. At any time the exposure time on the camera could also be changed to produce darker or brighter images. These recorded images were transferred to a computer for further analysis.

4.5. MEASUREMENTS

4.5.1. Measurement of Total Voltage and Arc Current

Total voltage of an arc was measured using a divider circuit. The divider was connected across the cathode and anode at the output of the high frequency generator. Arc current was measured using a shunt which was placed in series with the anode. The outputs of both devices were connected to the data acquisition system.

4.5.2. Measurement of Erosion Rate of the Cathodes

The erosion rate of an electrode (E), in general, has been defined as the mass loss normalized to the total electric charge passing through the cathode and is presented as the following equation:

$$E = \frac{M(\tau)}{\int_0^{\tau} I(t)dt} \tag{4-3}$$

where $M(\tau)$ is the total mass loss of the electrode for an arcing time τ; I(t) is the arc current evolution (Kim, 1995). In this work, the integration in Equation (4-3) was not needed because the average arc current could be obtained from the data file of each run. Therefore, the equation (4-3) was simplified as the following equation:

$$E = \frac{\Delta M}{t * I} \tag{4-4}$$

where ΔM is the total mass loss of the cathode for arc duration, t; I is the average arc current. The total mass loss was determined by measuring the cathode weight before and after each experiment.

4.5.3. Measurement of Cathode Surface Temperature

For the measurement of the cathode surface temperature using the single wavelength pyrometer, a blackbody hole was prepared just above the cathode tip as shown in Figure 4-6. The diameter of the blackbody hole for the both cathodes was 1 mm; the depth of

that was 5 mm for cathode I and 2 mm for cathode II. The filament of the single pyrometer was focused on the blackbody hole and thus the color comparison between the filament and the hole was possible. When the two colors were matched, the temperature was recorded.

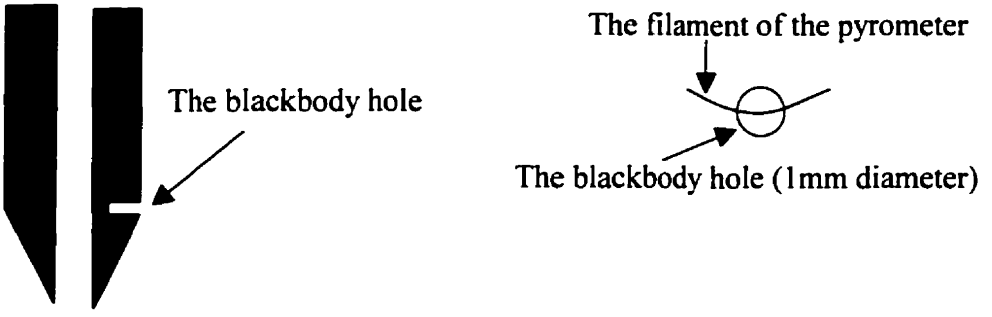

Figure 4-6: The position of the blackbody hole and the overlapping of the filament and the hole.

The two-wavelength pyrometer was installed in front of the widow located in the upper chamber, and it was connected to a strip chart recorder (Graphtec Corp., SR6211) to record the cathode surface temperature. The target size for this temperature measurement was about 5 mm determined using the figure of "target diameter vs. distance to target" in the manual of the two-wavelength pyrometer, provided by Capintec Instrument, Incorporation. The recorder output of the pyrometer is between 0 and 1 V DC full scale. Normal recording paper speed of the chart recorder was 1 mm per minute. Chen (1991), previously used the pyrometer, reported that the intensity of the plasma arc could interfere with the measurement of the surface temperature of a body. Therefore, to estimate the cathode surface temperature without the effect of the arc radiation, the cooling curve of

the cathode was recorded. In that case, the recording paper speed was increased to 500 mm per minute as soon as the plasma was shut off.

4.6. EXPERIMENTAL PROCEDURE

4.6.1. Pre-Experimental Preparation

1) The inside of the chamber was cleaned with a vacuum cleaner to remove any debris left from the previous experiment. The cathode and the anode were weighed and their masses were recorded. A new cathode was used for the measurement of the erosion rate. The remainder of the apparatus components were cleaned and assembled. The electrical isolation of the cathode was verified.
2) Argon gas was injected into the chamber according to the procedure previously mentioned for the argon atmosphere. The O_2 concentration, the relative humidity, and the temperature of the inside of the chamber were measured.
3) The cathode and the anode cables were connected with the power supply. The power controller and the emergency stop cables were installed.
4) The internal resistance (about 8 kΩ) of the power supply was inspected.
5) The data acquisition system was inspected.
6) All related utility lines were inspected and cooling water flows were started. Operation of the exhaust vent was verified.
7) The power supply was turned on.

4.6.2. Arc Ignition

In this work, two arc ignition methods were used. The first method was drawing an arc from short circuit, and the second one was using the high frequency generator. The arc drawing method was performed by separating graphite electrodes which were in contact. The contact of the graphite electrodes was verified using a multimeter. Because the anode was fixed, the cathode was lowered to contact the anode using a DC motor controller. The lowering speed of the cathode was 0.04 cm per second to minimize mass loss of the cathode when the electrodes contacted. To draw an arc, the cathode was lifted up relatively quickly. The speed of the lifting was 0.1 cm per second. As soon as the arc ignited, the current was increased to 100 A to help in drawing the arc. This method was employed to avoid the electrical interference caused by the high frequency generator and thus allow the voltage and the current to be recorded from the beginning of the arc ignition. In the high frequency generator method, the most common arc ignition method currently used in transferred arc plasma systems, the cathode was lowered to within a few millimeters of the stationary anode surface and then a high frequency spark was struck between the electrodes. The high frequency generator method was used to measure erosion rates without the mass loss due to the contact. For 150 A experiments the drawing an arc method was used, and for 300 and 400 A experiments the high frequency generator method was used.

4.6.3. Execution of an Experiment

1) The argon gas flow rate, the initial interelectrodes gap, and the current were adjusted to their desired levels.

2) The data acquisition was begun. For the drawn arc method there was no time delay from arc ignition to the start of the data acquisition system. In case of the high frequency generator method, however, the time delay was approximately 3 minutes since the computer could only be started after the high frequency was off.

3) An experiment was terminated by shutting down the rectifier bank. Argon and cooling water were continued until the apparatus had cooled.

4.6.4. Post Experimental Procedure

1) The cathode and the anode were cleaned with a brush or a compressed air duster to remove soot attached on the surfaces of the electrodes.

2) The cathode was weighed to determine its mass loss during the experiment.

3) Average arc current was obtained from the ASCII text file of the data acquisition.

4) Erosion rate of the cathode was calculated.

CHAPTER V

EQUILIBRIUM COMPOSITION

A free energy minimization was performed to calculate the equilibrium composition as a function of temperature. It was aimed at understanding the behavior of carbon and ionized species under a high temperature condition in the argon atmosphere at atmospheric pressure. The Outokumpu HSC Chemistry Program (Roine, 1994) was used for the calculation of the equilibrium compositions. The equilibrium compositions calculated was limited because chemical species available in the database of the HSC program were restricted. Also, thermodynamic equilibrium in the chamber could not be expected due to the temperature distribution in the chamber.

5.1. SPECIES CONSIDERED

The carbon species considered here were C (s), C (g), C_2 (g), C_3 (g), C_4 (g), C_5 (g), C (+g), C (-g), C_2 (+g), and C_2 (-g). The s in the parentheses stands for a solid compound and the g represents a gaseous one. The +g and the -g mean charged compounds, positive and negative gaseous species, respectively. The electron was also included in this calculation for the ionization of gaseous compounds. Diamond was excluded since it was thought that diamond was not produced under this condition. For the calculation of the equilibrium composition, the HSC program needs the charge balance between positive and negative species of input compounds. Therefore, 1E-20 moles of C_2 (+g) and 1E-20 moles of C_2 (-g) were initially given in the input condition. For the argon gas species, Ar (g) and Ar (+g) were used.

5.2. EQUILIBRIUM COMPOSITION

Figure 5-1 presents the equilibrium composition as a function of temperature. For the

calculation, the system pressure was 1 bar, and the molar ratio of the argon gas to the solid carbon species was 1. For this program, the increase of the number of moles of the argon gas, i.e. the increase of the molar ratio, did not affect the equilibrium composition of the carbon species. However, as the ratio is increased, the lowering of the ionization energies of the species in the vicinity of charged particles may be expected because the densities of charged particles are increased, thus providing higher fields and lowering the ionization energies.

In Figure 5-1, the input mole of the solid carbon (1 mole) starts to drop sharply at about 3200 K. That is vaporization of the solid carbon. Before this temperature, the number of the input moles of the solid carbon is constant because there is no oxygen in the argon atmosphere. After the vaporization of the solid carbon, C (g), C_2 (g), C_3 (g), C_4 (g), and C_5 (g) starts to appear at about 4000 K. The carbon species of C (g), C_2 (g), and C_3 (g) are noticeable, but C_4 (g) and C_5 (g) are negligible in this calculation. Therefore, in the figure only C (g), C_2 (g), and C_3 (g) are presented. According to Mentel's study (1978), the temperature of graphite vapor jets was between 4000 and 5000 K. In this temperature range, it can be expected that several carbon species exist and they may be the source of the carbon redeposition, which has been reported for carbon arcs producing fullerences. Between 5,000 and 10,000 K, C (g) is the most stable component among the carbon species. After 10,000 K, equilibrium moles of C (g) start to decrease greatly because of its ionization; its ionization energy is 11.3 eV. Also, the ionization of Ar (g) appears; the ionization energy of argon gas is 15.7 eV. Over than 20,000K, uncharged species almost do not exist and C (+g), Ar (+g), and electrons are major components.

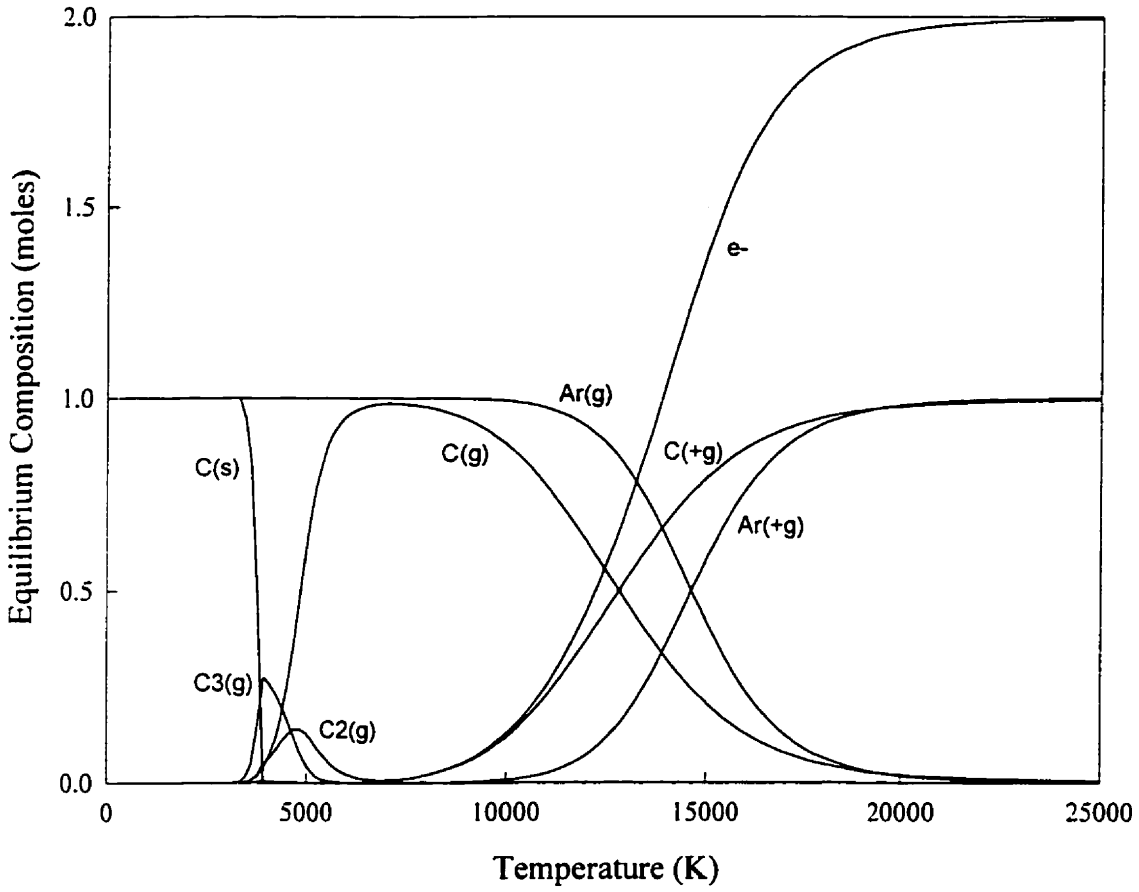

Figure 5-1: Equilibrium composition of the carbon and argon components as a function of temperature. Input compositions are argon (g) 1 mole, C_2 (+g) 1E-20 mole, C_2 (-g) 1E-20 mole, and C (s) 1 mole.

CHAPTER VI

RESULTS AND DISCUSSIONS

This chapter consists of three parts: 1) characteristics of the arcs, 2) the arc stability at the hollow graphite cathode, and 3) the erosion behavior of the hollow graphite cathode. The first part includes interpretation of the total voltage as a function of the operating conditions. Arc pictures are also presented. The second part deals with identification of the mode transition of the cathode. This is followed by the erosion behavior of the cathode.

6.1. CHARACTERISTICS OF THE ARCS

6.1.1. Total Voltage Patterns

In this work, two completely different total voltage patterns appeared as a function of the operating conditions and the geometry of the cathode. One is almost constant total voltage pattern termed "stable" operation; the other is great fluctuation of total voltage pattern termed "unstable" operation as shown in Figures 6-1, 6-2, and 6-3. These figures present typical total voltage patterns of the stable and the unstable arcs recorded at 150 A. Total arc duration in these figures was separated into 3 regimes; initial, stable, and unstable arc duration. The initial arc duration of 3 minutes is introduced for only 150 A runs due to the arc drawing method, which did not have the time delay (3 minutes) for the start of the data acquisition system.

As shown in Figure 6-1, for the stable operation the total voltage was almost unchanging, but for the unstable operation in Figures 6-2 and 6-3, some time after the arcs ignited, the total voltage fluctuated greatly with time. This fluctuation was one of the characteristics of the unstable operation. A run displaying this unstable part always started in stable arc

region. This initial stability was associated with a sharp cathode tip; before the cathode tip eroded, the arcs were always stable; after the cathode tip eroded, the fluctuation of the total voltage appeared according to the operating conditions. Details are presented later (see 6.2.2. Effect of the Cathode Tip Geometry on The Arc Stability). The stable arc duration before unstable operation was not constant. It was different for different operating conditions and even for different experiments under the same operating conditions. For EXP-21 the stable arc operation time was about 63 minutes and the unstable arc duration was about 54 minutes as shown in Figure 6-2. Figure 6-3 shows another total voltage pattern recorded at the same operating conditions of EXP-21. In this case, the stable arc operation and the unstable arc operation times were 73 and 44 minutes, respectively. It was thought that this difference might be related to different graphite cathode tip surface conditions and random ignition positions. The raw data of the operating conditions as well as the erosion rates measured in this study are included in Appendix 2 and 3. In case of 300 and 400 A experiments, the trends of the total voltage patterns were similar. Some total voltage patterns recorded at 300 and 400 A runs are introduced below.

The arc operation change from the stable to the unstable region was associated with the appearance of an acoustical noise and a sudden increase of the voltage, normally a few volts. The acoustical noise is associated with the arc power fluctuations. At this time stretched arcs could be seen through visual observation of arcs, performed by the digital camera. In addition, the anodic arc root moved radially outward from its normal location beneath the cathode.

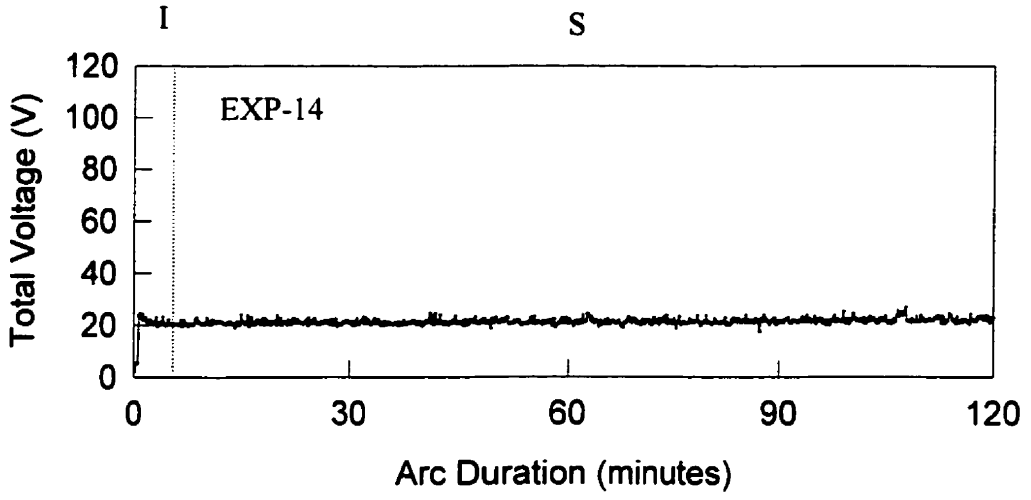

Figure 6-1: Typical total voltage pattern of the stable operation using cathode I for an initial interelectrode gap of 0.5 cm, an argon gas flow rate of 15 slpm, and an arc current of 150 A. I stands for initial arc duration (3 minutes); S is for stable arc duration (117 minutes).

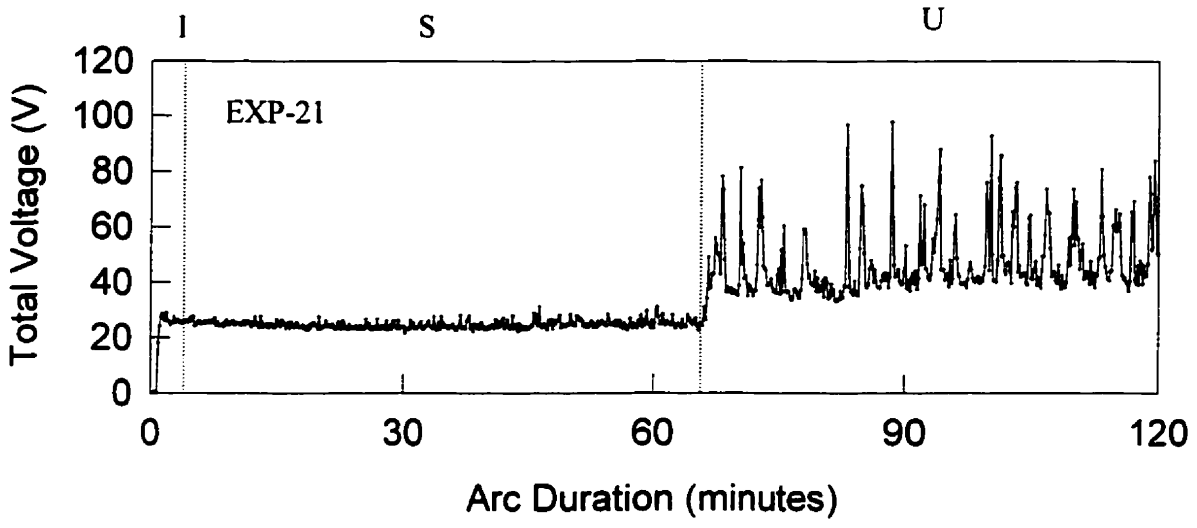

Figure 6-2: Typical total voltage pattern of the unstable operation using cathode I for an initial interelectrode gap of 3.0 cm, an argon gas flow rate of 4.5 slpm, and an arc current of 150 A. I stands for initial arc duration (3 minutes); S is for stable arc duration (63 minutes); U is for unstable arc duration (54 minutes).

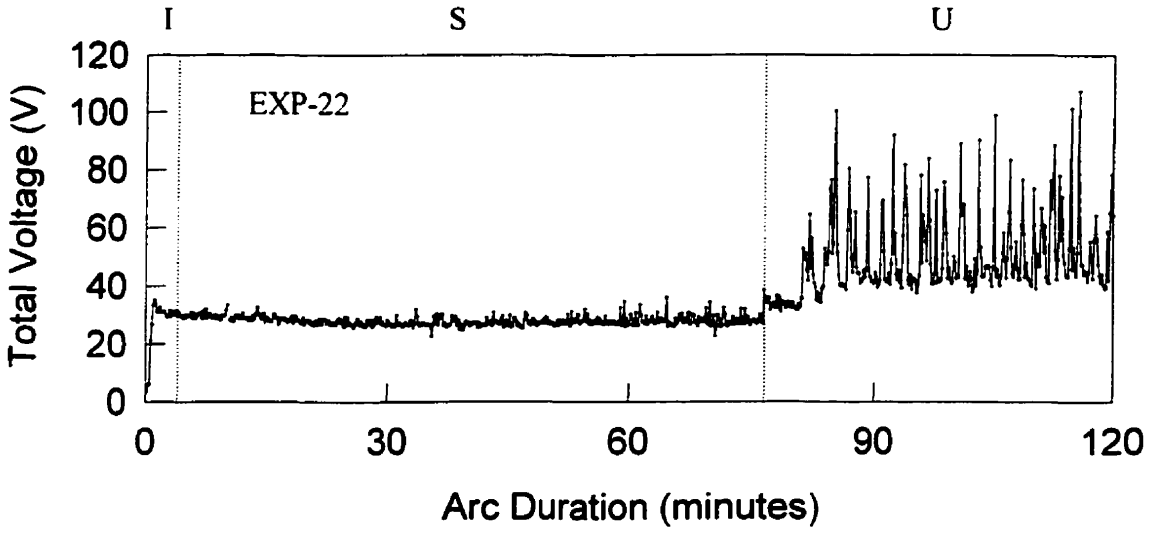

Figure 6-3: Typical total voltage pattern of the unstable operation using cathode I for an initial interelectrode gap of 3.0 cm, an argon gas flow rate of 4.5 slpm, and an arc current of 150 A. I stands for initial arc duration (3 minutes); S is for stable arc duration (73 minutes); U is for unstable arc duration (44 minutes).

6.1.2. Influence of Initial Interelectrode Gap on Total Voltage

Figures 6-4 and 6-5 show the influence of the initial interelectrode gap on the total voltage. Since the graphite cathode was eroded with the time, the average values of the total voltage between 3 and 6 minutes of the stable operation are used in these figures. As the initial interelectrode gap rose, the total voltage increased because the rise of the initial interelectrode gap provided higher arc length. This was expected since arc resistance increases with arc length. The slope, i.e. $\Delta V/\Delta gap$, for the run at 0 slpm is higher than other runs. This slope represents strength of the mean electric field between the electrodes; the arc current divided by this slope, i.e. $I / (\Delta V/\Delta gap)$, is the electrical conductivity between the electrodes. A higher slope, therefore, means higher electric field and lower electrical conductivity at a constant current. It could be seen that the injection of the argon gas reduced the slope and thus increased the electrical conductivity. It seems that the argon gas might wash out condensed carbon particles, thus causing enhanced the argon atmosphere and the increase of the electrical conductivity.

Figure 6-6 presents a comparison of the total voltage between cathode I and II for an argon gas flow rate of 15 slpm and an arc current of 300 A. The total voltage of cathode II was always higher. It appeared that the reduced outer diameter of cathode II might provide increase of the total resistance of cathode II and influence electrical properties of the arcs, thus offering the higher total voltage of cathode II. The total resistances of the cathodes measured at room temperature are 0.34 Ω for cathode I and 0.46 Ω for cathode II.

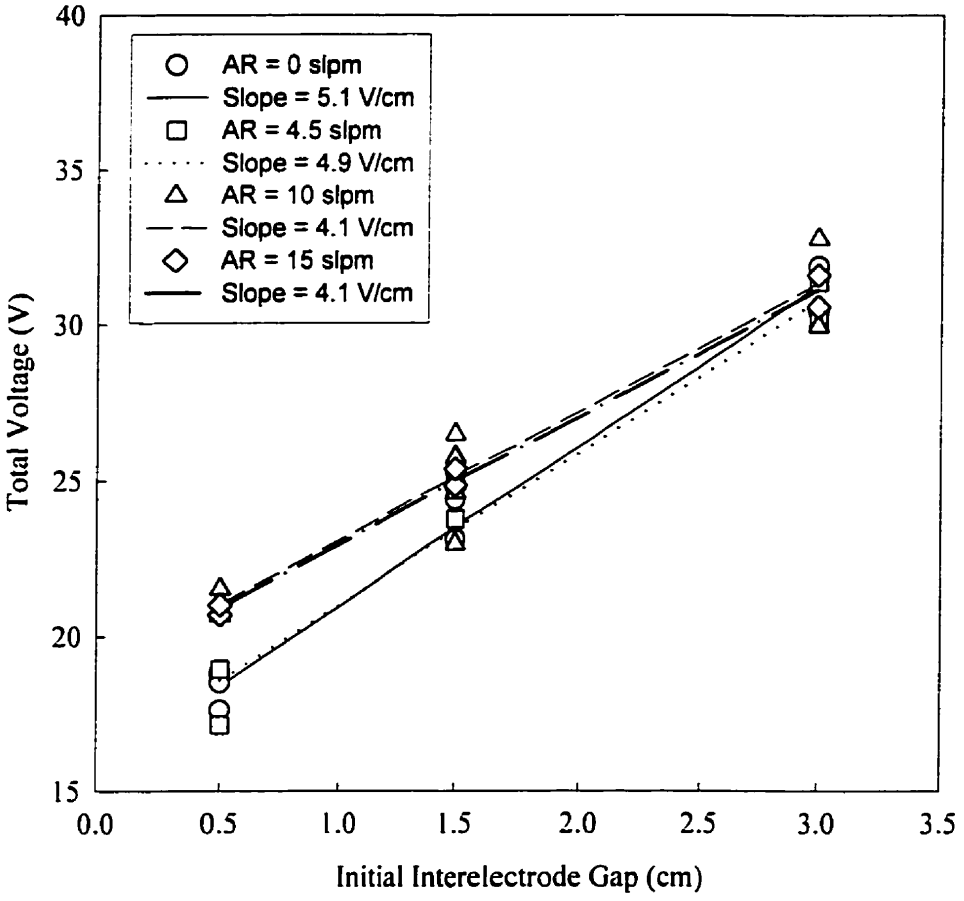

Figure 6-4: Total voltage as a function of the initial interelectrode gap using cathode I at 150 A.

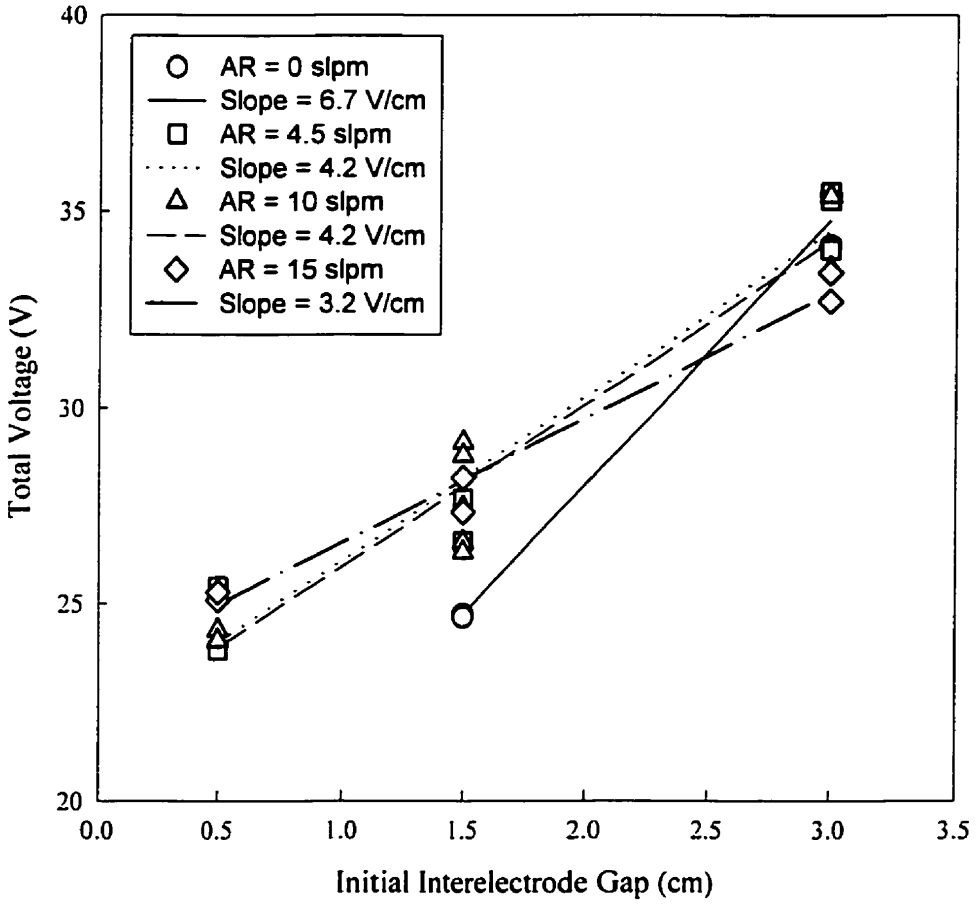

Figure 6-5: Total voltage as a function of the initial interelectrode gap using cathode I at 300 A.

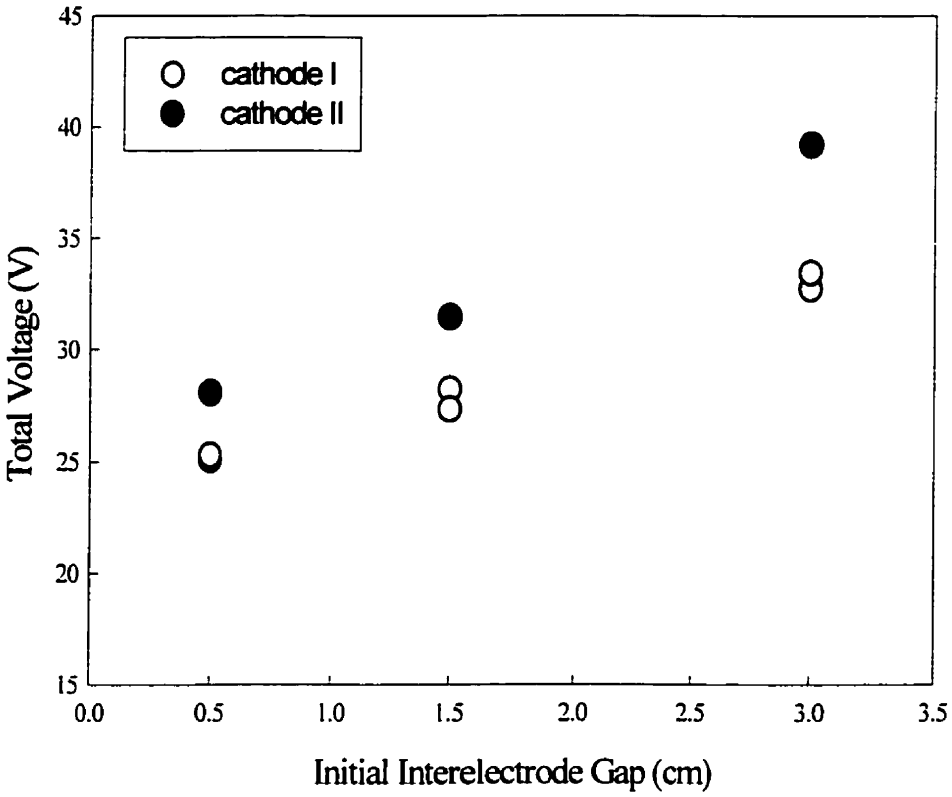

Figure 6-6: Comparison of the total voltage between cathode I and II for an argon gas flow rate of 15 slpm at 300 A.

6.1.3. Influence of Argon Gas Flow Rate on Total Voltage

The influence of the argon gas flow rate on the total voltage is presented in Figures 6-7 and 6-8. The average values of the total voltage between 3 and 6 minutes of the stable operation are used. Pfender et al. (1989) stated that an increase of gas flow rate causes enhanced cooling of the arc fringes, thus providing a higher rate of ionization in the core of the arc column to compensate the electron losses of the arc fringes. This also increases the field strength, and therefore, the arc voltage has to rise. In addition, Mehmetoglu (1980) reported the effect of the argon gas flow rate on the arc voltage in a transferred-arc plasma using tungsten electrodes; the arc voltage increased with the argon gas flow rate. His experimental conditions were arc currents of 150, 250, and 350 A, interelectrode gaps of 4, 6, 8, and 10 cm, and argon gas flow rates of 14, 17, and 20 slpm. He stated that the influence of the argon gas flow rate was almost negligible for short arcs, but was significant for long arcs. His conclusion about this effect could not be directly compared with the results of this work because of the different operating conditions, especially the interelectrode gap. The shortest interelectrode gap of his work was 4 cm, while the longest initial interelectrode gap of this study was 3 cm. In this work, it was thought that at 0.5 and 1.5 cm, the voltage increased slightly with increasing argon gas flow rate, but at a gap of 3.0 cm the effect of gas flow rate on voltage was negligible. An important difference between this work and work with transferred arcs to metal cathodes is that the latter had a converging section through which the gas was injected. In the present work the gas enters through a constant diameter hole in the middle of the cathode so that the argon gas jets leaving the cathode are relatively weaker and thus changes in gas flow rate have little effect on the voltage.

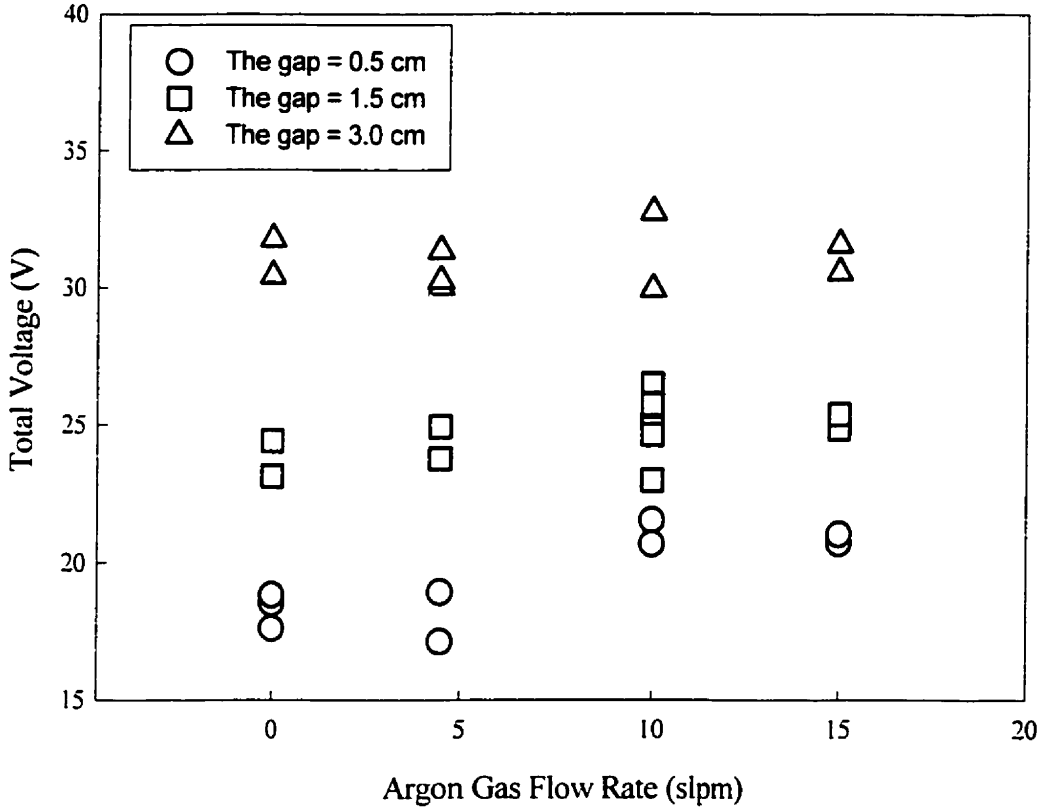

Figure 6-7: Total voltage as a function of the argon gas flow rate using cathode I at 150 A.

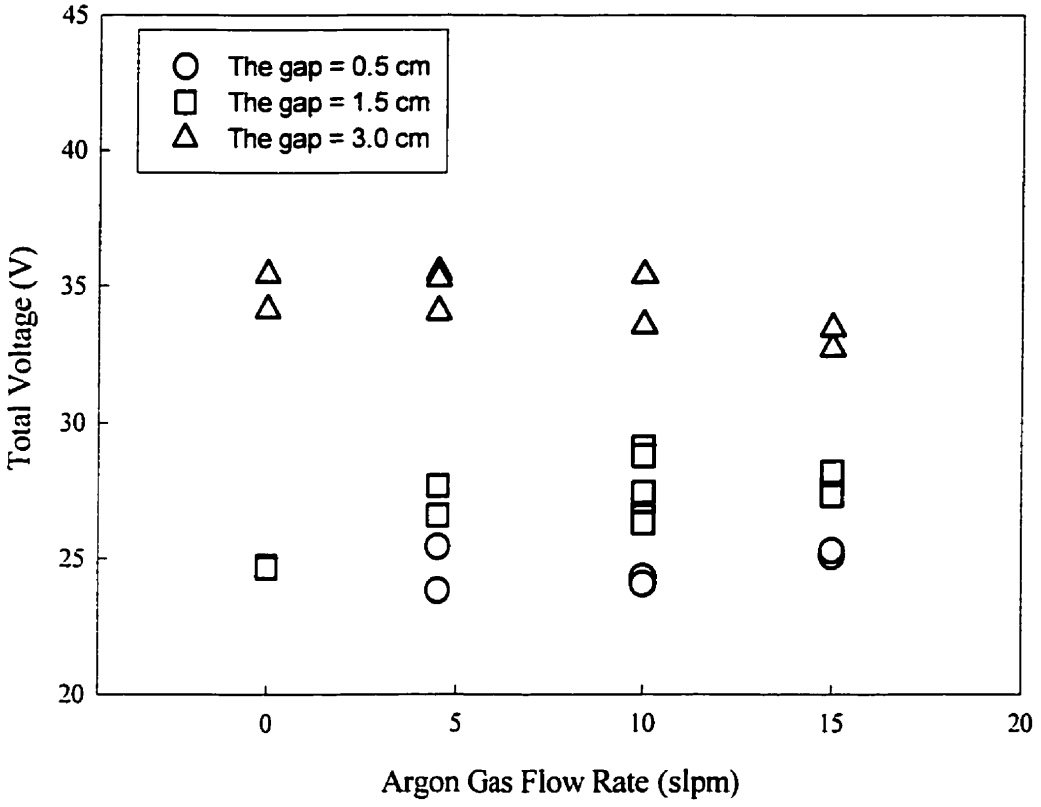

Figure 6-8: Total voltage as a function of the argon gas flow rate using cathode I at 300 A.

6.1.4. Voltage-Current (V-I) Characteristic

The V-I characteristic of the hollow graphite cathode is a slowly rising characteristic as presented in Figure 6-9. Roth (1995) stated that generally the arc regime in more than 20 to 50 A are called the thermal or high intensity arcs and their V-I characteristics are a nearly flat or slowly rising like the V-I characteristic of this work. This V-I characteristic confirms that arcs in this study are in the thermal arc regime. The rise of the total voltage with the increase of the argon gas flow rate discussed in section 6.1.3 is also evident in Figure 6-9.

6.1.5. Visual Observation of The Arcs

This visual observations and digital video camera photography were used to characterize the behavior of the arcs. This also included the distinction between the stable and the unstable arcs, by considering the voltage at any moment.

6.1.5.1. Arc Observation of Cathode I

Arc pictures for the stable and the unstable arcs of cathode I are presented in the following figures. The operating conditions selected for this run were a current of 300 A, an initial interelectrode gap of 3.0 cm, and an argon gas flow rate of 4.5 slpm. The total voltage pattern of this run is presented in Figure 6-10. The experiment ran for 60 minutes; the first 18 minutes fell into the stable region and the rest was unstable. A schematic drawing of this visual arc observation is presented in Figure 6-11.

The pictures in Figure 6-12 were taken at random intervals during the stable arc

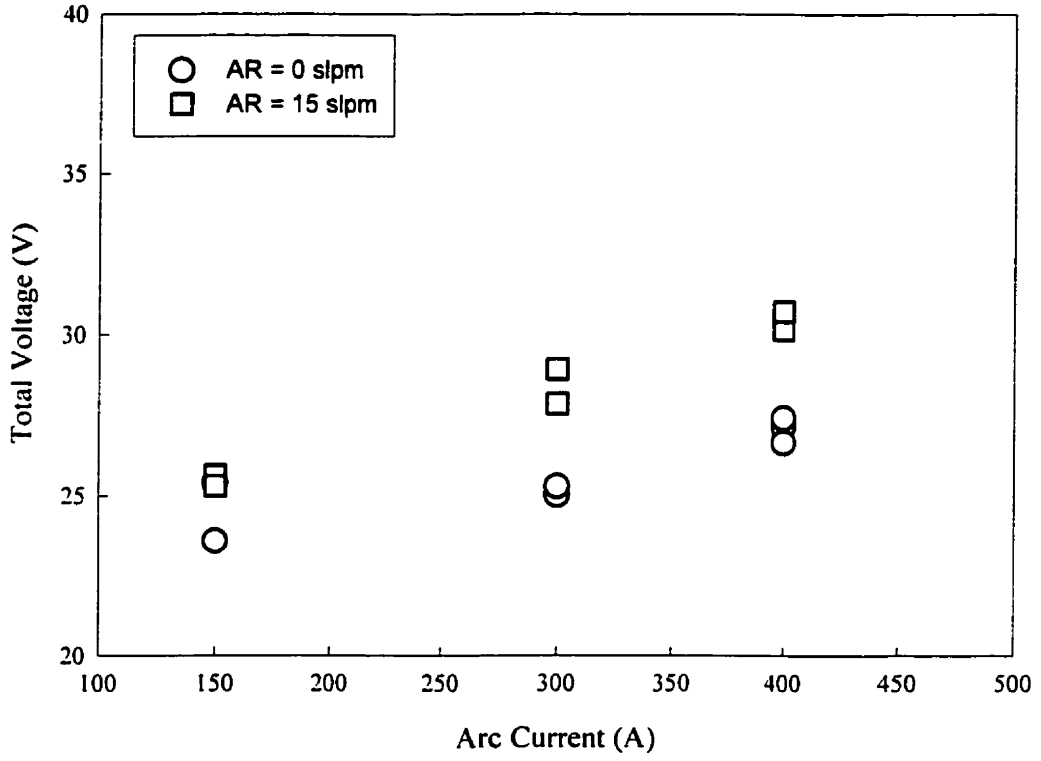

Figure 6-9: Voltage-current (V-I) characteristic of the arcs using cathode I for an initial interelectrode gap of 1.5 cm.

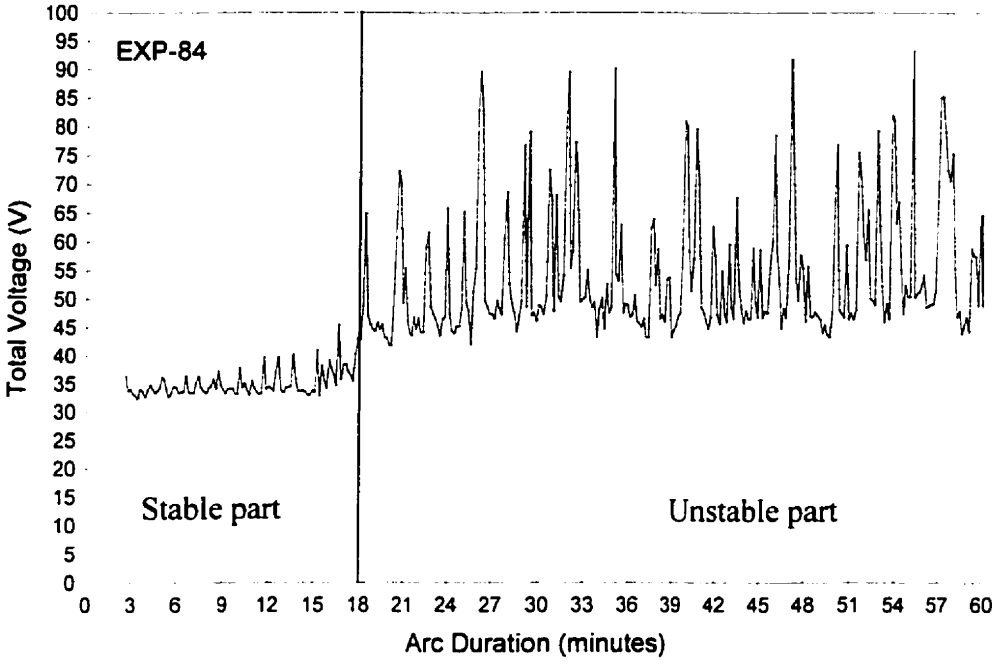

Figure 5-10: Total voltage pattern of an unstable arc recorded using cathode I for an initial interelectrode gap of 3.0 cm, an argon gas flow rate of 4.5 slpm, and an arc current of 300 A.

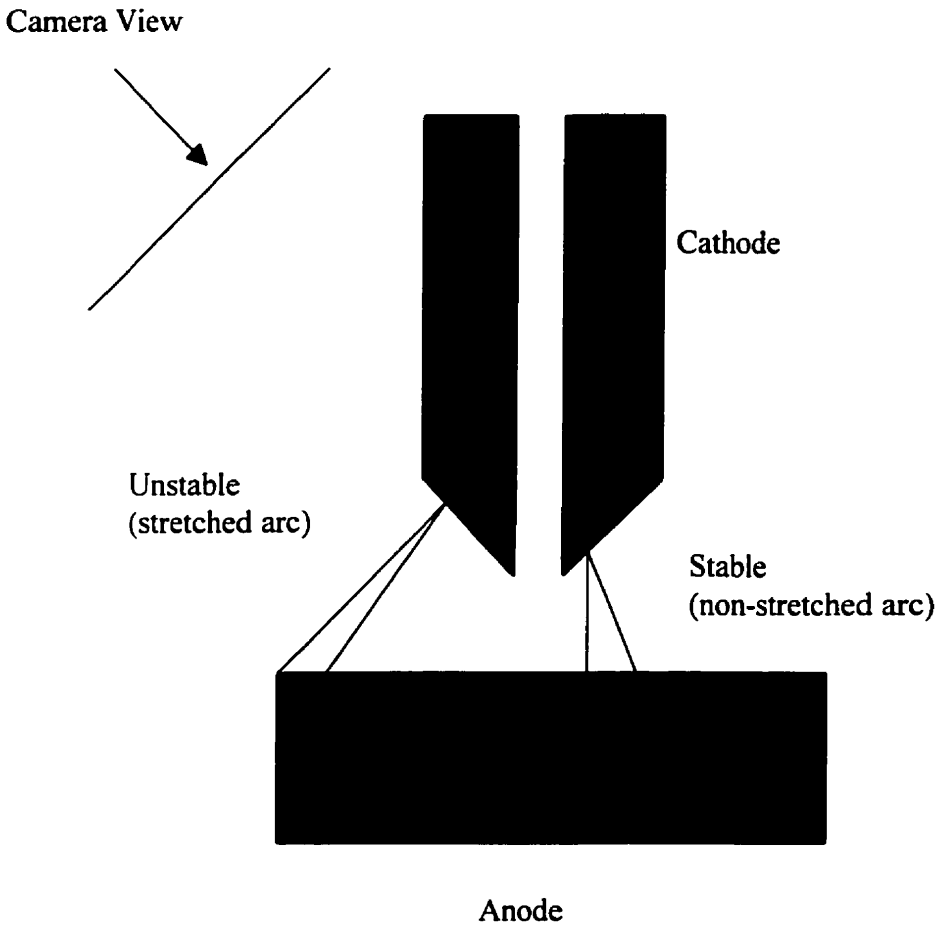

Figure 6-11: The schematic diagram of visual arc observation

operation. The exposure time on the camera was changed to make the pictures brighter. The unit of the exposure time is arbitrary. In the stable arc operation the arc was not stretched, but sometimes, at the end of the stable operation, the arc started to be stretched with small voltage fluctuations as shown in the total voltage between 15 and 18 minutes in Figure 6-10. At that time the arc looked like picture (e) in Figure 6-12. Pictures for the unstable arc operation were randomly taken 18 minutes after the arc started and are presented in Figure 6-13. When the arc was unstable, it was highly stretched and touched the anode at a radial position far from location directly beneath the cathode. Acoustical noise could be heard at this time. Also, in this case anodic vapor jets were easily visible. These vapor jets often contacted the arc and were very fast moving. The connecting vapor jets are presented in pictures (b), (c), (g), (i), (l), (m), and (r) in Figure 6-13.

Figure 6-14 shows 33 sequential pictures of the unstable arc taken within 1 second using the digital camera. The pictures were taken at 48 minutes 55 seconds after the arc started. This figure provided good information about the connection between the arc and the anodic vapor jets for an unstable arc. In these pictures the movement of the anodic vapor jets could also be seen; the vapor jets moved even in less than 1 second. It is believed that this movement is good evidence of how fast the vapor jets move. The connecting anodic vapor jet is normally present in one stream but sometimes even up to three streams were observed.

6.1.5.2. Arc Observation of Cathode II

Arc pictures of cathode II are presented in Figures 6-16 and 6-18. The operating

(a) Voltage=30 V, Exposure=8

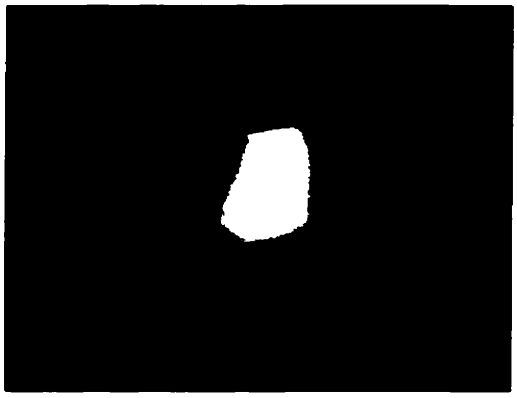

(b) Voltage=33 V, Exposure=9

(c) Voltage=31 V, Exposure=11

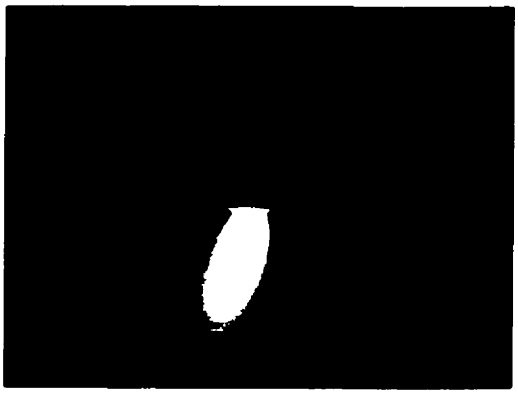

(d) Voltage=31 V, Exposure=12

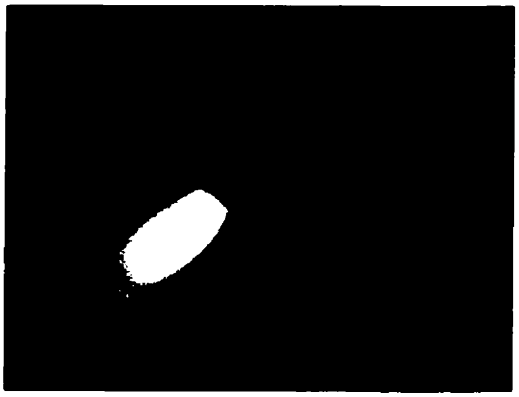

(e) Voltage=37 V, Exposure=11

Figure 6-12: Arc pictures randomly taken for the stable arc operation of EXP-84.

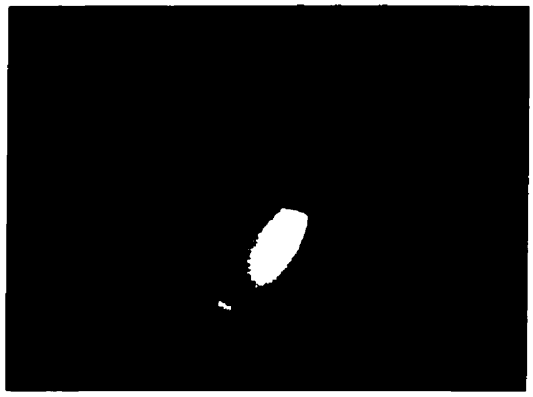

(a) Voltage=45 V, Exposure=8

(d) Voltage=43 V, Exposure=8

(b) Voltage=60 V, Exposure=11

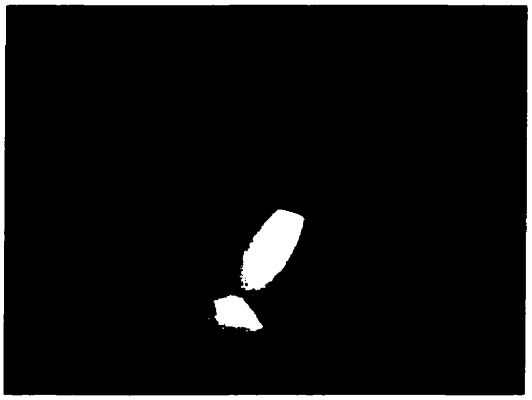

(e) Voltage=45 V, Exposure=9

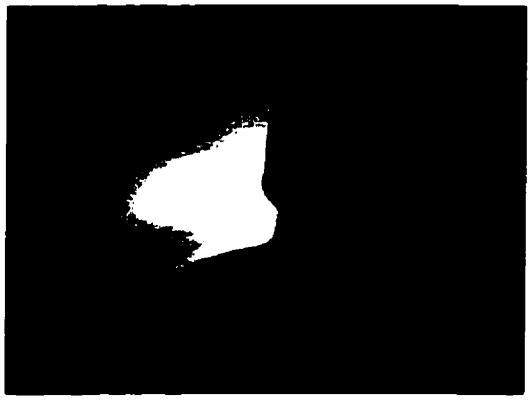

(c) Voltage=70 V, Exposure=11

(f) Voltage=45 V, Exposure=9

Figure 6-13: Arc pictures randomly taken for the unstable arc operation of EXP-84.

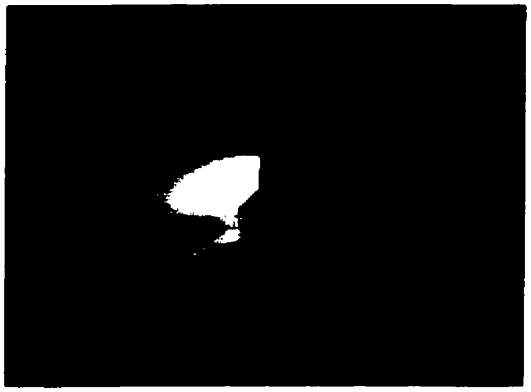

(g) Voltage=70 V, Exposure=9

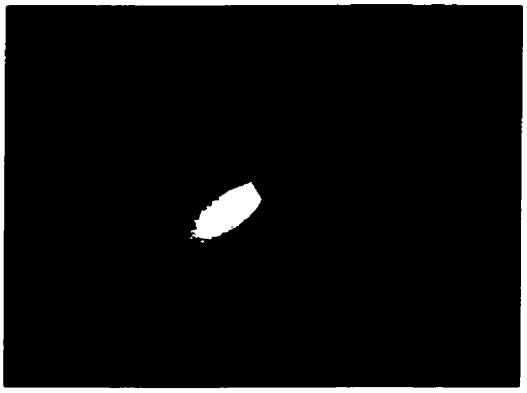

(j) Voltage=80 V, Exposure=8

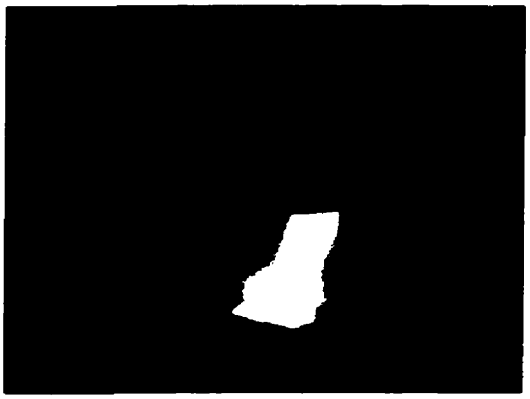

(h) Voltage=42 V, Exposure=9

(k) Voltage=47 V, Exposure=9

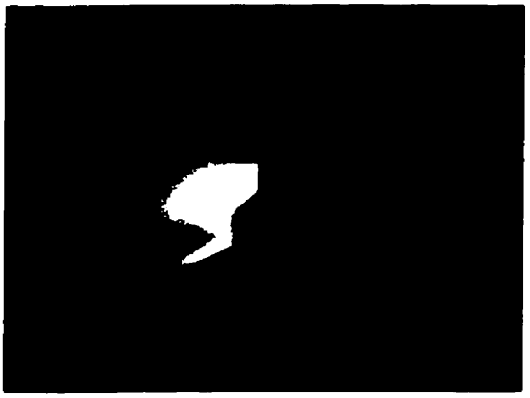

(i) Voltage=80 V, Exposure=9

(l) Voltage=81 V, Exposure=8

Figure 6-13: Arc pictures randomly taken for the unstable arc operation of EXP-84. (continued)

(m) Voltage=75 V, Exposure=8

(p) Voltage=75 V, Exposure=8

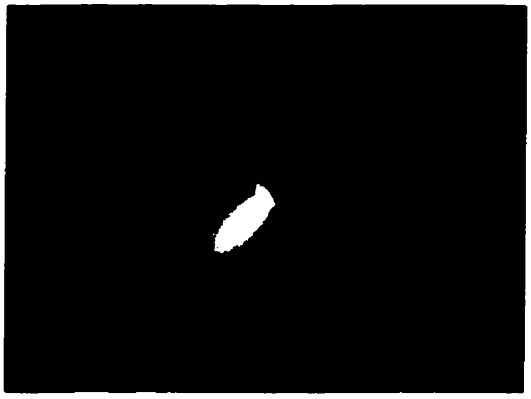

(n) Voltage=81 V, Exposure=8

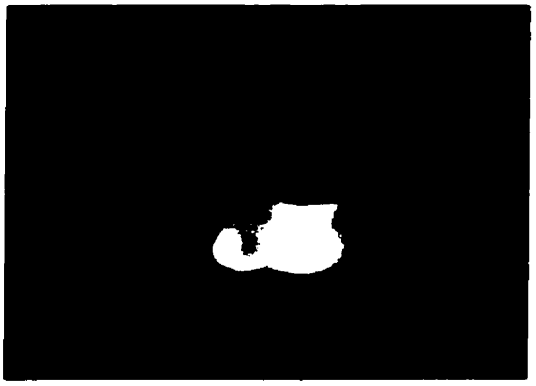

(q) Voltage=45 V, Exposure=8

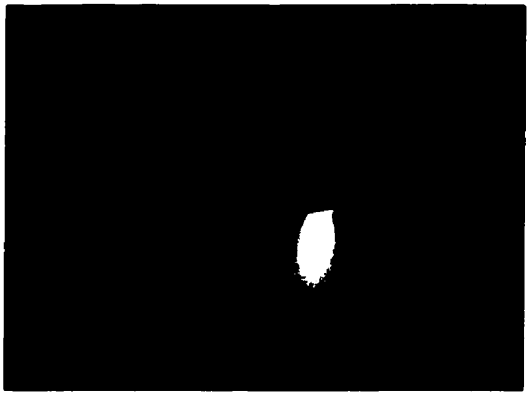

(o) Voltage=41 V, Exposure=8

(r) Voltage=61 V, Exposure=9

Figure 6-13: Arc pictures randomly taken for the unstable arc operation of EXP-84. (continued)

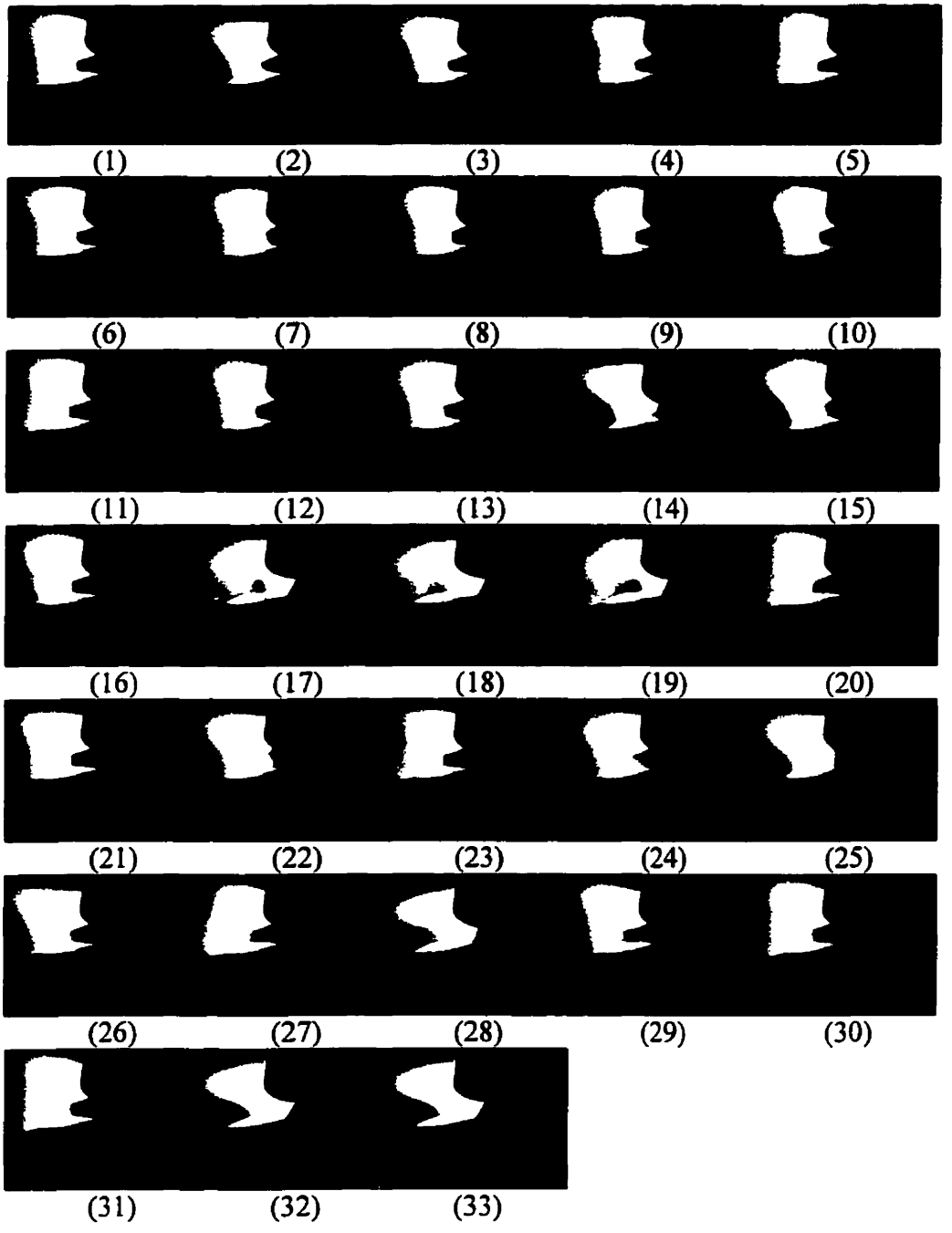

Figure 6-14: Arc pictures taken within 1 second at 48 minutes 55 seconds of EXP-84.

conditions selected for the run of Figure 6-16 were a current of 300 A, an argon gas flow rate of 0 slpm, and an initial interelectrode gap of 3.0 cm. The total voltage pattern of this run is presented in Figure 6-15. The experiment ran for 30 minutes and the arc was stable for the whole run. For 0 slpm the arc of cathode I changed from the stable to the unstable region and showed the great voltage fluctuation; however, for cathode II the arc was always stable and the voltage fluctuated little even after the arc stretched. Figure 6-15 presents the stretched arc voltage pattern of cathode II. At about 6 minutes the voltage started to increase corresponding to the stretching of the arc. The arc had a slow and uniform motion all over the cathode tip. The voltage was fairly constant fluctuating only by 2~3 volts, with a mean value of about 43 V.

Another total voltage pattern and arc pictures using cathode II are presented in Figures 6-17 and 6-18. This run lasted for 30 minutes at 300 A for an argon gas flow rate of 4.5 slpm and an initial interelectrode gap of 3.0 cm. The difference of total voltage patterns between EXP-81 and EXP-82 is that in the total voltage pattern of EXP-82, there was no voltage increase, as was observed after about 6 minutes in EXP-81. The increase of the argon gas flow rate might make the arc region more electrically conductive between the electrodes by washing out the vaporized graphite particles and thus the arc length change was less. That was also observed in other experiments at 10 and 15 slpm.

An incandescence at the tips of cathode I and II resulting from arc heating could be observed through the chamber window. Also some arc pictures show a color difference between two cathodes. For cathode II, the red zone at the tip was both longer and

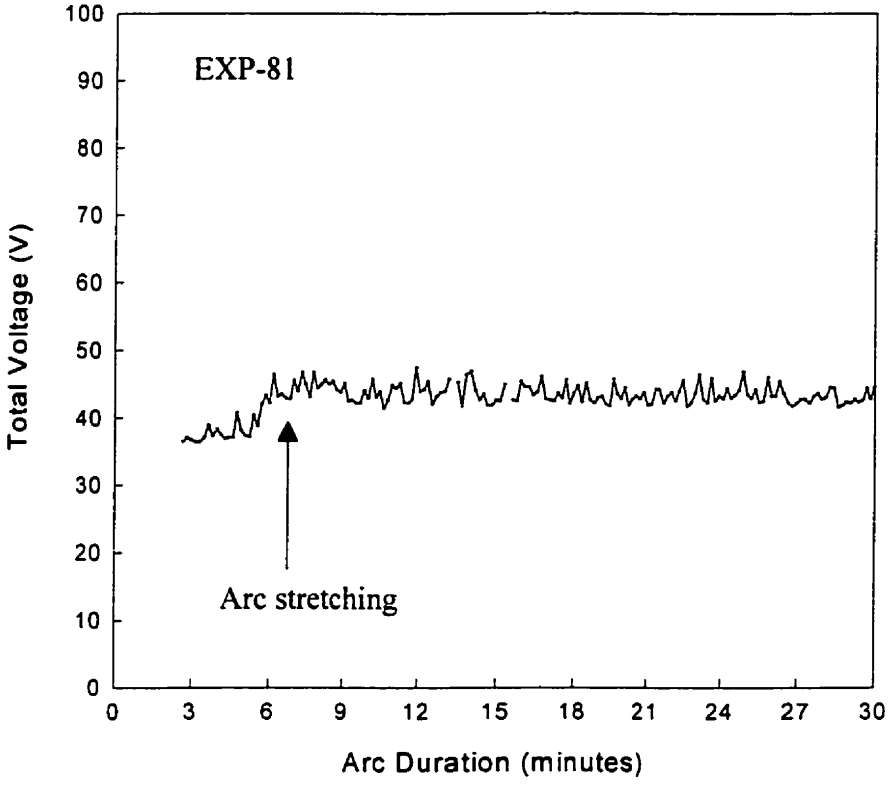

Figure 6-15: Total voltage pattern of a stable arc using cathode II recorded for an initial interelectrode gap of 3.0 cm, an argon gas flow rate of 0 slpm, and an arc current of 300 A.

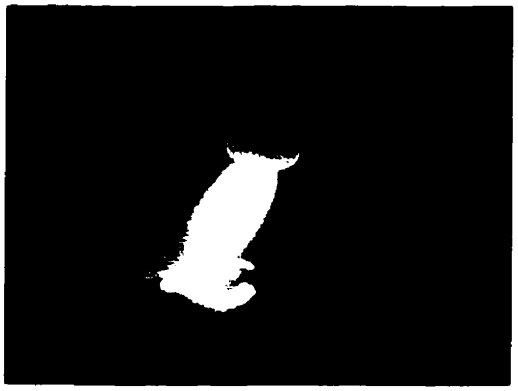

(a) Voltage=41 V, Exposure=13

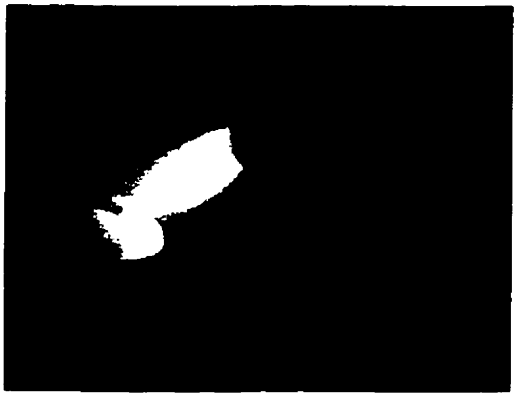

(b) Voltage=41 V, Exposure=11

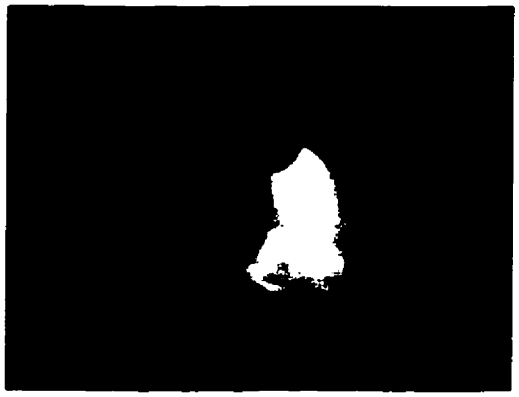

(c) Voltage=41 V, Exposure=10

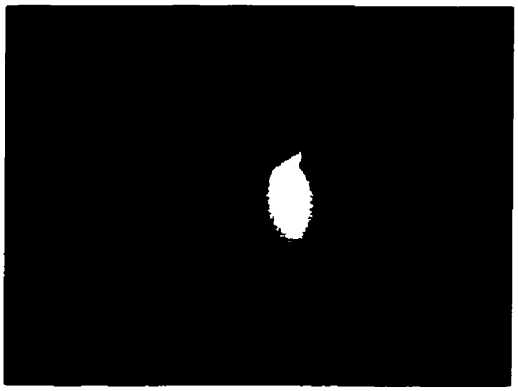

(d) Voltage=42 V, Exposure=9

(e) Voltage=43 V, Exposure=8

Figure 6-16: Arc pictures randomly taken using cathode II (EXP-81).

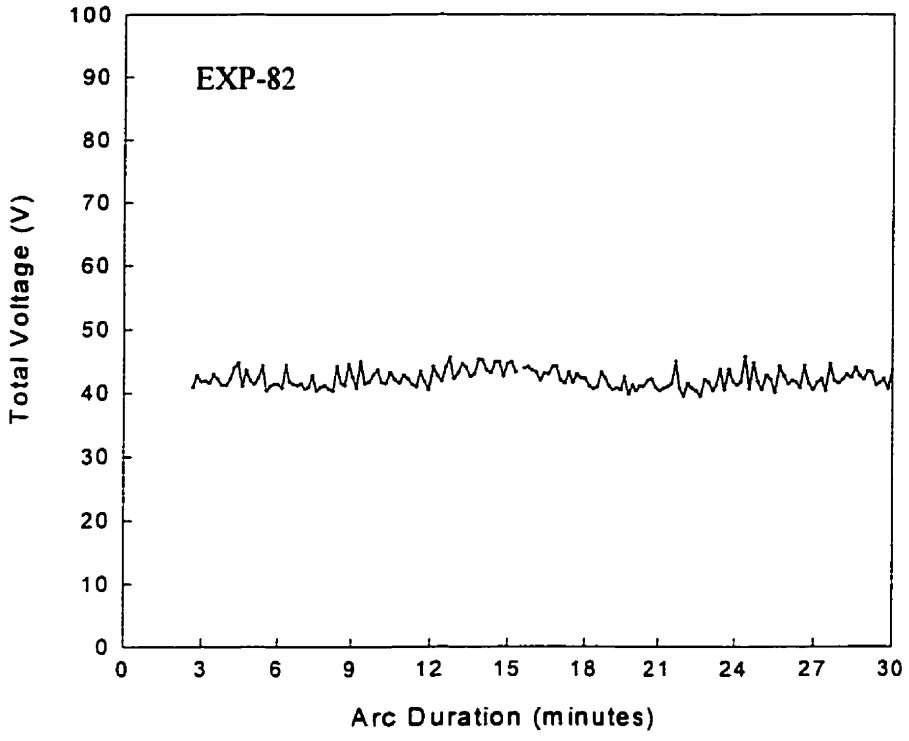

Figure 6-17: Total voltage pattern of a stable arc using cathode II recorded for an initial interelectrode gap of 3.0 cm, an argon gas flow rate of 4.5 slpm, and an arc current of 300 A.

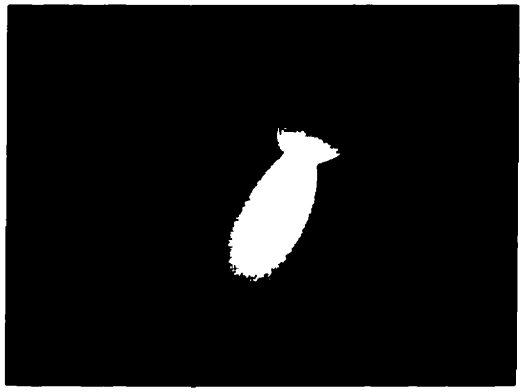

(a) Voltage=41 V, Exposure=13

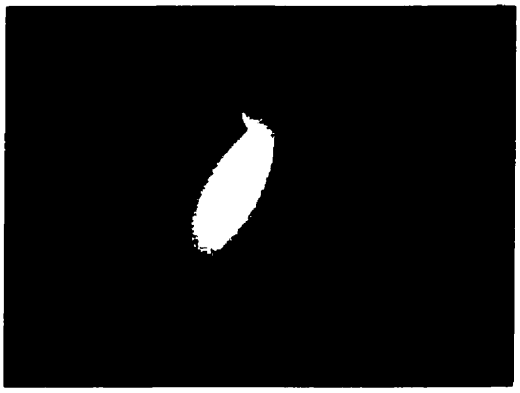

(d) Voltage=41 V, Exposure=11

(b) Voltage=41 V, Exposure=13

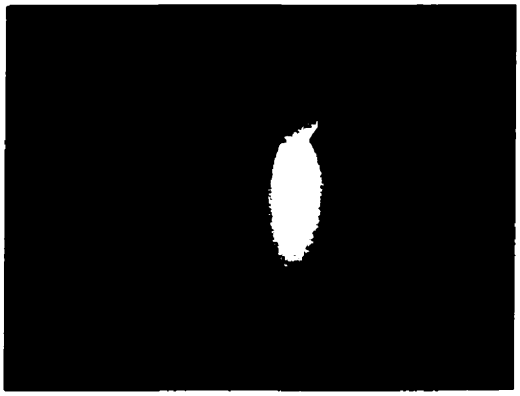

(e) Voltage=41 V, Exposure=10

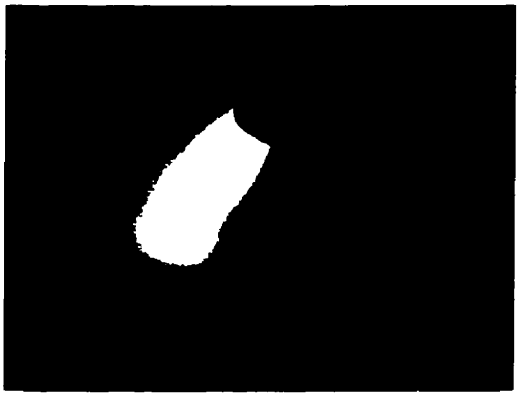

(c) Voltage=41 V, Exposure=12

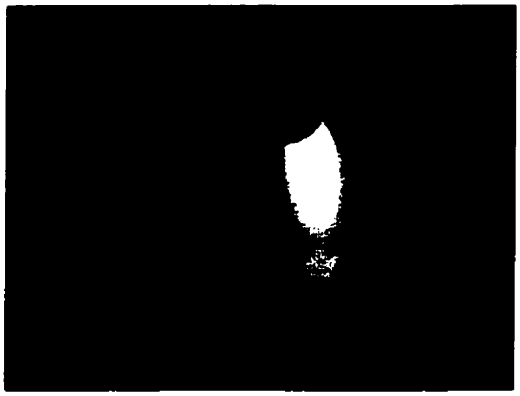

(f) Voltage=41 V, Exposure=9

Figure 6-18: Arc pictures randomly taken using cathode II (EXP-82).

brighter; it was believed that this was due to less conduction heat loss through the cathode due to the smaller outer diameter as discussed earlier.

6.2. THE ARC STABILITY OF THE HOLLOW GRAPHITE CATHODE

Instability is indicated by electrical and acoustic noise as well as rapid motion of the arc on the cathode surface. Since plasma reactors are often closed and neither the acoustic noise nor the arc root motion is evident, it is better to rely on electrical noise, i.e. voltage fluctuations as an indicator of stability. In principle, either the standard deviation of the total voltage (ΔV) or the ratio of the standard deviation of the total voltage to the total voltage ($\Delta V/V$) could be used. The data for both parameters are examined below and it was concluded that in the present work ΔV is the better indicator. An absolute value of $\Delta V > 3$ V seems to separate the operation of the arcs examined here from the stable and unstable regimes consistent with the observations of acoustic noise, voltage fluctuations, and arc movement.

6.2.1. The Arc Stability Indicator

Firstly, ΔV and $\Delta V/V$ are plotted as a function of the initial interelectrode gap and the argon gas flow rate for all the conditions and cathodes examined as shown in figures from 6-20 to 6-27. Secondly, to select the arc stability indicator, a comparison between ΔV and $\Delta V/V$ is made as follows. In the figures separation of the total voltage into the stable and the unstable part is performed to see trends of the arc stability indicators for each operation. In case of the ΔV, the borderline between the stable and the unstable part is clearly distinguished. The stable region is less than the ΔV of 3 V; the unstable region is greater than the ΔV of 3 V. This borderline of 3 V, of course, might change in a different transferred-arc system; however, it was useful in this work for the classification of the stable and the unstable operation. Meanwhile, for the $\Delta V/V$, the borderline is not

clear. Normally, operation is stable for the ΔV/V less than 0.10. However, in some cases, as shown in Figures 6-21, 6-23, 6-25, and 6-27, the stable and the unstable operation co-existed between the ΔV/V is of 0.10 and 0.15. This was caused by two factors. The first factor was low frequency, low amplitude fluctuations of the voltage in some stable arcs (see Figure 6-19). For the stable part at 0.5 cm, 4.5 slpm, and 150 A, this caused increase of the ΔV and the ΔV/V. These fluctuations were completely different from the large voltage fluctuations in the unstable operation in that there were not high amplitude random fluctuations. The second factor was that in the unstable part, V as well as ΔV increased simultaneously, thus affecting the ΔV/V. This could be seen in the runs for 1.5 cm, 4.5 slpm, and 120 minutes at 150 A (EXP-10) and for 1.5 cm, 0 slpm, and 120 minutes at 150 A (EXP-30). The ΔV and the ΔV/V of these runs are presented in Table 6-1. Between these two runs, the only different operating condition was the argon gas flow rate. In this work the ΔV increased as the argon gas flow rate decreased. Therefore, increase of the ΔV/V was also expected for EXP-30 due to the decrease of the argon gas flow rate. However, the ΔV/V decreased even though the argon gas flow rate was 0 slpm. It seemed that because V as well as ΔV increased together in the unstable part, the higher V lowered the ΔV/V.

From the comparison, the ΔV was selected as the arc stability indicator in this study. It does not mean that the ΔV is an absolutely better indicator. The comparison just indicates that the ΔV is more proper to analyze the results of the arc stability in this study. In the following part, therefore, basically the ΔV is used as the arc stability indicator for discussions of the arc stability.

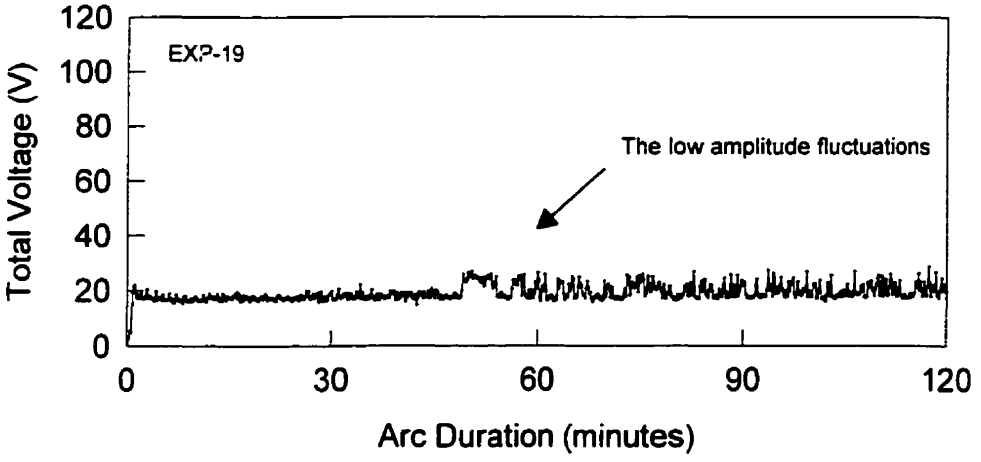

Figure 6-19: Low amplitude fluctuations of the arc voltage in a stable arc. This run used cathode I for an initial interelectrode gap of 0.5 cm, an argon gas flow rate of 4.5 slpm, and an arc current of 150 A.

Table 6-1: A comparison between the ΔV and the ΔV/V

EXP-NO.	The stable operation			The unstable operation		
	ΔV	V	ΔV/V	ΔV	V	ΔV/V
EXP-10[1)]	1.27	24.81	0.05	5.76	34.35	0.17
EXP-30[2)]	1.28	23.58	0.05	7.69	47.78	0.16

1) Operating conditions: 1.5 cm, 4.5 slpm, 120 minutes, and 150 A.

2) Operating conditions: 1.5 cm, 0 slpm, 120 minutes, and 150 A.

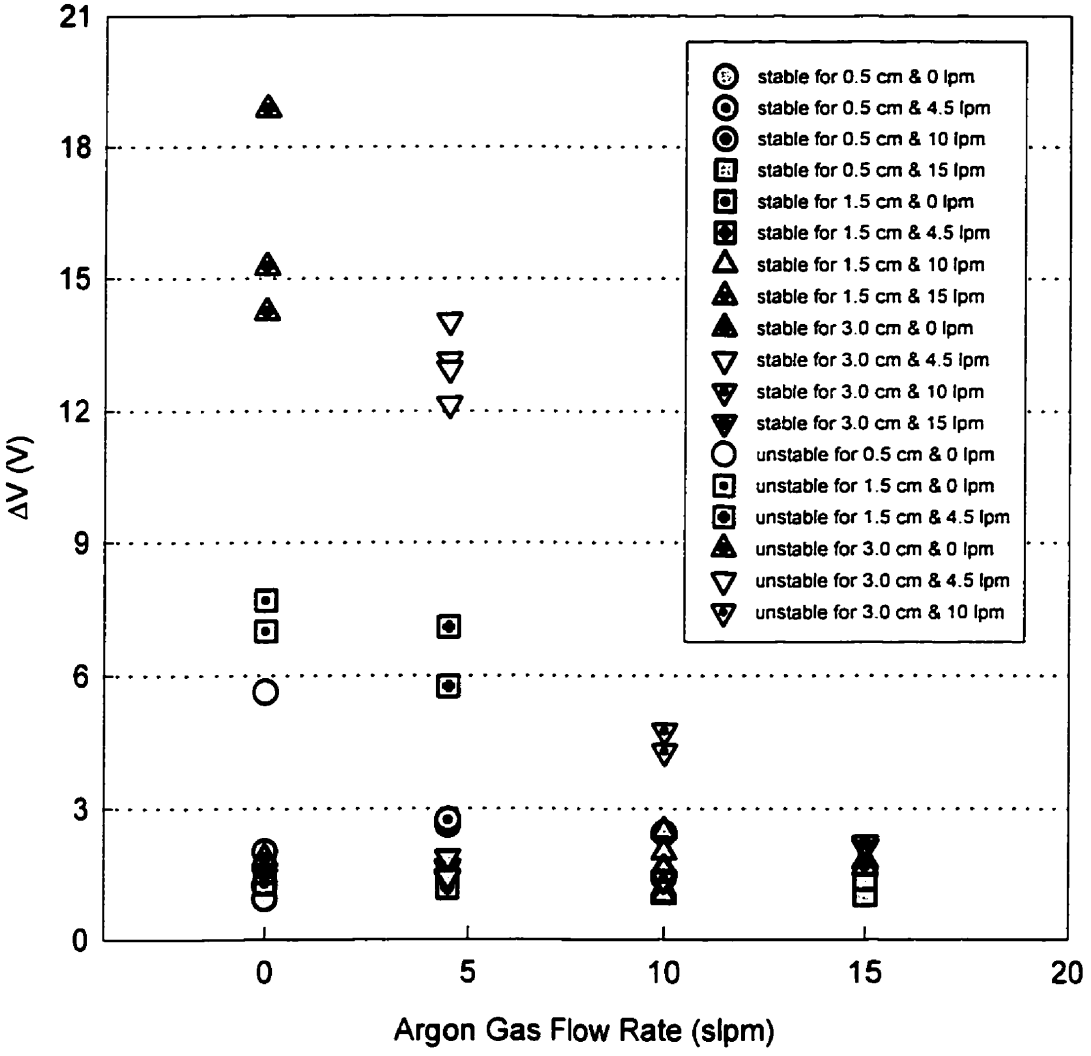

Figure 6-20: ΔV for the stable and the unstable operation separated as a function of the argon gas flow rate using cathode I at 150 A.

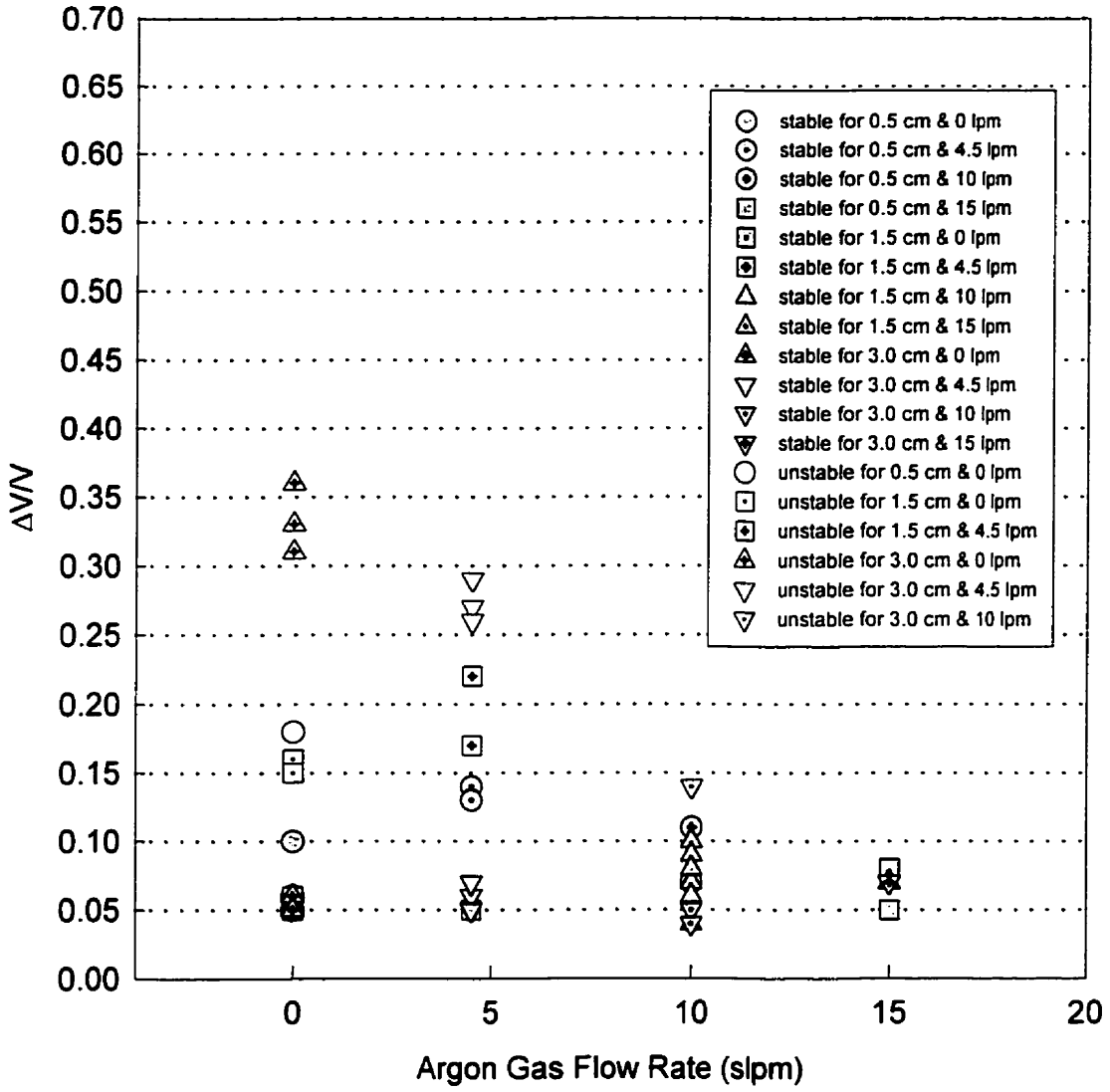

Figure 6-21: ΔV/V for the stable and the unstable operation separated as a function of the argon gas flow rate using cathode I at 150 A.

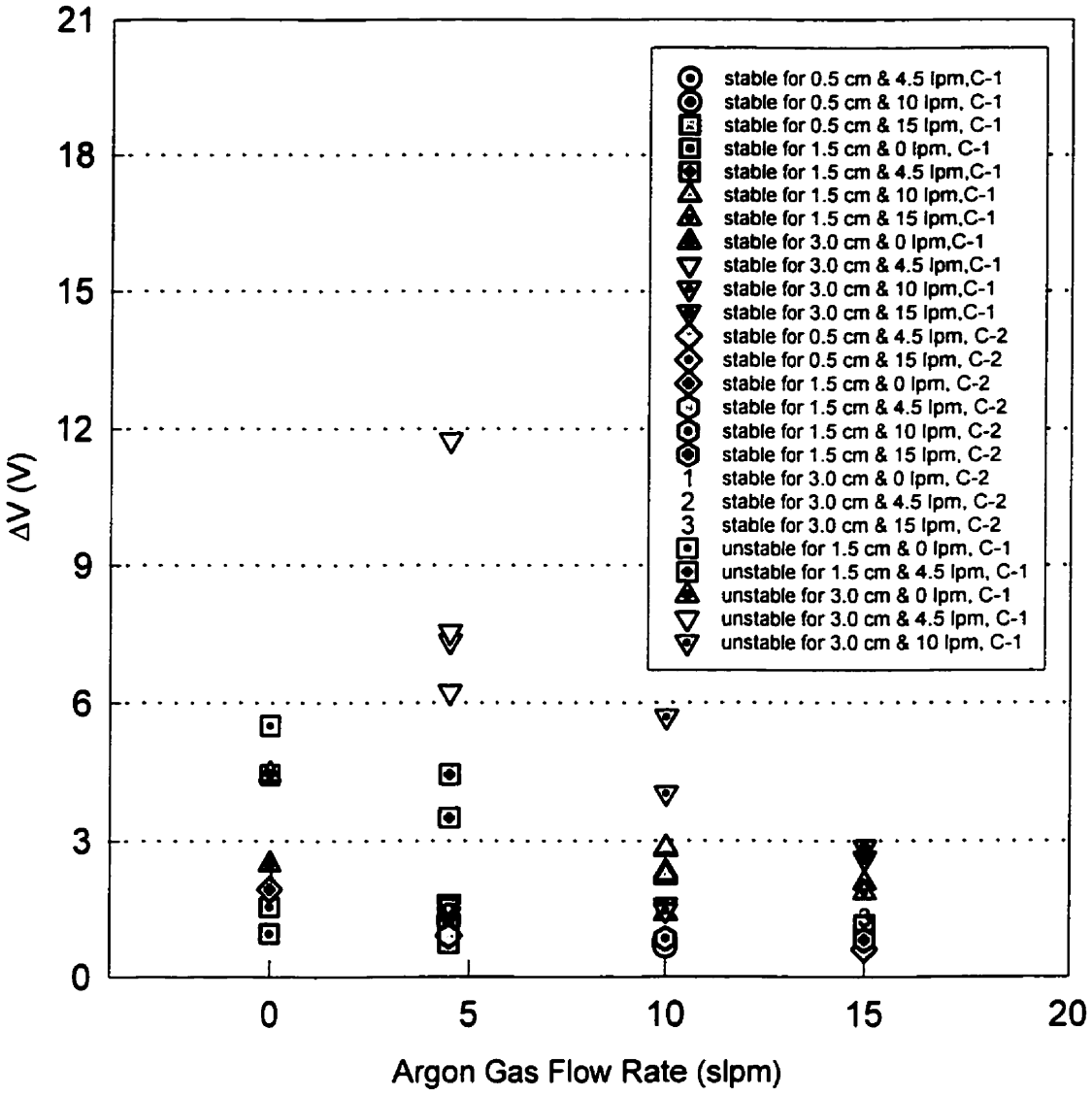

Figure 6-22: ΔV for the stable and the unstable operation separated as a function of the argon gas flow rate at 300 A. C-1 stands for cathode I; C-2 is for cathode II.

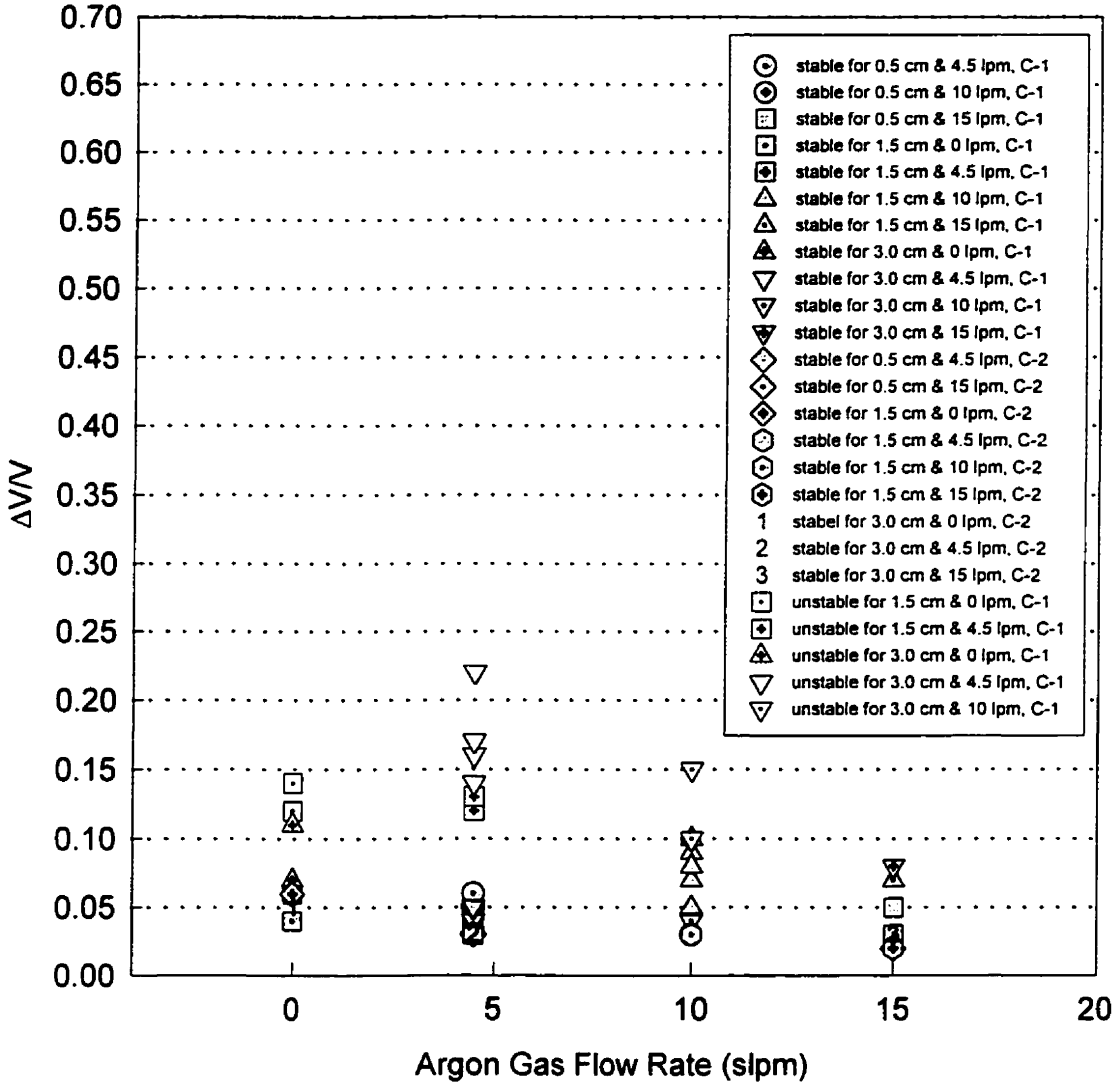

Figure 6-23: ΔV/V for the stable and the unstable operation separated as a function of the argon gas flow rate at 300 A. C-1 stands for cathode I; C-2 is for cathode II.

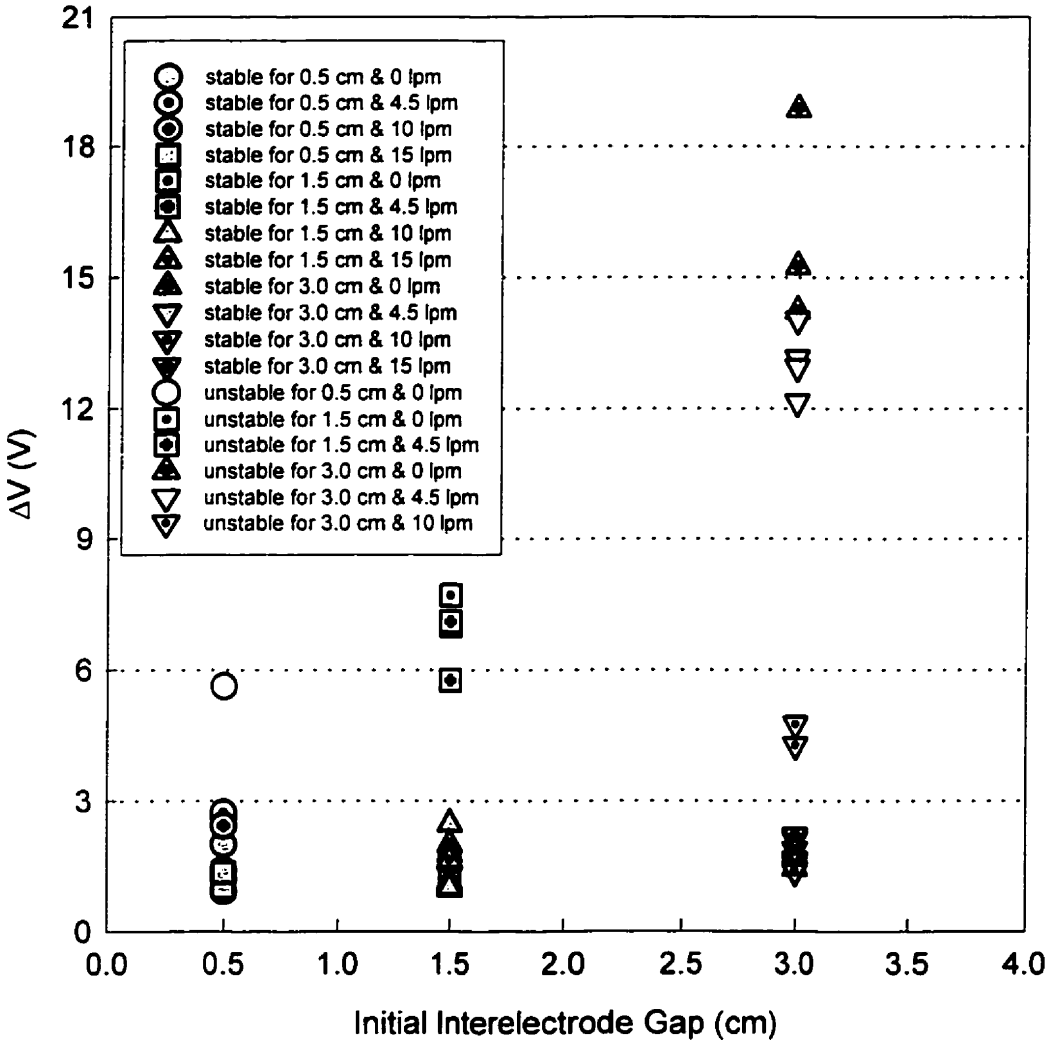

Figure 6-24: ΔV for the stable and unstable operation separated as a function of the initial interelectrode gap using cathode I at 150 A.

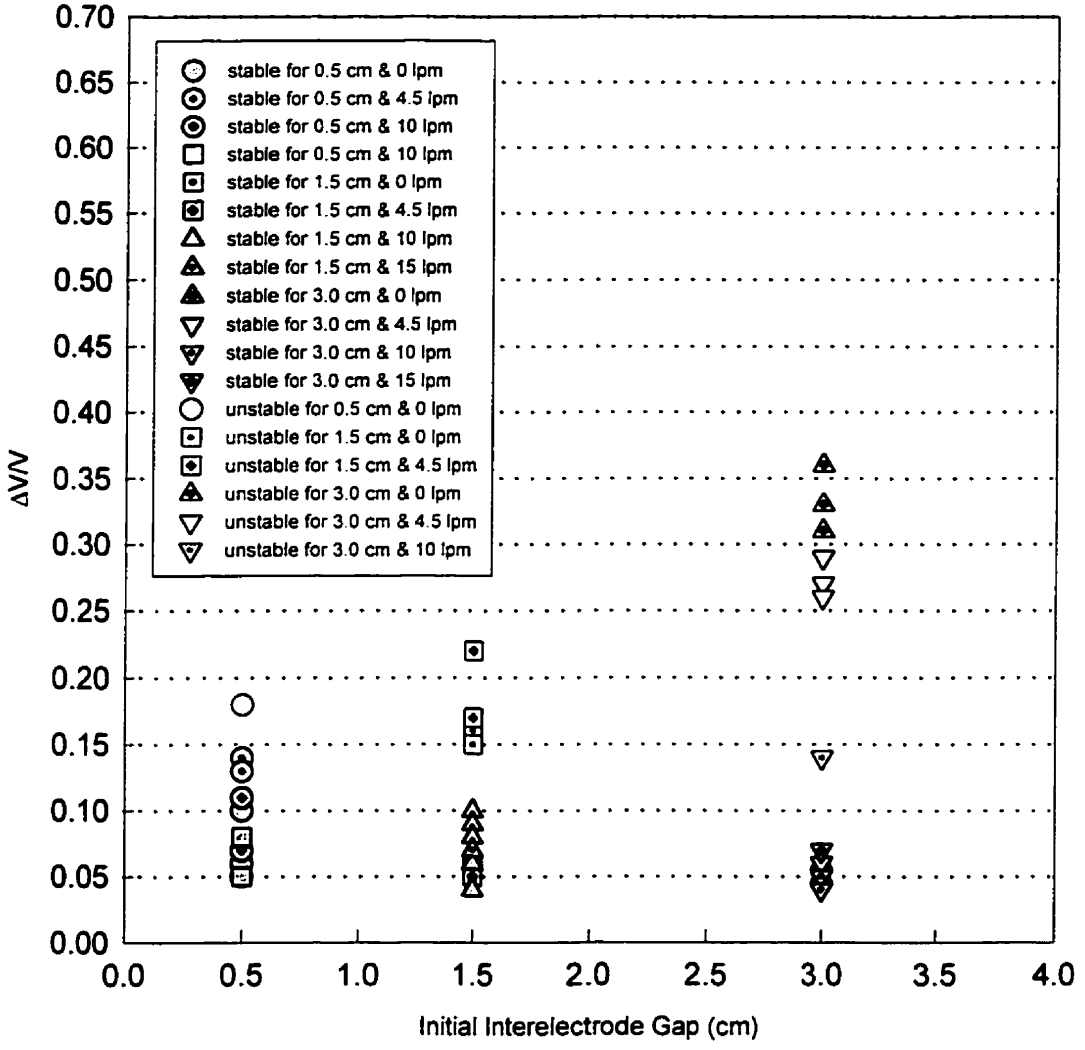

Figure 6-25: ΔV/V for the stable and unstable operation separated as a function of the initial interelectrode gap using cathode I at 150 A.

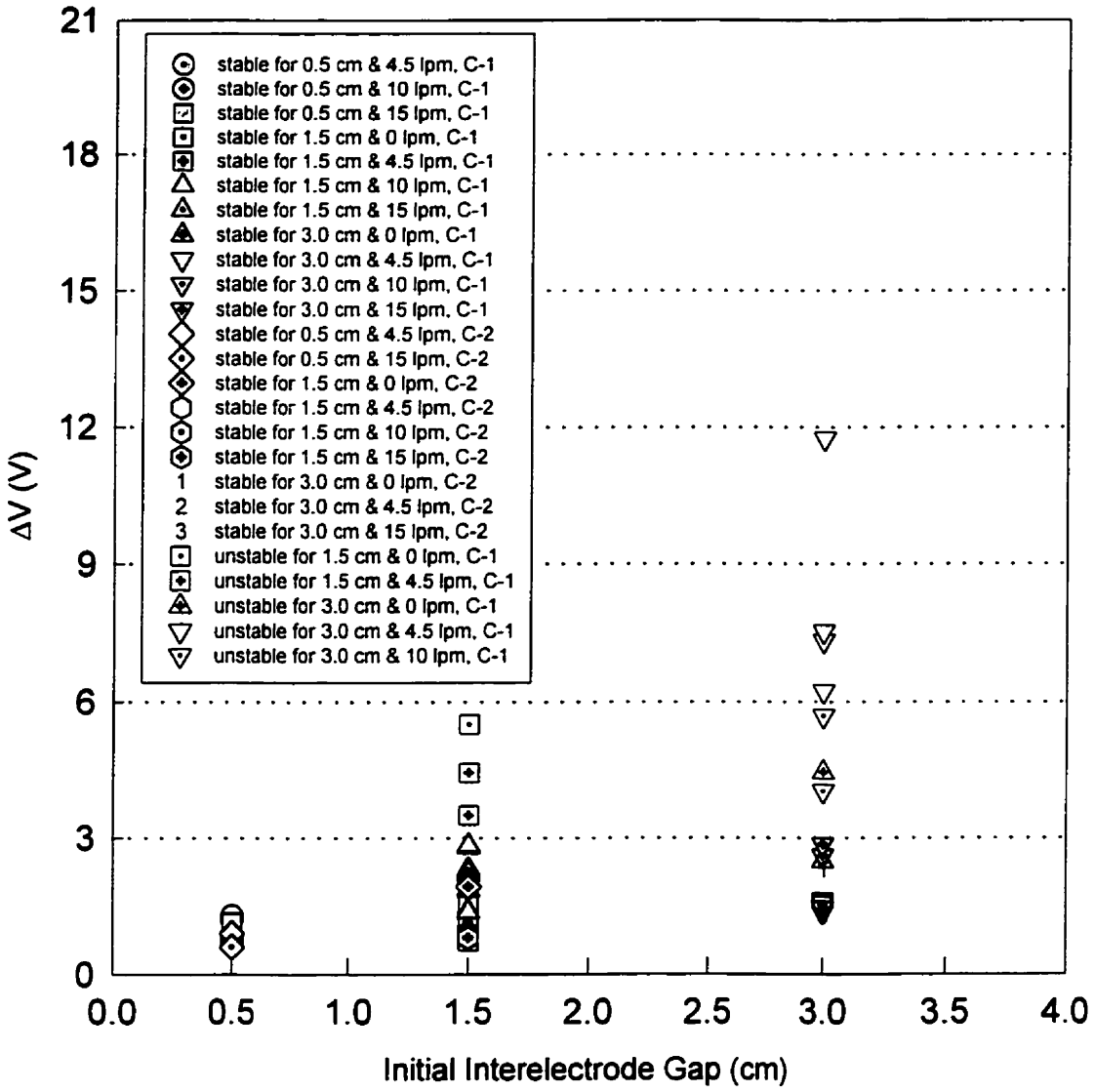

Figure 6-26: ΔV for the stable and the unstable operation separated as a function of the initial interelectrode gap at 300 A. C-1 stands for cathode I; C-2 is for cathode II.

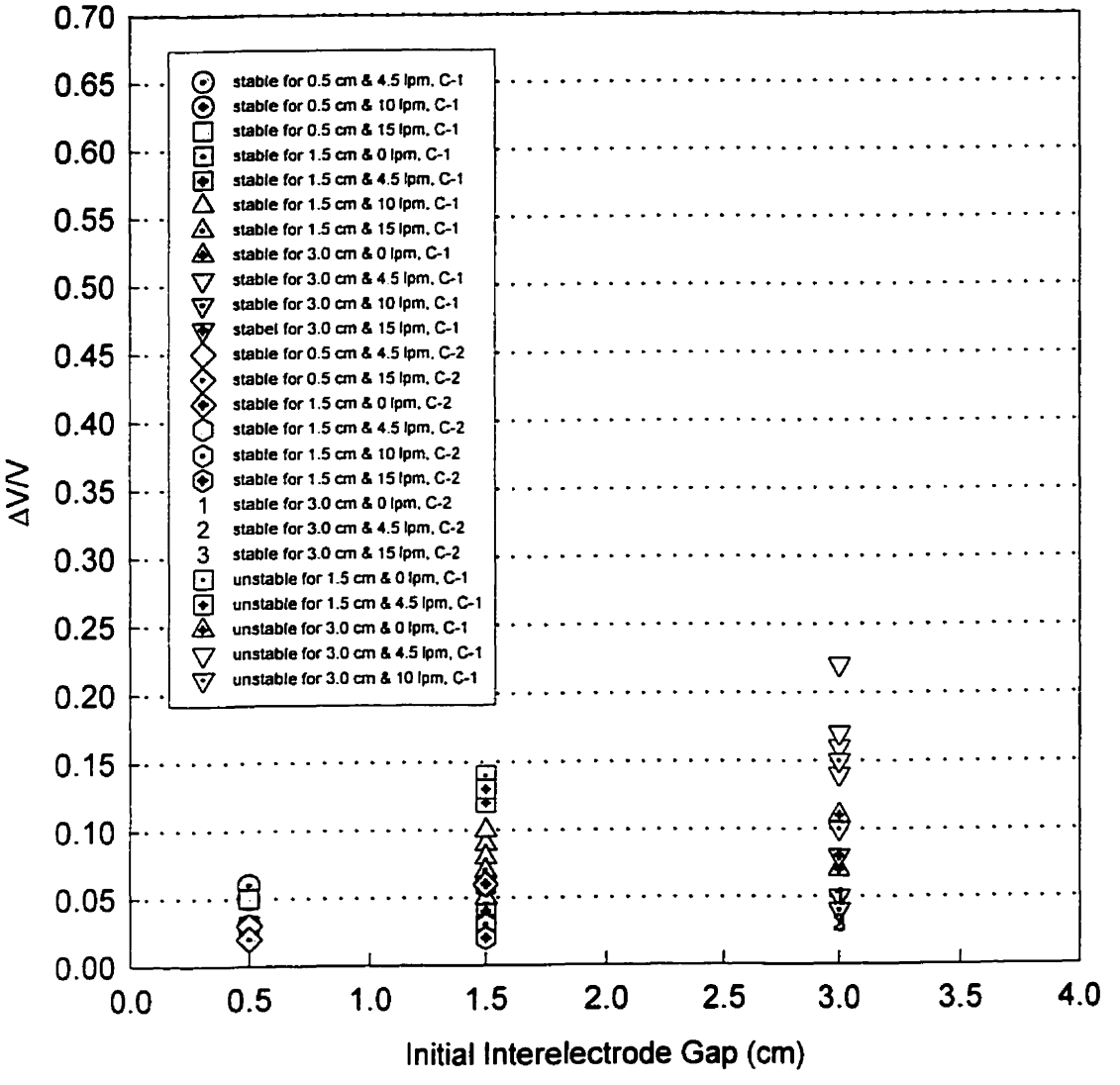

Figure 6-27: ΔV/V for the stable and the unstable operation separated as a function of the initial interelectrode gap at 300 A. C-1 stands for cathode I; C-2 is for cathode II.

In the following section, to discuss the arc stability as a function of the argon gas flow rate and the initial interelectrode gap, previous Figures 6-20, 6-22, 6-24, and 6-26 are used. Before the discussions, effect of the cathode tip geometry on the arc stability and overview of the arc stability are presented.

6.2.2. Effect of The Cathode Tip Geometry on The Arc Stability

Discussion of this effect is first given because it was performed using a used cathode, i.e. a cathode without the pointed tip. As briefly mentioned earlier, before the cathode tip eroded the arc was always stable. It seems that before the tip eroded, the cathode tip temperature might be higher because the cross-sectional area of the tip is smaller than that of the normal cathode body. This might increase the arc root temperature. In addition, the self-magnetic force produced by the tip might affect the arc stability. According to Montgomery et al.' (1969) study, carbon arcs for an arc current of 400 ~ 2,000 A at atmospheric pressure were stable before a sharp edge on the cathode eroded. This sharp edge might correspond to the tip of the cathode used in this study. They used various graphite rod cathodes with different edge angles on the cathode and reported that before the edge eroded the arcs were stable because of the self-magnetic force.

A run using an used cathode was performed to examine this effect by recording the voltage. Figure 6-28 shows the total voltage pattern of the used cathode. The run was started with an argon gas flow rate of 4.5 slpm and an initial interelectrode gap of 3.0 cm at 150 A. As can be seen in the figure, the arc was unstable as soon as the arc was ignited.

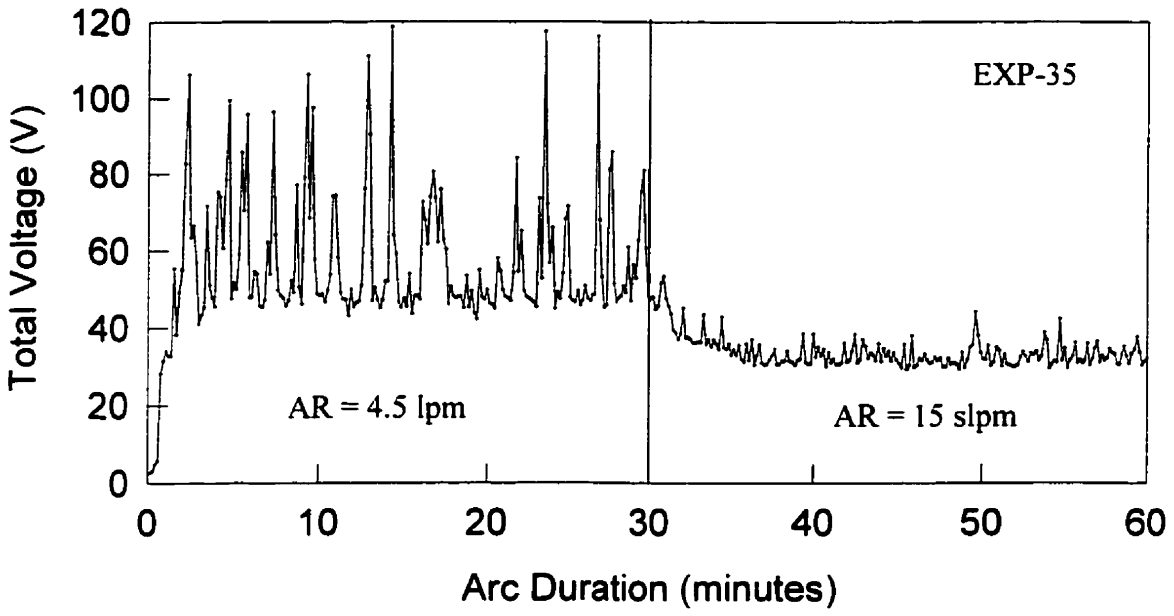

Figure 6-28: Total voltage pattern of the used cathode I for an initial interelectrode gap of 3.0 cm at 150 A.

Because the used cathode had no sharp tip and the argon gas flow rate was lower, the electron emission of the cathode was believed to be in the thermofield emission regime, thus providing the great voltage fluctuations. At 30 minutes the argon gas flow rate was increased to 15 slpm and the voltage fluctuations began to disappear as soon as the argon flow rate was increased. It was believed that the higher argon flow rate increased the arc root temperature as well as the electrical conductivity of the arc, thus making the arc stable. Details of the effect of the argon gas flow rate on the arc stability are presented in the section of 6.2.4.

6.2.3. Overview of The Arc Stability

An overview of the arc stability in this study is presented in Figures 6-29 and 6-30 for 150 A and 300 A runs, respectively. For stable arc runs, given by the open symbols, the ΔVs taken over an entire run are used because the ΔVs for stable arc operation were always less than 3 V and did not affect the behavior of the ΔVs during a complete run. Meanwhile, for unstable arc runs, given by the black symbols, the ΔVs captured during unstable arc operation are used. These ΔVs are included in Appendix 4. As shown in the figures, the arcs shift from the unstable region to the stable region as the argon gas flow rate increases and as the initial interelectrode gap decreases.

6.2.4. Effect of Argon Gas Flow Rate on The Arc Stability

Figures 6-20 and 6-22 show the ΔV as a function of the argon gas flow rate for the 150 and 300 A experiments. In the stable operation, the ΔV was almost constant under 3 V, but in the unstable operation, as the argon flow rate was increased, the ΔV generally was

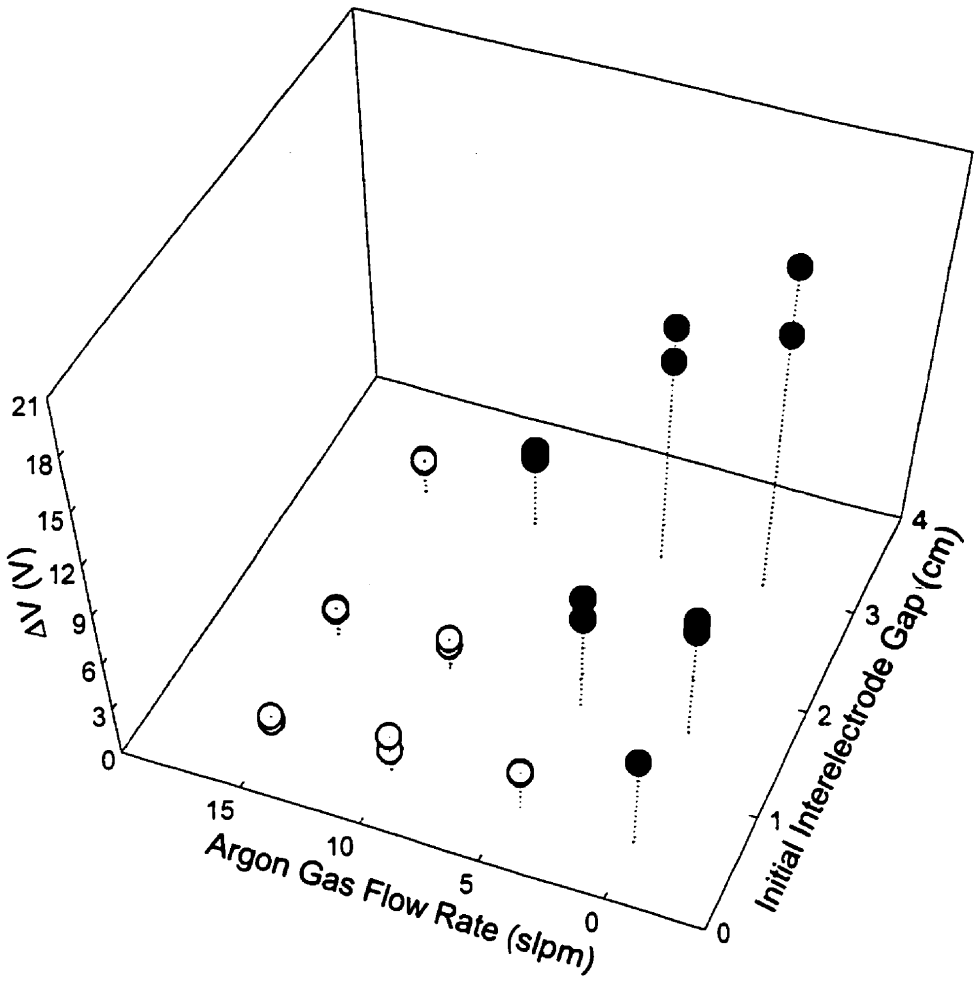

Figure 6-29: 3-D overview of the arc stability for an arc duration of 120 minutes and an arc current of 150 A. The white circles are for the stable arcs and the black circles are for the unstable arcs.

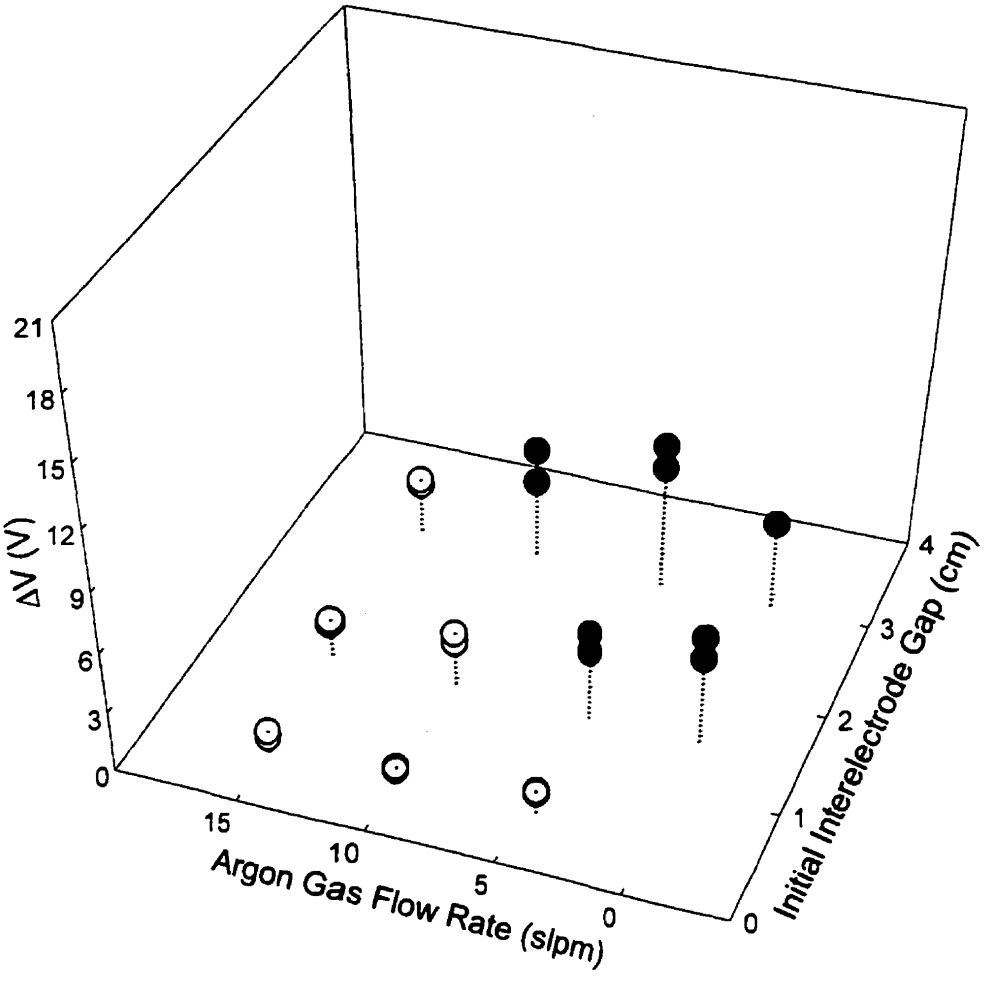

Figure 6-30: 3-D overview of the arc stability for an arc duration of 30 minutes and an arc current of 300 A. The white circles are for the stable arcs and the black circles are for the unstable arcs.

decreased. This meant that the arc was more stable for higher argon gas flow rate runs at the same initial interelectrode gap. However, a different trend appeared in unstable operation at 3.0 cm, 0 slpm, and 300 A. The ΔV of this run was lower than that at 1.5 cm, 0 slpm, and 300 A (see Figure 6-22) even though higher ΔV was expected at 3.0 cm, 0 slpm, and 300 A because of the higher interelectrode gap. This was due to abnormal total voltage patterns (see Figure 6-31); unlike the large voltage fluctuations in the typical unstable operation, the total voltage of this run increased gradually. This kind of the total voltage pattern was difficult to classify into stable or unstable operation, but it was categorized as an unstable arc because the ΔV of this run was greater than 3 V. It was believed that the arc was approaching instability at a time of about 27 minutes.

Figure 6-32 presents the ΔV of cathode II compared with that of cathode I. The ΔVs in this figure were taken over an entire run. For cathode I, the argon gas flow rate affected the arc stability. However, in the case of cathode II, the arc stability was independent of the operating conditions; the runs using cathode II were always stable. There were not the great voltage fluctuations, and the ΔV was always less than 3 V. The arcs of cathode II were stable even at 0 slpm. In this case the arc was stretched because of the presence of condensed carbon particles in the argon atmosphere. This stretching caused an increase of the arc length and small fluctuations of the total voltage; therefore, the ΔV at 0 slpm were little higher than the other runs, which the argon gas was injected.

For cathode I, the arc was more stable at higher argon flow rate operation. It has been understood that increasing the argon gas flow rate has three important effects on the arc

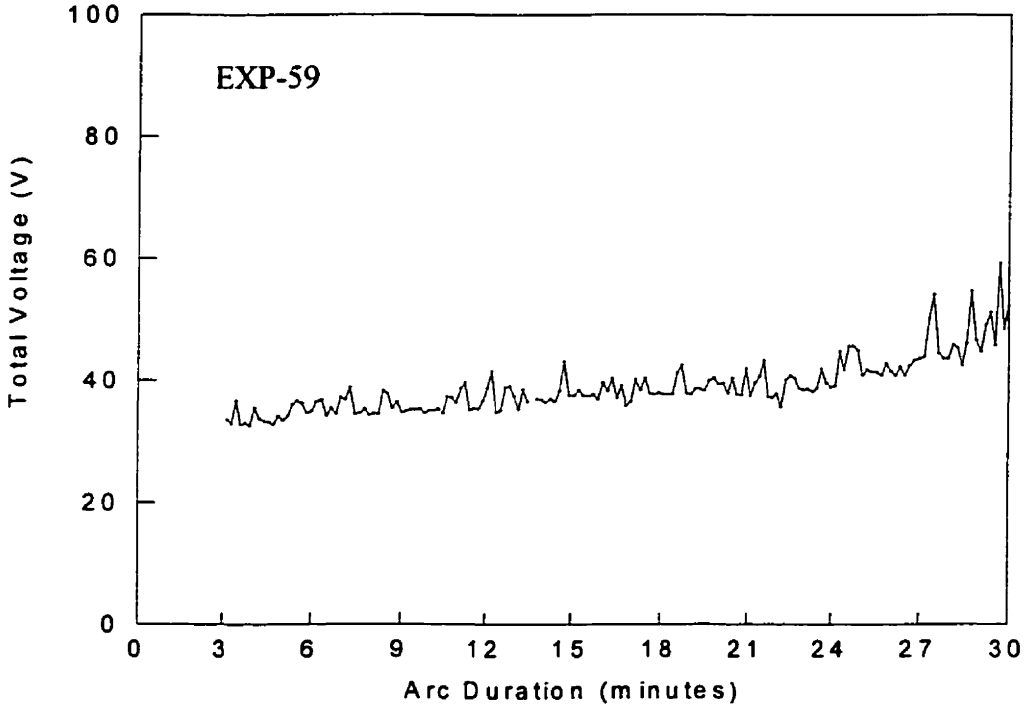

Figure 6-31: Total voltage pattern using cathode I for an argon gas flow rate of 0 slpm, an initial interelectrode gap of 3.0 cm at 300A.

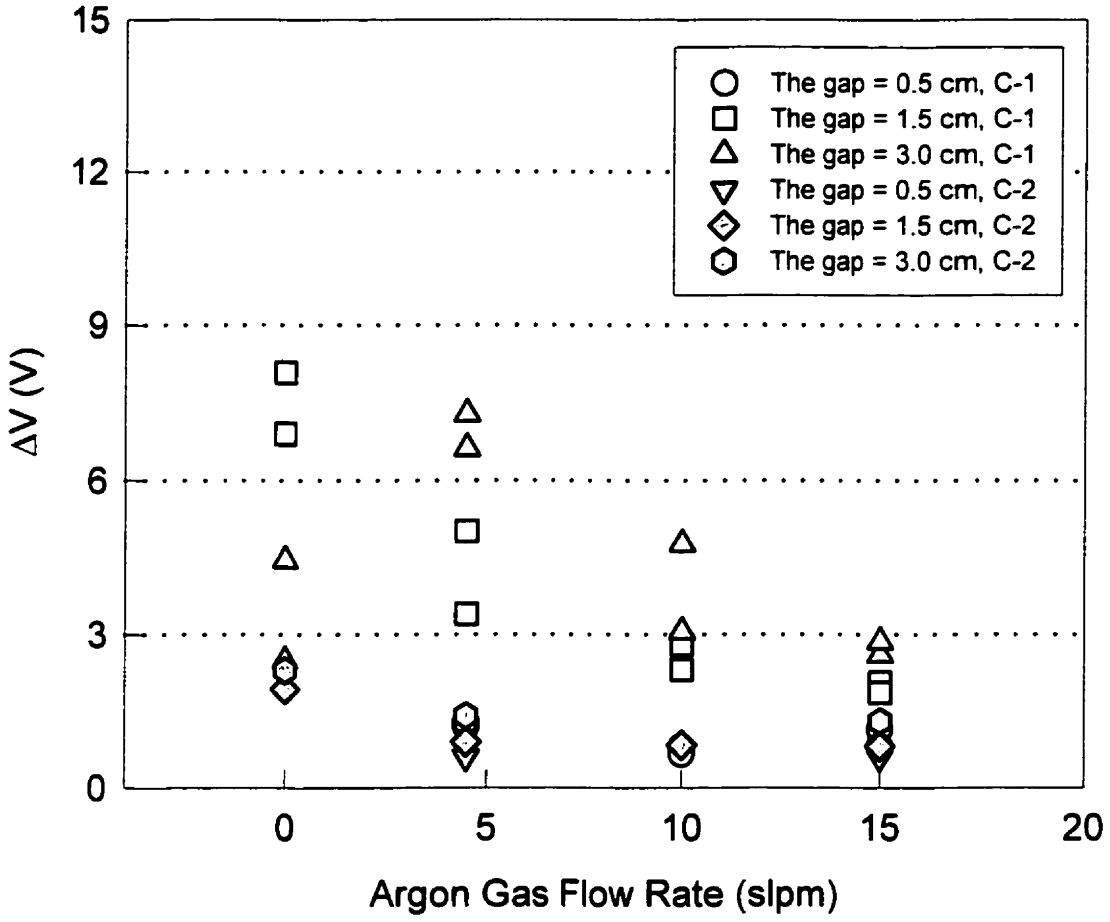

Figure 6-32: ΔV of cathode I and II as a function of the argon flow rate for a current of 300 A and an arc duration of 30 minutes. C-1 stands for cathode I; C-2 is for cathode II.

stability. First, it increases the electrical conductivity of the arc by washing out vaporized graphite or recondensed carbon particles near the arc. Second, it may also steepen the thermal gradient at the arc root by internal cooling of the electrode, thus giving a higher arc root temperature, which shifts the emission from the thermofield emission to the thermionic emission. Third, the increased gas flow rate may increase cooling on the periphery of the arc, which results in increasing ion-electron recombination on the outside and ionization phenomena inside the arc as stated by Pfender et al. (1987) and Roth (1995). This will also tend to increase the arc root temperature. In summary, it appears that higher argon gas flow rates might increase the arc root temperature, reduce electron emission by cathode spots, and eliminate the large voltage fluctuations. The disappearance of the large voltage fluctuations at higher argon gas flow rate is good evidence for the thermionic emission under this condition. Desaulniers-Soucy and Meunier (1995) studied the voltage fluctuations using a copper cathode, i.e. a cold cathode operated in the thermofield emission. They reported that the voltage fluctuations were caused by the arc length change and the cathode spot emission in the thermofield emission. In the present study, the voltage pattern of the stretched arc of cathode II showed that the voltage fluctuations due to the arc length change were relatively small. Therefore, it was thought that the voltage fluctuations in the unstable part were primarily due to the electron emission by the cathode spots in the thermofield emission regime.

In case of cathode II, the arcs were always stable. Since cathode II was designed to reduce the heat conduction loss through the bulk cathode body, it is logical that higher arc root temperature leads to the thermionic emission.

A higher argon gas flow rate also affected the cathode surface structure after a run as shown in Figure 6-33. A JOEL-840 scanning electron microscope (SEM) was used to see the surface structure. These SEM pictures present the cathode surface structure after treatment by stable arcs using cathode II at 300 A. Figure 6-33 (a) shows the surface structure after a run at 0 slpm, 3.0 cm, 30 minutes, and 300 A; Figure 6-33 (b) presents the surface structure after a run at 15 slpm, 3.0 cm, 30 minutes, and 300 A. The only different operating condition is the argon gas flow rate. It is clear that higher argon gas flow rate cooled the cathode surface. For 0 slpm the center of cathode II was strongly heat treated by the stable arc, and modification of the surface structure at the center could be seen clearly. This appears to be a coarsening of grain structure. However, for 15 slpm the shape of the center was conserved like that before the arc treatment because of the cooling by the argon gas.

6.2.5. Effect of Initial Interelectrode Gap on The Arc Stability

The initial interelectrode gap also affected the arc stability. Figures 6-24 and 6-26 show the effect of the initial interelectrode gap on the arc stability at 150 and 300 A. Generally, as the initial interelectrode gap decreased, the arc stability increased. However, the ΔV at 3.0 cm and 0 slpm, and 300 A was lower than that at 1.5 cm, 0 slpm, and 300 A (see Figure 6-26) due to the abnormal unstable voltage pattern, already introduced in Figure 6-31. It seemed that the reduced interelectrode gap might suppress the radial arc movement. At higher interelectrode gap, the arc could move further radially; this increase of the radial arc movement might contribute somewhat to the voltage fluctuations.

(a)

(b)

Figure 6-33: SEM pictures of the cathode surface structure after treatment by stable arcs. The operating conditions were 0 slpm, 3.0 cm, 30 minutes, and 300 A for (a), EXP-81 and 15 slpm, 3.0 cm, 30 minutes, and 300 A for (b), EXP-83.

6.2.6. Effect of Arc Current on The Arc Stability

Figure 6-34 shows ΔV for complete runs at gas flow rates of 0 and 15 slpm as a function of arc current. For the higher gas flow rate, the arcs were always stable. For 0 slpm, the stability increased with increasing arc current as is expected. This is probably due to a combination of higher arc root temperature caused by the higher heat flux at higher currents as well as increased electromagnetic pumping. This pumping, known as the Maecker effect, stiffens the arcs making them more resistant to lateral motion and thus reducing voltage fluctuations.

6.2.7. Hypothesis about The Arc Stability of The Hollow Graphite Cathode

As discussed in the previous parts, the arc stability of the cathode may be associated with the mode transition of the arc cathode operation. The following hypothesis was based on observations from this work as well as the mode transition introduced in the literature review.

<u>The Hypothesis</u>

The stable operation of the hollow graphite cathode is in the thermionic emission regime; the unstable operation is in the thermofield emission regime.

In the next part, proof of this hypothesis is given by presenting results of 1) estimation of current densities with SEM pictures, 2) Fast Fourier Transform (FFT) of the total voltage, and 3) cathode surface temperatures.

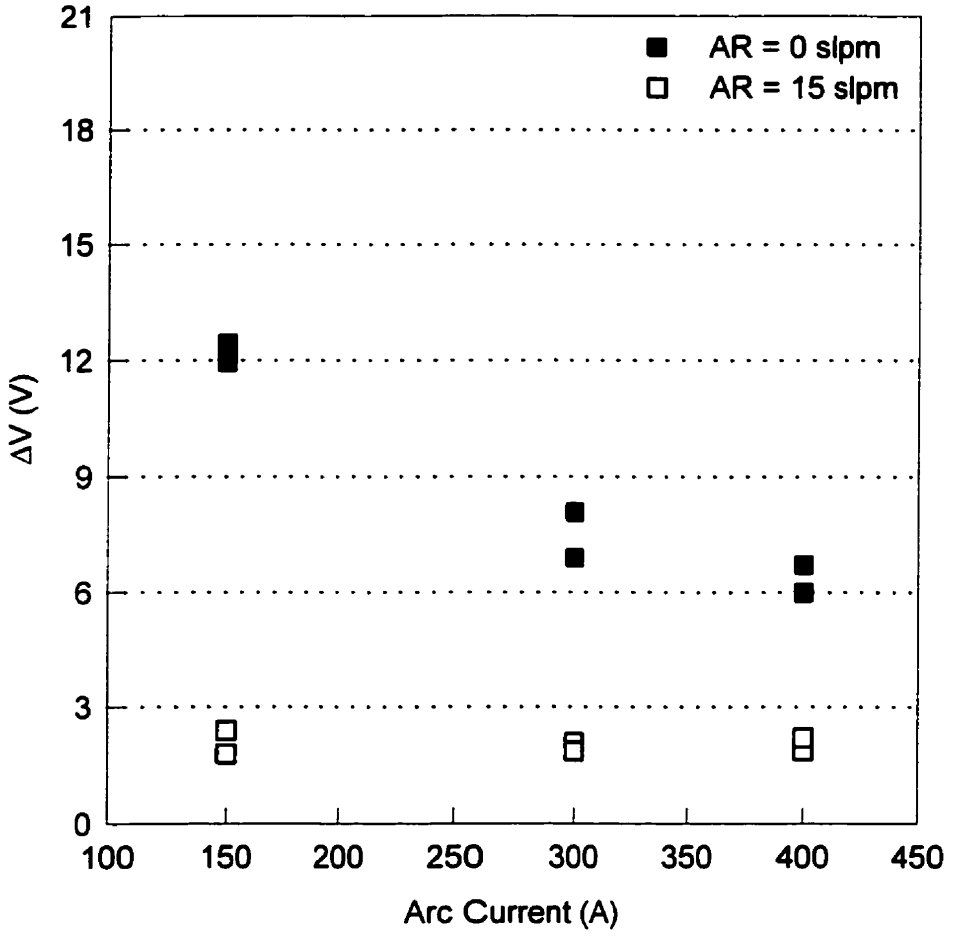

Figure 6-34: Effect of the arc current on the arc stability using cathode I at different argon gas flow rates for an initial interelectrode gap of 1.5 cm and an arc duration of 120 minutes for 150 A and 30 minutes for 300 and 400 A.

6.2.8. Proof of The Hypothesis

6.2.8.1. Estimation of Current Densities of The Stable and The Unstable Operation

After each stable run, arc tracks on the surfaces of cathode I could be seen without a microscope. Figure 6-35 (a) shows the arc tracks on the surface after a stable 150 A run (EXP-12). On the cathode surface several arc tracks could be observed, and the width of the arc track was about 2 mm. The SEM was used to examine the surface structure of the arc track; an example is shown in Figure 6-35 (b). The surface structure is quite uniform and looks like crystal growth. The surface structure before arc treatment is presented in Figure 6-35 (c) to compare the structures before and after a stable arc; before arc treatment the structure looks rough and irregular. For stable 300 A runs the width of the arc track was thicker; for EXP-52 operated at the same initial interelectrode gap and argon gas flow rate of EXP-12, it was about 4 mm. For 150 A runs some thermionic spots could be observed; however, for 300 A runs they could not be seen. The shape of the thermionic spot observed was almost circular, and the diameter was about 2 mm. Using this size, the current density (J) of 4.8×10^7 A/m^2 could be estimated for the stable 150 A run. This current density belongs to the general range of the current density of the thermionic emission regime (10^7~10^8 A/m^2). In addition, the temperature at the thermionic spot surface was estimated using the current density (J) of 4.8×10^7 A/m^2 and the Richardson equation. The Richardson equation is given as follow:

$$J = AT^2 \exp(-\frac{e\phi}{kT}) \qquad (6\text{-}1)$$

where J is the current density estimated; T is the temperature of the thermionic spot surface; A is the emission constant of 1.2×10^6 A/m^2-K^2; k is the Boltzmann's constant

of 1.381 X 10^{-23} J/K; and ϕ is the work function of 5 V. The values of the emission constant and the work function were taken from Roth (1995). The temperature of 4430 K was estimated at the thermionic spot surface for the stable 150 A run.

The unstable operation did not produce the arc tracks on the cathode surfaces, and therefore, the SEM was used to search for cathode spots. Figure 6-36 (a) shows some cathode spots found after an unstable arc 150 A run. There were several different sizes of the cathode spots. Normally diameters of the cathode spots in the picture are about 40 ~ 50 μm. A diameter of about 45 μm of the cathode spot indicated by the arrow in Figure 6-36 (a) was selected to estimate the current density. The current density of 9.4 x 10^{10} A/m^2 was estimated for the cathode spot. However, because there are several cathode spots at the arc root in the thermofield emission regime, it was assumed that 2 cathode spots made up the arc root. It was based on the spot current of 200 A reported by Kimblin (1973). With this assumption the current density of 4.7 x 10^{10} A/m^2 was estimated. This current density is in the general range of the current density of the thermofield emission regime (10^{10}~10^{11} A/m^2). For unstable 300 A runs, the cathode spots could not be found, but remnants of the cathode spots could be observed. One such remnant is the cauliflower structure as shown in Figure 6-36 (b). Kandah (1997) reported that the cauliflower structure is one of the characteristics of the cathode spots of graphite cathodes operated in the thermofield emission regime.

The surface structure of the EXP-29 cathode for Figure 6-36 (a) was further investigated. Attention was focused on finding the structure difference after stable and unstable arc

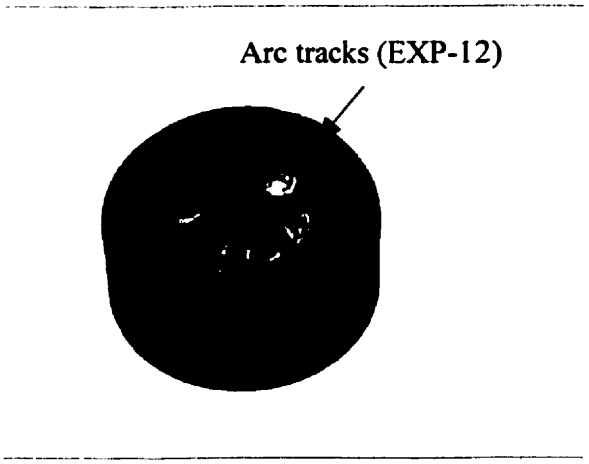

(a): arc tracks after stable arc treatment.

(b): surface structure inside an arc track after stable arc treatment.

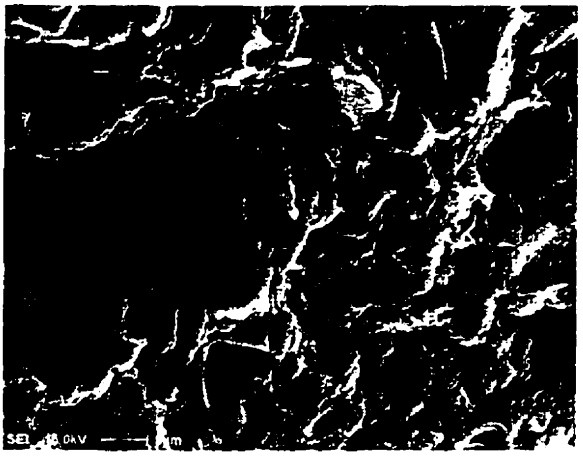

(c): surface structure before arc treatment.

Figure 6-35: The arc tracks, the surface structure inside an arc track after a stable arc run, and the surface structure before arc treatment. The stable run used cathode I at 1.5 cm, 15 slpm, and 150 A.

treatment; the arc was first stable and then unstable. Figure 6-37 shows the difference. During the stable operation the arc remained mainly in the central part of the cathode because of the absence of the argon gas injection while during the unstable operation the arc moved rapidly over the outer surface of the cathode. Figures 6-37 (b) and (c) are two different magnifications of the cathode surface taken in the area labeled "stable" and "unstable" in Figure 6-37 (a). Figure 6-37 (b) shows the structure characteristic after the stable arc treatment. The crystal structure of the original graphite has coarsened due to the thermal treatment by the stable arc. This modification in structure was possible because the arc remained in one location over a considerable length of time giving a high temperature in this regime. Figure 6-37 (c) presents the surface structure after the unstable arc treatment. It is possible to see many circular holes on the cathode surface. These vary in diameter from about 10 μm to about 60 μm and are believed to be cathode spots resulting from operation in the thermofield emission. The cathode spots in Figure 6-36 (a) were found in this area.

6.2.8.2. Total Voltage and Total Voltage FFT Analysis of The Stable and The Unstable Operation

FFT of the total voltage during the stable and the unstable operation was performed using an oscilloscope. The operating conditions of the run for this analysis were an initial interelectrode gap of 3.0 cm and an argon gas flow rate of 4.5 slpm at 150 A. Figure 6-38 shows the total voltage pattern of the run recorded by the data acquisition system. Before the arc duration of about 30 minutes the arc was stable, and after that the arc became unstable.

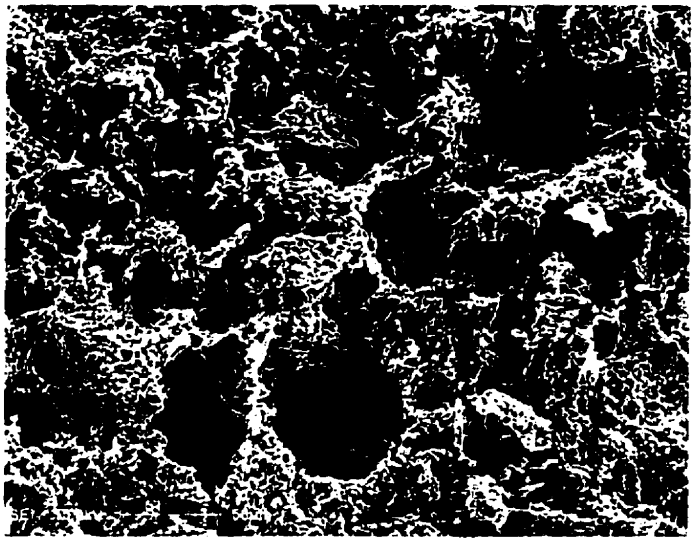

(a): the cathode spots (150A, EXP-29)

(b): the cauliflower structure (300A, EXP-59)

Figure 6-36: The cathode spots and the cauliflower structure after an unstable run using cathode I for an initial interelectrode gap of 3.0 cm, an argon gas flow rate of 0 slpm, and an arc current of 150 A (EXP-29) and 300 A (EXP-59).

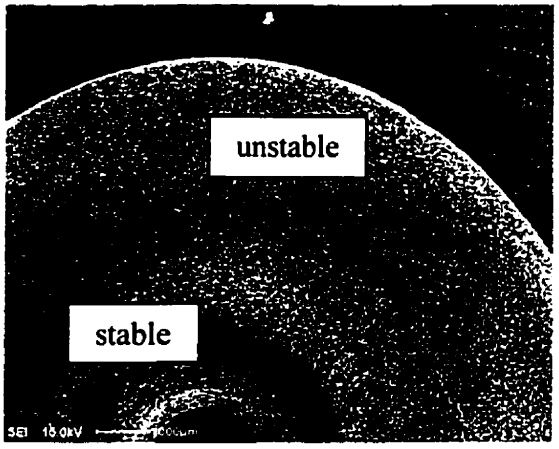

(a)

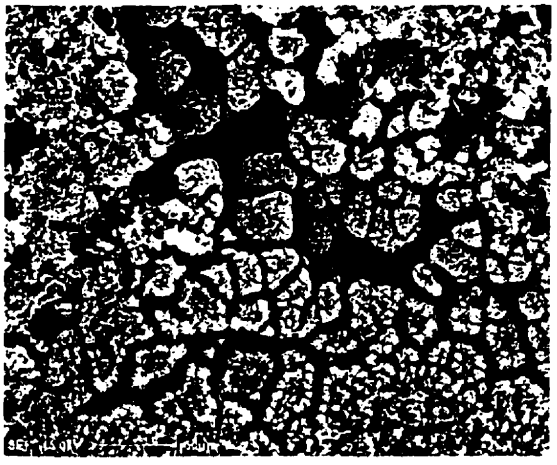

(b)

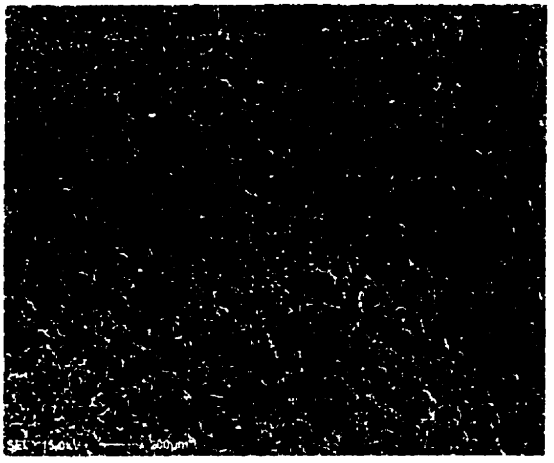

(c)

Figure 6-37: SEM micrographs of a cathode after operation using cathode I for an initial interelectrode gap of 3.0 cm, an argon gas flow rate of 0 slpm, and an arc current of 150 A (EXP-29). The macroscopic view of the regions examined is (a); the surface structure after the stable arc treatment is (b) and after the unstable arc treatment is (c).

The FFT waveforms of the total voltage were randomly printed during the stable and the unstable operation using hard copy and the single mode of the scope. The valid range of the FFT waveforms using this scope was determined by standard sine waveforms of 180 Hz and 1 MHz, produced by a signal generator. The 180 Hz signal was chosen for the analysis of a low frequency region, and the FFT waveforms in this region were reliable to 5 KHz. The 1 MHz signal was for the analysis of a high frequency region, and the FFT waveforms in this region were reasonable to 250 MHz.

Firstly, total voltage patterns in a time of the order of subseconds measured by the scope are presented in Figure 6-39. Like the total voltage patterns recorded by the data acquisition system, these total voltage patterns showed a clear difference between the stable and the unstable arc runs. For the stable operation, the voltage signal is a rectified sine wave and is periodic as shown in Figure 6-39 (a). The period of the voltage signal in the stable part is 5.6 ms. This period is the same for the other time scales. Peak to peak voltage (V_{pp}) in this stable part is in the range of 3.0 ~ 4.0 V. Meanwhile, the voltage signals of the unstable operation are irregular waveforms as shown in Figures 6-39 (b), (c), and (d). They resemble saw-tooth waveforms incorporating with several sharp peaks. Ghorui et al. (2000) presented similar voltage patterns; they studied the relationship between the fluctuations of the arc voltage and the arc root movement using copper electrodes and reported that the peaks were associated with the movement of the arc root. They did not mention the arc cathode operation mode, but copper electrodes normally operate in thermofield emission. It seems that the irregular voltage patterns and the peaks of this work are also related to the arc operation in the thermofield emission. In addition,

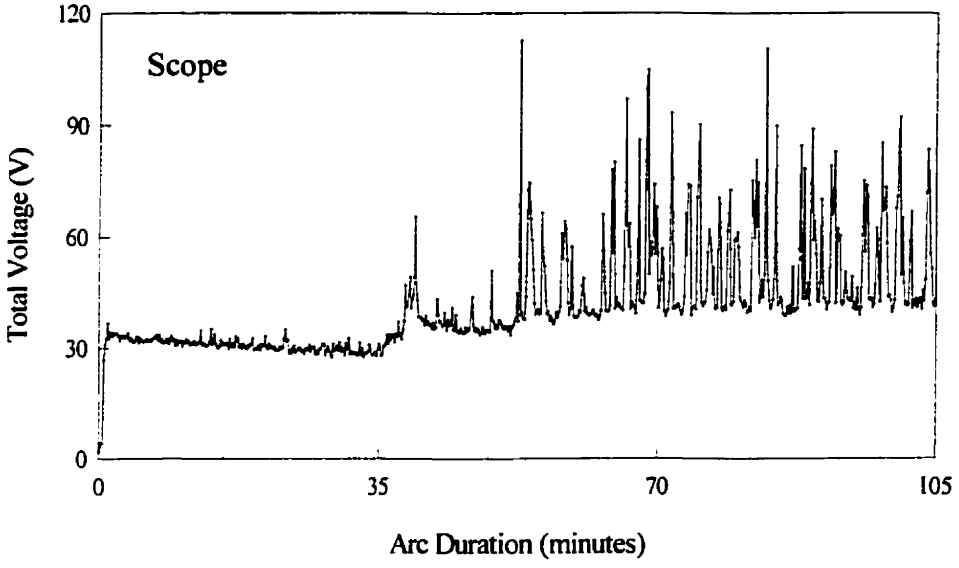

Figure 6-38: Total voltage pattern using cathode I for an initial interelectrode gap of 3.0 cm and an argon gas flow rate of 4.5 slpm at 150 A.

in the unstable operation the negativity of the cathode was increased, i.e. higher total voltage. In Figure 6-39 (a) the voltage of the stable operation is about –30 V; however, some peaks in the unstable operation in Figures 6-39 (b), (c), and (d) reaches about –100 V. Also, the V_{pp} in the unstable operation showed a wider and higher range; it is between about 10 and 60 V in the figures.

The FFT waveforms for the stable and the unstable operation are presented in Figures 6-40 and 6-41, respectively. For the stable arc run, the FFT waveforms show a periodic phenomenon as shown in Figure 6-40. The fundamental frequency is 180 Hz, and the main harmonic frequencies are 0, 360, 540, 720, 900, and 1080 Hz. Ghorui et al. (2000) stated that this harmonic series is a quasi-periodic waveform which is defined as comprising a peak at zero frequency and integral multiples of the fundamental frequency present in the waveform. The fundamental frequency of 180 Hz in the FFT waveforms was the same as the frequency of the total voltage of the stable part, and this quasi-periodic FFT waveform came from the operation of the power supply. In the unstable operation, the FFT waveforms are totally different as shown in Figure 6-41. They showed a continuous broadband noise waveform. This noise waveform includes the fundamental frequency of 180 Hz and higher frequencies that do not exist in the stable arc run. The arrow in Figure 6-41 (a) indicates 180 Hz. Therefore, it is believed that frequencies in this noise spectrum come from both the operation of the power supply and the unstable arc. To find the end point of this continuous broadband noise waveform in this run, the horizontal scale of the scope was increased, and the results are presented in Figure 6-41

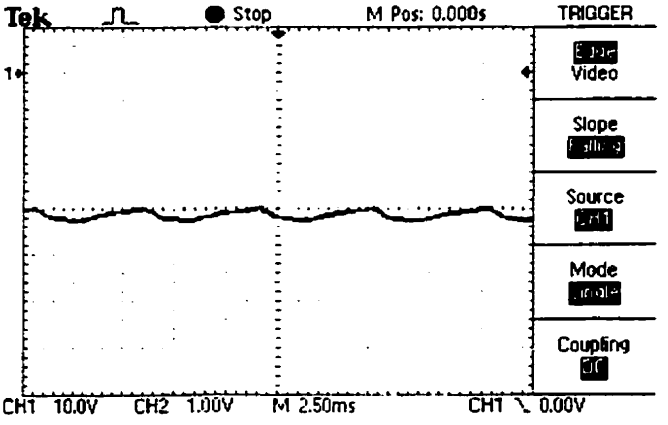

(a)-stable

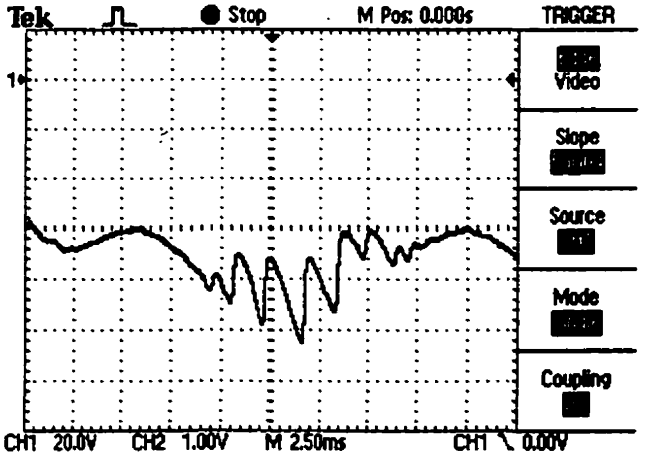

(b)-unstable

Figure 6-39: Total voltage patterns using cathode I for an initial interelectrode gap of 3.0 cm and an argon gas flow rate of 4.5 slpm at 150 A. The 1 indicates 0 V. The horizontal scales of (a) and (b) are 2.5 ms per division. The vertical scale is 10 V per division for (a) and is 20 V per division for (b).

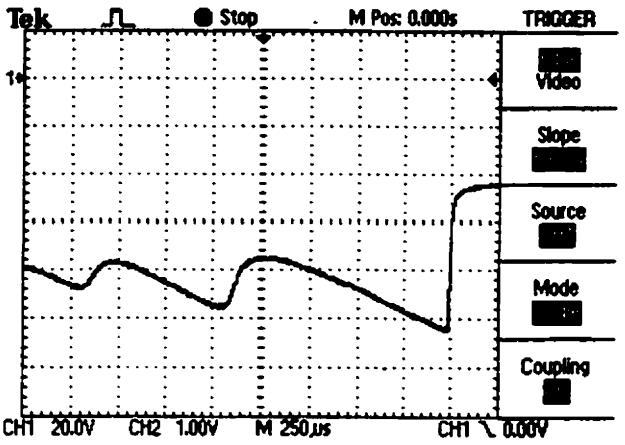

(c)-unstable

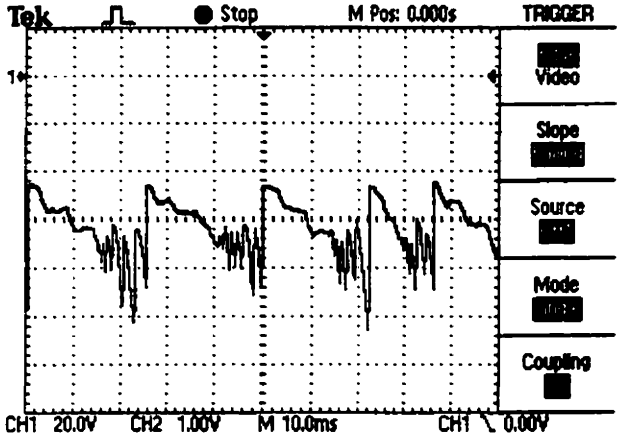

(d)-unstable

Figure 6-39: Total voltage patterns using cathode I for an initial interelectrode gap of 3.0 cm and an argon gas flow rate of 4.5 slpm at 150 A. The 1 indicates 0 V. The horizontal scale is 250µs per division for (c) and is 10 ms per division for (d). The vertical scales of (c) and (d) are 20 V per division. (continued)

(d). The continuous broadband noise waveform might end at about 100 kHz for this run. Some frequencies higher than 100 kHz appeared, but they are discrete.

In the stable operation characteristic FFT frequencies associated with the stable arc could not be found because of much stronger intensities of the FFT waveforms from the power supply operation. However, in the unstable operation, it seems that especially, the higher frequencies around 100 kHz in the noise waveform may represent the lifetime scale of the macrospot in the thermofield emission. As discussed in the literature review, the lifetime scale of the macrospot in the thermofield emission regime is much less than 1 ms scale and probably of the order of 1 μs. The higher frequencies of 100 kHz in the unstable operation correspond to a time of the order of 10 μs. Therefore, it could be thought that the higher frequencies might be associated with the extinction and the re-ignition of the macrospot in the thermofield emission regime.

6.2.8.3. Cathode Surface Temperature

The cathode surface temperature for the stable operation could be measured using the single wavelength pyrometer, and the results of these temperature measurements are presented in Table 6-2. The cathode surface temperature at the blackbody hole depended strongly on the arc root position. The color of the blackbody hole of cathode II was bright when the arc was close to the hole and was black when the arc was far away from the hole. For the unstable operation, however, the temperature measurement could not be performed because the arc radiation was too strong to see the color of the hole, and the position of the arc changed very rapidly.

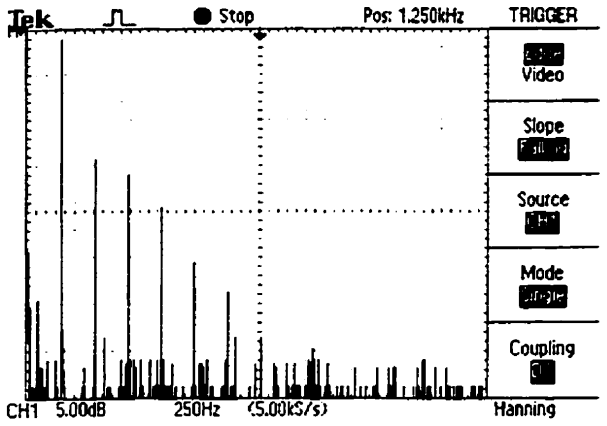

(a)

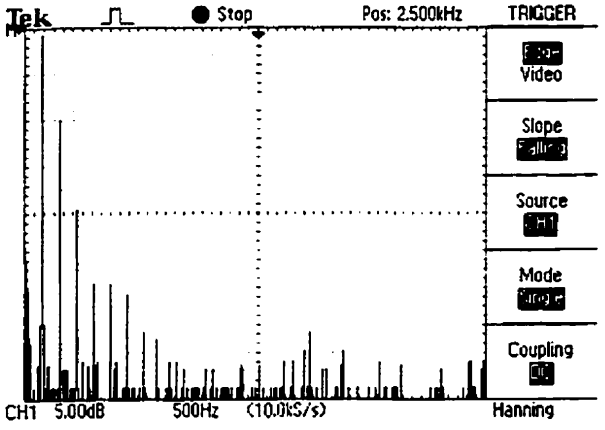

(b)

Figure 6-40: FFT waveforms of the stable arc run using cathode I for an initial interelectrode gap of 3.0 cm and an argon gas flow rate of 4.5 slpm at 150 A. The horizontal scale is 250 Hz per division for (a) and is 500 Hz per division for (b). The vertical scales of (a) and (b) are 5 dB per division.

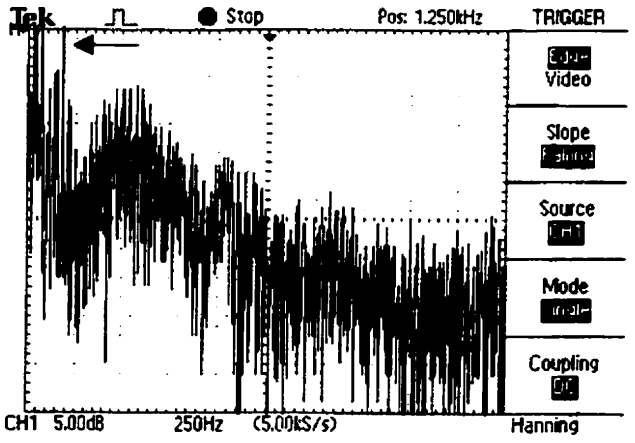

(a)

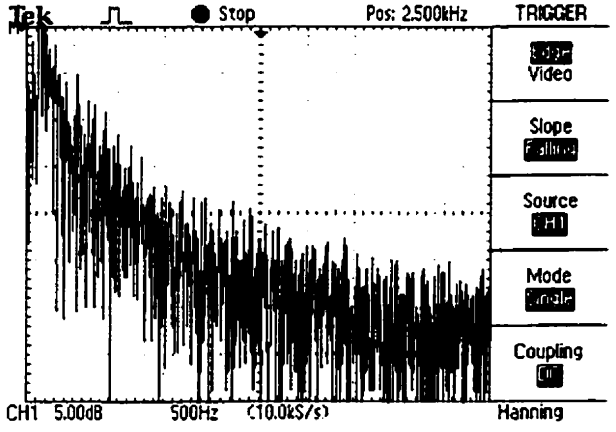

(b)

Figure 6-41: FFT waveforms of the unstable arc run using cathode I for an initial interelectrode gap of 3.0 cm and an argon gas flow rate of 4.5 slpm at 150 A. The horizontal scale is 250 Hz per division for (a) and is 500 Hz per division for (b). The vertical scales of (a) and (b) are 5 dB per division.

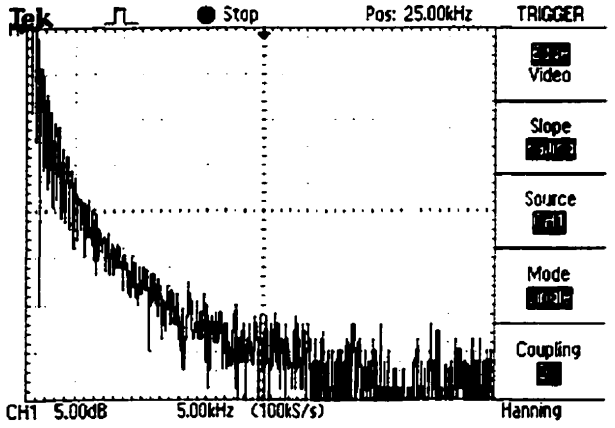

(c)

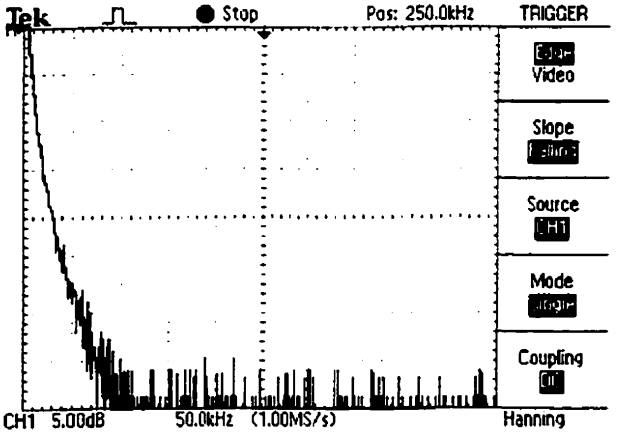

(d)

Figure 6-41: FFT waveforms of the unstable arc run using cathode I for an initial interelectrode gap of 3.0 cm and an argon gas flow rate of 4.5 slpm at 150 A. The horizontal scale is 5 kHz per division for (c) and is 50 kHz per division for (d). The vertical scales of (c) and (d) are 5 dB per division. (continued)

The stable experimental conditions for this temperature measurement were an initial interelectrode gap of 3.0 cm and an argon gas flow rate of 4.5 slpm at 150 and 300 A. For 150 A the temperature of cathode I at the hole was about 1340 K. When considering the temperature of the thermionic spot estimated at 150 A (4430 K), it could be seen that the temperature gradient from the arc root to the hole was very steep. For 150 A the temperature of cathode II at the hole was between about 1600 ~ 1710 K. Direct comparison between this temperature at 150 A using cathode II and the temperature of 1340 K at 150 A using cathode I could not be done because of the different hole positions. The hole was made just above the cathode tip. Due to the different outer diameter, the hole position of cathode I was 8 mm and that of cathode II was 4 mm from the end of the cathode tip. Therefore, arc pictures were used for direct comparison. The arc pictures taken during stable 300 A runs shows the temperature distribution difference between cathode I and II as presented in Figure 6-42. These pictures are already introduced in Figures 6-12 and 6-18. These pictures of the same exposure time and the similar arc root position were chosen to compare the tip surface colors of the cathodes. The colors of the tips show the temperature difference. As presented in Figure 6-42, the tip of cathode II near the arc root is red and brighter. The red zone of cathode II extends to about 7 mm above the tip; therefore, it reaches to about 11 mm from the end of the cathode tip. Meanwhile, the color just above the cathode I tip, which is 8 mm from the end of the cathode I tip, is black. It indicates that operation of cathode II was at higher temperature. Other red zones of cathode II, which are longer than that of Figure 6-42 (b), can be also seen in Figures 6-18 (a) and (b). This higher temperature of cathode II was due to the smaller diameter of cathode II. That caused less heat dissipation through the

conduction from the arc root to the bulk cathode, thus giving the higher temperature. The temperature of cathode II at the hole for 300 A was increased as expected and was between 1760 and 1910 K.

Comparison of the temperature difference between the stable and the unstable operation could not be made using the single wavelength pyrometer because of the rapidly fluctuating arc radiation. This arc radiation also interfered with the temperature measurement with the two-wavelength pyrometer. Therefore, cooling curves after the arc shut down were considered to see the temperature difference between the stable and the unstable arc runs at 150 A. Figures 6-43 and 6-44 present the temperature recording using the two-wavelength pyrometer and the cooling curves after the stable and the unstable operation, respectively. During the stable arc runs, a constant temperature of 2996 K was maintained. That was much higher than the stable part temperature of 1340 K measured by the single wavelength pyrometer at 150 A. The temperature of 2996 K represents the maximum temperature of the two-wavelength pyrometer. It corresponds to an output of 1 V which is the maximum output for this instrument. Thus, during the entire arc operation, the two-wavelength pyrometer showed its maximum temperature because of the arc radiation. In contrast to the constant temperature of 2996 K in the stable operation, in the unstable operation the temperature recording fluctuated greatly as did the total voltage. To avoid the interference of the arc radiation when using the two-wavelengths pyrometer, the starting temperatures of the cooling curves were used to examine the temperature difference between the stable and the unstable operation. The starting temperature after the stable operation was always higher than that after the

Table 6-2: The cathode surface temperature for the stable operation

Cathode Type	Arc Current (A)	Temperature (K)
Cathode I	150	1340 K [1)]
Cathode II	150	1600 ~ 1710 K [2)]
Cathode II	300	1760 ~ 1910 K [2)]

1) Measured at 8 mm from the end of the cathode tip.

2) Measured at 4 mm from the end of the cathode tip.

(a) Cathode I

Voltage: 31 V, Exposure:11

(b) Cathode II

Voltage: 41 V, Exposure: 11

Scale 1:1.03

Figure 6-42: Arc pictures taken during stable arc runs to compare the cathode surface temperature between cathode I and II at 3.0 cm, 4.5 slpm, and 300 A.

unstable operation if other operating conditions were the same; an example is shown in Figures 6-43 and 6-44. Thus, although the measurements are approximate because they were taken relatively far from the arc root, it has been shown that the cathode tip is hotter under stable arc conditions. This supports the hypothesis that the stable arc is in the thermionic mode of emission.

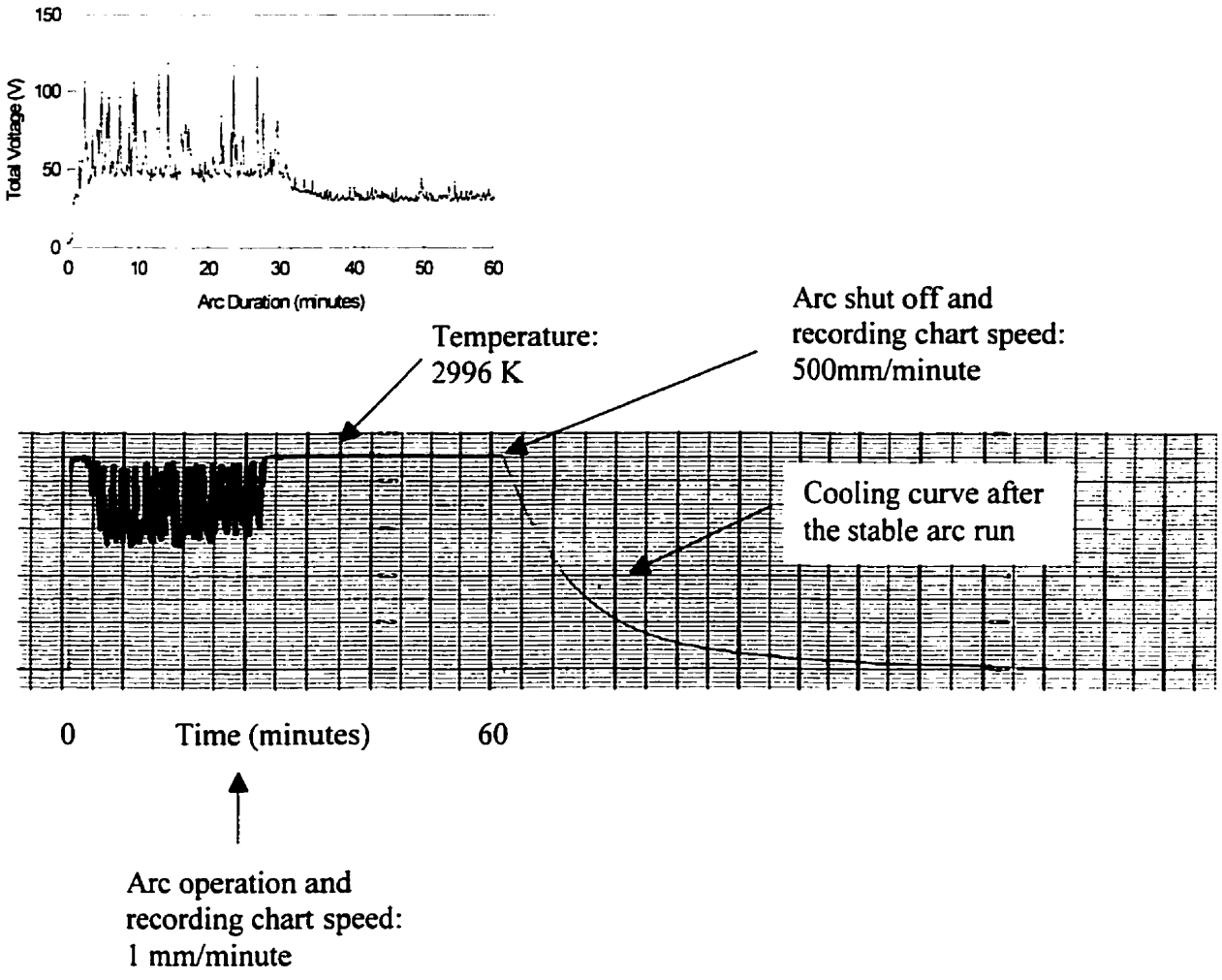

Figure 6-43: The cooling curve after the stable arc run using cathode I for an initial interelectrode gap of 3.0 cm, an argon gas flow rate of 4.5 slpm (the unstable part) and 15 slpm (the stable part), and an arc current of 150 A.

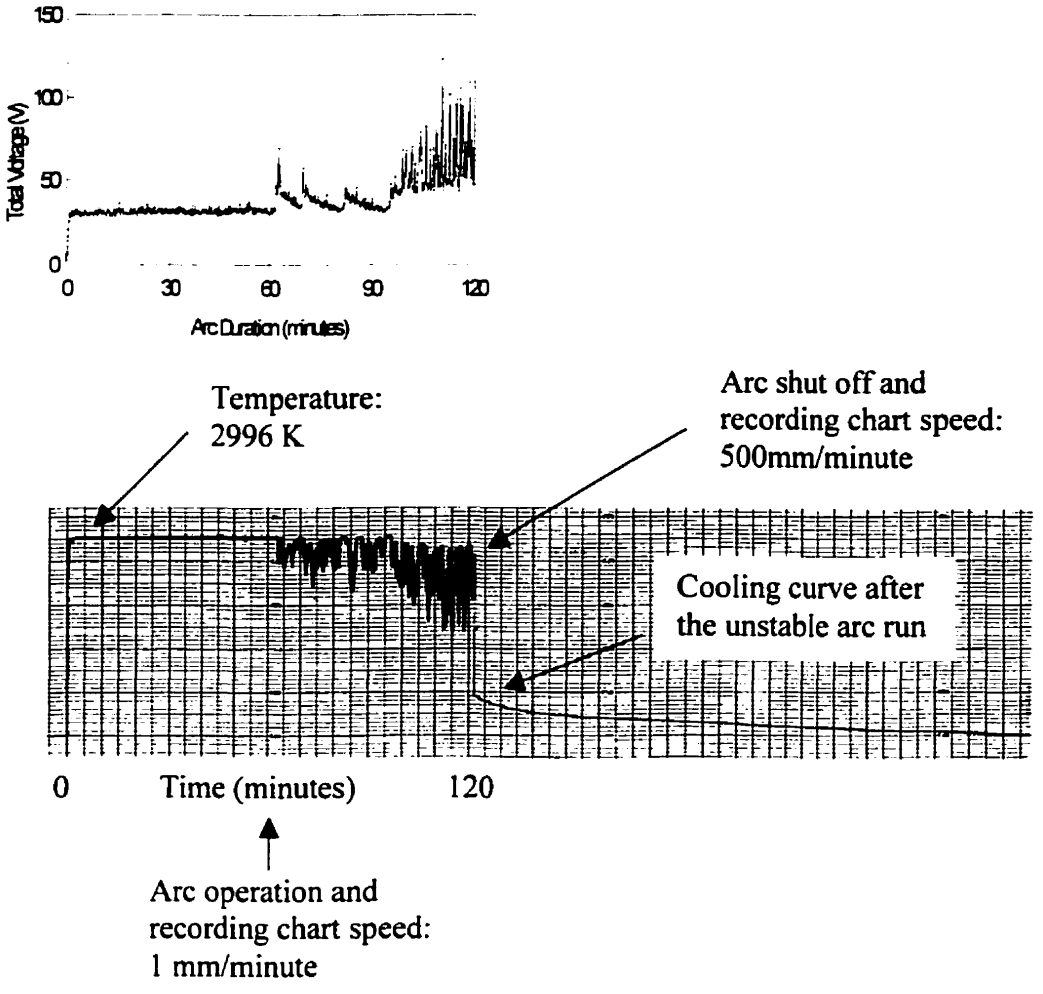

Figure 6-44: The cooling curve after the unstable arc run using cathode I for an initial interelectrode gap of 3.0 cm, an argon gas flow rate of 0 slpm, and an arc current of 150 A.

6.3. EROSION BEHAVIOR OF THE HOLLOW GRAPHITE CATHODE

Erosion rates of the graphite cathode were measured at 150, 300, and 400 A with variation of the argon gas flow rate and the initial interelectrode gap. The measurement of the erosion rate was performed through weighing the mass loss of the cathode before and after each run. This was determined to ± 0.01 g giving a maximum uncertainty in the erosion measurements of about ± 2 %. By analyzing the erosion rates, general erosion behavior of the cathode using a graphite anode could be understood. Effects of the argon gas flow rate and the initial interelectrode gap on the erosion rate are first presented because these effects were related to the arc stability. This is followed by the relationship between the erosion rate and the arc stability. A correlation model for the erosion rate is introduced last.

In the 150 A experiments, since the arc was ignited by separating the electrodes after the contact, a small amount of graphite from the cathode might have been lost by breakage even though the lowering speed of the cathode was only 0.04 cm per second. Therefore, to find optimal arc duration at 150 A to measure the erosion rate, different arc times were tried. Figure 6-45 shows the effect of run time on the erosion rate for the initial interelectrode gap of 1.5 cm and the argon gas flow rate of 10 slpm at 150 A. All runs in Figure 6-45 were stable, i.e. the same arc cathode operation mode. There is a slight initial decrease in the erosion rate with time, which is probably due to the mass loss on contact; then the erosion rate becomes independent of time after about 80 minutes. Therefore, 120 minutes was determined as the arc duration for 150 A runs. Meanwhile, for 300 and 400 A runs the arc duration was 30 minutes. Those runs did not contain the mass loss due to

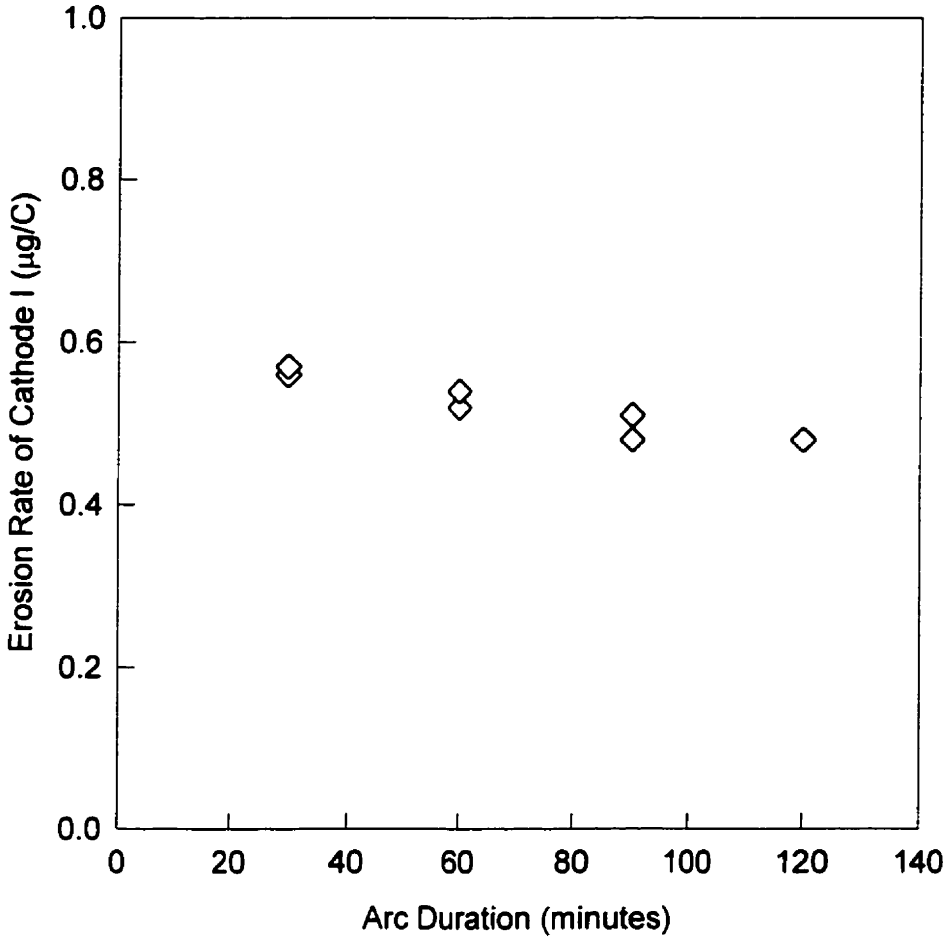

Figure 6-45: Erosion rates of cathode I as a function of time for an initial interelectrode gap of 1.5 cm and an argon gas flow rate of 10 slpm at 150 A.

the contact because of the use of the high frequency arc starter.

6.3.1. Effect of Argon Gas Flow Rate on Erosion Rate

Figure 6-46 presents the erosion rates as a function of the argon gas flow rate at 150 A. Compared with the argon gas flow rates of 10 and 15 slpm runs, the erosion rates for the argon gas flow rates of 0 and 4.5 slpm and the initial interelectrode gap of 1.5 and 3.0 cm runs were much higher. The difference between the lower and the higher argon gas flow rate runs was the mode of the arc cathode operation as discussed in the earlier section. For the higher argon gas flow rates the cathode operated in the thermionic emission regime, while in case of the lower argon gas flow rates the cathode included both the thermionic emission regime for the stable part and the thermofield emission regime for the unstable part. Therefore, it was believed that the unstable arc operation in the thermofield emission regime produced more erosion of graphite from the cathode. It is well known that the current density of the thermofield emission regime is greater than that of the thermionic emission regime; therefore, during the unstable arc operation of the lower argon gas flow rate runs, probably the local heat flux to the cathode spots by the ion bombardment was higher, thus resulting in more erosion of the graphite. Ejection of graphite particles caused by the arc movement would also influence the erosion rate. For the higher argon gas flow rates, the argon gas flow rate affected the erosion rates only slightly. It was believed that this was because the thermionic emission regime was maintained for each complete run. In addition, in Figure 6-46 the erosion rates for the initial interelectrode gap of 3.0 cm at 0 slpm were lower than those for 1.5 cm and 0 slpm. That was due to the shorter arc duration, especially shorter unstable arc duration.

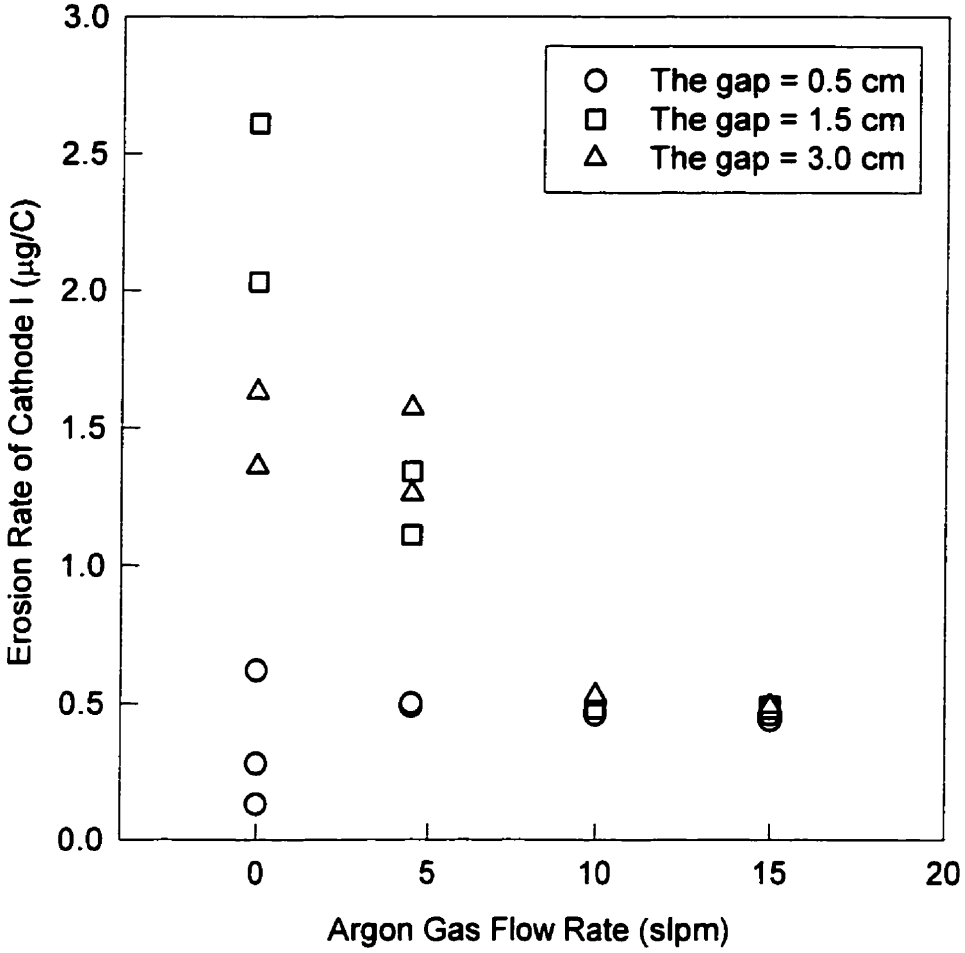

Figure 6-46: Erosion rates as a function of the argon gas flow rate using cathode I for an arc duration of 120 minutes at 150 A. The arc times of the runs at 3.0 cm and 0 slpm were 100 and 105 minutes.

The unstable arc duration for 3.0 cm at 0 slpm were about 49 and 63 minutes and that for 1.5 cm at 0 slpm were about 92 and 70 minutes.

Erosion behavior between 150 and 300 A was quite different, especially at the argon gas flow rate of 0 slpm. Figure 6-47 shows the erosion rates measured at 300 A and Figure 6-48 presents a comparison of the erosion behavior between 150 and 300 A runs at an initial interelectrode gap of 1.5 cm. Even though the highest erosion rate at 150 A was for the argon gas flow rate of 0 slpm, the lowest erosion rate at 300 A was also for the same argon gas flow rate, 0 slpm. The arc was unstable for 300 A and 0 slpm runs, but the erosion rates were lower. It is believed that these lower erosion rates were due to the redeposition of the carbon vapor, which was introduced in the equilibrium compositions. In case of fullerences synthesis using graphite electrodes, it has been reported that vaporized graphite from the electrodes can deposit on the cathode surface, thus reducing the erosion rate of the cathode. Figure 6-49 shows the cathode tip with a great deal of redeposited carbon for an experiment with an argon gas flow rate of 0 slpm and an initial interelectrode gap of 0.5 cm at 300 A. The mass of the cathode after the experiment increased and the erosion rate of this run was −1.30 μg/C. As the argon gas flow rate and the initial interelectrode gap increased, this carbon vapor redeposition became relatively weaker since the higher argon gas flow could wash out graphite species near the arc and the longer interelectrode gap could reduce the redeposition from the anode vapor jets.

The erosion rates for cathode I and II at 300 A as a function of the argon gas flow rate are plotted in Figure 6-50 for comparison. Table 6-3 shows operating conditions and the ΔVs

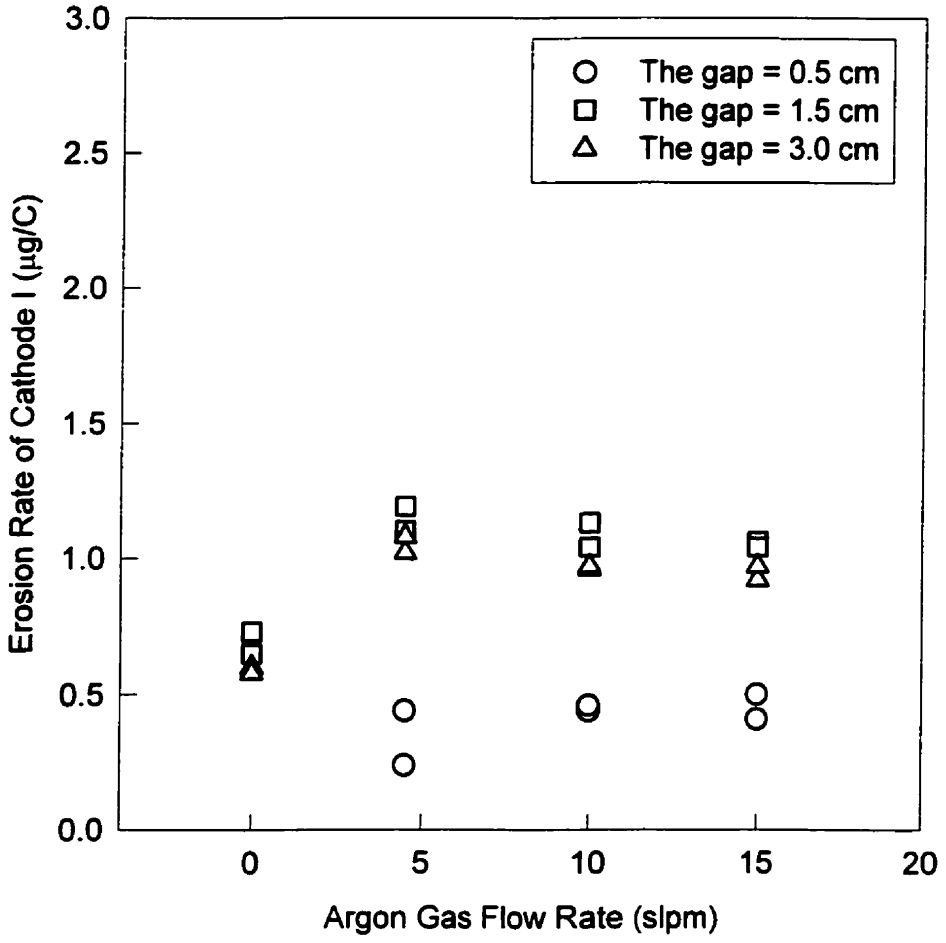

Figure 6-47: Erosion rates of cathode I as a function of the argon gas flow rate for an arc duration of 30 minutes at 300 A.

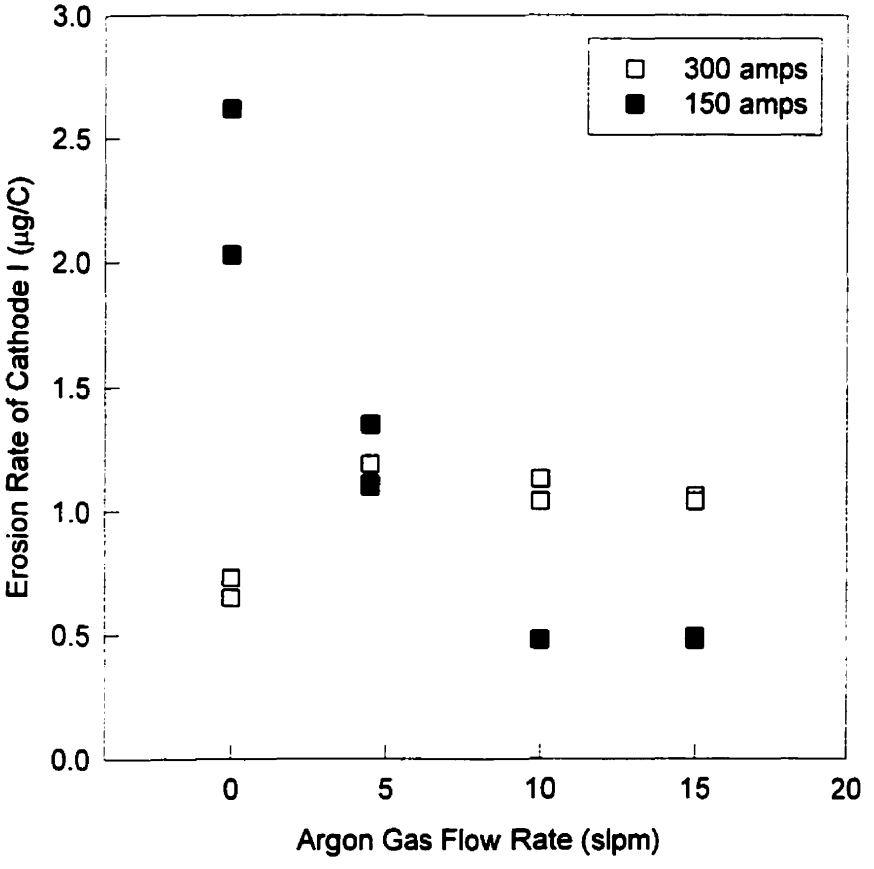

Figure 6-48: Comparison of erosion rates of cathode I between 150 and 300 A runs for an initial interelectrode gap of 1.5 cm, an arc duration of 120 minutes for 150 A runs, and an arc duration of 30 minutes for 300 A runs.

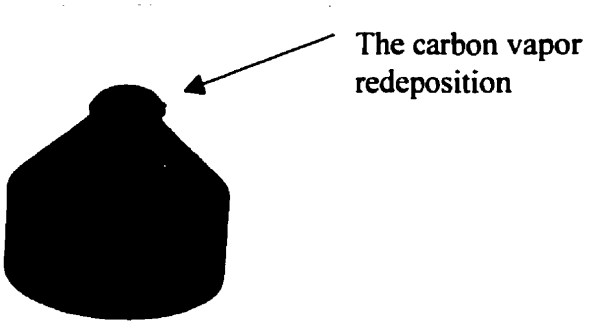

Figure 6-49: The highly redeposited cathode tip with carbon vapor.

of each whole run in Figure 6-50. The runs using cathode II were always stable operations while those using cathode I were stable or unstable according to the operating conditions. Regardless of the initial interelectrode gap change, the erosion rates of cathode I and II at 0 slpm were lower because of the redeposition of the carbon vapor. To compare erosion behavior between cathode I and II, the erosion rates at 15 slpm were considered because the runs were always stable. For the argon gas flow rate of 0 and 4.5 slpm, it was believed that this comparison was not reasonable because those runs included both the stable and the unstable operation. The erosion rates of cathode II at 15 slpm are slightly higher, and it is believed that the reduction of the cathode diameter resulted in higher arc root and cathode bulk temperatures, thus increasing the erosion rates.

Table 6-3: Operating conditions and ΔVs for cathode I & II at 300 A.

Cathode type	EXP-No.	Argon gas flow rate (slpm)	Initial interelectrode gap (cm)	ΔVs (V)
Cathode I	EXP-47&48	0	1.5	6.90 , 8.08
	EXP-59&60	0	3.0	4.45 , 2.49
	EXP-53&54	4.5	0.5	1.20 , 1.29
	EXP-49&50	4.5	1.5	3.40 , 5.01
	EXP-61&62	4.5	3.0	6.62 , 7.28
	EXP-55&56	10	0.5	0.80 , 0.66
	EXP-41&42	10	1.5	2.31 , 2.80
	EXP-63&64	10	3.0	3.06 , 4.77
	EXP-57&58	15	0.5	1.14 , 0.81
	EXP-51&52	15	1.5	2.07 , 1.86
	EXP-65&66	15	3.0	2.61 , 2.86
Cathode II	EXP-74 ~ EXP-83	0,4.5,10,15	0.5,1.5,3.0	0.60 ~ 2.30

6.3.2. Effect of Initial Interelectrode Gap on Erosion Rate

Erosion rates for the argon gas flow rate of 15 slpm at 150 and 300 A were used to study the effect of the initial interelectrode gap on the erosion rate because the arcs were always in the stable regime for these conditions, i.e. the same arc cathode operation mode. Figure 6-51 shows the erosion rates as a function of the initial interelectrode gap for the argon gas flow rate of 15 slpm at 150 A. The erosion rates increased slightly as the initial interelectrode gap increased. It seems that as the initial interelectrode gap increased, the

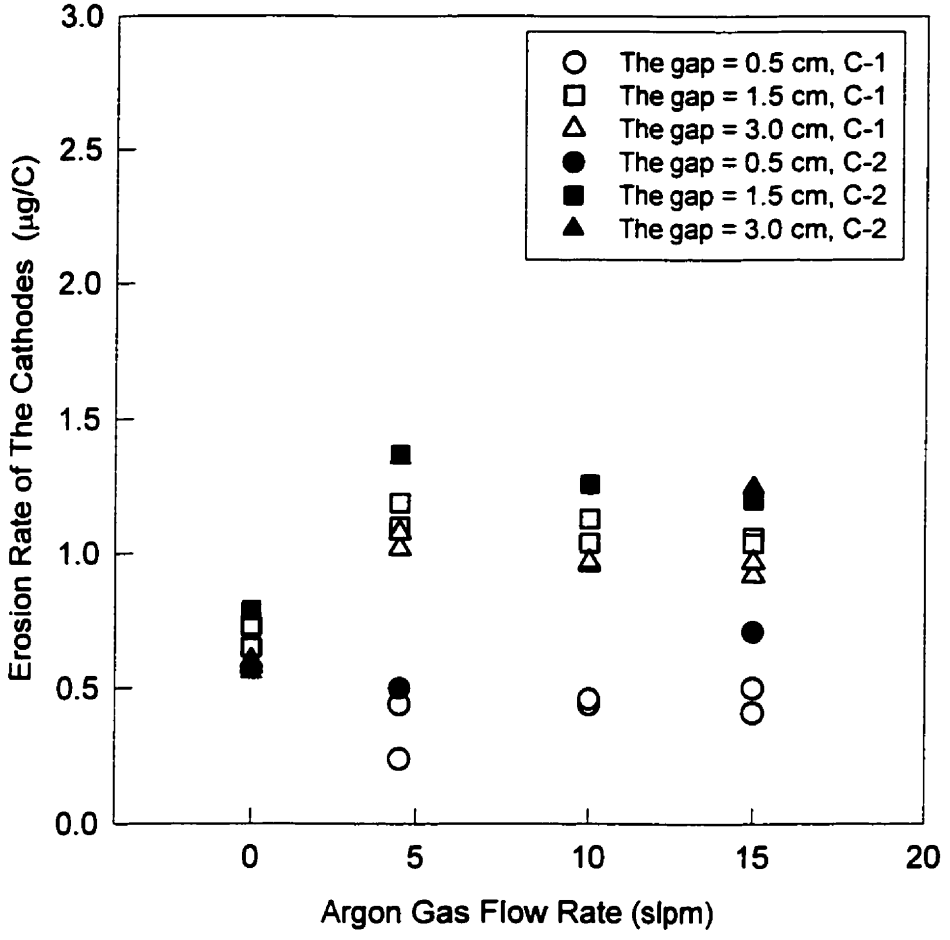

Figure 6-50: Comparison of the erosion rates between cathode I and II for an arc duration of 30 minutes at 300 A. C-1 stands for cathode I and C-2 is for cathode II.

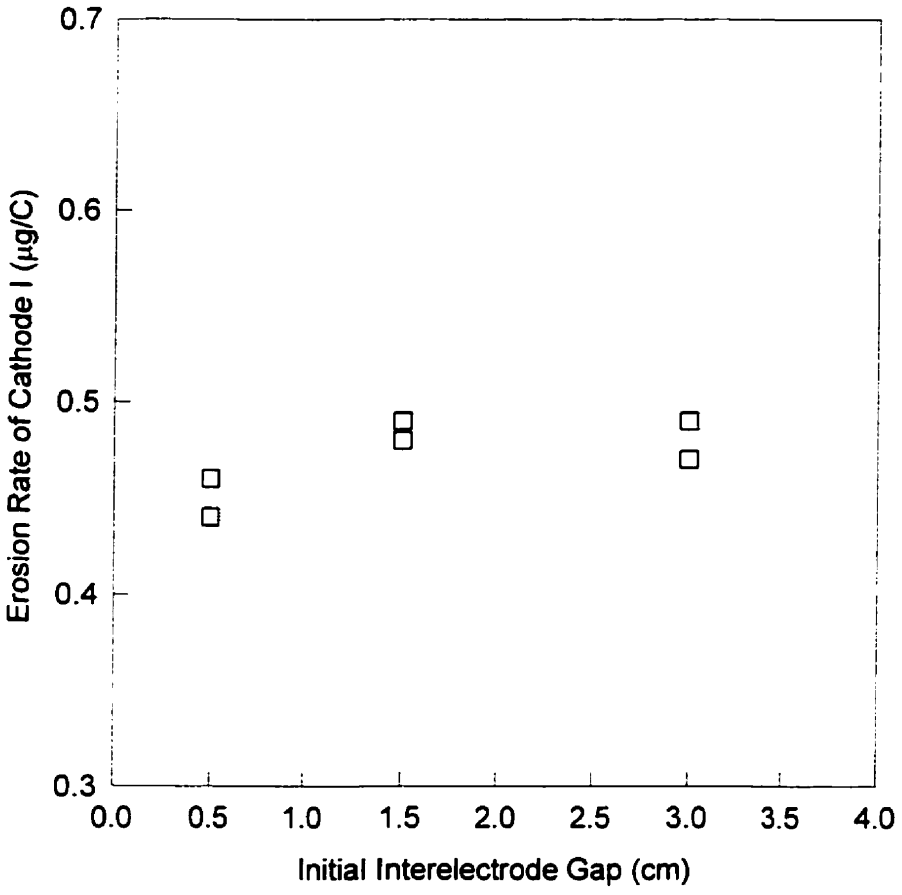

Figure 6-51: Erosion rate of cathode I as a function of the initial interelectrode gap for an argon gas flow rate of 15 slpm, an arc current of 150 A, and an arc duration of 120 minutes.

erosion rate might be affected by two factors: reduction of the carbon vapor redeposition and increase of graphite particles ejection due to the arc movement. Between them, probably the influence of the redeposition of the carbon vapor on the erosion rates was greater. The difference between the minimum and the maximum erosion rates was 0.05 μg/C at the 150 A runs. For the 300 A runs, the difference was much greater, i.e. 0.65 μg/C (see Figure 6-52). It is believed that the big difference between the 150 A runs of 0.05 μg/C and the 300 A runs of 0.65 μg/C was especially due to the redeposition of the carbon vapor for the initial interelectrode gap of 0.5 cm at 300 A. In case of the run at 0.5 cm and 300 A, the redeposition, providing the lowest erosion rate for the 300 A runs, was higher because heat flux to the anode was higher, thus resulting in relatively stronger anode graphite vapor jets.

6.3.3. Effect of Arc Current on Erosion Rate

Figure 6-53 presents the erosion rates as a function of the arc current for an argon gas flow rate of 15 slpm and an initial interelectrode gap of 1.5 cm. These operating conditions were selected for the discussion of this effect because the arc cathode operation mode was the same, i.e. the thermionic emission regime. As the arc current increased, the erosion rates also increased. This was expected because higher arc currents increase the heat flux to the thermionic spot, thus causing the higher erosion rates. This is a well-known phenomenon and is reflected in the traditional empirical models, prepared using graphite electrodes of EAFs, to represent erosion rates as a function of arc currents as discussed in chapter II.

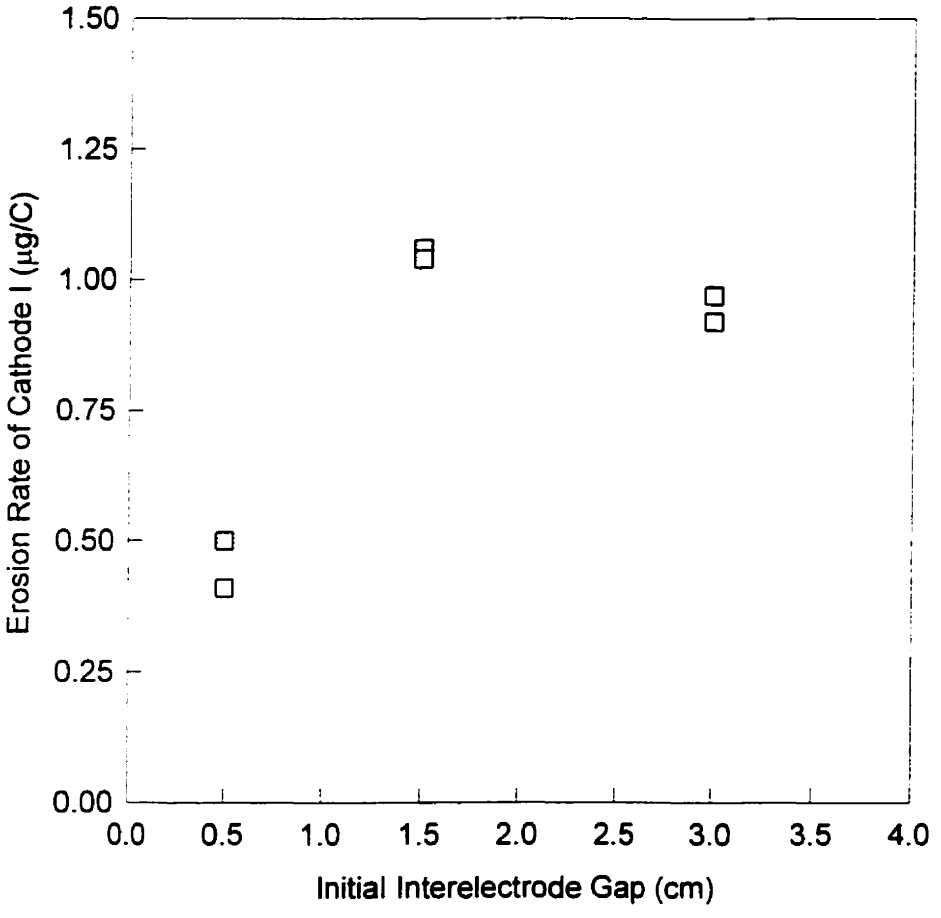

Figure 6-52: Erosion rate of cathode I as a function of the initial interelectrode gap for an argon gas flow rate of 15 slpm, an arc current of 300 A, and an arc duration of 30 minutes.

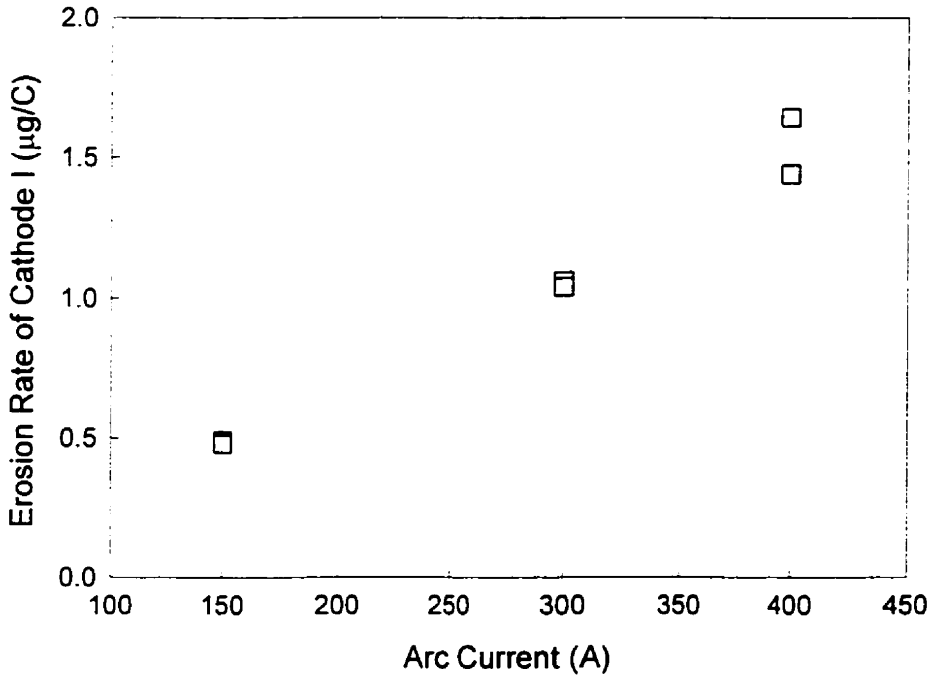

Figure 6-53: Erosion rates of cathode I as a function of the arc current for an argon gas flow rate of 15 slpm, an initial interelectrode gap of 1.5 cm, and an arc duration of 120 minutes for 150 A and 30 minutes for 300 and 400 A.

6.3.4. Effect of The Arc Stability on Erosion Rate

In the previous parts, it was shown that the erosion rates including the unstable arc runs were higher. This means that the arc stability, i.e. the arc cathode operation mode, influenced the erosion rates. In this part, a relationship between the arc stability and the erosion rates is derived, Then, the erosion rates are separated into the stable and the unstable erosion rate to study the effect of the arc stability on the erosion rates. The erosion rates measured for argon gas flow rates of 0 and 4.5 slpm at 150 A were used to investigate this effect because these runs included both the stable and the unstable arc operation. Even though the arcs for the same argon gas flow rate runs at 300 A displayed both the stable and the unstable parts, these erosion rates could not be used due to the strong redeposition of the carbon vapor.

The erosion rates were separated into the stable erosion rate (E_s) and the unstable erosion rate (E_u) using the following mass balance:

Total mass loss of the cathode =
Mass loss of the cathode for the stable arc operation
+ Mass loss of the cathode for the unstable arc operation (6-2)

From the definition of the erosion rate in equation (4-4), the total mass change of the mass balance above can be written as follows:

$$M = E\,t\,I \tag{6-3}$$

$$M_s = E_s\,t_s\,I \tag{6-4}$$

$$M_u = E_u\,t_u\,I \tag{6-5}$$

$$E\,t\,I = E_s\,t_s\,I + E_u\,t_u\,I \qquad (6\text{-}6)$$

where M is the total mass loss of the cathode (μg); E is the total erosion rate for a whole run (μg/C); t is the total arc duration (seconds); I is the arc current (A); M_s is the mass loss of the cathode for a stable arc run (μg); E_s is the erosion rate for a stable arc run (μg/C); t_s is the arc duration for a stable arc run (seconds); M_u is the mass loss of the cathode for an unstable arc run (μg); E_u is the erosion rate for an unstable arc run (μg/C); t_u is the arc duration for an unstable arc run (seconds). Furthermore, because the arc current was constant, the equation (6-6) could be simplified as follows:

$$E\,(t_s+t_u) = E_s\,t_s + E_u\,t_u \qquad (6\text{-}7)$$

where E is the total erosion rate for a whole run (μg/C); E_s is the erosion rate for a stable arc run (μg/C); t_s is the arc duration for a stable arc run (seconds); E_u is the erosion rate for an unstable arc run (μg/C); t_u is the arc duration for an unstable arc run (seconds).

Five cases of the separation of the erosion rates into the stable part erosion rate, E_s, and the unstable part erosion rate, E_u, were studied using equation (6-7). Table 6-4 outlines the operating conditions for sets of runs in which both the stable and the unstable regimes were encountered at 150 A. The time for the stable and the unstable operation was determined from the voltage data. The problem, which remained, was to determine E_s for the various operating conditions. For low stability conditions (case I to IV) the time for the stable operation was too short to allow accurate measurements to be made of E_s. The

Table 6-4: Operating conditions* for the separation of the erosion rates into E_s and E_u.

Case	EXP-NO.	Argon gas flow rate (slpm)	Initial interelectrode gap (cm)	Stable arc duration (minutes)	Unstable arc duration (minutes)
Case I	EXP-31	0	0.5	49.18	67.64
Case II	EXP-30	0	1.5	24.98	91.86
	EXP-37	0	1.5	46.86	69.97
Case III	EXP-29	0	3.0	48.50	48.81
	EXP-36	0	3.0	38.84	62.77
Case IV	EXP-10	4.5	1.5	44.94	71.87
	EXP-11	4.5	1.5	39.43	77.27
Case V	EXP-21	4.5	3.0	62.71	54.11
	EXP-22	4.5	3.0	73.11	43.71
	EXP-27	4.5	3.0	50.35	-
	EXP-28	4.5	3.0	59.42	27.28

*) Runs for an arc current of 150 A using cathode I

solution used was to measure E_s under the stable conditions, i.e. at the current of 150 A and an argon gas flow rate of 15 slpm and assumes that this same value could be used for lower argon gas flow rates. This information is summarized in Table 6-5. For case V, E_s was measured directly from a run, which was stable throughout (EXP-27, Table 6-4) by stopping the experiment as soon as the acoustic noise and the voltage increase were detected. Figure 6-54 shows the voltage pattern for that run. The results of the separation of the overall erosion rate into the stable and the unstable erosion rates are summarized in Table 6-6. It is clear that the unstable erosion rates were always much higher than the stable erosion rates. The higher erosion rates in the unstable arc operation means that the arcs in the thermofield emission regime eroded the cathode more.

Table 6-5: The stable part erosion rates*, E_s.

Case	EXP-NO.	Argon gas flow rate (slpm)	Initial Interelectrode gap (cm)	E (μg/C)	E_s (μg/C)
Case I	EXP-14	15	0.5	0.44	0.45
	EXP-16	15	0.5	0.46	
Case II	EXP-12	15	1.5	0.49	0.49
	EXP-13	15	1.5	0.48	
Case III	EXP-25	15	3.0	0.47	0.48
	EXP-26	15	3.0	0.49	
Case IV	EXP-12	15	1.5	0.49	0.49
	EXP-13	15	1.5	0.48	
Case V	EXP-27	4.5	3.0	0.61	0.61

*) Runs for an arc current of 150 A using cathode I

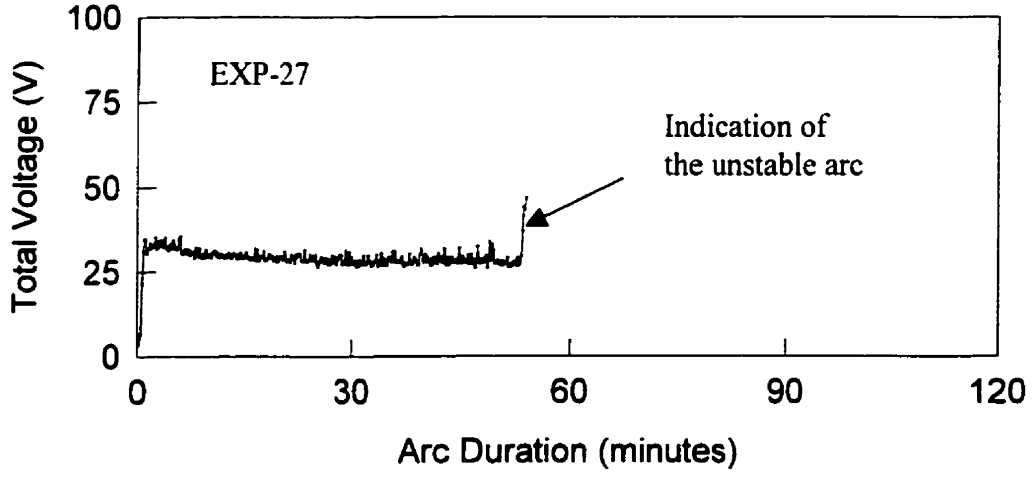

Figure 6-54: The voltage pattern for the experimental determination of E_s using cathode I for an argon gas flow rate of 4.5 slpm and an initial interelectrode gap of 3.0 cm at 150 A.

Table 6-6: The results of the separation of the erosion rates*.

Case	EXP-No.	Argon gas flow rate (slpm)	Initial interelectrode gap (cm)	E (μg/C)	E_s (μg/C)	E_u (μg/C)
Case I	EXP-31	0	0.5	0.62	0.45	0.74
Case II	EXP-30	0	1.5	2.61	0.49	3.19
	EXP-37	0	1.5	2.03		3.06
Case III	EXP-29	0	3.0	1.63	0.48	2.77
	EXP-36	0	3.0	1.36		1.91
Case IV	EXP-10	4.5	1.5	1.34	0.49	1.87
	EXP-11	4.5	1.5	1.11		1.43
Case V	EXP-21	4.5	3.0	1.57	0.61	2.68
	EXP-22	4.5	3.0	1.26		2.35
	EXP-27	4.5	3.0	0.61		0
	EXP-28	4.5	3.0	1.07		2.07

*) Runs for an arc current of 150 A using cathode I

The separate values of the E_u and the E_s are plotted as a function of the ΔV in Figure 6-55. The stable arc region ($\Delta V \leq 3$ V) is given as the open symbols; while the unstable arc region ($\Delta V > 3$ V) is given by the black symbols. The values of E_s are clustered together and are always less than those of E_u. The values for unstable arcs show much more scatter both in E_u and ΔV; therefore, it was difficult to analyze the E_u behavior. However, it was thought that E_u increased as the ΔV increased. As discussed earlier, principally the higher local heat flux to the cathode spots in the thermofield emission might increase the erosion rates. Figure 6-56 presents the erosion rates separated as a function of the $\Delta V/V$. Like Figure 6-55, the E_s are clustered together at the $\Delta V/V$ of 0.5 and the E_u are highly scattered.

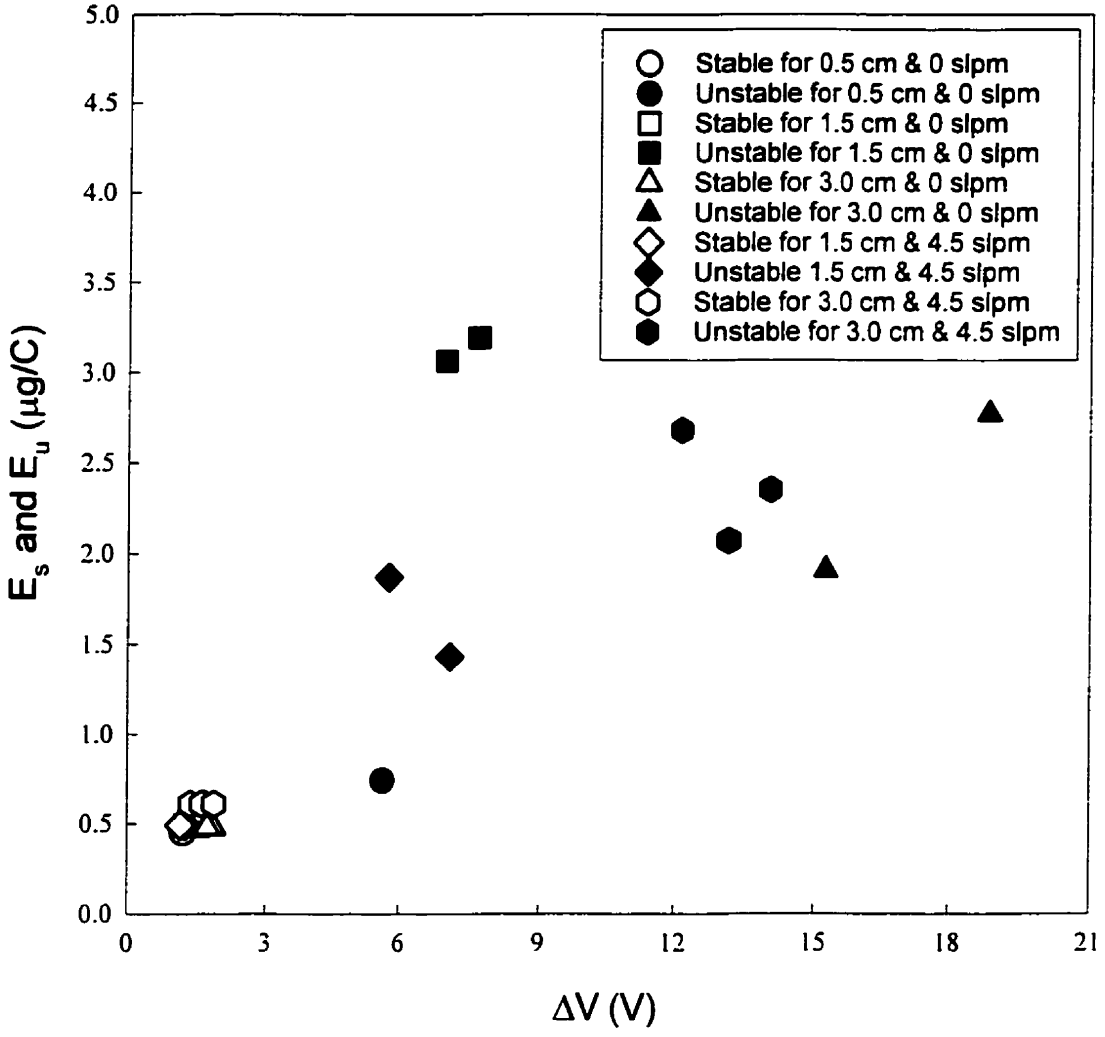

Figure 6-55: Stable part erosion rate (E_s) and unstable part erosion rate (E_u) as a function of ΔV using cathode I for an arc current of 150 A.

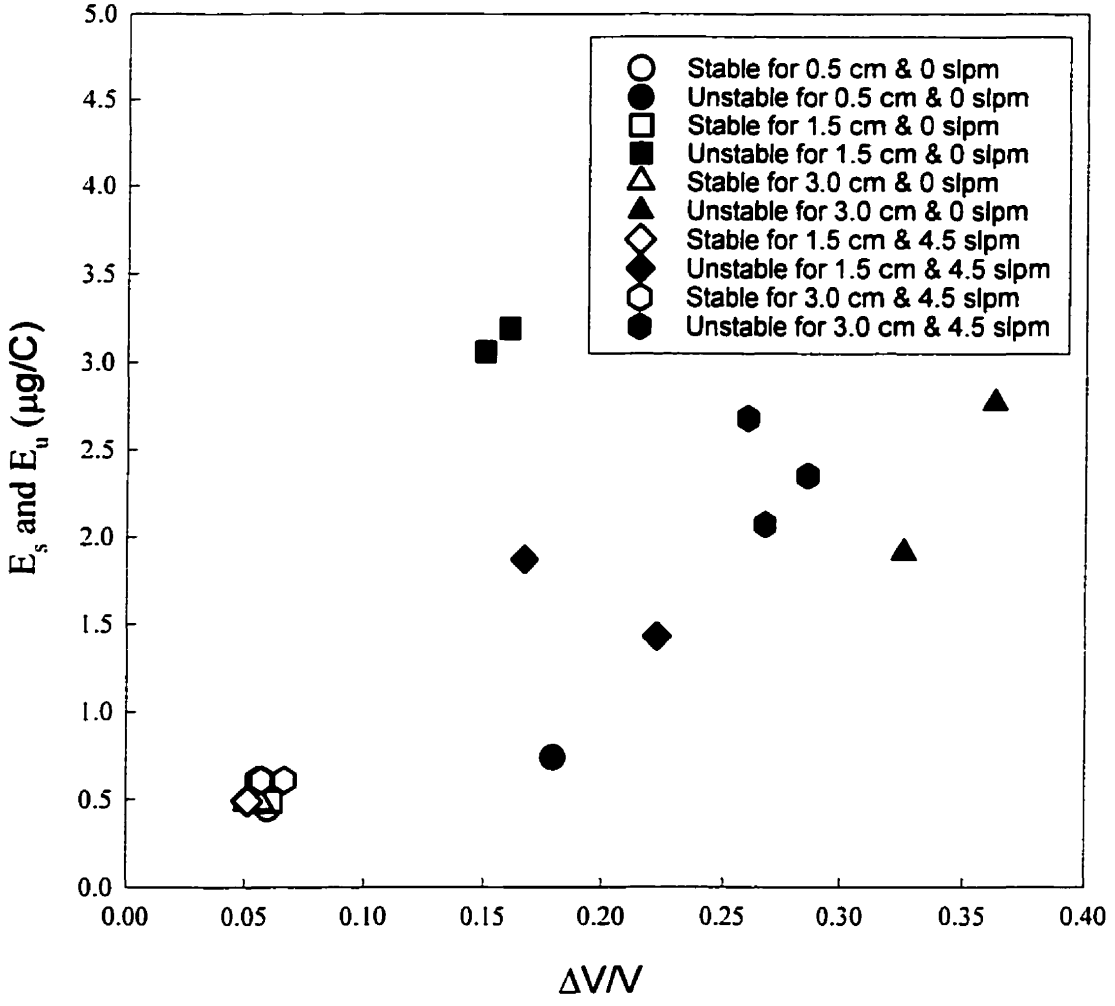

Figure 6-56: Stable part erosion rate (E_s) and unstable part erosion rate (E_u) as a function of $\Delta V/V$ using cathode I for an arc current of 150 A.

6.3.5. Comparison of Erosion Rates with Other Work

Erosion rates of this work were compared with those reported by Mentel (1977), Lefort et al. (1993), Drouet et al. (1995), and Neuschutz et al. (1996). The erosion rates of Mentel (1977), Lefort et al. (1993), and this work were obtained at the laboratory scale while the rates of Drouet et al. (1995) and Neuschutz et al. (1996) were obtained at the industrial operation. For this comparison the apparent current density was used primary because operating currents and cathode diameter varied greatly between the laboratory and industrial scale operation. The results are presented in Table 6-7 and procedures to estimate the rates are included in the notes of Table 6-7.

For the laboratory scale, the apparent current densities of Mentel (1977) are much greater than those of this work. The cathode II apparent current density of 375 A/cm^2, marked by **, in this work may be used to distinguish between the thermionic and the thermofield mode of graphite rod cathodes. The apparent current density of more than 375 A/cm^2 is able to indicate the thermionic mode of graphite rod cathodes because the runs at 0 slpm using cathode II in this work were always stable and were in the thermionic mode. For hollow graphite cathodes, however, the thermionic mode can be achieved even if the apparent current density is lower than 375 A/cm^2 due to argon gas injection. This suggests that the arc cathode operation mode of Mentel (1977), who used graphite rod cathodes, was in the thermionic emission regime. The erosion rates of this work and Mentel (1977) in the table were first compared because it was believed that they were in the same arc cathode operation mode, the thermionic emission mode, in argon. At 300 A the erosion rate of Mentel (1977) is higher, probably because of the higher current

density. Also, the prevention of the carbon redeposition of Mental (1977) might contribute somewhat to the higher rate. The erosion rates of Mentel (1977) were correlated using the general form of the erosion rates of the graphite electrodes, introduced in chapter 2, as follows:

$$E = 7.5 \times 10^{-7} I^{2.7} \qquad (6\text{-}8)$$

where E is the erosion rate (μg/C); I is the arc current (A). The erosion rates in this work were correlated as follows:

$$E = 1.4 \times 10^{-3} I^{1.2} \qquad (6\text{-}9)$$

where E is the erosion rate (μg/C) ; I is the arc current (A). Lefort et al. (1993) reported much higher erosion rate than that of this work and even the rate of Mentel (1977) at 300 A. Since Lefort et al. (1993) did not provide information of the atmosphere of their operation, their rates may include some oxidation. Owing to the quite lower current and the current density of Lefort et al. (1993), their operation probably included the thermofield mode, leading to the higher erosion rate. In the table the highest unstable erosion rate of 3.2 μg/C in this work, marked by ***, is presented; the rate was estimated using only the unstable operation. The higher rate of Lefort et al. (1993) than 3.2 μg/C in this work supports the inclusion of the thermofield mode in their operation.

Direct comparison of the erosion rates between the laboratory and the industrial scale was difficult due to the different size of the cathodes and different operating conditions. Their arcs might include the thermionic mode despite operation of the industrial scale because Drouet et al. (1995) and Neuschutz et al. (1996) used argon for the arc stabilization.

Table 6-7: Comparison of erosion rates

	Current (A)	Cross-sectional area of the cathodes (cm^2)	Apparent current density (A/cm^2)	Erosion rates (μg/C)	Remarks
This work [1]	150*	2.8	54	0.5	Hollow cathode; Erosion
	300*	2.8	107	1.1	
	400*	2.8	143	1.5	
	300**	0.8	375	1.2	
	150***	2.8	54	3.2	
Mentel (1977) [2]	297	0.3	980	3.0	Rod cathode; Erosion
	594	0.3	1980	31.7	
	891	0.3	2970	66.7	
	1040	0.3	3467	85.7	
Lefort et al. (1993) [3]	70	3.1	22	11.4	Rod cathode; Erosion
Drouet et al. (1995) [4]	2500	81.7	31	85.6	Rod cathode; Consumption
Neuschutz et al. (1996) [5]	2000	75.4	27	63.9	Hollow cathode; Consumption

Notes:

1) For cathode I, marked by *, the stable erosion rates of EXP-12, 13, 51, 52, 72, 73 operated at 1.5 cm and 15 slpm presented in Figure 6-53 were used; for cathode II, marked by **, the stable erosion rate of EXP-77 operated at 1.5 cm and 15 slpm was used; for the unstable erosion rate, marked by ***, the unstable rate of EXP-30 operated at 1.5 cm and 0 slpm using cathode I was used because the rate was the highest. The outer diameter was 1.91 cm for cathode I and was 1.07 cm for cathode II. The inner diameter was 0.32 cm for both cathodes.

2) The estimation of the erosion rates was introduced in Table 2-3. The diameter of the cathode was 0.615 cm.

3) The erosion rate reported was 0.8×10^{-6} kg/second; it was divided by the current of 70 A, and thus estimating the erosion rate of 11.4 μg/C. The diameter of the cathode was 2 cm.

4) The estimation of the rate was performed as follows. The diameter of the cathode was 10.2 cm.

① Electrode consumption per ton-dross reported: 0.88 kg/ton-dross

② Dross treatment capacity: 0.87 ton-dross/hour

③ Electrode consumption per hour: 0.77 kg/hour = 2.14×10^{-4} kg/second

④ At 2500 A, consumption is 86 μg/C

5) The estimation of the rate was performed as follows. The outer diameter of the cathode was 10 cm and the inner diameter of the cathode was 2 cm.

① Electrode consumption rate reported: 0.46 kg/hour = 1.28×10^{-4} kg/s

② At 2000 A, consumption is 64 μg/C

The rate of Neuschutz et al. (1996) at 2000 A is close to the rate of Mentel (1977) at about 900 A; the rate of Drouet et al. (1995) at 2500 A is about the same to the rate of Mentel (1977) at around 1000 A. Higher erosion rates than the rates of Mentel (1977) at about 900 ~ 1000 A were expected for the experiments of Drouet et al. (1995) and Neuschutz et al. (1996) due to higher currents and the oxidation of graphite. However, the rates of Drouet et al. (1995) and Neuschutz et al. (1996) are on the order of the rates of Mentel (1977) at about 900 ~ 1000 A. Probably this is due to the lower apparent current densities of Drouet et al. (1995) and Neuschutz et al. (1996). Compared with the rates of this work, their rates were much greater, because of much higher currents, the oxidation of graphite and possibly the thermofield mode resulting from the lower current densities.

CHAPTER VII

CONCLUSIONS

AND RECOMMENDATIONS

7.1. CONCLUSIONS

1. Characteristics of Arcs at Hollow Graphite DC Cathode

The arc characteristics of the graphite cathode were studied as a function of initial interelectrode gap, argon gas flow rate, and arc currents. As the initial interelectrode gap increased, the total voltage also increased due to an increase of total resistance of the arcs. Higher argon gas flow rates slightly increased the voltage at lower interelectrode gap. At higher interelectrode gap, however, the effect of the argon gas flow rate on the voltage was negligible; it is believed that because of an increase of divergence of argon gas jets at the higher gap, less cooling of the arcs was caused and thus providing the very little effect on the voltage. The voltage increased slightly as the current increased. This voltage-current (V-I) characteristic showed that the arcs in this work are thermal arcs.

2. Arc Stability at a Hollow Graphite DC Cathode

The arc stability, i.e. the mode of the graphite arc cathode operation, was studied as a function of argon gas flow rate, initial interelecrode gap, arc currents, and cathode tip geometry. This mode transition is a spontaneous phenomenon of thermal arcs at the graphite cathode.

Two completely different total voltage patterns were observed. Arcs exhibiting a nearly constant voltage pattern were termed stable arcs. Arcs exhibiting noisy voltage patterns which coincided with rapid arc motion and acoustic noise were termed unstable arcs. It was hypothesized that the stable arcs were in thermionic emission and the unstable arcs were in thermofield emission. The mode transition from the thermionic emission to the

thermofield emission occurred at rounder cathode tip geometry and lower argon gas flow rate. The hypothesis was supported by estimation of current densities, FFT of total voltage yielding time scales consistent with cathode spots for the thermofield emission for the unstable arcs, SEM evidence of cathode spots for the unstable arcs and crystal growth indicating higher mean temperature for the stable arcs, and measurements of cathode temperatures showing higher temperatures for the stable arcs.

3. Erosion Behavior of a Hollow Graphite DC Cathode

Erosion rates were measured of the graphite cathode using a graphite anode as a function of argon gas flow rate, initial interelectrode gap, and arc currents. As the argon gas flow rate increased, the erosion rate decreased at 150 A and increased at 300 A and 400 A. These opposite trends were due to the redeposition of the carbon vapor at higher arc currents. The redeposition reduced the erosion rate; especially at shorter initial interelectrode gap, lower argon gas flow rate, and higher arc currents.

Erosion rates of the cathode were strongly influenced by the arc stability at 150 A; as the arc stability increased, the cathode eroded at a lower rate. It is believed that in the thermofield emission regime of the unstable arc operation, the local heat flux to the cathode spots by the ion bombardment is higher, thus resulting in the more erosion of the graphite. The overall erosion rates were separated into stable (E_s) and unstable (E_u) erosion rate. The E_u was always higher than E_s and showed much more scatter.

Erosion of graphite electrodes can be controlled through regulating the arc stability.

Therefore, it is believed that the mode of graphite arc cathode operation may be selected to meet purposes of thermal arc processing using graphite electrodes.

7.2. CONTRUIBUTIONS TO KNOWLEDGE

The followings have been achieved as contributions to knowledge of this study:

1. Study of arc characteristics at a hollow graphite DC cathode.
2. Identification of the stable operation of the graphite cathode with thermionic emission and the unstable operation of the graphite cathode with thermofield emission.
3. Measurements of erosion rates of the graphite cathode using a graphite anode in argon at atmospheric pressure.

7.3. RECOMMENDATIONS FOR FUTURE WORK

The following experimental and theoretical studies are recommended as further work.

1. Arc Core Temperature

Both experimental and theoretical work is needed on arc core temperature as a function of argon gas flow rate. Spectroscopic methods and high speed video photography are believed to be viable techniques for the temperature and temperature distribution measurements.

2. Modeling of Arc Root Temperature

The measurement of arc root temperature is believed to be impractical with present technology; therefore, modeling work is believed to be a better approach to verify variation of the arc root temperature as a function of argon gas flow rate, interelectrode gap, and cathode tip geometry.

3. Experimental work at more than 1000 A for longer arc length is needed.

REFERENCES

Anders, S. and Anders, A., " On Modes of Arc Cathode Operation", IEEE Transactions on Plasma Science, Vol. 19, no. 1, February, pp. 20-24 (1991).

Anders, A. and Jütter, B., "Cathode Mode Transition in High-Pressure Discharge Lamps at Start-Up", Lighting Res. Technol., **22**, (2), pp. 111-115 (1990).

Barcza, N. A., "The Development of Large-Scale Thermal Plasma Systems", Journal of the South African Institute of Mining and Metallurgy, Vol. 86, no. 8, August, pp. 317-333 (1986).

Benilov, M. S., "Heating of Cathodes of High Pressure Arc Discharge", ISPC-14 Praha, Symposium Proceeding, Vol. 1, pp. 55-60 (1999)

Burkhard, R., Hoffelner, W., and Eschenbach, R.C., "Recycling of Metals from Waste with Thermal Plasma", Resources, Conservation and Recycling, Vol. 10, pp. 11-16 (1994).

Chen, G., "Vitrification of Simulated Medium and High Level Canadian Nuclear Waste in a Continuous Transferred Arc Plasma Melter", PhD Thesis, McGill University (1991).

Choi, Hyun-Koo, "Energy Distribution in Transferred-Arc System", PhD Thesis, McGill University (1981).

Cohn, D.R., "Hot and Cold Plasma Processing of Wastes", Selected Topics in Plasma Science and The Environment, edited by Manheimer, W., Sugiyama, L.E., and Stix, T.H., AIP Press, Woodbury, NY, USA, pp. 209-229 (1997).

Coulombe, S., "A Model of the Electric Arc Attachment on Non-Refractory Cold Cathodes", PhD Thesis, McGill University (1997).

Coulombe, S. and Meunier, J.-L., "Thermo-Field Emission: A Comparative Study", J. Phys. D: Appl. Phys. 30, pp. 776-780 (1997).

Coulombe, S. and Meunier, J.-L., "Importance of High Local Cathode Spot Pressure on the Attachment of Thermal Arcs on Cold Cathodes", IEEE Trans. on Plasma Sci., Vol. 25, no. 5, pp. 913-918 (1997).

Counts, D.A., Sartwell, B.D., Peterson, S.H., Kirkland, R., and Kolak, N.P., "Thermal Plasma Waste Remediation Technology: Historical Perspective and Current Trends", US Naval Research Laboratory, NRL/MR/6170-99-8335 (1999).

Desaulniers-Soucy and Meunier, J.-L., "A Study of Magnetically Rotating Arc Stability Using Fluctuations in Voltage, Velocity and Emission Line Intensity", J. Phys. D: Appl. Phys. 28 pp. 2505-2513 (1995).

Dolan, W.W. and Dyke, W.P., "Temperature-and-Field Emission of Electrons from Metals", Physical Review, Vol. 95, no.2, pp. 327 (1954).

Drouet, M. G., Handfield, M., Meunier, J., and Laflamme, C.B., "Dross Treatment in a Rotary Arc Furnace with Graphite Electrodes", JOM, May, pp. 26-27 (1994).

Drouet, M.G., Meunier, J., Laflamme, C.B., Handfield, M.D., Biscaro, A., and Lemire, C., "A Rotary Arc Furnace for Aluminum Dross Processing", Proceedings of the International Symposium on Environmental Technology: Plasma Systems and Applications, Atlanta, GA, USA, October, Vol. II, pp. 539-548 (1995).

Eddy, T.L., "Treating Waste with PAM", JOM, October, pp. 20-21 (1999).

Encyclopedia of Chemical Technology, Kirk and Othemer Eds, Wiley, New York, USA, Vol. 4, pp. 609 (1980).

Encyclopedia of Chemical Technology, Kirk and Othemer Eds, Wiley, New York, USA, Vol. 4, pp. 1039-1040 (1992).

Fauchais, P. and Vardelle, A., "Thermal Plasmas", IEEE Transactions on Plasma Science, Vol. 25, no. 6, December, pp. 1258-1280 (1997).

Ghorui, S., Sahasrabudhe, S. N., Murthy, P. S. S., Das, A. K., and Venkatramani, N., "Experimental Evidence of Chaotic Behavior in Atmospheric Pressure Arc Discharge", IEEE Transactions on Plasma Science, Vol. 28, no. 1, February, pp. 253-260 (2000).

Guile, A.E., " Arc-Electrode Phenomena", Proc. IEE, IEE Reviews, Vol. 118, no. 9R, September, pp. 1131-1154 (1971).

Holm, R., "The Vaporization of the Cathode in the Electric Arc", Journal of Applied Physics, Vol. 20, July, pp. 715-716 (1949).

Holm, R., "Electric Contacts", Springer-Verlag New York, USA, pp. 423-438 (1967).

Holman, J.P., "Experimental Methods for Engineers", McGraw-Hill Inc., USA, pp 315-321 (1989).

Jurewicz, J.W., Lecture Notes of Thermal Plasma Technology, Plasma Technology Research Center (CRTP), McGill University and Sherbrooke University (1997).

Jütter, B., "Properties of Arc Cathode Spots", J. Phys. IV France, 7, pp. C4-31-C4-45 (1997).

Jütter, B., "Nanosecond Displacement Times of Arc Cathode Spots in Vacuum", IEEE Transactions on Plasma Science, Vol. 27, no. 4, August, pp. 836-844 (1999).

Kaltenhauser, R. H. and Gimbel, F. M., "Coated Electrodes to Reduce Graphite Consumption", Electric Furnace Proceedings, pp. 285-290 (1983).

Kandah, M.I., "Particles Emission Control at Graphite Cathodes in Arc Ion Plating Deposition", PhD Thesis, McGill University (1997).

Kim, George, "The Effects of Low Pressure Nitrogen on Titanium Cathode Sources in TiN Arc-Ion Plating", PhD Thesis, McGill University (1995).

Kimblin, C. W., "Erosion and Ionization in the Cathode Spot Regions of Vacuum Arcs", Journal of Applied Physics, Vol. 44, no. 7, pp. 3074-3081 (1973).

Lefort, A., Parizet, M. J., El-Fassi, S. E., and Abbaoul, M., "Erosion of Graphite Electrodes", Journal of Physics D: Applied Physics, Vol. 26, pp. 1239-1243 (1993).

Lefrank, P. A., Supon, M. F. and Jesberger, T.J., "Performance Evaluation of Graphite Electrodes under Varying Conditions in a Modern Arc Furnace Shop", Electric Furnace Proceedings, pp 297-309 (1983).

Maddever, W.J. and Segsworth, R.S.,"The Influence of Gas Injection Arc Stabilization and Electrode Consumption in Electric Furnaces", Canadian-Metallurgical Quarterly, Vol. 15, no. 1, pp. 49-52 (1976).

Mehmetoglu, M. T., "Characteristics of a Transferred-Arc Plasma", PhD Thesis, McGill University (1980).

Mentel, J., "The Influence of Vaporization upon The Roots of A High Current Arc, Part I Different Forms of Vaporization in the Arc Roots", Applied Physics, Vol. 14, pp. 269-276 (1977).

Mentel, J., "The Influence of Vaporization upon The Roots of A High Current Arc, Part II Spectroscopic Determination of the Composition and Temperature of a Plasma in the Neighbourhood of a Graphite Cathode", Applied Physics, Vol. 14, pp. 361-366 (1977).

Mentel, J., "The Influence of Vaporization upon The Roots of A High Current Arc, Part III Determination of the Vapour Temperature by Molecular Spectroscopy and Conclusions concerning the Arc-Root Instability", Applied Physics, Vol. 15, pp. 179-183 (1978).

Meunier, J.-L. and Drouet, M.G., "Experimental Study of the Effect of Gas Pressure on Arc Cathode Erosion and Redeposition in He, Ar, and SF_6 from Vacuum to Atmospheric Pressure", IEEE Transactions on Plasma Science, Vol. PS-15, no.5, October (1987).

Montgomery, R.W. and Sharp, C.M.H., "The Effect of the Cathode Geometry on the Stability of Arcs", J.Phys.D., Ser. 2, Vol. 2, pp. 1345-1348 (1969).

Murphy, E.L. and Good, R.H., "Thermion Emission, Field Emission, and The Transition Region", Physical Review, Vol. 102, no. 6, pp. 1464-1473 (1956).

Neuschutz, D., "Plasma Processing of Dusts and Residues", Pure & Applied Chemistry, Vol. 68, no. 5, pp. 1159-1165 (1996).

Neuschutz, D., Stadler, P., and Bebber, H.J., "Arc Heating in the Tundish with a Graphite Electrode in Comparison to a Metallic Plasma Torch", Steel Research, Vol. 67, no. 11, pp. 475-478 (1996).

Ochs, T.L., Hartman, A.D., and Wright, J.B.,"Improved Arc Stability in Electric Furnace Steelmaking", Iron and Steel Engineer, May, pp. 26-31 (1989).

Pfender, E., Boulous, M., and Fauchais, P., "Methods and Principles of Plasma Generation", Plasma Technology in Metallurgical Processing, Iron and Steel Society, pp. 27-47 (1987).

Roine, A., "Outokumpu HSC Chemistry for Windows", User's Guide, Outokumpu Research (1994).

Roth, J.R., "Industrial Plasma Engineering", I.O.P. Publishing, Philadelphia, PA, USA, pp. 352-390 (1995).

Rozelle, P.L., Baranski, J.P., Bitler, J.A., and Exide Corporation, "Introduction to Exide Corporation's High Temperature Metals Recovery Systems", Proceedings of the International Symposium on Environmental Technologies: Plasma Systems and Applications, Atlanta, GA, USA, October, Vol. II, pp. 561-582 (1995).

Schwabe, W.E., "The Mechanics of Consumption of Graphite Electrodes in Electric Steel Furnaces", Electric Furnace Proceedings, pp. 140-148 (1971).

Schumacher, R.F., "High-Temperature Vitrificatin of Low-Level Radioactive and Hazardous Wastes", Proceedings of the International Symposium on Environmental Technologies: Plasma Systems and Applications, Atlanta, GA, USA, October, Vol. II, pp. 461-470 (1995).

Siemroth, P., Schülke, T., and Witke, T., "Microscopic High Speed Investigations of Vacuum Arc Cathode Spots", IEEE Transactions on Plasma Science, Vol. 23, no. 6, December, pp. 919-925 (1995).

Sommerville, I.D., McLean, A., and Alcock, C.B., "Materials Processing in Plasma Furnaces Equipped with Graphite Electrodes", Plasma Technology in Metallurgical Processing, Iron and Steel Society, pp. 89-101 (1987).

Szente, R.N., Munz, R.J., and Drouet, M.G., "Electrode Erosion in Plasma Torches", Plasma Chemistry and Plasma Processing, Vol. 12, no. 3, pp. 327-343 (1992).

Themelis, N.J. and Gauvin, W.H., "A Two-Wavelength Pyrometer for Temperature Measurements in Gas-Solids Systems", The Canadian Journal of Chemical Engineering, August, pp.157-161 (1962).

UIE, Electroheat Technologies Committee, and Plasma Processing Working Group, "Arc Plasma Processes; A Maturing Technology In Industry; UIE Arc Plasma Review", Chapter 8 (1988).

Wittle, J.K., Titus, C.H., Hamilton, R.A., Cohn, D.R., Smatlak, D.L., Woskov, P.P., Thomas, P., and Surma, J.E., "DC Graphite Arc Furnace and Diagnostic System for Soils", Hazardous Wastes and Hazardous Materials, Vol. 11, no. 1, pp. 237-248 (1994).

Zhou, X. and Heberlein, J., "Analysis of the Arc-Cathode Interaction of Free-Burning Arcs", Plasma Sources Sci. Technol. Vol. 3, pp. 564-574 (1994).

APPENDICIES

Appendix 1. Estimation of the mass loss of the graphite cathode due to the oxygen in the argon atmosphere of the chamber

Bases:

1) Oxygen concentration in the chamber: 0.1 volume %.
2) Relative humidity in the chamber: 1% at 20 °C.
3) Volume of the chamber: 40 liters.

1. Graphite consumption mass loss due to the oxygen

Step-1: Determination of the moles of the oxygen.

The oxygen volume: 0.04 liters.

The oxygen moles: 0.0017 moles from the ideal gas law.

Step-2: The mass loss due to the oxygen: 4.08×10^{-2} g from $2C + O_2 \rightarrow 2CO$.

- The mass loss may be zero because of the accuracy of the O_2 meter ($\pm$ 0.5 volume %).

2. Graphite consumption mass loss due to the water vapor

Step-1: Obtain the vapor pressure of water at 20.0 °C from the steam table. The vapor pressure was 17.535 mm Hg.

Step-2: By using the definition of the RH, calculate the partial pressure of the water vapor in the chamber. The partial pressure of the water vapor was 0.17535 mm Hg.

Step-3: By using the definition of the molar humidity, calculate moles of the water vapor in the chamber per mole of dry air.

$$H_n = \frac{mole_{H2O}}{mole_{dryair}} = \frac{p_{H2O}}{P - p_{H2O}}$$

where P is the chamber pressure (760 mm Hg) and p_{H2O} is the partial pressure of the water vapor. The moles of the water vapor was 2.31 x 10^{-4} per mole of dry air.

Step-4: By using the relationship between the absolute humidity and the molar humidity, calculation of the mass of the water vapor, g per g of dry air.

$$H = H_n(\frac{18}{29})$$

The mass of the water vapor was 1.43 x 10^{-4} g per g of dry air.

Step-5: Estimation of the water mass in the chamber.

The mass of the water vapor is 1.43 X 10^{-4} x the mass of dry air. The mass of the dry air in the chamber (48.24 g) was obtained using the ideal gas law. The mass of the water vapor was 6. 90 X 10^{-3} g (3.83 X 10^{-4} moles).

Step-6: The mass loss due to the water vapor: 4.60 x 10^{-3} g from $C + H_2O \rightarrow H_2 + CO$.

3. The mass loss of the graphite cathode due to the oxygen: 4.60 x $10^{-3} \sim 4.54$ x 10^{-2} g.

Appendix 2. Operating Conditions

EXP NO.	Relative Humidity and Temperature (%)	(°C)	O_2 Concentration (volume %)	Total Arc Duration (minutes)	Initial Interelectrode Gap (cm)	Argon Gas Flow Rate (slpm)	Remarks
150 A Experiments (Cathode I, EXP 1 ~ EXP 40)							
EXP-1	-	-	0.40	30.00	1.50	10.00	
EXP-2	-	-	0.40	60.00	1.50	10.00	
EXP-3	-	-	0.40	90.00	1.50	10.00	
EXP-4	-	-	0.20	30.00	1.50	10.00	
EXP-5	-	-	0.20	60.00	1.50	10.00	
EXP-6	-	-	0.20	90.00	1.50	10.00	
EXP-7	-	-	0.20	30.00	1.50	10.00	
EXP-8	-	-	0.20	120.00	1.50	10.00	
EXP-9	-	-	0.20	120.00	1.50	10.00	
EXP-10	-	-	0.20	120.00	1.50	4.50	
EXP-11	-	-	0.20	120.00	1.50	4.50	
EXP-12	-	-	0.20	120.00	1.50	15.00	
EXP-13	-	-	0.20	120.00	1.50	15.00	
EXP-14	-	-	0.20	120.00	0.50	15.00	
EXP-15	-	-	0.10	95.00	0.50	15.00	RF Interference
EXP-16	-	-	0.20	120.00	0.50	15.00	
EXP-17	-	-	0.20	120.00	0.50	10.00	
EXP-18	-	-	0.20	120.00	0.50	10.00	
EXP-19	-	-	0.20	120.00	0.50	4.50	
EXP-20	-	-	0.20	120.00	0.50	4.50	
EXP-21	-	-	0.30	120.00	3.00	4.50	
EXP-22	-	-	0.40	120.00	3.00	4.50	

EXP NO.	Relative Humidity and Temperature (%)	(°C)	O_2 Concentration (volume %)	Total Arc Duration (minutes)	Initial Interelectrode Gap (cm)	Argon Gas Flow Rate (slpm)	Remarks
EXP-23	-	-	0.30	120.00	3.00	10.00	
EXP-24	-	-	0.30	120.00	3.00	10.00	
EXP-25	-	-	0.20	120.00	3.00	15.00	
EXP-26	-	-	0.20	120.00	3.00	15.00	
EXP-27	-	-	0.10	54.00	3.00	4.50	
EXP-28	0.90	20.80	0.10	90.00	3.00	4.50	
EXP-29	0.90	20.30	0.10	100.00	3.00	0.00	Self-Extinguished
EXP-30	0.70	20.70	0.10	120.00	1.50	0.00	
EXP-31	0.60	20.40	0.10	120.00	0.50	0.00	
EXP-32	0.70	20.60	0.10	84.00	3.00	4.50	Arcing
EXP-33	1.80	21.00	0.10	120.00	3.00	4.50/15.00	Changing AR
EXP-34	0.90	20.60	0.10	120.00	3.00	0.00	Anode Thread
EXP-35	0.90	20.80	0.10	60.00	3.00	4.50/15.00	Changing AR
EXP-36	0.80	20.70	0.10	105.00	3.00	0.00	Self-Extinguished
EXP-37	1.10	20.80	0.10	120.00	1.50	0.00	
EXP-38	0.70	20.80	0.10	120.00	0.50	0.00	
EXP-39	1.00	20.90	0.10	180.00	0.5/3.0/0.5	0.00	Changing Gap
EXP-40	1.30	20.50	0.10	120.00	0.50	0.00	
300 A Experiments (Cathode I, EXP 41 ~ EXP 68)							
EXP-41	1.30	20.70	0.10	30.00	1.50	10.00	
EXP-42	1.20	20.90	0.10	30.00	1.50	10.00	
EXP-43	1.30	20.50	0.10	60.00	1.50	10.00	
EXP-44	1.40	21.00	0.10	60.00	1.50	10.00	
EXP-45	0.90	20.20	0.10	10.00	1.50	10.00	

EXP NO.	Relative Humidity and Temperature (%)	(°C)	O_2 Concentration (volume %)	Total Arc Duration (minutes)	Initial Interelectrode Gap (cm)	Argon Gas Flow Rate (slpm)	Remarks
EXP-46	0.90	20.70	0.10	10.00	1.50	10.00	
EXP-47	1.00	20.80	0.10	30.00	1.50	0.00	
EXP-48	1.00	20.50	0.10	30.00	1.50	0.00	
EXP-49	0.90	20.90	0.10	30.00	1.50	4.50	
EXP-50	0.80	20.90	0.10	30.00	1.50	4.50	
EXP-51	1.30	20.70	0.10	30.00	1.50	15.00	
EXP-52	1.20	20.80	0.10	30.00	1.50	15.00	
EXP-52-1	0.90	20.30	0.10	3.00	0.50	0.00	3 Minutes Run
EXP-53	1.30	22.70	0.10	30.00	0.50	4.50	
EXP-54	1.40	21.10	0.10	30.00	0.50	4.50	
EXP-55	1.90	20.80	0.10	30.00	0.50	10.00	
EXP-56	1.40	20.80	0.10	30.00	0.50	10.00	
EXP-57	1.40	20.80	0.10	30.00	0.50	15.00	
EXP-58	1.70	20.80	0.20	30.00	0.50	15.00	
EXP-59	1.50	21.10	0.10	30.00	3.00	0.00	
EXP-60	2.10	20.70	0.10	30.00	3.00	0.00	
EXP-61	1.30	20.70	0.20	30.00	3.00	4.50	
EXP-62	2.10	20.60	0.20	30.00	3.00	4.50	
EXP-63	2.00	20.40	0.20	30.00	3.00	10.00	
EXP-64	1.90	20.90	0.20	30.00	3.00	10.00	
EXP-65	1.70	20.40	0.20	30.00	3.00	15.00	
EXP-66	1.90	20.60	0.20	30.00	3.00	15.00	
EXP-67	1.50	20.60	0.10	40.00	3.00	4.50	
EXP-68	0.80	20.70	0.10	60.00	3.00	4.5/15/4.5	Changing AR

EXP NO.	Relative Humidity and Temperature (%)	(°C)	O_2 Concentration (volume %)	Total Arc Duration (minutes)	Initial Interelectrode Gap (cm)	Argon Gas Flow Rate (slpm)	Remarks
400 A Experiments (Cathode I, EXP 69 ~ EXP 73)							
EXP-69	1.60	21.20	0.10	21.50	1.50	0.00	
EXP-70	1.20	21.20	0.10	30.00	1.50	0.00	
EXP-71	1.30	21.00	0.10	30.00	1.50	0.00	
EXP-72	1.10	20.80	0.10	30.00	1.50	15.00	
EXP-73	1.70	21.10	0.10	30.00	1.50	15.00	
300 A Experiments (Cathode II, EXP 74 ~ EXP 83)							
EXP-74	2.20	20.80	0.10	30.00	0.50	15.00	
EXP-75	1.30	21.10	0.10	30.00	0.50	4.50	
EXP-76	1.80	20.90	0.10	30.00	0.5/0.7	0.00	Changing Gap
EXP-77	2.30	21.10	0.10	30.00	1.50	15.00	
EXP-78	2.10	21.20	0.10	30.00	1.50	10.00	
EXP-79	2.10	20.50	0.10	30.00	1.50	4.50	
EXP-80	1.20	20.80	0.10	30.00	1.50	0.00	
EXP-81	2.60	21.30	0.10	30.00	3.00	0.00	
EXP-82	2.20	21.20	0.10	30.00	3.00	4.50	
EXP-83	2.80	21.30	0.10	30.00	3.00	15.00	
300 A Experiments (Cathode I, EXP 84)							
EXP-84	1.40	21.30	0.10	60.00	3.00	4.50	

Appendix 3. Erosion Rate of The Graphite Cathode

EXP NO.	Arc Duration (minutes)	Arc Current (A)	Mass Change of The Graphite Cathode Before EXP (g)	After EXP (g)	Mass Change (g)	Erosion Rate (μg/C)
EXP-1	30.00	147.66	130.96	130.77	0.19	0.71
EXP-2	60.00	148.64	131.07	130.79	0.28	0.52
EXP-3	90.00	149.18	130.78	130.39	0.39	0.48
EXP-4	30.00	147.95	130.85	130.70	0.15	0.56
EXP-5	60.00	149.32	131.30	131.01	0.29	0.54
EXP-6	90.00	149.06	131.53	131.12	0.41	0.51
EXP-7	30.00	146.12	132.16	132.01	0.15	0.57
EXP-8	120.00	147.20	131.03	130.52	0.51	0.48
EXP-9	120.00	147.25	131.00	130.49	0.51	0.48
EXP-10	120.00	147.81	130.98	129.55	1.43	1.34
EXP-11	120.00	147.27	131.14	129.96	1.18	1.11
EXP-12	120.00	147.97	132.13	131.61	0.52	0.49
EXP-13	120.00	147.29	130.30	129.79	0.51	0.48
EXP-14	120.00	148.06	131.00	130.53	0.47	0.44
EXP-16	120.00	147.23	131.47	130.98	0.49	0.46
EXP-17	120.00	147.03	131.89	131.39	0.50	0.47
EXP-18	120.00	147.72	130.91	130.42	0.49	0.46
EXP-19	120.00	148.41	131.28	130.76	0.52	0.49
EXP-20	120.00	147.05	130.75	130.22	0.53	0.50
EXP-21	120.00	148.59	131.28	129.60	1.68	1.57
EXP-22	120.00	146.50	131.28	129.95	1.33	1.26
EXP-23	120.00	147.08	131.35	130.80	0.55	0.52
EXP-24	120.00	148.57	131.15	130.58	0.57	0.53

EXP NO.	Arc Duration (minutes)	Arc Current (A)	Mass Change of The Graphite Cathode Before EXP (g)	After EXP (g)	Mass Change (g)	Erosion Rate (μg/C)
EXP-25	120.00	147.37	131.10	130.60	0.50	0.47
EXP-26	120.00	147.82	131.12	130.60	0.52	0.49
EXP-27	54.00	147.79	132.03	131.74	0.29	0.61
EXP-28	90.00	146.70	131.63	130.78	0.85	1.07
EXP-29	100.00	146.25	131.04	129.61	1.43	1.63
EXP-30	120.00	146.70	132.04	129.28	2.76	2.61
EXP-31	120.00	147.22	131.65	130.99	0.66	0.62
EXP-34	120.00	145.54	130.60	129.46	1.14	1.09
EXP-36	105.00	145.94	131.34	130.09	1.25	1.36
EXP-37	120.00	145.38	130.79	128.67	2.12	2.03
EXP-38	120.00	149.07	130.90	130.76	0.14	0.13
EXP-40	120.00	149.26	130.92	130.61	0.31	0.28
EXP-41	30.00	299.56	131.14	130.53	0.61	1.13
EXP-42	30.00	299.85	130.80	130.24	0.56	1.04
EXP-43	60.00	300.41	131.01	129.80	1.21	1.12
EXP-44	60.00	300.07	131.53	130.39	1.14	1.06
EXP-45	10.00	301.98	130.50	130.31	0.19	1.05
EXP-46	10.00	302.48	131.72	131.47	0.25	1.38
EXP-47	30.00	297.91	130.92	130.57	0.35	0.65
EXP-48	30.00	298.80	131.35	130.96	0.39	0.73
EXP-49	30.00	299.26	131.47	130.83	0.64	1.19
EXP-50	30.00	298.53	130.14	129.55	0.59	1.10
EXP-51	30.00	299.64	130.53	129.96	0.57	1.06
EXP-52	30.00	298.09	130.51	129.95	0.56	1.04
EXP-53	30.00	301.46	131.86	131.73	0.13	0.24
EXP-54	30.00	299.89	130.98	130.74	0.24	0.44

EXP NO.	Arc Duration (minutes)	Arc Current (A)	Mass Change of The Graphite Cathode Before EXP (g)	After EXP (g)	Mass Change (g)	Erosion Rate (μg/C)
EXP-55	30.00	300.16	130.50	130.26	0.24	0.44
EXP-56	30.00	300.40	131.47	131.22	0.25	0.46
EXP-57	30.00	300.38	131.03	130.81	0.22	0.41
EXP-58	30.00	300.65	131.73	131.46	0.27	0.50
EXP-59	30.00	297.89	131.43	131.11	0.32	0.60
EXP-60	30.00	298.98	130.83	130.52	0.31	0.58
EXP-61	30.00	294.22	130.87	130.33	0.54	1.02
EXP-62	30.00	293.05	131.13	130.56	0.57	1.08
EXP-63	30.00	295.81	131.00	130.49	0.51	0.96
EXP-64	30.00	297.14	132.15	131.63	0.52	0.97
EXP-65	30.00	294.51	130.93	130.44	0.49	0.92
EXP-66	30.00	297.35	132.23	131.71	0.52	0.97
EXP-67	40.00	292.57	130.87	130.02	0.85	1.21
EXP-69	21.50	388.69	131.21	130.84	0.37	0.74
EXP-70	30.00	386.95	130.81	130.27	0.54	0.78
EXP-71	30.00	387.89	130.50	129.95	0.55	0.79
EXP-72	30.00	386.47	131.73	130.73	1.00	1.44
EXP-73	30.00	383.76	131.42	130.29	1.13	1.64
EXP-74	30.00	298.46	46.13	45.75	0.38	0.71
EXP-75	30.00	299.70	46.31	46.04	0.27	0.50
EXP-77	30.00	296.41	46.42	45.78	0.64	1.20
EXP-78	30.00	299.13	45.72	45.04	0.68	1.26
EXP-79	30.00	296.05	43.85	43.12	0.73	1.37
EXP-80	30.00	297.06	46.17	45.75	0.42	0.79
EXP-81	30.00	295.32	46.33	46.03	0.30	0.56
EXP-82	30.00	298.00	46.24	45.51	0.73	1.36

EXP NO.	Arc Duration (minutes)	Arc Current (A)	Mass Change of The Graphite Cathode Before EXP (g)	After EXP (g)	Mass Change (g)	Erosion Rate (μg/C)
EXP-83	30.00	293.29	46.22	45.56	0.66	1.25
EXP-84	60.00	287.63	131.29	129.71	1.58	1.53

Appendix 4. Separation of The Overall ΔV into Stable and Unstable ΔV

EXP NO.	Arc Duration (minutes)	The Gap (cm)	AR Flow Rate (slpm)	Arc Current (A)	The Overall V & ΔV		Stable V, ΔV, ΔV/V, & Time				Unstable V, ΔV, ΔV/V, & Time			
					V (V)	ΔV (V)	V (V)	ΔV (V)	ΔV/V	s-time (minutes)	V (V)	ΔV (V)	ΔV/V	u-time (minutes)
EXP-1	30.00	1.50	10.00	147.66	24.76	0.99	24.76	0.99	0.04	26.88				
EXP-2	60.00	1.50	10.00	148.64	24.74	1.66	24.74	1.66	0.07	56.87				
EXP-3	90.00	1.50	10.00	149.18	17.64	1.16	17.64	1.16	0.07	86.98				
EXP-4	30.00	1.50	10.00	147.95	25.00	1.09	25.00	1.09	0.04	26.95				
EXP-5	60.00	1.50	10.00	149.32	24.80	2.48	24.80	2.48	0.10	56.90				
EXP-6	90.00	1.50	10.00	149.06	22.28	2.01	22.28	2.01	0.09	86.99				
EXP-7	30.00	1.50	10.00	146.12	24.59	1.02	24.59	1.02	0.04	26.92				
EXP-8	120.00	1.50	10.00	147.20	24.09	2.01	24.09	2.01	0.08	116.98				
EXP-9	120.00	1.50	10.00	147.25	25.35	1.61	25.35	1.61	0.06	116.97				
EXP-10	120.00	1.50	4.50	147.81	30.67	6.53	24.81	1.27	0.05	44.94	34.35	5.76	0.17	71.87
EXP-11	120.00	1.50	4.50	147.27	28.80	7.26	22.71	1.17	0.05	39.43	31.92	7.09	0.22	77.27
EXP-12	120.00	1.50	15.00	147.97	25.63	1.80	25.63	1.80	0.07	116.98				
EXP-13	120.00	1.50	15.00	147.29	25.30	1.65	25.30	1.65	0.07	116.97				
EXP-14	120.00	0.50	15.00	148.06	21.28	1.02	21.28	1.02	0.05	117.00				
EXP-15	95.00	0.50	15.00	145.32	21.82	1.01	21.82	1.01	0.05	66.13				
EXP-16	120.00	0.50	15.00	147.23	17.46	1.37	17.46	1.37	0.08	116.99				
EXP-17	120.00	0.50	10.00	147.03	22.86	2.44	22.86	2.44	0.11	116.86				
EXP-18	120.00	0.50	10.00	147.72	20.73	1.42	20.73	1.42	0.07	116.96				
EXP-19	120.00	0.50	4.50	148.41	19.13	2.63	19.13	2.63	0.14	116.98				
EXP-20	120.00	0.50	4.50	147.05	20.90	2.74	20.90	2.74	0.13	116.98				
EXP-21	120.00	3.00	4.50	148.59	34.83	13.64	24.80	1.38	0.06	62.71	46.45	12.15	0.26	54.11
EXP-22	120.00	3.00	4.50	146.50	35.90	13.41	27.99	1.62	0.06	73.11	49.09	14.03	0.29	43.71
EXP-23	120.00	3.00	10.00	147.08	28.57	3.07	27.55	1.41	0.05	79.69	30.73	4.29	0.14	37.31
EXP-24	120.00	3.00	10.00	148.57	32.10	3.51	30.77	1.38	0.04	76.87	34.64	4.76	0.14	39.95
EXP-25	120.00	3.00	15.00	147.37	29.67	2.12	29.67	2.12	0.07	116.99				
EXP-26	120.00	3.00	15.00	147.82	29.75	2.21	29.75	2.21	0.07	116.99				
EXP-27	54.00	3.00	4.50	147.79	29.00	1.66	29.00	1.66	0.06	50.35				
EXP-28	90.00	3.00	4.50	146.70	34.71	12.36	28.07	1.88	0.07	59.42	49.12	13.15	0.27	27.28
EXP-29	100.00	3.00	0.00	146.25	42.24	16.60	32.43	1.86	0.06	48.50	52.02	18.86	0.36	48.81
EXP-30	120.00	1.50	0.00	146.70	42.64	12.04	23.58	1.28	0.05	24.98	47.78	7.69	0.16	91.86
EXP-31	120.00	0.50	0.00	147.22	26.46	7.27	19.64	1.22	0.06	49.18	31.42	5.63	0.18	67.64

EXP NO.	Arc Duration (minutes)	The Gap (cm)	AR Flow Rate (slpm)	Arc Current (A)	The Overall V & ΔV		Stable V, ΔV, ΔV/V, & Time				Unstable V, ΔV, ΔV/V, & Time			
					V (V)	ΔV (V)	V (V)	ΔV (V)	ΔV/V	s-time (minutes)	V (V)	ΔV (V)	ΔV/V	u-time (minutes)
EXP-32	84.00	3.00	4.50	146.04	35.99	12.52	28.67	1.43	0.05	42.26	48.93	12.95	0.26	23.86
EXP-34	120.00	3.00	0.00	145.54	38.33	12.31	31.31	1.46	0.05	58.66	45.39	14.23	0.31	58.03
EXP-36	105.00	3.00	0.00	145.94	41.95	13.57	33.98	1.74	0.05	38.84	46.89	15.25	0.33	62.77
EXP-37	120.00	1.50	0.00	145.38	38.11	11.76	25.41	1.56	0.06	46.86	46.60	7.00	0.15	69.97
EXP-38	120.00	0.50	0.00	149.07	17.73	0.93	17.73	0.93	0.05	116.85				
EXP-40	120.00	0.50	0.00	149.26	19.38	2.01	19.38	2.01	0.10	116.99				
EXP-41	30.00	1.50	10.00	299.56	29.44	2.31	29.44	2.31	0.08	26.84				
EXP-42	30.00	1.50	10.00	299.85	29.97	2.80	29.97	2.80	0.09	27.34				
EXP-43	60.00	1.50	10.00	300.41	29.35	2.19	29.35	2.19	0.07	56.84				
EXP-44	60.00	1.50	10.00	300.07	28.68	2.84	28.68	2.84	0.10	56.84				
EXP-45	10.00	1.50	10.00	301.98	26.19	1.38	26.19	1.38	0.05	6.84				
EXP-46	10.00	1.50	10.00	302.48	26.69	2.25	26.69	2.25	0.08	6.84				
EXP-47	30.00	1.50	0.00	297.91	29.56	6.90	25.02	0.95	0.04	17.73	38.41	4.44	0.12	8.95
EXP-48	30.00	1.50	0.00	298.80	31.82	8.08	25.29	1.54	0.06	14.38	39.43	5.51	0.14	12.30
EXP-49	30.00	1.50	4.50	299.26	28.87	3.40	26.56	1.15	0.04	3.81	29.27	3.50	0.12	22.87
EXP-50	30.00	1.50	4.50	298.53	33.27	5.01	27.86	0.73	0.03	6.99	35.18	4.44	0.13	19.69
EXP-51	30.00	1.50	15.00	299.64	28.92	2.07	28.92	2.07	0.07	26.84				
EXP-52	30.00	1.50	15.00	298.09	27.85	1.86	27.85	1.86	0.07	26.84				
EXP-53	30.00	0.50	4.50	301.46	24.30	1.20	24.30	1.20	0.05	26.84				
EXP-54	30.00	0.50	4.50	299.89	22.62	1.29	22.62	1.29	0.06	26.84				
EXP-55	30.00	0.50	10.00	300.16	24.13	0.80	24.13	0.80	0.03	26.84				
EXP-56	30.00	0.50	10.00	300.40	24.04	0.66	24.04	0.66	0.03	26.84				
EXP-57	30.00	0.50	15.00	300.38	24.64	1.14	24.64	1.14	0.05	26.84				
EXP-58	30.00	0.50	15.00	300.65	25.52	0.81	25.52	0.81	0.03	26.84				
EXP-59	30.00	3.00	0.00	297.89	38.90	4.45					38.90	4.45	0.11	26.84
EXP-60	30.00	3.00	0.00	298.98	36.28	2.49	36.28	2.49	0.07	26.84				
EXP-61	30.00	3.00	4.50	294.22	40.28	6.62	35.18	1.37	0.04	12.30	44.59	6.23	0.14	14.38
EXP-62	30.00	3.00	4.50	293.05	39.84	7.28	34.84	1.50	0.04	13.09	44.84	7.33	0.16	13.09
EXP-63	30.00	3.00	10.00	295.81	36.07	3.06	34.97	1.57	0.04	19.22	38.82	4.03	0.10	7.46
EXP-64	30.00	3.00	10.00	297.14	35.78	4.77	33.41	1.45	0.04	13.92	38.20	5.69	0.15	13.76
EXP-65	30.00	3.00	15.00	294.51	32.95	2.61	32.95	2.61	0.08	26.84				
EXP-66	30.00	3.00	15.00	297.35	34.11	2.86	34.11	2.86	0.08	27.34				
EXP-67	40.00	3.00	4.50	292.57	39.74	8.26	33.07	1.64	0.05	16.44	45.03	7.53	0.17	20.74

EXP NO.	Arc Duration (minutes)	The Gap (cm)	AR Flow Rate (slpm)	Arc Current (A)	The Overall V & ΔV		Stable V, ΔV, ΔV/V, & Time				Unstable V, ΔV, ΔV/V, & Time			
					V (V)	ΔV (V)	V (V)	ΔV (V)	ΔV/V	s-time (minutes)	V (V)	ΔV (V)	ΔV/V	u-time (minutes)
EXP-69	21.50	1.50	0.00	388.69	33.41	7.74	27.16	0.85	0.03	10.21	41.38	4.61	0.11	7.97
EXP-70	30.00	1.50	0.00	386.95	33.83	6.72	26.66	0.68	0.03	6.71	36.27	6.07	0.17	19.97
EXP-71	30.00	1.50	0.00	387.89	32.66	5.99	27.42	1.02	0.04	13.35	37.60	4.28	0.11	13.83
EXP-72	30.00	1.50	15.00	386.47	30.15	1.87	30.15	1.87	0.06	27.34				
EXP-73	30.00	1.50	15.00	383.76	30.71	2.20	30.71	2.20	0.07	26.84				
EXP-74	30.00	0.50	15.00	298.46	28.12	0.60	28.12	0.60	0.02	27.34				
EXP-75	30.00	0.50	4.50	299.70	26.78	0.90	26.78	0.90	0.03	27.84				
EXP-77	30.00	1.50	15.00	296.41	32.67	0.81	32.67	0.81	0.02	26.84				
EXP-78	30.00	1.50	10.00	299.13	33.48	0.84	33.48	0.84	0.03	27.34				
EXP-79	30.00	1.50	4.50	296.05	33.75	0.90	33.75	0.90	0.03	27.34				
EXP-80	30.00	1.50	0.00	297.06	32.16	1.93	32.16	1.93	0.06	27.34				
EXP-81	30.00	3.00	0.00	295.32	42.92	2.30	42.92	2.30	0.05	27.34				
EXP-82	30.00	3.00	4.50	298.00	42.16	1.41	42.16	1.41	0.03	27.34				
EXP-83	30.00	3.00	15.00	293.29	38.70	1.30	38.70	1.30	0.03	26.84				
EXP-84	60.00	3.00	4.50	287.63	48.92	12.94	34.42	1.57	0.05	12.42	52.98	11.75	0.22	44.76

Note: The Definition of Standard Deviation

$$s = \left[\frac{1}{n-1} \sum_{i=1}^{n} (x_i - \bar{x})^2 \right]^{0.5}$$

where s is the standard deviation; n is the number of the data; x_i is the data; $\bar{x}$ is the average of the data.